Integration of MEMS in Silicon Photonics

Alain Yuji TAKABAYASHI

Acknowledgements

I would like to start by thanking my thesis supervisor, Prof. Niels Quack, for providing not only the means and motivation for the work that I carried out with the Quack group at EPFL but for also being a constant source of encouragement and support. I am grateful for the positive and collaborative working environment that he fostered in the group and for always making himself available. I want to thank my MORPHIC consortium project partners: even though our meetings rarely ended on time, being a part of these discussions helped me appreciate the greater signficance and context of my work. A special thank you to Pierre Edinger, Prof. Kristinn B. Gylfason, and Prof. Wim Bogaerts, who as collaborators and co-authors to all my published/presented works provided critical feedback and ideas for the MEMS designs and cleanroom processing. On that note, I would like to thank the staff at CMi for their unwavering support in discussing process flows and for maintaining the impressive cleanroom infrastructure. It would be remiss of me to not thank the individuals of Q-Lab, Beatrice Raball, Marcell Kiss, Teodoro Graziosi, Sichen Mi, Adrien Toros, Yu Zhang, Gergely Huszka, Anna Varini, Elena Losero, Duarte Silva, Luigi Basso, Hernán Furci, Anton Lagosh, Hamed Sattari, Micol Previde Massara, and Dorian Herle for contributing to what I consider the perfect research group. It was a balance of technical prowess and intellectual stimulation with congeniality and simple fun: I hope you all know how grateful I am for your help and consider you all not just colleagues, but also life-long friends. Thank you especially Hamed for your optics expertise and thank you Duarte for your countless hours spent in lab measuring devices: you two contributed a lot to this work as well. Micol and Dorian, we "Three Amigos" surely had some good times in and out of the cleanroom and office, and I will always look back fondly on our dinner parties and non-technical discussions. Dorian, I owe you a great deal of gratitude, not only for all the technical support and for the clever ideas you shared with me, but also for constantly being here for me in all aspects, all the way until this thesis was submitted. Not to forget those close to home and heart, I would like to thank Annie, Marie, Mrudhula, Ziga, and Léa for being a reason to not stay in the office all the time and to enjoy the beautiful things life has to offer besides Silicon Photonics. I also want to thank the friends at EPFL, in Zürich, and back in the U.S. who I may not have been able to mention by name, but also deserve acknowledgement for their friendship and support. And last, but not least, an enormous thank you to my family, who have always provided open ears and arms and never stopped believing in me, thank you for your love and support!

Lausanne, November 10, 2021   Alain Yuji Takabayashi

Abstract

Like integrated electronics, integrated photonics such as Silicon Photonics benefit from increased device-density on a single chip. Silicon is an excellent material for integrated photonics because its high refractive index allows devices to be made small, and the established silicon CMOS fabrication infrastructure provides a convenient route towards scaling up production. However, standard Silicon Photonics faces a bottleneck in scaling up device-density due to excessive power consumption and high optical losses associated with individual devices. Microelectromechanical systems (MEMS) provide a unique solution to this problem by providing a physical redistribution of optical media to perform the necessary active functions in photonic integrated circuits (PICs) with minimal power consumption and low loss.

This thesis tackles two important aspects needed for implementing large-scale MEMS-enabled PICs in silicon. First, the required microfabrication processes are developed for the first-time, by full process integration of MEMS in an established foundry platform, the Interuniversity Microelectronic Centre's (IMEC) iSiPP50G Silicon Photonics technology. By demonstrating MEMS-compatibility, the barrier to adopting this new technology is reduced, and the devices and circuits themselves benefit from co-integration with high-performance standard components. Second, a new class of electrostatic MEMS-enabled photonic building blocks are designed, simulated, and experimentally characterized. Demonstrated devices include a set of remarkably broadband (bandwidth > 80 nm) tunable couplers capable of continuous optical power tuning between output ports to produce extinction ratios greater than 20 dB with minimal insertion loss (reaching < 0.4 dB). In terms of switching, a very low-voltage, six-port count device and a particularly compact (65 µm x 62 µm) photonic MEMS switch with sub-microsecond switching time are also presented. Further MEMS-enabled functionality is demonstrated with a wavelength-selective add-drop filter and a discussion of phase-shifters and multi-device sub-circuits. These components can be repeated and combined with one another to create complex and reconfigurable networks, and therefore represent an essential stepping stone towards the realization of very large-scale PICs. Together, these key developments in microfabrication and device design promise PIC designers MEMS-enabled photonic components as standard elements in their circuits to efficiently implement functions such as switching, tuning, and filtering for application in photonic switch matrices, weighted interconnects for neural networks, and programmable PICs.

Keywords: microelectromechanical systems (MEMS), Silicon Photonics, microfabrication

Zusammenfassung

Wie der integrierte Schaltkreis profitiert auch eine integrierte Photonik-Plattform von einer erhöhten Bauelementendichte auf einem einzigen Chip. Silizium ist ein ideales Material für die integrierte Photonik, da sein hoher Brechungsindex es ermöglicht, die Bauteile klein zu halten und gleichzeitig bei der Produktion auf den Skaleneffekt der etablierten CMOS Fertigungsinfrastruktur zurückzugreifen. Bei der Standard-Silizium-Photonik gibt es jedoch einen Engpass bei der Erhöhung der Bauelementedichte aufgrund des übermäßigen Stromverbrauchs und der hohen optischen Verluste der einzelnen Bauelemente. Mikroelektromechanische Systeme (MEMS) bieten eine innovative Lösung für dieses Problem, indem sie eine physikalische Umverteilung optischer Medien ermöglichen, um die erforderlichen aktiven Funktionen in photonischen integrierten Schaltungen (PICs) mit minimalem Stromverbrauch und geringen Verlusten auszuführen.

Diese Doktorarbeit befasst sich mit zwei wichtigen Aspekten, die für die Verwirklichung großer MEMS-basierter PICs in Silizium erforderlich sind. Erstens werden die erforderlichen Mikrofabrikationsprozesse zum ersten Mal durch die vollständige Prozessintegration von MEMS in eine etablierte Foundry-Plattform entwickelt: die iSiPP50G Silicon Photonics-Technologie des Interuniversity Microelectronics Centre (IMEC). Durch den Nachweis der MEMS-Kompatibilität wird die Hürde für die Einführung dieser neuen Technologie gesenkt, als auch die Ko-Integration mit leistungsstarken Standardkomponenten ermöglicht. Zweitens wird eine neuartige Klasse elektrostatischer MEMS-gestützter photonischer Bausteine entworfen, simuliert und experimentell charakterisiert. Zu den demonstrierten Bauelementen gehören eine Reihe bemerkenswert breitbandiger (Bandbreite > 80 nm) abstimmbarer Koppler. Diese ermöglichen eine kontinuierliche optische Leistungsregelung zwischen Ausgängen, um Extinktionsverhältnisse von mehr als 20 dB bei minimaler Verlustleistung zu erreichen (< 0.4 dB). Des Weiteren werden zwei Schaltungen vorgestellt: eine mit sechs Anschlüssen welche mit sehr geringen Spannungen arbeitet und eine besonders kompakte (65 μm x 62 μm) photonische MEMS-Schaltung die Schaltzeiten im Submikrosekundenbereich aufweist. Weitere erforschte MEMS-basierte Elemente umfassen einen wellenlängenselektiven Add-Drop-Filter und Phasenschieber und Multi-Device-Teilschaltungen. All diese Komponenten können repliziert und miteinander kombiniert werden, um komplexe und rekonfigurierbare Systeme zu schaffen. Sie stellen daher ein wesentliches Fundament für die Realisierung von sehr großen PICs dar. Die hier vorgestellten Entwicklungen in der Mikrofertigung wie auch

im individuellen Komponentendesign eröffnen den Entwicklern von PICs die Möglichkeit, MEMS-fähige photonische Komponenten als Standardelemente in ihren Schaltungen einzusetzen. Sie ermöglichen eine effiziente Implementierung photonischer Schaltungen, Regeler, und Filter für Anwendungen in photonischen Schaltmatrizen, gewichteten Verbindungen für neuronale Netze und programmierbare PICs.

Schlüsselwörter: Mikroelektromechanische Systeme (MEMS), Silizium-Photonik, Mikrofabrikation

Contents

Contents

1 Introduction

Today, holding a real-time videocall with individuals halfway across the globe does not seem a large feat. However, this convenience has humble origins and is the culmination of many years of technological development. In fact, the earliest long-distance communication involved optical telegraphy, i.e., semaphores, such as fire beacons, smoke signals, and flags [1]. With the development and growth of electric power distribution in the 1800s, electrical telegraphs and subsequently, telephones, supplanted semaphores due to their ability to transmit information faster and over greater distances [2]. Roughly 100 years later, wireless communication first through radio, and then later television, was made possible; the key enabling technology for the latter was the vacuum tube.

The next step in this evolution, the development of semiconductor solid-state devices (i.e., transistors), which were more compact and consumed less power than vacuum tubes, introduced a new paradigm that has lasted for the past 80 years - scaling through enhanced integration. In general, by reducing physical dimensions, individual devices could be made faster and more power efficient. From a circuit-level perspective these smaller devices could also be connected to one another in more dense and sophisticated configurations to provide enhanced functionality. In fact, it would be difficult to find an electrical engineer or computer scientist unfamiliar with Gordon Moore's prescient prediction that "the complexity for minimum component costs has increased at a rate of roughly a factor of two per year" [3]. Although later revised to reflect a doubling every two years instead of one, the pervasiveness and long-standing impact of this observation is something that even those not in the field can profit from and appreciate. From easily accessible computation and communication through mobile devices, to the convenience offered by the internet's global reach in the infrastructural core, the drive towards miniaturization has entrenched itself in modern-day society.

The effects of this impressive scaling is nicely illustrated by comparing the first digital computer, the Electronic Numerical Integrator and Computer (ENIAC), with a top performance processor from today (**Figure 1.1**). The former occupied a staggering 167 m^2 of space, relied on 18'000 vacuum tubes, consumed 150 kW of power, and performed 5'000 instructions per second [4]. A representative example of the latter has a footprint of 74 mm^2, contains 3.8

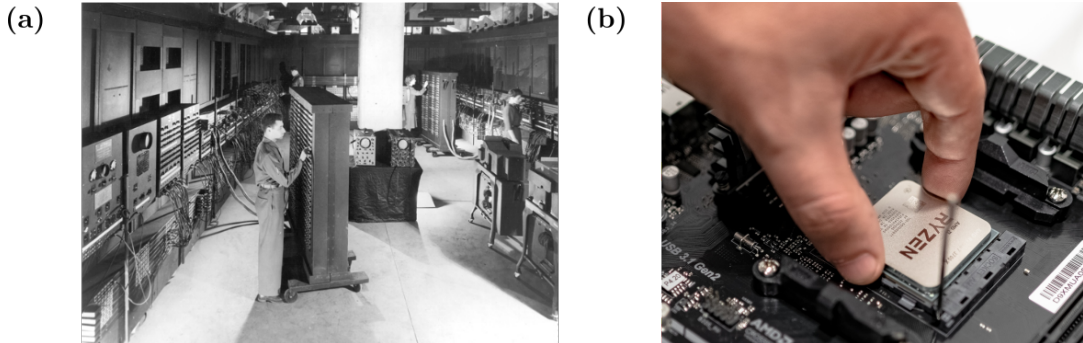billion transistors, consumes a modest 105 W, and executes hundreds of billions of instructions per second.

Figure 1.1 – Comparison of the (a) ENIAC (167 m^2) (Reprinted from [5], Public Domain) (b) modern-day microprocessor (74 mm^2) indicating the drastic reduction in dimensions made possible by scaling and enhanced integration (Reprinted from [6], Pexels License)

However, as device dimensions approach fundamental physical limits, a new focus on diversification of functionality has risen. This "More than Moore" as it is referred to, reflects a perspective whereby "added value to devices is provided by incorporating functionalities that do not necessarily scale according to "Moore's Law"" [7]. The focus is not on faster central processing units, more memory, or more sophisticated logic for better information processing, but rather on real-world interactions through sensing and actuation. Examples include sensory devices in the Internet of Things (IoT) such as wearables for personalized healthcare/monitoring and LIDAR for autonomous vehicles.

In parallel, a "Beyond Moore" trend for exploring material and technological alternatives beyond the standard scaling down of devices has grown. Among others, optical/photonic technologies, spintronic devices, and tunnel field-effect transistors (TFETs) have emerged as attractive candidates. This first category of photonic devices is already in a mature stage of development that has allowed them to be incorporated in commercial applications. For example, with global network traffic officially well within the "Zettabyte Era," (10^{21} bytes), energy-efficient optical interconnects and optical switching in datacenters have proven helpful in keeping pace with the heavy bandwidth demands of video services, cloud computing, and machine-learning applications [8]. An illustration providing context for these two burgeoning trends and how they can enhance system-value is given in **Figure 1.2**.

Integrated photonics and in particular Silicon Photonics, offers an interesting synthesis between "Beyond Moore" and "More than Moore" that follows the original guiding principle of scaling down and integrating more devices on a single chip while introducing novel and richer functionality. For example, integrated photonics provides a compact approach for precision metrology and spectroscopy, as well as optical coherence tomography (OCT) and quantum processing and communication [9].

Silicon, as the dominant material used in the electronics industry not only serves as an excel-
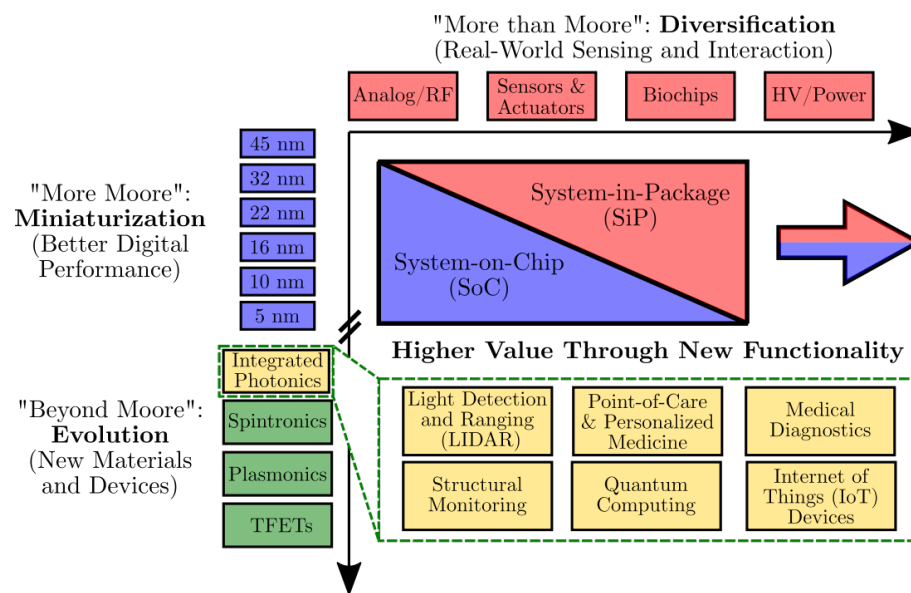
Figure 1.2 – Visualization of how system value can be increased by integrating new functionality alongside powerful computation and exploring new material and device technologies as an alternative to continued miniaturization. The highlighted field of integrated photonics combines a new "technology" with diverse application-areas ranging from medical diagnostics to quantum computing.

lent semiconductor for conduction of electrical signals, but can also be used in conjunction with its natural oxide, SiO_2 to confine and guide optical signals. As such, it is possible to leverage the decades of technical knowledge that semiconductor manufacturers have acquired, to produce sophisticated, high-volume, and consequently, low per-unit cost, photonic integrated circuits. In a manner that conspicuously mirrors the trend seen in electronics, photonics now undergoes a scaling trend of its own and this is nicely captured in **Figure 1.3**, which compares the dimensions of a modern day optical switch with a Silicon Photonic-based switch matrix containing several of the devices fabricated in this thesis.

The Integrated Photonics Systems Roadmap - International (IPSR-I) recently provided a set of high-level goals for Silicon Photonics in the next 20 years, with "short cycle times from prototype to commercial manufacturing" identified as a specific milestone [11]. Reconfigurable or programmable photonic circuits fulfill this requirement because they provide a general, multi-use platform suitable for accelerating design prototype development [12]. Furthermore, technologies that can provide such functionality are also typically able to compensate for Silicon Photonic's inherent sensitivity to changes in device geometry caused by stochastic variation in fabrication. In fact, it is the inability to efficiently compensate for these variations that currently holds back the desired scaling needed for larger and more complex photonic integrated circuits (PICs). Photonic microelectromechanical systems (MEMS) offer a potential route to achieving this tuning and performing active functions like switching, wavelength-selective filtering, and phase-shifting.

(a)

(b)

8 x 8
Switch
Matrix

Figure 1.3 – Comparison of (a) CALIENT's S320 Optical Switch which has a 7-rack unit form factor (44.5 cm x 31.0 cm x 48.3 cm) and provides a 320 x 320 switching configuration (Reprinted with permission from [10], Calient Technologies) with (b) a 725 μm thick Silicon Photonics chip that provides an 8 x 8 on-chip switch network with a 3 mm x 3 mm footprint

1.1 Thesis Scope and Outline

This work addresses the current bottleneck in the continued scaling of PICs by developing a process flow for the first-time integration of MEMS with an existing Silicon Photonics platform. However, this thesis encompasses more than the fabrication feat of introducing a new technology to a foundry. As MEMS-enabled photonic devices can also perform active functions, this work performs the full design-fabrication-test cycle of several photonic MEMS components that are themselves, high-performance, compact, optical building blocks suitable for use in larger-scale systems. The confluence of electronics, mechanics, and optics and the desire to build smaller, faster, better systems can all be found with integrated Silicon Photonic MEMS and truly embodies the spirit of both "More than Moore" and "Beyond Moore."

2 Integrated Photonics

Increasing levels of integration has been key to the miniaturization of electronic devices and the continuous enhancement of computational power and functionality. The smartphone is a device that serves as a representative example of what can be achieved through integration. It incorporates the functionality of many standalone devices/products, e.g., physical maps, music players, calculators, digital cameras, etc. The space-savings alone of not needing to carry each of these individual items presents a tremendous convenience. Other interesting synergies include the automatic "geotagging" of photos/videos thanks to the GPS-camera integration and the ability to identify sounds and songs through the phone's microphone.

While these applications may seem superficial, "sensor fusion" is an interesting research topic, with one example being the use of smartphones' global positioning system (GPS) for probing crowd density in city-scale mass gatherings to prevent dangerous incidents [13]. Another example is the use of the smartphone microphone as a pre-diagnostic system for analyzing coughs, which could be symptomatic of a more serious illness [14]. In this sense, integration provides not only a more compact solution, but also one that is able to provide functionality beyond the sum of its parts.

The smartphone is a high-level example of integration wherein the final product consists of smaller sub-components, which are themselves the results of continued efforts to integrate more devices and functionality into a single unit. The integrated circuit (IC) can be considered one of these fundamental components in an electronic system and exemplifies the benefits that come through integration. The earliest electronic equipment was limited by the cost, size, and reliability of individual hand-soldered components, whose manufacturing was non-standardized [15]. Having functional, individual transistors was one feat, but producing them at large-scale directly alongside other components, such as resistors and capacitors, was an entirely different challenge. The monolithic integration of active and passive components onto a single semiconductor wafer or chip increased the volume of production, and lowered fabrication costs: this was the promise of the IC.

2.1 Overview of Photonic Integration

Early experimental work in optics relied on freely propagating beams that passed through bulky components separated by centimeter-scale distances and the full systems not only needed careful alignment, but were also sensitive to thermal, mechanical, and acoustic ambient changes [16, 17]. As such, these configurations more closely resembled the unwieldy, first-generation electronic circuits than the compact and sleek Photonic ICs (PICs), one might find in a modern-day optical transceiver. However, already then, it was proposed that a physically smaller arrangement would be preferable.

After the pioneering work of Prof. Charles Kao, who vindicated the feasibility of fiber optic communication by identifying the glass-impurities that led to high losses, researchers also began working on integrated optics. In particular, Ping King Tien proposed the following three guiding ideas that nicely summarize the initial endeavors in this emerging field [17].

1. Thin-film technology, which is already common in the electronics industry, can be used to create optical devices and circuits; dielectric films with a large refractive index contrast to their surroundings, for example, serve as ideal optical waveguides

2. Use waveguides as the basic interconnect structure between optical components for efficient transmission

3. By incorporating multiple optical components made of the same thin-films on a single substrate, it is possible to create large-scale PICs

As such, it became clear that guided-wave optics and a thin-film technology-based approach would be the two guiding elements of integrated photonics [17]. By depositing thin films at wafer-scale, and using the corresponding microfabrication processing techniques developed for electronics, it is possible to process multiple chips/dies in parallel and leverage existing fabrication technology, which drastically reduces the cost of production. Furthermore, by creating components all from the same material and connecting them with integrated interconnects, the overall system can be made more compact and reliable, as no additional assembly is required. The miniaturization of individual components allows for a greater packing density per unit area and in some cases can also boost performance, for example in terms of switching speed or power consumption.

Photonic integration provides many advantages in terms of performance, but because the field is less mature than its electronic counterpart, the application areas for PICs may be less well known. For those who spend an appreciable amount of time in front of a computer, it is nigh impossible to forgo an encounter with some kind of cloud computing data service. And while Apple, Microsoft, or Google, are not typically categorized as environmental menaces like ExxonMobil or BP, the annual power consumption of 200 terawatt hours (TWh) for their data centers paint a slightly different picture [18]. The datacenters operated by these technology

giants process the ever-increasing amount of internet- and mobile-data traffic and integrated optical interconnects are a viable solution for meeting their bandwidth and latency demands within a reasonable power budget [19].

As an another example, microwave photonics is a cross-disciplinary application of integrated photonics alongside radio frequency (RF) engineering enabling key functionalities that are either impossible or too difficult to implement solely in the RF domain [20]. Using the GHz-precision and large bandwidth available in the optical domain, PICs can perform high-fidelity signal processing on RF signals to boost system performance.

PICs can also be used in both biological- and light-sensing applications. With respect to the former, because of photons' sensitivity to the specific optical properties of a material, they can be used in label-free bio-sensing [21]. Using this approach, it is possible to identify air/water contaminants, and when the optical system is tuned to detect physiological abnormalities, can provide point-of-care and personalized biometric sensing. Light imaging, detection, and ranging (LiDAR) implemented on a PIC is an example of a light-sensing application that has been implemented to measure phase delays and Doppler frequency shifts in reflected light as a complement to conventional radar in order to reconstruct 3D images of objects [22]. This technology holds promise for sensing in autonomous vehicles where current implementations rely on moving parts and are hence large, slow, low-resolution, costly, and prone to mechanical vibration.

One final category where photonic integration finds use is in quantum computing based on photons instead of electrons, which allows the quantum computer to operate at room temperatures instead of at temperatures well below freezing. In fact, a recent demonstration by a photonic quantum computer performing Gaussian boson sampling, a computational task originally proposed to prove the "quantum advantage" over classical computers, indicated a speed advantage of a factor of 10^{14} over that of a supercomputer [23].

From quantum computing to bio-sensing and LiDAR, as intricate and impressive these PICs may be, like any integrated system, a PIC's functionality is realized through a collection of functional building blocks. It is the connecting of various blocks in varying numbers and topologies that allows for the realization of a variety of diverse circuits and systems.

2.2   Mathematical Framework for Light in PICs

Before delving into a discussion of PIC building blocks , it is instructive to establish a concise, yet sufficiently accurate model for the light interacting with these structures. Focusing on its wave-like nature, light in a medium can be represented as the vector field of a harmonic electromagnetic wave of the following form:

$$U(\vec{r}, t) = A(\vec{r}, t) e^{-j\left(\vec{k}\cdot\vec{r} - \omega t\right)} \tag{2.1}$$
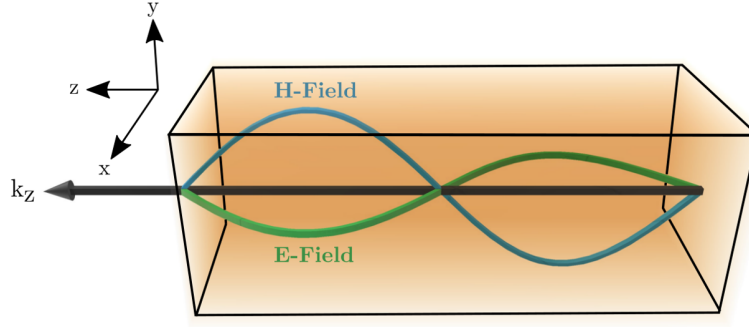
Figure 2.1 – Schematic diagram depicting a confined electromagnetic wave travelling in the positive z-direction

Where A represents the wave amplitude, which exhibits both spatial and temporal dependence, $\vec{k}$ is the wavenumber vector, and ω is the angular frequency.

Note that the modulus of the wavenumber vector is given by:

$$|\vec{k}| = \sqrt{k_x^2 + k_y^2 + k_z^2} = k = n\frac{\omega}{c} \equiv \frac{2\pi n}{\lambda} \tag{2.2}$$

Where k_x, k_y, k_z are the individual wavenumbers in each dimension, n is the refractive index of the material, c is the speed of light, and λ is the wavelength.

In PICs, the light-interacting structures typically have cross-sectional geometries that vary more in the direction perpendicular to the direction of propagation than along it [24]. Consequently, Equation 2.1 can be reduced to the vector field of an electromagnetic wave travelling in the positive z-direction, exhibiting harmonic time dependence (with $e^{j\omega t}$) as:

$$U(\vec{r}, t) \rightarrow A(x, y)\, e^{-jkz} \tag{2.3}$$

A visualization of such an electromagnetic wave confined to a PIC waveguide is shown in **Figure 2.1**.

In this form, $A(x, y)$ represents the amplitude of the wave and the exponential term e^{-jkz} is the phase factor. The phase factor is typically written as $e^{-\gamma z}$, where γ is the wave's propagation constant. However, both the wavenumber vector and the propagation constant quantify the same property, i.e., the wave's phase delay per unit propagation distance: one is simply a vector, while the other is its modulus.

Note that γ in turn can be expressed as $\gamma = \alpha + j\beta$, with α representing the attenuation constant, which for low-loss media is often neglected, and β the phase constant.

2.3   Functional Photonic Building Blocks

Classical building blocks in microelectronics consist of passive components like resistors, capacitors, inductors, and electrical interconnects, as well as active components like transistors and diodes. A similar taxonomy exists for integrated photonics and enables a richness of functionality that can be fully appreciated and exploited when multiple devices are composed with one another.

2.3.1   Passive Components

Schematic diagrams for five passive building blocks that have been used extensively, or form key operations, in the tunable couplers, photonic switches, and other MEMS-enabled photonic devices that have been designed in this thesis are presented in **Figure 2.2**. It should be noted that the components discussed here in detail represent a small subset of all passive photonic building blocks. They have been selected for their particular relevance to the devices presented later in this work and a short summary of other important integrated photonic components has been included at the end of this section.
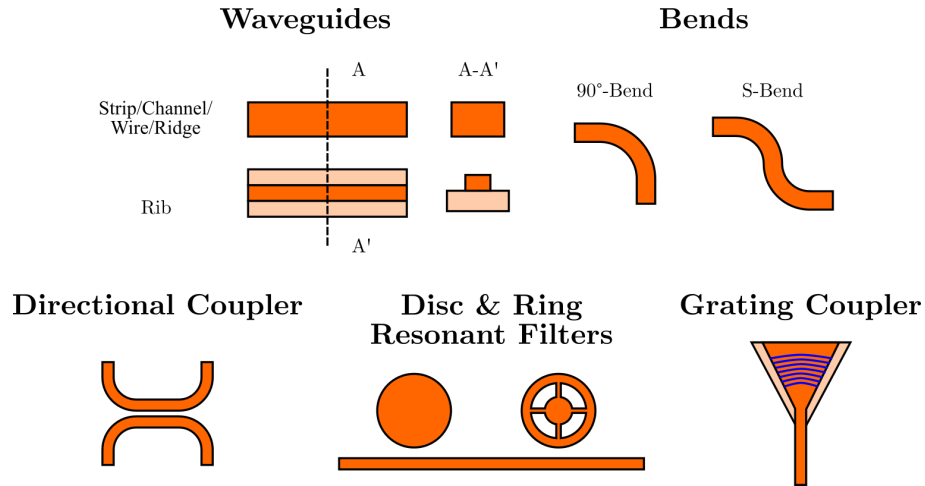
Figure 2.2 – Schematic depiction of the selected passive components employed in this work. Waveguides, both straight and bent, route light around PICs and directional couplers enable arbitrary power splitting ratios between various waveguides. Grating couplers serve as optical input(s)/output(s) (I/Os) to the PIC and the use of disk and ring resonant structures allow for wavelength-selective filtering.

The most basic, yet hardly the least significant, element of all PICs is the **waveguide**, which confines and guides light within a high refractive index material (the core) that is surrounded by a lower refractive index material (the cladding). Although a ray optics interpretation is useful for describing the propagation of injected light in waveguides with large dimensions, i.e., those greater than the wavelength, for sub-wavelength dimensions, like those used in PIC waveguides, a wave description is necessary.

In this case, for each particular optical frequency, ω, there is an associated vector field distribu-

tion where each wave can be described by Equation 2.3 with a unique propagation constant. The waves that propagate along the waveguide with only a constant change in phase are known as the waveguide *modes* and are unique in that their propagation constants allow these waves to constructively interfere with themselves to sustain their propagation. Waves that cannot be decomposed into one of these modes are not guided and may propagate into the cladding or be reflected.

The number of guided modes in a waveguide can be approximated as,

$$M \approx 4 \, \frac{width_{core} \cdot thickness_{core}}{\lambda} \left(n_{core}^2 - n_{cladding}^2 \right)$$ (2.4)

Where the term in parenthesis captures a proportionality to refractive index contrast, Δn. From this expression, it is clear that when single mode operation, as required by telecommunication and also as implemented in this work, is required, the physical dimensions of the core should be small and the refractive index contrast between core and cladding, large.

Propagation loss, typically reported in units of [dB/cm], is an important parameter characterizing the quality of a waveguide. Contributions arise from light-material interactions, which include absorption, imperfections in the waveguide's physical geometry or grain boundaries in polycrystalline materials which can lead to scattering, and imperfect guiding, which leads to radiative losses.

Waveguides can come in a variety of geometries including, strip (=channel, wire, ridge), rib, diffused, and buried channel. In the context of this work, however, priority will be given to the first two with discussions of other geometries included when appropriate. For strip waveguides, light is tightly confined (i.e., there is a strong refractive index contrast in all directions), which allows them to bend sharply with small bending radii, leading to more compact circuits. Rib waveguides on the other hand provide weaker confinement by only providing high contrast in the vertical direction and therefore, they require larger bends. However, the geometry of the rib variant limits interactions with potentially rough sidewalls, leading to lower propagation losses than strip waveguides.

The discussion of bending radii differences between strip and rib waveguides introduces the point that light in a PIC cannot exclusively travel in straight lines. Consequently, **waveguide bends** also become important photonic building blocks. These elements are typically circular arcs or S-bends that connect straight portions of waveguides, allowing light to be routed around other devices and to efficiently utilize chip area. It is worth noting that in a bend, light is no longer fully confined, with portions "leaking" out of the waveguide if the curvature (i.e., bending radius) is too small. This leaking leads to radiative losses and its minimization can be achieved by larger bends, which introduces a trade-off between bending losses and footprint.

Grating couplers serve as an out-of-plane coupling method commonly used as the optical I/O to interface PICs with off-chip devices. Their operation can be summarized as the constructive

interference of light waves at the grating teeth and the in-/out-coupling angle θ for an in-plane waveguide mode with effective refractive index n_{eff} is given by:

$$\Lambda n_{eff} - \Lambda n_{clad} \, sin\,\theta = m\lambda \tag{2.5}$$

Where Λ is the grating period, n_{clad} is the effective refractive index of the guided mode, and λ is the wavelength.

The **directional coupler** is a device that allows light propagating in a single waveguide to be proportionally distributed or combined into one or more outputs. It consists of two parallel waveguides, which for a specific distance, i.e., their *coupling length*, have a small gap spacing. This small gap allows the evanescent field, or portion of the guided light extending beyond the waveguide core, in the initial waveguide to excite/initiate a guided mode in the second waveguide. If the coupling length is long enough, 100% of the light can be transferred from one waveguide to the other.

The defining relationship for the coupling behavior in a directional coupler is:

$$\kappa^2 = \frac{P_{coupled}}{P_0} = sin^2\,(C \cdot L) \tag{2.6}$$

Where κ is the coupling, $P_{coupled}$ is the coupled power, P_0 is the input power, C is the coupling coefficient that is gap- and wavelength-dependent, and L is the coupling length.

By adjusting the coupling length or coupling gap, it is possible to design a directional coupler capable of achieving an arbitrary split in the optical power between two waveguides, as light that is not coupled over the coupling length continues in the original waveguide.

Disk and ring resonant filters are examples of devices that modify the spectral characteristics of light. In the standard configuration, light from a bus waveguide is coupled into a disk or ring structure that has an optical path length difference (OPD) given by:

$$OPD = 2\pi r n_{eff} \tag{2.7}$$

Where r is the disk/ring radius and n_{eff} is the effective refractive index.

When the wavelength of the light is an integer multiple of the OPD, the waves constructively interfere and this is known as the resonant condition. In this manner, only wavelengths that match the modes of the disk or ring resonator persist.

$$OPD = m\lambda_m \tag{2.8}$$

Where m is the mode number of the disk/ring resonator and λ_m is the resonant wavelength.

Because only a few wavelengths match this resonance/mode-matching condition, these devices act as optical filters, effectively removing them from the bus waveguide output. The primary difference between the disk and ring geometries is that it is harder to operate a disk resonator with a single mode on account of the wide cross section, but potentially offers lower scattering losses because only the outside edge is etched [25, 26].

With the preceding five elements, it is already possible to implement a simple, passive PIC that can for example perform the key add/drop operations needed in a wavelength division multiplexing (WDM) system. Light is injected into the circuit using the grating couplers and the straight and bent waveguides route it to the resonant filters that selectively add or remove wavelengths satisfying their resonance conditions. Additional operations can be implemented by expanding the selection of passive components and **Table 2.1** presents a more complete list of these devices alongside their key functions.

Device	Function
Waveguide Junction	Provide a transition between a strip waveguide to a rib waveguide or vice versa with low losses
Waveguide Crossing	Improve usage of space by allowing orthogonal waveguides to intersect with minimal crosstalk
Y-Branch	Provide 3-dB power splitting or combining between waveguides
Mach-Zehnder Interferometer (MZI)	Measure interference characteristics resulting from phase differences between light travelling along different paths
Multi-Mode Interferometer (MMI)	Expand single guided mode(s) to multiple modes, thereby enabling wavelength- and polarization-dependent power splitting
Waveguide Bragg Grating Filter	Reflect certain wavelengths and transmit others (i.e., filtering) using periodic variation in n_{eff}
Arrayed Waveguide Grating (AWG)	Multiplex multiple wavelengths into a single waveguide/fiber and vice versa using increments in optical path length
Rotator, Polarization Beam Splitter (PBS), Polarization-Splitter-Rotator (PSR)	Provide on-chip polarization handling of TE_0 and TM_0 modes to ensure proper function of polarization-dependent components
Edge Coupler	Polarization-independent coupling of light into a PIC with very low loss

Table 2.1 – Additional Key Passive Photonic Building Blocks

2.3.2   Active Components

A visual summary of the three primary active building blocks in PICs is provided in **Figure 2.3**. Note that other types of modulators exist; the presented two are simply commonly used variants.
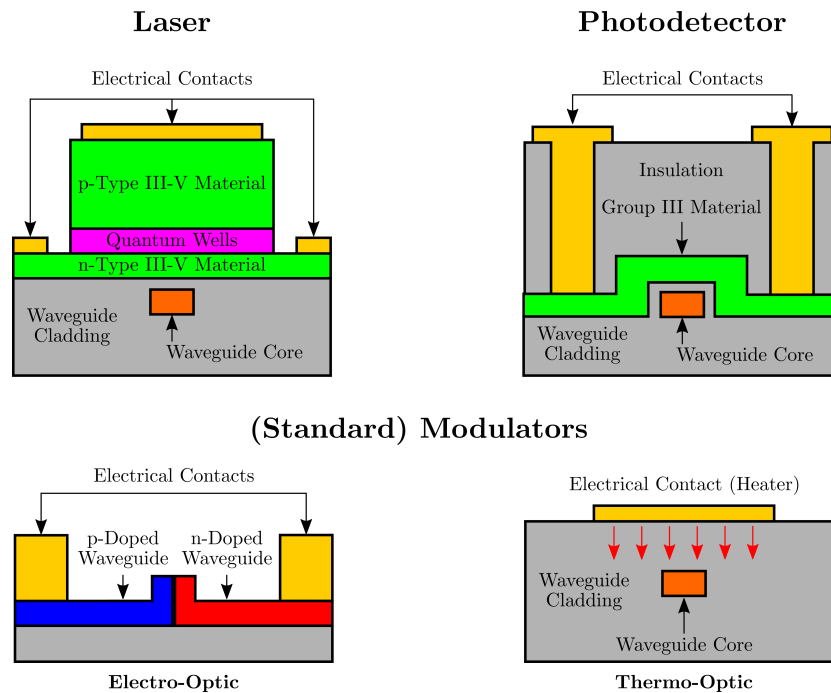

Figure 2.3 – Schematic diagram depicting the primary active components used in PICs. Active components utilize electrical and optical effects to generate, modulate, and detect light. Light generated by a laser source can be coupled into a PIC through a grating coupler and then routed via waveguides to passive devices, or to modulators for particular functions like phase shifting, switching, or variable power coupling. Once a particular operation has been performed, instead of coupling light back out of the PIC and measuring the light characteristics with a power detector, the analysis can be performed in the electrical domain by a photodetector.

Lasers are a key active device and provide the optical input to PICs; they can be integrated on-chip, or have their light coupled in. Structurally, they consist of a gain medium that allows light to be amplified by means of stimulated emission, a mechanism to energize the gain medium, and a structure for optical feedback, e.g., an optical cavity. Operationally, an electrical or optical source energizes or excites the gain medium such that it undergoes population inversion so that the rate of stimulated emission in the medium is larger than the rate of absorption. The gain medium is enclosed in an optical cavity so that light circulates back and forth and is subsequently amplified after each passing. This feedback mechanism efficiently amplifies light of particular wavelengths and continues until one such wavelength (frequency) dominates; this becomes the frequency of the laser, which is a coherent beam.

PICs typically employ semiconductor-based **photodetectors** that convert photons into current. More specifically, the absorption of photons with an energy equal to or greater than

the bandgap of a material $E = h\nu \geq E_g$ generates electron-hole pairs. Their generation and subsequent movement in the conduction and valence band for electrons and holes, respectively, under the influence of an applied electric field constitute the photocurrent. Typically, photodetectors consists of p-i-n diodes that have been reverse-biased so that the electron-hole pairs generated in the wide intrinsic region are quickly swept to and collected at the contacts.

Optical modulation, or the modification of a variety of a light wave's properties (e.g., phase, power, direction, polarization, etc.) by an external stimulus is performed by a **modulator**. These devices typically perform electro-optical transduction by taking advantage of Pockels/Kerr, Franz-Keldysh, carrier-based, thermal, and mechanical effects to change the refractive index or absorption in a material. Note that not all materials exhibit each of these mechanisms and that the speed and magnitude of the effects varies as well. In fact, the order from Pockels/Kerr to mechanical reflects a decrease in the speed of the effect, while at the same time indicating a gradual increase in its magnitude. Generally speaking, the stronger the effect, the slower it can be enacted.

The Pockels/Kerr effects are electro-optic phenomena whereby application of an electric field induces a linear or quadratic, for the Pockels and Kerr effects, respectively, change in the effective refractive index of a material. This change is nearly instantaneous but requires high electric field, and in the case of the Pockels effect, only occurs in materials lacking centrosymmetry. Application of an electric field can also instigate changes in the optical absorption by a semiconductor via the Franz-Keldysh effect. However, this effect also requires high electric fields and only exists in uniform, bulk semiconductors with the correct bandgap structure (e.g., III-V semiconductors and SiGe compounds).

The refractive index of a material exhibits dependence on the local carrier density; therefore, modulation of the free-carrier density in a waveguide can modulate its refractive index. Such carrier-based modulation, also referred to as plasma dispersion, can inject carriers via a p-i-n diode, deplete them in a p-n diode, or accumulate them in a capacitor. Devices relying on the last two variants can be quite fast as their speed is only limited by the RC time constant of the driving circuitry.

Many materials' refractive indices exhibit a temperature dependence dn/dT thereby enabling the use of heaters to produce changes in the refractive index. Typically, such devices are implemented as metallic resistors through which current is driven such that heat is generated. While the efficiency and speed of this mechanism depends heavily on the thermo-optic coefficients of a material, it is in general not a power-efficient modulation scheme and thermal crosstalk can be problematic. Waveguide displacement on the other hand, produces a physical redistribution of optically-active material, to modify the n_{eff} of guided modes. Even if there is no displacement, material strain can also produce a change in refractive index [27]. In both cases, if the displacement or strain can be produced using electrostatic actuation, this method of physical modulation is a power-efficient alternative to thermal tuning and in fact produces the strongest electro-optic effect.

2.4   Material Platforms for Integrated Photonics

Having identified the principle functional building blocks for integrated photonics, it is instructive to examine the various materials that are amenable to implementing these devices. There are four mature technology platforms, III-V semiconductors like indium phosphide (InP), planar lightwave circuits (PLC) based on silica (SiO_2), Silicon Photonics, and silicon nitride. Other material platforms like lithium niobate ($LiNbO_3$), aluminum nitride, and diamond also exist, but are in a nascent stage of integration and will therefore only be discussed in brief.

For the basis of comparison, it is instructive to not only look at the propagation loss, but also at the refractive index difference or contrast,

$$\Delta = \frac{n_{core} - n_{cladding}}{n_{core}} \tag{2.9}$$

Assuming that the core and cladding themselves can be made small, light confined in materials with high refractive index contrast can efficiently follow waveguides that make tight bends and the resulting circuits can be made more compact. As a quantitative measure, Melloni provides an approximation for the minimum bending radius that guarantees 0.1 dB/rad of radiation loss [28]:

$$R_{min} \approx 5\Delta n^{-1.5} \left[\mu m \right] \tag{2.10}$$

The range of wavelengths for which each material can guide light also plays an important role in what end-applications each technology platform finds use.

Silica, or silicon dioxide, as the material of choice in fiber optic communication is an ideal candidate to begin the evaluation of materials for photonic integration. It is a material that is well understood, with a proven track record for high performance, has a refractive index of $n = 1.44$, and exhibits optical transparency from 200 nm to 3.5 - 5 µm. While propagation loss in silica-based optical fibers is typically less than 0.2 dB/km, on-chip waveguides in silica exhibit losses orders of magnitude greater, with record low propagation losses of 0.045 dB/m [29, 30]. This discrepancy can be attributed to the difference in physical dimensions of the cores in optical fiber and integrated waveguides: for the former, the core diameter is roughly 10 µm, while for integrated waveguides, the core has dimensions roughly on the order of 0.2 x 0.5 µm. For a smaller core cross-section, a more significant portion of the guided mode interacts with the structures' edges, which if rough, can lead to enhanced scattering losses.

In terms of structure, silica waveguide PLCs typically consist of a planar arrangement of glass waveguides buried in a glass of lower refractive index. The higher refractive index in the core can be achieved through germanium (Ge), phosphorous (P), or boron (B) doping, resulting in

index differences below 1 %, typically around 0.69%; however, one demonstration of Ge:SiO$_2$ achieved a difference of 3.5% [31]. As a result of the relatively low index contrast in silica PLCs, the minimum achievable radius of curvature of waveguides ranges from 5 mm to 7 mm. Consequently, compact devices and circuits are elusive and the possibility to increase device density for large scale integration is small.

Despite its disadvantage with regard to scaling and high-density integration, silica still enjoys significant success due to its reliability, low insertion loss, integration capability, and ease of coupling to optical fibers [32]. With regard to this final point, because silica waveguides have roughly equal indices of refraction to the optical fiber with which they interface, losses at the fiber-chip junction can be minimized. Specific devices implemented in this technology primarily include passives such as optical couplers/splitters and arrayed waveguide gratings (AWGs) for wavelength de/multiplexing.

If silica PLC technology can be considered the material platform of choice for low-loss passives, then the **III-V InP**-based platform is the preferred material for active component integration. Development of the indium gallium arsenide phosphide (InGaAsP)/InP material system began in the 1980s following a demand for monolithic integration in PICs. High-performance (i.e., low-loss) passive components that still required off-chip optical I/O and detection would be inherently more lossy, due to the requisite in-/out-coupling, and more costly, due to heterogeneous material integration steps. In fact, the commercial sale of PICs is dominated by InP-based solutions because it is the most popular and advanced platform and for now is the only platform where optical transceivers can be built as fully integrated PICs with semiconductor optical amplifiers (SOAs) [33].

The transparency window of the InP technology is from 0.9 to 2 μm and the waveguide core is typically InGaAsP, which has a refractive index of $n = 3.25$ at 1550 nm, and the cladding is InP ($n = 3.16$) [33, 34]. The refractive index difference is small ($\Delta n \approx 2.7\%$), as it is in silica PLCs, which means the minimum bending radius for this standard configuration of InP waveguides is roughly 1.1 mm. It should be noted, though that for the standard InP waveguide configuration, the cladding can be replaced with InAlAs ($n = 2.4$) or even SiO$_2$ to achieve a larger refractive index difference, $\Delta n \approx 26\%$ for InAlAs cladding, or $\Delta n \approx 56\%$ for SiO$_2$ cladding [35, 36]. These larger refractive index differences allow the minimum bending radius to be reduced to tens of micrometers.

Propagation loss in waveguides fabricated using standard InP foundry processes fall below 0.4 dB/cm and allow for monolithic integration of active and passive components [37]. The ability to fabricate active components is due in part to the direct band gap of InP, which allows for efficient absorption and emission of photons without phonon-based energy losses. As such, it is possible to integrate laser diodes, modulators, and photodetectors on-chip, which by obviating the need for coupling optics, offers superior performance and power consumption over other platforms. Additionally, as a non-centro symmetric material, InP can take advantage of the Pockels and Kerr electro-optic effects for its modulators, which tend to be less lossy and

power efficient than other modulation schemes, such as the plasma dispersion effect.

Silica waveguide PLCs and InP are arguably the two most established and entrenched integrated photonic material platforms. However, drawing parallels to the field of electronics once again, there is a material platform that possesses an even greater manufacturing legacy and knowledge base than either two, and that is silicon. **Silicon Photonics (SiPh)** based on silicon-on-insulator (SOI) technology uses this versatile and abundant material that is not only a suitable semiconductor for the conduction of electrons, but whose refractive index of $n = 3.47$ and that of its naturally occurring oxide, silicon dioxide ($n = 1.44$) make it well-suited for tightly confining and guiding light as well. In fact, its refractive index difference of $\Delta n \approx 58\%$ makes it one of the materials with the strongest light-confinement capabilities, thereby allowing silicon waveguides to follow tight bending radii on the order of a few microns [38]. Consequently, PICs utilizing many Silicon Photonic devices can be made compact and opens up the possibility for very-large scale integration.

The transparency window for silicon is between 1.1 and 3.7 µm, which makes it ideal for near-infrared and mid-wave infrared wavelength applications. In terms of propagation losses, silicon strip waveguides can achieve 0.5 dB/cm [39]. Silicon is a centro-symmetric material and can therefore not take advantage of the Pockels effect for modulation. Its Kerr effect has been shown to be relatively weak, leaving the free carrier plasma dispersion effect as a suitable high-speed modulation scheme [40]. Although slower, a more compact means of modulation is through thermal tuning and is a widely-used tuning approach.

Unfortunately, silicon does not possess a direct bandgap and therefore cannot provide efficient sources and detectors. That being said, because silicon is one of the few material platforms that promises the large, wafer-scale volume throughput and cost reduction that the electronics industry relies on, research on heterogeneous integration is well underway. Sources have already been introduced to SiPh via III-V gain regions bonded on Si as well as through direct epitaxial growth of III-V layers. Such heterogeneous integration will not only allow the platform to provide gain, detection, and modulation, but it also promises the inclusion of more exotic materials such as LN and cerium yttrium iron garnet (Ce:YIG) for non-linear optics and magneto-optic effects [41].

Silicon nitride (SiN) is a related material to silicon, but is a distinct material with properties that make it attractive for use in PICs. With a slightly lower refractive index than pure silicon, $n = 1.99$, SiN based waveguides surrounded by a silicon oxide core tend to require larger minimum bending radii, i.e., approximately 25 µm [42]. With an optical transparency window from 405 nm to 2.35 µm, it can be used in applications requiring shorter wavelengths, e.g, in the therapeutic window for biological media, or those in the visible range [43]. Particularly noteworthy is the low propagation loss that is achievable: using a photonic Damascene process with a novel reflow process, researchers were able to demonstrate waveguides exhibiting losses of roughly 0.05 dB/cm [29]. Compared to silicon, SiN, is more promising for non-linear optics and is more suitable for high-power applications as it does not suffer as much from two-photon

absorption (TPA). As a dielectric material, it lacks the conventional electro-optic tuning and high-speed modulation mechanisms used in other materials, but it is possible to compensate for this limitation by using a hybrid Si/SiN approach [44, 45]. Because silicon nitride is already a common material in CMOS foundries, this material platform can be seen as a means of extending SiPh by providing a broader spectral window of operation with low losses.

Lithium niobate (LN) has long been known to be a versatile and attractive material for photonics; it has a respectably high refractive index of $n = 2.21$, a broad transparency window from 320 nm to 6 μm and exhibits strong electro-optic and nonlinear-optic effects. Moreover, LN modulators find widespread use in fiber-optics because they combine ultra-low propagation loss, fast and low-loss optical modulation, and efficient all-optical nonlinearities [46]. The theoretical limit for propagation loss in LN is 0.001 dB/cm and is set by the absorption of LN crystals, but the best demonstrations to date exhibit 0.027 dB/cm loss [47] Moreover, by doping LN with rare-earth ions it is possible to fabricate amplifiers and lasers, which adds active component integration capabilities. The primary reason why LN has not been able to compete with other integrated photonic platforms is the difficulty in processing the material and the inability to scale-down device dimensions. Traditional LN waveguides are made by diffusing titanium into LN or utilizing proton exchange in bulk LN. These two approaches yield refractive index differences limited to 3% or 10% for titanium indiffusion or proton exchange, respectively, and the processing techniques themselves also place a lower limit on waveguide diameter (i.e., roughly 10 μm) [48]. Thus, not only are the waveguides already 10 μm wide, which is much larger than the 450 nm width seen in Silicon Photonics, but the minimum bending radius is roughly 150 μm. The end result is devices with large footprints that are bulky and more suitable for use as discrete components. These major drawbacks limiting integration, however, may be alleviated with the recent introduction of a LN on insulator platform which incorporates a LN film on a silica buried layer, much like the silicon in the SOI platform of SiPh, to increase the refractive index difference [49].

Aluminum nitride (AlN) is a material for integrated photonics that possesses an optical transparency window into the UV range, from 200 nm to 13.6 μm. As such, this platform is attractive for applications including UV spectroscopy, optical waveguides for modular quantum computing with atomic memories, and solar-blind communications [50]. AlN possesses a refractive index of $n = 2.12$ and can be used with a low refractive index cladding such as silica, meaning the minimum achievable bending radii lie below 30 μm. In addition to promising compact devices, the propagation losses at telecom wavelengths have been shown to be as low as 0.6 dB/cm at telecom wavelengths [51]. Regarding material composition, AlN exhibits good technology compatibility with silicon and other substrates and even exhibits superior thermal conductivity and a lower refractive index sensitivity to temperature than silicon. Coupled with a large electro-optic coefficient and demonstration of high-speed modulation up to 4.5 GB/s, AlN seems to be a material platform that holds promise for large scale integration [50]. However, propagation losses in the wavelength range in which AlN holds the most promise are still rather large, i.e., 8 dB/cm, and the growth of single crystal bulk AlN substrates are still limited to 25 mm wafers [52].

Diamond is another interesting platform for integrated photonics because of its unique material properties. With the broadest optical transparency window (220 nm to 20 μm) of any of the other listed materials, diamond reaches the near ultraviolet to the far infrared. Its high stiffness is a well known mechanical property and paired with its low intrinsic damping, it is an ideal material for mechanical oscillators and low-noise optomechanical resonators [53]. Additional application areas well-suited to its chemical resistance against most acids and bases and high thermal conductivity include spectroscopy in harsh environments, and high-power beam combining amplifiers [54]. A particularly special property of single-crystal diamond is its ability to host color centers, which can be used for single photon emission needed for a variety of quantum technologies [54]. Diamond has a refractive index of $n = 2.4$; thus, when combined with an oxide or air cladding, should in theory be capable of bending radii below 12 μm. Reported propagation losses for polycrystalline diamond (1.5 dB/cm) are higher compared to the other materials, but this is expected given the scattering at grain boundaries and the increased surface roughness of a polycrystalline material [55]. However, integration of single-crystal diamond membranes with silicon microring resonators have shown losses below 0.4 dB [56]. Despite these remarkable optical properties, the diamond platform must still overcome the difficulty in its processing and the dearth of affordable, high-quality, single-crystal substrates, which could then enable the large-scale production of photonic and microoptical devices.

Having discussed seven different material platforms for photonic integration, it is both instructive and helpful to compare them all together. A summary of their pertinent properties is presented in **Table 2.2**.

Similar to how one can marvel at the progress of electronic integration in the past 70 years, a look at **Table 2.2** and comparing these values with those from decades ago reveals an impressive trend for integrated photonics. It is not only the inclusion of new materials for added active devices and broadening of the spectral window for PIC applications, but also the refinement of early-adopted materials in terms of reducing propagation losses and minimum bending radii. Overall, the trend is one that supports denser integration of devices per chip, which will enable novel circuit topologies and functionality. Each material platform offers a unique set of properties, well suited for a particular wavelength range or photonic building block function, but one technology is particularly interesting. As the material that has sustained Moore's law for the past 50+ years and serves as the backbone for the electronics industry, silicon, and specifically Silicon Photonics holds great promise for integrated photonics.

2.5 Silicon Photonics - From Building Blocks to Circuits

As introduced in the previous section, silicon is a material whose optical properties make it particularly amenable for use in PICs operating in the mid- to mid-wave infrared wavelength ranges (e.g., telecommunication applications). Moreover, with the highest refractive index contrast of all the primary integrated photonic material platforms, silicon PICs can be made

Material Platform	Optical Transparency [µm]	Propagation Loss [dB/cm]*	Maximum Refractive Index Difference †	Minimum Bending Radius [µm]
Silica (SiO$_2$)	0.2 to 3.5 [57]	0.00045 [30]	3.5%	2000 [58]
Indium Phosphide (InP)	0.9 to 2 [34]	0.4 [37]	56%	7 [36]
Silicon (Si)	1.1 to 3.7 [59]	0.5 [39]	58%	5 [60]
Silicon Nitride (SiN)	0.4 to 7 [61]	0.05 [29]	28%	25 [42]
Lithium Niobate (LN)	0.32 to 6 [62]	0.027 [47]	10%	20 [63]
Aluminum Nitride (AlN)	0.2 to 13.6 [64]	0.6 [51]	32%	40 [65]
Diamond	0.22 to 20 [53]	1.5 [53]	58%	11

* Listed propagation losses are experimentally reported values; theoretical limits are lower

† The listed value is with respect to the lowest reported refractive index cladding

Table 2.2 – Comparison of Materials for Integrated Photonics

particularly dense and compact. In the past few decades, advances in the field of silicon photonics have introduced a plethora of high-performance passive and active devices and this section discusses some of these state-of-the-art demonstrations for the selected set of building blocks presented in **Figure 2.2**.

2.5.1 State-of-the-Art Silicon Photonic Building Blocks

Integrated waveguides are a fundamental component present in all SiPh PICs and from early demonstrations where propagation loss hovered around 2 dB/cm, researchers have been able to reduce this number to roughly 0.5 dB/cm [66, 39]. As propagation loss in silicon-based waveguides can be primarily attributed to scattering at the rough, etched sidewalls, the improvement reflects advances in the fabrication process, e.g., lithography and etching, steps. In a similar vein, Wilmart et. al, was able to reduce propagation losses in by reducing edge roughness through use of a post-etching hydrogen anneal [67]. Although lower waveguide losses can be interpreted as a technology-driven/-enabled improvement, novel topologies and design strategies can also bolster performance. In waveguide bends, for example, the straight waveguide can be adiabatically transformed into a circular bend by introducing a small spline section at the straight-bend interface, which reduces mode mismatch without a large footprint or loss penalty [60]. The advantage of such a technique is that the geometry can be applied alongside any other processing-related improvements.

Light can be coupled into and out of SiPh PICs by means of grating couplers, which exhibit

some inherent loss. Loss mechanisms include diffraction towards the substrate, poor mode-matching between the guided mode in the fiber and that of the integrated waveguide, and in the case of perfectly vertical coupling, reflection due to second-order Bragg diffraction. This second source of loss arising from difficulty in aligning the input fiber to the waveguide can be reduced by using a grating to butt-couple light perpendicular to the surface, which allows for denser integration and also enables wafer-scale testing without the need for cleaving [68]. When defining the gratings, by using a silicon overlay, and etching it separately from the waveguide, it is possible to decouple the parameters defining the directionality and efficiency of the coupler to achieve efficiencies of -1.6 dB and a 3-dB bandwidth of 80 nm [69].

For directional coupler, the two primary figures of merit, in addition to the ever-present desire for compact devices, are the insertion loss (IL) and spectral bandwidth. Gupta et. al, optimized the wavelength independence of a Silicon Photonic directional coupler using semianalytical mode theory and obtained a broadband device (over 100 nm) with an average insertion loss of 0.8 dB [70]. By using asymmetric-waveguide based phase control, arbitrary splitting ratios can be achieved and such devices also exhibit broadband behavior and small footprint (i.e., 32 μm x 1.4 μm) with less than 1 dB IL [71].

High performance silicon ring and disk resonators find applications spanning the gamut of spectral filtering and switching to label-free biosensing. Bogaerts' et. al, comprehensive review of silicon microring resonators emphasizes the utility of these passive devices and the benefit that silicon as a material presents in enabling their unprecedented size reduction [72]. Representative of this miniaturization is the ultra-compact, silicon photonic tunable notch filter demonstrated by Brunetti, et. al, which has a footprint of only 150 μm^2, a large bandwidth of 10.43 GHz, and achieves a large extinction ratio of 41 dB [73]. In a slightly different vein, capillary electrophoresis is an efficient means of separating analytes in small volumes and the optical detectors on which this technique rely to identify species require labeling and are limited by spectral resolution. By using arrays of silicon microring resonators that detect bulk refractive index changes, it is possible to implement label-free biosensing with a high degree of sensitivity and linearity [74].

Although light generation is not an inherent strength of SiPh due to silicon's indirect bandgap, an abundance of research in the past few decades has focused on introducing integrated light sources, either by obtaining lasing in silicon or heterogeneous/hybrid integration of III-V semiconductors on silicon. The initial report of optical gain in silicon nanocrystals and the first demonstration of a silicon Raman laser, as well as more recent work on improving optical gain, capture the ingenuity and persistence in attempting to develop efficient light sources in silicon [75, 76, 77]. Unfortunately, hitherto all silicon-based lasers require optical pumping by an external light source, which contradicts the goal of a fully silicon photonics platform. Until an electrically pumped silicon laser is demonstrated, integrating electrically-pumped III-V sources onto silicon like the AlGaInAs-silicon evanescent laser from Bowers' group is an attractive alternative [78]. Such heterogeneous integration, where the III-V die is directly bonded on the silicon, or a hybrid approach where the completed III-V laser is flip-chip

bonded or assembled with the completed silicon PIC, are both promising ways of bringing sources on-chip.

Photodetectors in silicon PICs are typically implemented as heterogeneously integrated InP or Ge devices because their direct bandgap allows them to efficiently generate electron-hole pairs by light absorption. However, following the motivation for integrated sources, the pursuit of a truly monolithically integrated Silicon Photonics platform necessitates the inclusion of silicon-based waveguide photodetectors. In this endeavor, researchers at Intel developed the first 50 Gb/s all-Si waveguide photodetector utilizing two-photon absorption, surface state absorption, and photon assisted tunneling in a PN-junction to obtain competitive (with regard to Ge and III-V photodetectors) performance in terms of responsivity, dark current, and signal to noise ratio [79].

The traditional electric field effects for modulation by opto-absorption (Franz-Keldysch effect) or electro-refraction (Pockels and Kerr effects) are weak in silicon, leaving plasma dispersion and thermo-optic effects as the preferred modulation schemes in SiPh. Noteworthy all-silicon modulators employing the plasma dispersion effect include a 40 Gbit/s modulator that uses a P-i-P-i-N diode with carrier depletion and a 60 GBit/s slow-wave, series push-pull, travelling wave modulator optimized for wide bandwidth operation [80, 81]. Although thermo-optic modulation cannot match the speeds needed in telecommunications, they tend to be more compact and broadband, making them suitable for use in applications such as programmable PICs and low-loss optical switch networks, where fast modulation speeds are not critical. As an example of a device suited for such a role, Chung, et. al demonstrated a low-power (2.56 mW for a π phase-shift), broadband (100 nm), compact (0.0023 mm^2) thermo-optic modulator [82].

This brief overview of state-of-the-art passive and active building blocks in SiPh naturally segues into a discussion of the circuit- and system-level devices that can be made from these constituent elements. A particularly convincing example of the high-level of integration that can be achieved in SiPh is the optical phased array demonstrated by Professor Michael Watt's group. Their phase array demonstrator consists of 12'000 individual optical elements, including directional couplers, thermo-optic phase shifters, and optical nanoantennas and is capable of producing complex interference patterns in the far field, as would be needed in three-dimensional holography and laser detection and ranging (LADAR) [83]. Silicon photonics has also found its way into quantum computing where photonic entangled states pose a potential challenge to today's classical computers. The trend is now to transition from bulk, table-top optics experiments to integrated photonics platforms [84]. A specific example of the advances made in photonic quantum computing is the demonstration of spatial multiplexing of silicon-based, correlated photon pair sources to enhance two-photon interference [85]. These two representative demonstrations corroborate the diverse functionality and high levels of integration achievable in Silicon Photonics, but material platform notwithstanding, these circuits must still be fabricated and silicon's second strength is its compatibility with existing processing infrastructure.

2.5.2 Standard Silicon Photonics Platforms

In research, it is common to fabricate devices on chip- or even 100-mm scale. Doing so allows for short-loop experiments and proof-of-concept demonstrations without prohibitive material costs. However, in order to truly take advantage of economies of scale, as is the trend in the semiconductor electronics industry, there must be a shift to foundry-based fabrication. CMOS foundries have decades of experience working with silicon and have optimized the tools and processing steps to achieve nanometer-scale devices with high accuracy and precision. Not only do the standardized and optimized processes in a foundry guarantee higher yields and quality (e.g, sidewall smoothness, uniformity, etc.) than most users in an academic or research cleanroom can achieve, but when using an established platform, designers also gain access to high-performance library standard components with which to interface their new designs and devices. Established Silicon Photonic foundries offer PIC designers the opportunity to profit from this tight process control and co-integration with optimized passive and active components by offering multi project wafer (MPW) runs. With an MPW, individuals, research groups, or companies purchase area on a wafer for their designs, which allows the cost of the processing to be shared amongst users, thereby lowering the threshold to participate in IC/PIC design. Foundries with a Silicon Photonics technology platform that offer MPW runs or fabrication services include GLOBALFOUNDRIES (GF), CEA-Leti, Cornerstone, Advanced Micro Foundry (AMF), CompoundTek, and the Interuniversity Microelectronics Centre (IMEC).

The work presented in this thesis was performed exclusively in collaboration with IMEC in Belgium. IMEC offers a standard silicon photonics platform called iSiPP50G that co-integrates a variety of passive and active components to support a wide range of optical transceiver architectures at data rates of up to 50 Gb/s [86]. Integrated components that are part of their process design kit (PDK) include low-loss waveguides, efficient grating couplers, high-speed silicon electro-optic modulators, high-speed germanium electro-absorption modulators, and high-speed germanium waveguide photodetectors. A representative cross-section indicating the various components of the iSiPP50G platform is provided in **Figure 2.4**.

The iSiPP50G platform is built on a 200 nm Si/2 µm buried oxide (BOX) SOI technology with silicon waveguides of three different thicknesses and oxide bottom and top cladding consisting of the BOX layer and back-end-of-line (BEOL) stack, respectively. Inspection of the "MEMS device" region in **Figure 2.4** identifies how designers can interface their devices with ancillary passive and active components. One option, originally intended for sensing applications, removes the BEOL stack above the device layer silicon in certain regions. This etch provides access to the embedded structures and underlying BOX and was key to the novel introduction of microelectromechanical systems (MEMS) to the iSiPP50G platform .

Overall, the ability to fabricate devices and circuits at 200 mm-scale in an industrial foundry is an advantage that Silicon Photonics holds over the other materials suitable for photonic integration. In fact, it is considered by many to be the only integrated photonics material
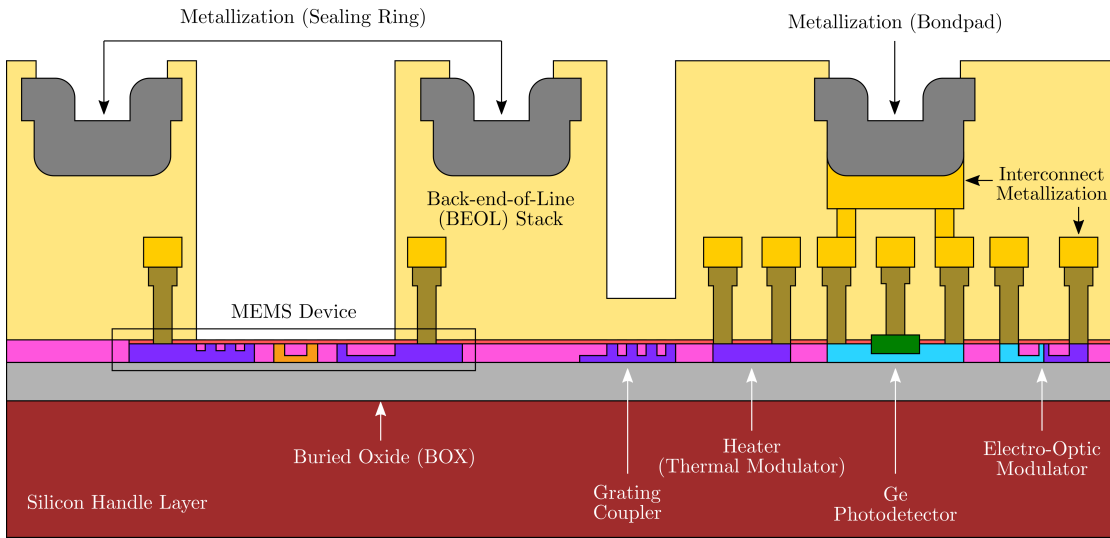
Figure 2.4 – Cross-section of IMEC's iSiPP50G platform, highlighting several of the passive and active components available to designers. Optical input/output is provided by the grating couplers and light detection is performed with the Ge photodetectors. Standard electro-optic and thermal modulators are available and their electrical connections are made by connecting doped silicon to the 2-layer copper metallization and aluminum bondpads. Note, the MEMS cavity on the left is non-standard and as such is one of the contributions of this work to the platform.

platform capable of achieving the high levels of integration needed to produce PICs that can fulfill the speed, power, and cost needs of information routing and processing in the future. Despite its promising qualities, SiPh still faces some limitations that prevent it from reaching the panacea-like status it has enjoyed in the CMOS industry as the most cost-effective means of providing high performance in the smallest form factor.

2.5.3   Open Challenges in Silicon Photonics

Lack of all-silicon on-chip sources and detectors aside, there is another hurdle that SiPh faces. The high refractive index difference in silicon photonics has been referred to by many as both a "blessing and a curse," as it enables high-performance, very-compact devices, while at the same time leaving waveguides susceptible to scattering losses due to nanometer-scale roughness of the sidewalls [59]. Likewise, a SiPH waveguide's refractive index is sensitive to its geometry, which means that the stochastic variation introduced by, yet inherent to, fabrication, even in the most sophisticated foundries, leads to deviation of the actual devices' performance as compared to simulation and design. Specific issues related to waveguide width variation include 1 nm wavelength errors in interferometric devices like MZIs or ring/disk resonators and exacerbated cross-talk in arrayed waveguide gratings [59].

Fortunately, one does not need to settle for imperfect devices: active tuning mechanisms are widely used in PICs to obtain the desired optical behavior. Thermal tuning by integrated heaters in particular is a commonly employed technique to adjust the refractive index of

waveguides, thereby compensating for geometric non-idealities. That being said, if every device in a PIC required thermal tuning, one can imagine that even with a mW/device power budget, the resulting circuits would be limited to thousands of devices. It would be quixotic to believe silicon photonics will reach the tens of billions of devices in very large scale integration (VLSI) electronics because there is also a fundamental limitation to the size of waveguides. A cross-sectional profile of 220 nm thick by 450 nm wide ensures single-mode operation for the TE polarization and also ensures acceptable propagation loss. Further reductions would lead to a larger fraction of the guided mode being outside the waveguide core, which would lead to unacceptably high excess losses.

Other key obstacles relate to the packaging of SiPh devices, which can significantly impact the performance and overall cost of the system. Packaging encompass the technology required to optically and electronically interface with the PIC, the fiber-coupling, laser-source integration, wire-bonding, and possibly even flip-chip process [87]. Although reduced dimensions are favorable for higher device-density, the resulting mode-size and refractive index mismatch between a SiPh waveguide and that of an optical fiber poses a challenge for coupling light into and out of a circuit with high efficiency. Unfortunately, both commonly used techniques, edge and vertical coupling, have drawbacks, either requiring high-accuracy in alignment and cleaving of facets which is neither space efficient nor possible mid-fabrication, or being intrinsically polarization-sensitive and lossy [88]. Integration of electronic ICs alongside silicon PICs also presents some difficulties when considering that I/O ports for each must be adequately spaced from one another and that thermal management is required for stable operation of the photonic components [87].

And yet, the fact remains that the complexity of a circuit is positively correlated with the number of devices and their connectivity. Stated differently, new and improved functionalities in PICs still necessitates scaling up the number of devices and improving integration. Furthermore, the implementation of perfect optical devices by imperfect components, as suggested by Miller, and programmable photonic circuits rely on adjustable/tunable devices [89, 12]. Thermal tuning is not power efficient and hence limits scalability, and the plasma dispersion technique, while fast and compact, introduces additional losses that also hinders its widespread use. One technique, that of electrical-mechanical-optical modulation by MEMS satisfies this particular need for a compact, power-efficient tuning mechanism, and furthermore introduces novel, high-performance integrated photonic devices that provide new and enhanced functionality in their own right.

3 MEMS for Silicon Photonics

Silicon Photonics has burgeoned as a promising material platform for the implementation of large-scale PICs due to its compatibility with the existing CMOS processing infrastructure and its high refractive index contrast, which allows the resulting devices to be compact. However, this size advantage comes with the inherent drawback that the optical behavior and properties of waveguides and other photonic devices become extremely sensitive to nanometer-scale variations. Current approaches of thermal tuning to compensate for these manufacturing-related non-idealities do not sustain continued scaling, and therefore other approaches must be considered.

Mechanics at the micro- and nanoscale, through the use of microelectromechanical systems (MEMS), provides an alternative approach, capable of strong and efficient tuning. These micrometer-scale systems employ electro-mechanical transduction to generate displacements, which depending on the actuation mechanism, range from several nanometers to hundreds of micrometers. In the context of photonics, by physically redistributing optically active media from its as-fabricated configuration, it is possible to influence device properties such as refractive index and coupling characteristics to tune system-level behavior.

If for example, a directional coupler designed for a 150 nm initial coupling gap arrives from the foundry with a 155 nm gap, the transmission to the desired output port will not be as designed. Traditionally, one of the branches is heated up using an integrated heater to provide the requisite refractive index shift via the thermo-optic effect. With the MEMS-based tuning approach, one branch of the directional coupler can be designed to be movable by means of an actuator while the other is fixed. Following fabrication, even if the gap deviates from the designed 150 nm, the two branches can be made free-standing through post-processing and the movable branch is displaced farther or closer to the fixed branch until the desired coupling gap is reached. Moreover, by utilizing a bistable or latching scheme, it is possible to implement non-volatility, which enables zero-power consumption states. For the case of thermal tuning, power must be continuously expended to maintain the desired state, but with a bistable or latchable MEMS-enabled device, power can be removed after compensation/tuning.

Such MEMS-enabled devices need not be limited to tuning, though. In the previous example, if the gap can be increased to the point where coupling between branches is insignificant, one has effectively switched "OFF" power transmission to one of the ports. Done digitally, i.e., with a rapid and distinct transition between small and large gaps, which represent significant and insignificant coupling between coupler branches, respectively, one implements the optical equivalent of an electronic switch. If the transition can be controlled such that the power splitting between branches is continuously varied, one has an analog/continuously tunable power splitter. Combined with phase shifters that are themselves tunable, one can implement a diverse array of linear optical circuits.

In order to understand and appreciate how the mechanical approach of MEMS provides optical modulation, one must return to the mathematical and physical representation of light in PICs.

3.1 Principles of MEMS-Based Optical Modulation

As introduced in Chapter 2, light that has been coupled into a PIC can be represented by a guided electromagnetic wave travelling in the positive z-direction whose amplitude and phase exhibit spatial and temporal dependence. By assuming that the cross-sectional profile of the wave is constant during propagation and varies less in the direction of propagation than that perpendicular to it, one obtains the following physical model.

$$U\left(x, y, z, t\right) \rightarrow A\left(x, y\right) e^{-j(kz-\omega t)} \tag{3.1}$$

Where $k = 2\pi n_{eff}/\lambda$ is the wave number, n_{eff} is the effective refractive index of the guided mode, and ω is the frequency at which the wave exhibits harmonic time dependence. In this form, the wave is characterized as the product of an amplitude factor $A(x, y)$ and a phase factor $e^{-j(kz-\omega t)}$.

Now, it is possible to examine how each of these terms can be mechanically or physically modified [24]:

1. Compressive or tensile stress in a semiconductor modifies its band structure, which enhances free-carrier absorption and carrier confinement [90]. If the stress introduces or enhances material absorption, the wave amplitude $A(x, y)$ decays exponentially as it propagates in z. Enhanced carrier confinement behaves slightly differently in that it modifies the mode's effective refractive index, n_{eff}, which as a component of the wave number k, alters the phase of the mode as it propagates. In this manner, a phase shift between the original mode travelling in the unstrained waveguide and that exiting the strained waveguide develops. Changes in the refractive index also leads to a different field distribution in x and y, so $A(x, y)$ is also modified.

2. The optical path length (OPL) of a structure can also be physically increased or decreased, which introduces a phase shift as the mode propagates in z as compared to an unmodified variant. If this lengthening or shortening is achieved through stress (i.e., as opposed to the introduction of a waveguide segment that would add additional OPL, for example), the resulting optical modification parallels that obtained by (2) above.

3. Displacement of a slab material within the evanescent field of a guided mode can yield one of two effects. If the material slab also supports a guided mode that is phase-matched to the original (i.e., similar effective refractive index n_{eff}), light couples between the two, resulting in a change in both amplitude and phase for the two modes. On the other hand, if this newly introduced optically active media does not support a guided mode, only the amplitude and phase of the original mode changes. In particular, the material slab can introduce losses by material absorption, radiation, or scattering by sidewall roughness and consequently, the amplitude decays. Alternatively, the addition or subtraction of refractive material can introduce phase shifts.

Using these three mechanical means of physically tuning the amplitude and phase of a guided mode, it is possible to perform a variety of optical functions. In fact, assuming access to optical I/O and routing, any arbitrary linear optical system can be constructed from a combination of just two functional building blocks, one of which modifies power, or amplitude, and the other, phase [24]. As such, power splitters and phase shifters represent the fundamental components of any PIC. However, space constraints and optimized performance necessitate the inclusion of bends and crossings and specialized components, like passive and active/tunable power splitting, switches, and filters.

Power splitting in PICs is typically achieved by directional couplers, which as introduced in Chapter 2, operate based on mode interference between two mode-matched waveguides. The characteristic equation presented for the coupling behavior was $\kappa^2 = P_{cross}/P_0 = sin^2(C \cdot L)$, where P_{cross} represented the coupled power, P_0 the input power, C the coupling coefficient, and L, the coupling gap. Having now defined the physical tuning approaches available with MEMS, it is instructive to elaborate on the coupling coefficient in order to obtain a form for the coupling behavior that illustrates how mechanical effects can be used for tuning. The coupling coefficient C can be obtained using the supermode, or eigenmode expansion method, and is:

$$C = \frac{\pi \Delta n_{eff}}{\lambda} \tag{3.2}$$

Where Δn_{eff} represents the difference between the effective refractive indices of the two waveguides and λ is the wavelength of operation. Substituting this expression for C into the directional coupler equation one obtains:

$$\kappa^2 = \frac{P_{cross}}{P_0} = sin^2(C \cdot L) = sin^2\left(\frac{\pi \Delta n_{eff} L}{\lambda}\right) \tag{3.3}$$

In this form, it becomes clear that mechanical tuning affecting the effective refractive index n_{eff} of either supermode in the directional coupler, or the coupling length, L can modify the amount of cross-coupled power.
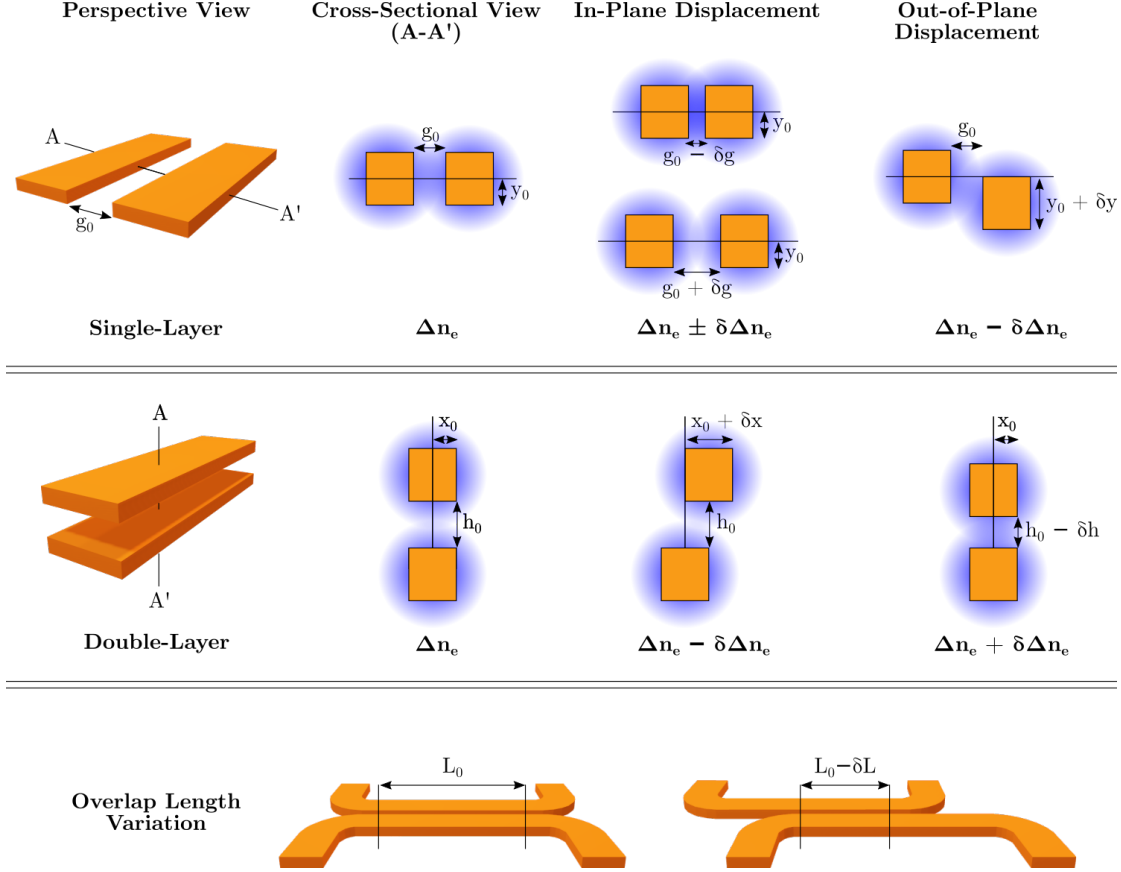

Perspective View	Cross-Sectional View (A-A')	In-Plane Displacement	Out-of-Plane Displacement
Single-Layer	Δn_e	$\Delta n_e \pm \delta \Delta n_e$	$\Delta n_e - \delta \Delta n_e$
Double-Layer	Δn_e	$\Delta n_e - \delta \Delta n_e$	$\Delta n_e + \delta \Delta n_e$

Figure 3.1 – Schematic of how physical rearrangement of material can alter the amount of cross-coupled power in a directional coupler. The blue auras represent the evanescent field of each waveguide and color variations indicate differences in field concentration, which corresponds to modulation of coupling, and hence power transmission. As MEMS can be fabricated in single-layer and multi-layer (typically, two-layer) technologies, the in-plane and out-of-plane displacement variants have been depicted. In addition to changing the separation gap between waveguides, it is also possible to vary the amount of overlap (coupling length) between waveguides.

Common methods for implementing these changes include in-plane and out-of-plane displacement in single and double-layer arrangements of waveguides to increase/decrease waveguide separation (i.e., coupling gap), which produces a corresponding change in refractive index. Illustrations of the in-plane and out-of-plane displacement schemes is provided in **Figure 3.1**. For modulation of the coupling length, two waveguides can be displaced in-plane and parallel to one another such that the amount of overlap length decreases.

The second key optical function that can be MEMS-enabled is phase shifting. Phase shifters should in general be able to produce 2π phase shifts, which can be accumulated in a guided mode with wavelength λ and effective refractive index n_{eff} over a distance/length L as follows:

$$\phi = \frac{n_{eff}L}{\lambda} \tag{3.4}$$

Operationally and structurally speaking, tunable phase shifters using MEMS are quite similar to tunable power couplers. One of the primary differences is that the slab material being displaced typically does not support a guided mode of its own. Consequently, the optically active waveguide is loaded such that the supported mode experiences a change in effective refractive index. This change in n_{eff} can also be achieved by strain tuning a piezoelectric material. A schematic visualization of these mechanisms is provided in **Figure 3.2**.

Switching provides the ability to route and manage the transmission of signals in a network of connected devices and in the context of digital communication systems, provides a straightforward method of implementing "ON" and "OFF" states. Such important functionality, while capable of being implemented by carrier-based modulation like plasma dispersion, or with a tunable phase shifter in an MZI configuration, finds such widespread use in PICs that switches often become functional building blocks of their own. The displacement enabled by MEMS is an efficient means of implementing switching because the geometric rearrangement of material can introduce absorption or break waveguide continuity, both of which will produce an "OFF" state. In a manner similar to that of tunable coupling and tunable phase shifting through proximity variation of a slab material, introduction of a lossy medium into the field of the active waveguide produces losses. With regard to the disruption of waveguide continuity, there are three primary approaches [24]:

1. The waveguide can be directly segmented by displacement of a waveguide portion

2. A portion of the waveguide can be replaced by a photonic crystal reflector

3. The wave vector direction can be changed by bending the waveguide

A visualization of the various physical switching mechanisms is provided in **Figure 3.3**.

Each of these MEMS-tuning approaches relies on the displacement of a structural component that must be generated by an actuator. This active component converts, or transduces, energy in one form, typically electrical, to mechanical energy in the form of motion. There are various actuation mechanisms available, each with its advantages and disadvantages, especially when it comes to compatibility with integrated photonics, and those with the most promise are discussed here.

3.2   Integrated MEMS Transduction Mechanisms

Depending on the transduction mechanism, MEMS actuators can produce displacements in the range of nanometers, micrometers, and even a millimeter. This impressive breadth
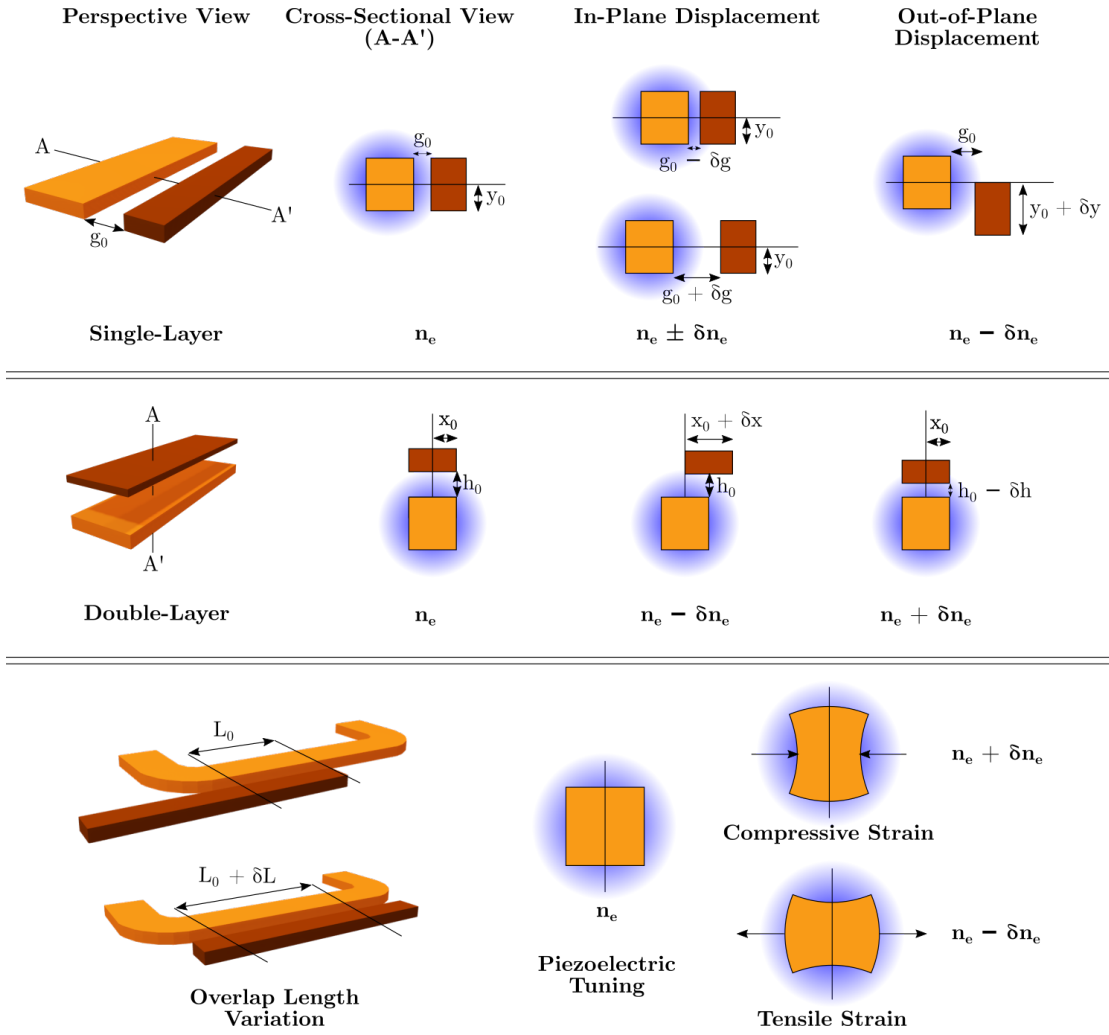
Perspective View	Cross-Sectional View (A-A')	In-Plane Displacement	Out-of-Plane Displacement
Single-Layer	n_e	$n_e \pm \delta n_e$	$n_e - \delta n_e$
Double-Layer	n_e	$n_e - \delta n_e$	$n_e + \delta n_e$

Figure 3.2 – Schematic of how physical rearrangement of material can produce a phase shift. Because the brown slab material does not support a guided mode of its own, its displacement into and out of the evanescent field of the waveguide only produces a shift in refractive index in the active waveguide. Once again, single-layer and multi-layer (typically, two-layer) topologies with in-plane and out-of-plane displacement have been depicted. In addition to changing the separation gap between waveguide and slab material, it is also possible to vary the amount of overlap (coupling length) between these bodies and to strain the waveguide via piezoelectric tuning.

of motion, which covers several orders of magnitude, is testament to the versatility of these devices, and because they are typically fabricated out of the same materials and with the same processing tools used in the CMOS industry, can be compact and cost-effectively produced. It turns out that the displacements discussed in the previous section for MEMS tunable couplers, phase shifters, and switches range from tens of nanometers to several micrometers [24, 91, 92]. These values are readily obtained by electrostatic, electrothermal, and piezoelectric transduction. Other approaches such as magnetic, pneumatic, and shape-memory alloys could also fulfill this need, but because their integration with PICs is not straightforward, they will only be touched upon briefly.
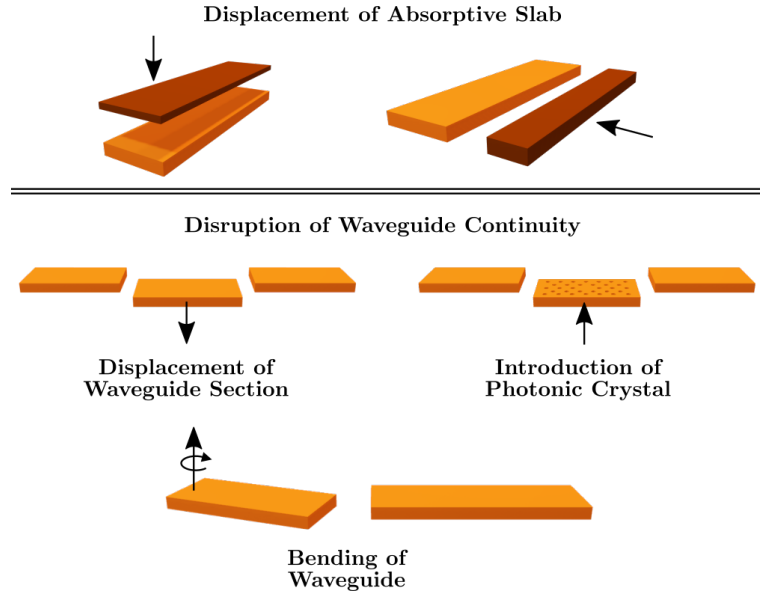
Figure 3.3 – Schematic of MEMS-enabled switching mechanisms. Displacement of an absorptive slab near an active waveguide introduces losses that can produce an "OFF" state. It is also possible to disrupt waveguide continuity by displacing a segment of the waveguide, introducing a photonic crystal for reflection, or to bend the waveguide and change the direction of the wave vector.

3.2.1 Electrostatic Actuation

Electrostatic actuation is the most commonly employed displacement mechanism in MEMS and relies on the attractive electrostatic force between two oppositely charged bodies. Because charge flow is only associated with setting up the potential difference and not with maintaining it, the power consumption of such devices is nominally zero for steady-state/DC operation. The simplest configuration consists of a fixed-free (i.e., cantilever) configuration for the suspension and a parallel-plate arrangement for the capacitor, as illustrated in **Figure 3.4a**. A voltage difference is applied between the suspended plate and the substrate to generate an electrostatic force that pulls the plate down. The balance between the restoring mechanical spring force F_{mech} of the suspension and the electrostatic force F_{elec} determines the displacement.

$$F_{mech} = kz \tag{3.5}$$

Where k is the spring constant of the structure and z is the displacement.

$$F_{elec,V1} = \frac{1}{2} \frac{\epsilon A_{el}}{\left(g_0 - z\right)^2} V^2 \tag{3.6}$$

Where ϵ is the material permittivity of the gap (almost always air, so $\epsilon \rightarrow \epsilon_0$, A_{el} is the area of

33

(a)

A-A'

Initial State

Actuated State

Direction of
Displacement

V

Full Thickness Si

Shallow-etched Si

Buried Oxide (BOX)

Si Substrate

(b)

A-A'

Initial State

Actuated State
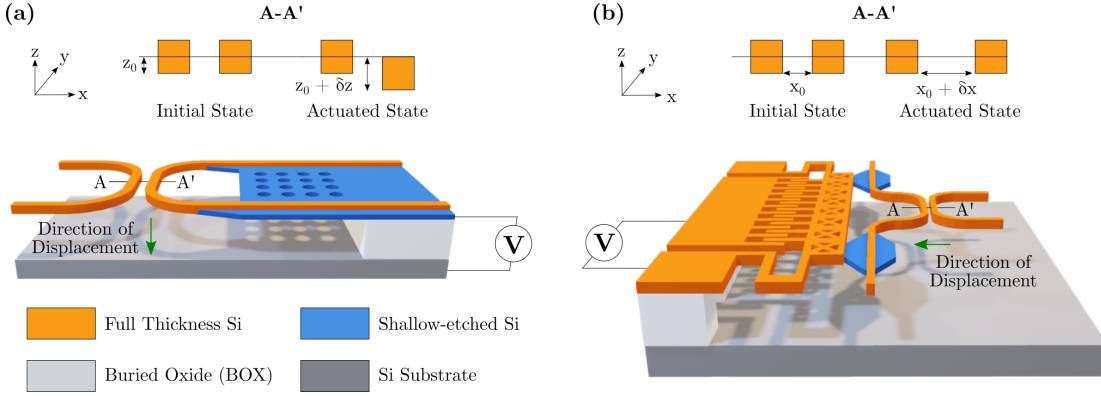
V

Direction of
Displacement

Figure 3.4 – Depiction of two electrostatic MEMS actuators, one producing out-of-plane displacement, the other in-plane displacement (a) Parallel-plate, cantilever geometry where voltage is applied between the suspended electrode and substrate. The attractive electrostatic force pulling the electrode down is counterbalanced by the restoring spring force of the suspension anchored to the fixed end by the BOX. (b) Comb-drive geometry where the voltage difference is applied between interdigitated fingers. Here, the attractive electrostatic force pulls the suspended and movable portion against the spring flexures towards the suspended and fixed region to produce in-plane displacement.

the suspended electrode, g_0 is the initial gap between suspended electrode and substrate, and V is the voltage difference between electrode and substrate.

Regarding the mechanical resonance frequency, which serves as a proxy for the switching time, these devices can be designed to have short response times by using stiff, light geometries as predicted by the standard equation

$$f = \frac{1}{2\pi}\sqrt{\frac{k}{m}} \tag{3.7}$$

Where k is the mechanical spring constant and m is the mass of the device.

Stiff devices are typically short and thick, and light devices have small volumes, so in general, the smaller the device geometry, the faster the response time. With this in mind, it may appear self-evident that electrostatic devices of this parallel-plate, cantilever geometry should be made as small as possible. However, this is not the case and there must be a trade-off between speed and actuation voltage. For small voltages, the linear restoring spring force finds equilibrium with the generated electrostatic force exhibiting quadratic behavior, and smooth controlled displacement is possible. At one point, though, the electrostatic force for a given gap exceeds that of the spring and the electrode rapidly snaps to the substrate. This non-linear phenomenon of instability is known as pull-in and the voltage at which it occurs is given by:

$$V_{pull-in} = \sqrt{\frac{8}{27}\frac{kg_0^3}{\epsilon A_{el}}} \tag{3.8}$$

In many cases, the limiting of the stable displacement range for a MEMS device is undesirable and in some cases, the collapse to the substrate can become permanent, leading to device failure. For applications requiring fast switching, though, this rapid transition can be useful and by controlling the collapse, e.g., through the use of mechanical stoppers to limit the contact area between electrodes so that they do not stick. In this particular case, it would be desirable to have a pull-in voltage that is not too large, as it becomes the ON-state switching voltage and driving electronics are typically limited in the output voltage that they can supply. For a fixed initial gap, g_0, when a device is made smaller, k increases and the mechanical restoring force increases, and A_{el} decreases (smaller electrostatic force). The consequence of this size reduction is that for a given voltage, smaller displacements are obtained and the pull-in condition is moved to higher voltages.

Within the context of mechanical tuning for PICs, by attaching a waveguide or slab material to the suspended electrode, it is possible to vary the vertical distance (from the line of symmetry between the aligned, i.e., non-actuated, waveguide centers), thereby changing the coupling and phase behavior of the active mode.

Figure 3.4b indicates a different topology of electrostatic device, the so-called "comb-drive" actuator. Named for its interdigitated fingers that resemble the teeth/fingers of a comb, this device also uses an attractive electrostatic force to generate displacements. In this case, a voltage difference is placed between the free, suspended and fixed, suspended electrodes so that the resulting electric field pulls the former towards the latter. The restoring force from the suspension exhibits the same linear relationship with spring constant and displacement as in Equation 3.5, but the lateral electrostatic force is slightly different as seen in:

$$F_{elec,V2} = \frac{n\epsilon t}{g}V^2 \tag{3.9}$$

Where n is the number of comb fingers on the movable electrode, t is the thickness of a comb finger, g is the gap spacing between fingers on the movable and stationary electrodes, and V is the actuation voltage.

A noteworthy difference between Equation 3.9 and Equation 3.6 is the absence of a displacement term, which suggests that the electrostatic force only depends on the applied voltage. While it is true that comb-drives exhibit better stability than parallel-plate, cantilever geometries, this desirable characteristic only holds for so long as the movable finger tips are at a distance $> 4g$ from the fixed side [93]. Any closer and the mechanical-electrostatic force balance is broken and pull-in occurs. Additionally, electrostatic forces perpendicular to the direction of displacement can lead to side instability at high actuation voltages.
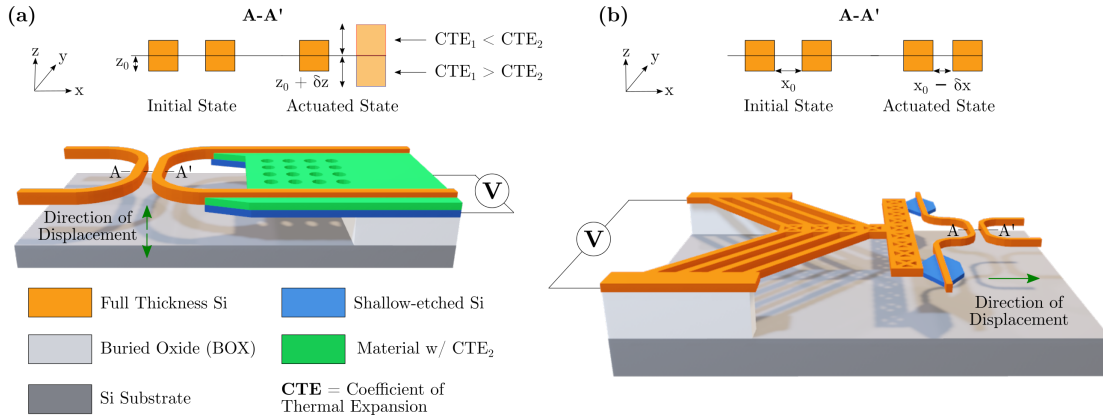
Figure 3.5 – Depiction of two electrothermal MEMS actuators, one producing out-of-plane displacement, the other in-plane displacement (a) Thermal bimorph consisting of two stacked materials with different coefficients of thermal expansion; when heated, one material expands/elongates more than the other to generate a stress that bends the structure up or down (b) V-Shape/Chevron actuator that uses symmetric thermal expansion to cause the structure to move in the direction of the vertex.

In general, this topology does a better job of decoupling the force generation from the achievable displacement than its parallel-plate counterpart. Moreover, with many comb fingers, n, it is possible to achieve large effective overlap capacitances, which leads to large forces and consequently, large displacements (e.g., tens of microns). Increasing the number of comb fingers may increase footprint in the lateral dimension, but by utilizing several parallel sets of comb drives in line with one another, these actuators can still be made compact. For tunable coupling, phase shifting, or switching, a waveguide or slab material is attached to the portion of the device with the movable electrode such that its displacement brings it closer to or farther away from its fixed counterpart.

3.2.2   Electrothermal Actuation

As opposed to traditional electrothermal tuning by an integrated heater, which simply relies on modifying material properties such as refractive index, electrothermally actuated MEMS also produce the displacement needed for mechano-optical tuning. The physical principle is that heating a material causes it to expand/elongate via thermal expansion: if this expansion is directed in a particular direction, the structure will extend, or be displaced, in that direction. These devices rely on joule heating generated by current flowing through a structure and can achieve large output forces and displacements. **Figure 3.5** depicts two common types of electrothermal actuators, one of which provides out-of-plane displacement and the other in-plane displacement.

The out-of-plane variant is commonly referred to as a thermal bimorph because of its stacked composition of two distinct materials with different coefficients of thermal expansion (CTEs). The CTE is related to the strain, or fractional change in physical dimensions of the structure by the temperature difference between initial and final states as

$$\epsilon = \alpha_T \Delta T = \alpha_T \left(T_{final} - T_{initial} \right) \tag{3.10}$$

Where α_T represents the material's CTE and $T_{initial}$ and T_{final} represent the temperature before and before after, respectively.

As ΔT increases, the layer with a larger CTE expands more than the one with a lower CTE, but because the two lie on top of one another and have a strongly bonded interface, the elongation is not unconstrained. Instead, the high CTE layer experiences compressive stress as it is squeezed to a length less than its equilibrium value. Analogously, the low CTE layer experiences tensile stress because it is stretched to a length beyond its equilibrium value. In order to minimize the internal strain energy due to these stresses, the bi-layer structure bends in the direction of the layer with a lower CTE. This bending produces an up or down out-of-plane displacement depending on whether this layer is on the bottom or top, respectively. By attaching a waveguide or slab material to the movable structure, it is possible to modulate the evanescent field interactions of the optical media by varying the vertical gap separation as in **Figure 3.5a**.

Figure 3.5b depicts an in-plane displacement type of electrothermal actuator, commonly referred to as a "V-Shape" or "chevron" actuator. Its behavior can also be understood in the context of thermal expansion. If one assumes small displacements so that Hooke's law can be used to approximate the elastic deformation, this strain can be related to the tensile stress σ through the Young's modulus of the material E:

$$\sigma = \epsilon E = \alpha_T E \left(T_{final} - T_{initial} \right) \tag{3.11}$$

The tensile stress has units of pressure, so scaling by the cross-sectional area of the beam, A, yields a first-order approximation for the electrothermal force:

$$F_{thermal} = \alpha_T A E \left(T_{final} - T_{initial} \right) \tag{3.12}$$

Like the electrostatic force generated by the parallel-plate and comb-drive actuators of the previous sub-section, this electrothermal force counteracts a separate mechanical restoring force. However, because the suspension is at thermal equilibrium with the other parts of the actuator, they will also undergo thermal expansion and the risk of instability phenomena, such as pull-in is minimal.

Heat exchange becomes efficient at the micro-/nanoscale because here, the convection coefficient scales inversely with dimensions, meaning structures can be heated and cooled quickly, which translates to fast switching. Additional advantages of electrothermal devices over electrostatic devices for example, include large forces and displacement, simple fabrication, and

low voltage operation. It should be noted, though, that in order to produce the temperature differences ΔT required to achieve appreciable displacements, a large amount of steady-state current must flow through the device. Large DC current leads to high power consumption and consequently limits the scalability of tunable photonic components using electrothermal actuation. Another drawback, also present with heaters for optical tuning, is the risk of thermal cross-talk: devices must be spaced sufficiently far apart from one another so as to not be influenced by adjacent tuning.

3.2.3 Piezoelectric Actuation

Piezoelectric actuators form a third category of MEMS transducers suitable for implementing mechanical tuning in PICs and typically consist of a thin crystal or ceramic layer fixed between two electrodes. The enclosed crystal or ceramic layers are unique in that they exhibit the converse piezoelectric effect which produces mechanical deformation under an applied electric field. This electromechanical coupling is captured by a pair of equations that relate the linear electric behavior of a material ($\mathbf{D} = \boldsymbol{\epsilon}\mathbf{E}$) to Hooke's law for elastic materials ($\mathbf{S} = \mathbf{sT}$) in the strain-charge form,

$$S = sT + d^T E \tag{3.13}$$

$$D = dT + \epsilon E \tag{3.14}$$

Where $\mathbf{S}$ represents the material strain, $\mathbf{s}$ is the compliance matrix under short-circuit conditions (i.e., $\frac{1}{stiffness}$ of the material when the electrodes are connected to one another so that the electric field is zero), $\mathbf{T}$ is the stress, $\mathbf{d}$ is the matrix for the direct piezoelectric effect where charge accumulates in response to mechanical stress, $\mathbf{E}$ is the electric field, $\mathbf{D}$ is the electric charge density displacement, and $\boldsymbol{\epsilon}$ is the permittivity of the material.

Thus, the entire structure can be made to expand or contract parallel to the direction of the applied electric field. The resulting displacements are generally in the nanometer scale and can be accurately controlled, making these types of actuators ideal for fine-step repositioning of waveguides and slab material. As was the case for electrostatic and electrothermal actuators, piezoelectric actuators enable both in-plane and out-of-plane displacement (see **Figure 3.6**).

In terms of performance, piezoelectric actuators strike a balance between the small form factor of electrothermal devices and the quick response time of electrostatic devices. Moreover, because they utilize static electric fields and not steady-state current flow, the power consumption of these actuators can be quite low. For application in PICs and specifically MEMS-enabled silicon photonics, however, there are a few drawbacks to this transduction mechanism. Generally, larger displacements require thicker piezoelectric layers, but for standard MEMS processing, thin films are preferable [24]. Thus, there is a trade-off to be made
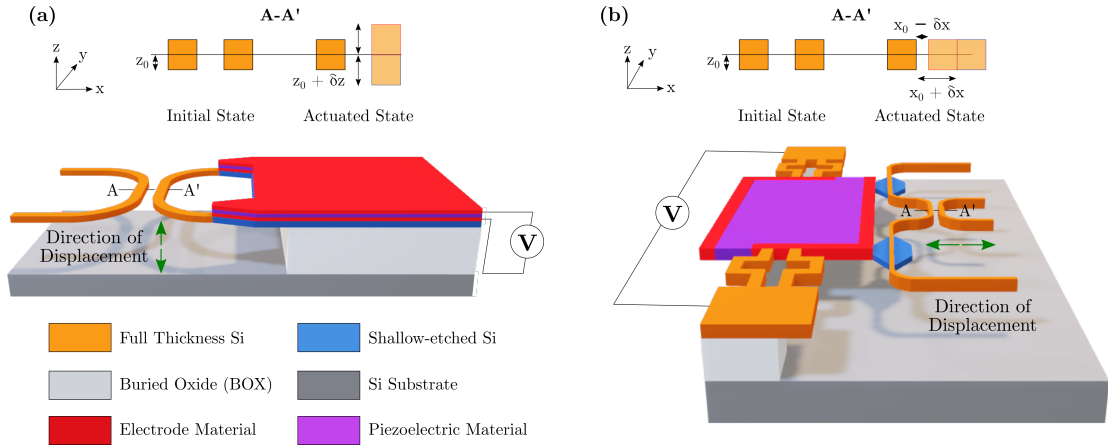
Figure 3.6 – Depiction of two piezoelectric MEMS actuators, one producing out-of-plane displacement, the other in-plane displacement (a) Piezoelectric cantilever in which a piezoelectric layer is vertically pinioned between two electrodes. Depending on the polarity of the applied voltage, this layer expands or contracts, thereby producing out-of-plane displacement (b) Schematic visualization of a possible in-plane piezoelectric actuator where the piezoelectric layer is not covered by the electrodes, but is instead framed by them so that the displacement can be parallel to the substrate.

between ease of fabrication and achieving the desired displacement for active photonic tuning. Furthermore, piezoelectric actuators typically exhibit strong hysteresis, which complicates their use for precise positioning.

Nevertheless, with additional work on the integration compatibility of piezoelectric materials in standard silicon photonic platforms, this class of actuators promises a power-efficient, fast, and compact, complement to the selection of established MEMS actuators.

3.2.4   Other Actuation Schemes

Electrostatic, electrothermal, and piezoelectric transduction are typically used for MEMS because they can be made compact and at large-scale using established fabrication techniques. There are a variety of other transduction schemes with favorable operating characteristics for photonic tuning but whose integration into established platforms is currently infeasible or too costly. Electromagnetic transduction, for example, uses an alternating current to produce a magnetic field that can be used in conjunction with an embedded permanent magnet to generate an attractive/repulsive force similar to that seen in electrostatic actuation. Here, the resulting magnetic force $\vec{F}_{mag}$ balances the restoring spring force of the structure's suspension to generate displacements.

$$\vec{F}_{mag} = L\vec{I} \times \vec{B} \tag{3.15}$$

Where L is the length of the conductor, I is the current flowing through the device and B is the external magnetic field produced by the permanent magnet.

The displacements produced using this type of actuation can be quite large and do not suffer nonlinear effects, nor do they require high voltages. Furthermore, electromagnetic actuation can be made rapid and the resolution and repeatability in positioning is excellent. The primary reasons why this transduction mechanism does not find more widespread use is the high power consumption associated with the current-driving scheme and the difficulty of integrating bulky permanent magnets or depositing magnetic thin films in standard fabrication process flows.

Other "exotic" or more exploratory MEMS transduction mechanisms include pneumatic actuation, which is typically combined with electrostatic actuation to provide high-speed deflections at low power consumption. Here, thin membranes surround an air-filled cavity and the electrostatic force between membranes compresses the air so as to increase air pressure and push one membrane outward or inward to create convex and concave shapes.

Shape memory alloys (SMAs) are another category of actuator that operate on a similar thermal-mechanical deformation as electrothermal actuators, except that devices made from these materials "remember" and revert to their original form after applying heat. These SMAs provide a desirable weight to force metric and can be made compact, but typically have low working frequency, high power consumption, and severe hysteresis [94]. Yet, there has been a demonstration of an SMA/Si bimorph nanoactuator that with a footprint of only 10 μm^2 achieved deflections up to 1 μm [95].

Phase change materials (PCMs) offer another interesting transduction mechanism, and the specific example of microbubble-powered actuators utilizing the phase change from liquid to vapor phase is an example of an application translated from the macro-scale (e.g., a steam engine) to the micro-scale [96]. Finally, even pyrotechnical, or pyroMEMS, wherein an energetic material like a nanothermite is integrated onto an electronic chip for controlled ignition and combustion to propel, weld, etc. have been demonstrated [97].

Undoubtedly, rapidly snapping waveguides or slab material on-chip via pneumatic pressure or contained explosions would be exciting and effective in generating displacements. Pragmatically, though, for a variety and combination of reasons, these approaches are either not amenable to the smooth, accurate, precise, and rapid displacement or small-form factor and simple fabrication desired for photonic tuning. These alternative actuation mechanisms have been included for completeness but a comparison of the main actuation principles is included in **Table 3.1** [24].

3.3   State-of-the-Art MEMS-Enabled Photonic Devices

The use of MEMS for mechanical tuning and implementing optical functions in PICs has attracted significant interest in academic research over the past 20 years and there is a plethora of high-performance devices demonstrating the versatility and utility of this approach. However, before discussing the results and impact of this work, it is instructive to provide a context

Acutation Principle	Footprint	Response Time	Power Consumption	Displacement	Photonics Compatibility
Electrostatic	+	++	++	+/++*	++
Electrothermal	++	+	–	++	++
Piezoelectric	+	++	++	+	+
Magnetic	–	++	–	++	–

	++ EXCELLENT	+ MEDIUM	– LIMITED

*Parallel Plate/Comb Drive

Table 3.1 – Qualitative Comparison of MEMS Actuation Mechanisms for Tunable PICs

for what types of silicon photonic MEMS already exist and their relevant performance metrics.

Couplers control optical power distribution in PICs and by making them continuously tunable, it is possible to compensate for fabrication variations that would otherwise limit circuit efficiency. While the focus in this brief review and this work is on silicon photonics, it should be noted that mechanically tunable couplers have been demonstrated in III-V platforms as well, which indicates that MEMS-tuning is not limited to a particular material. A selection of MEMS-tunable couplers is provided in **Figure 3.7**. The electrostatically tunable cantilever used in a GaAs coupler to vary the amount of out-of-plane separation between two waveguides, and hence, the power splitting in the output arms, is a prime example of III-V MEMS integration in photonics [98]. A compact ($5 \times 30\,\mu m^2$) in-plane variant with low insertion loss (IL), 0.67 dB, and fast response time ($< 1\,\mu s$) has also been shown for single-photon routing in a GaAs chip (**Figure 3.7a**) [99].

Efficient in-plane and out-of-plane tunable coupling have also been demonstrated in silicon photonics with examples of the former employing compact double- and single-comb drive actuators from the Hane group [100, 101]. A recent work describes a $125 \times 125\,\mu m^2$ tunable adiabatic coupler using three comb drives that achieves 35.6 dB and 16.7 dB extinction ratio (ER) for the drop and through ports, respectively, low IL (< 1 dB), and 36.7 μs switching time (**Figure 3.7b**) [102]. An example of an out-of-plane variant is the tunable silicon microdisk resonator that can operate in the under-, critical-, and over-coupled regimes by vertically adjusting the gap spacing between the disk and suspended waveguides to achieve high ER (30 dB) and high quality factor (100,000) [103]. Similar tuning can also be used to implement wavelength-selective filters as shown by the use of a gap-tuning, optical path length (OPL)-varying notch filter that produces a 9.96 nm resonant wavelength shift (**Figure 3.7c**) [104]. Tunable coupling need not only take place betweeen waveguides, but can also be performed for photonic crystal (PhC) nanocavities where the gap between two such cavities is varied to tune optical resonances (**Figure 3.7d**) [105].

Switching can be considered a natural extension of tunable coupling in that one would also like to modify the amount of power sent to the output branches. Where the two differ, though,
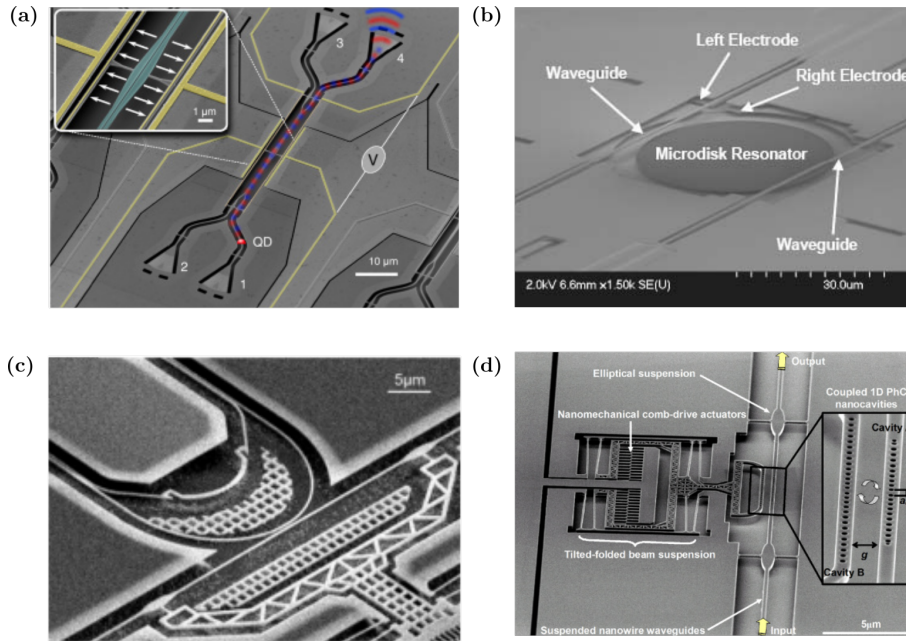
Figure 3.7 – SEM recordings of in-plane and out-of-plane tunable coupling approaches (a) Single photon routing through gap-variation (Reprinted with permission from [99] ©The Optical Society) (b) Variation of microresonator-bus waveguide coupling regimes with vertical gap separation tuning (Reprinted with permission from [103] ©The Optical Society) (c) Notchfilter with OPL and lateral-gap tuning (Reprinted with permission from [104] ©The Optical Society) (d) Tuning of optical resonances by modification of the lateral gap separation between photonic crystal nanocavities (Reprinted with permission from [105] ©The Optical Society)

is that in switching, one typically transfers all the power to one output branch, leaving only residual power in the other. In this manner, switching can be considered a "digital" operation, whereas tunable coupling can be viewed as an "analog" procedure that smoothly varies the gap to obtain the desired operational state and leaves power in both output branches. Nevertheless, in both cases, waveguides are physically displaced closer or farther to one another to achieve modulation of power transmission. It should also be noted that in the context of PICs, tunable couplers and switches often fulfill different roles: the former are typically used in a tuning capacity to compensate for fabrication variations, whereas the latter play an active role in routing and reconfiguring the light path. Examples of integrated photonic switching using MEMS is provided in **Figure 3.8**.

An early demonstration of MEMS-enabled switching used a segmented geometry operating on the principle of disrupting waveguide continuity as schematically illustrated in Figure 3.3 and captured in the SEM recording of **Figure 3.8a**. This compact (40 x 60 μm^2) device displaced a waveguide segment by 540 nm for an ER of 15 dB using a single electrostatic comb drive [106]. Disruption of waveguide continuity can also be accomplished by the introduction of a photonic crystal reflector and can be both broadband (65 nm optical bandwidth) and fast (0.5 ms switching time) while offering 11 dB ER (**Figure 3.8b**) [107]. Out-of-plane displacement of an absorptive media, like a lossy aluminum membrane suspended above a ring resonator has
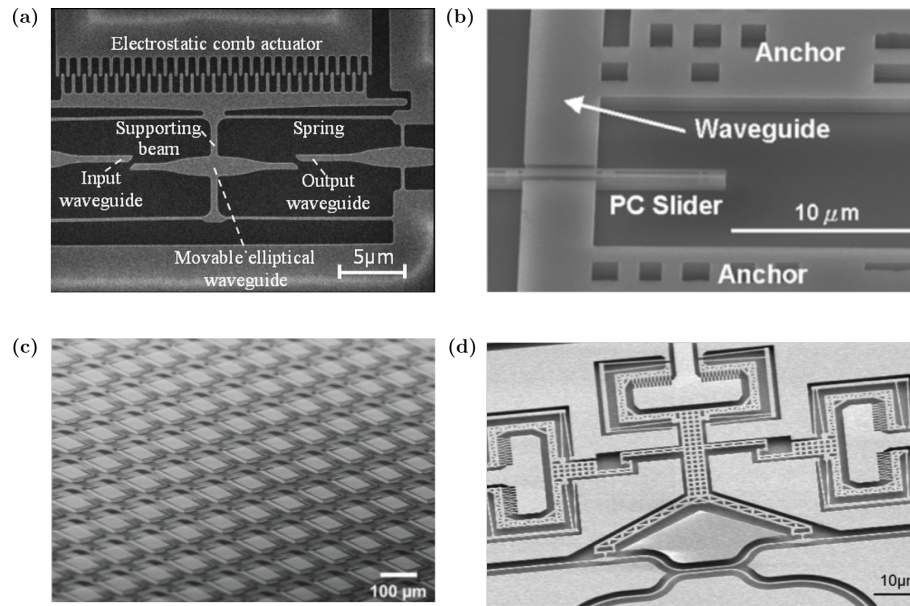
Figure 3.8 – SEM recordings of in-plane and out-of-plane tunable switching approaches by breaking waveguide continuity and large-range displacement for 0 to 100% output power transfer in tunable couplers (a) Displacement of a waveguide segment (Reprinted with permission from [106] ©AIP Publishing) (b) Introduction of a photonic crystal reflector (Reprinted with permission from [107] ©The Optical Society) (c) Large-scale out-of-plane displacements in a switch matrix (Reprinted with permission from [108] ©IEEE) (d) Non-volatile switching with a nano-latching mechanism (Reprinted with permission from [109] ©IEEE)

been shown to reduce transmission by 15 dB and constitutes another switching mechanism [110].

Another class of MEMS-enabled switches include tunable couplers whose operating displacements allow them to transfer the full 0 to 100% power range between outputs. A good III-V example is the InP gap- and coupling length-modifying switch utilizing electrostatic pull-in to provide ON/OFF states with a 37 dB ER, a small IL of 0.5 dB, and switching times around 4 µs, all within a comparatively compact, for InP standards, (500 µm x 5 µm) footprint [111]. With silicon photonics, because devices can be made significantly smaller, the number of switches can be increased and large scale 50 x 50 and even 240 x 240 matrices have been fabricated, each switching unit cell of which achieves an ER > 30 dB, IL of 0.2 dB, and 2.4 µs switching time (**Figure 3.8c**) [112, 108].

Non-volatile switches maintain their state after removing the actuation voltage and are highly desirable for low-power operation, but only a few such devices have been reported. One prominent example, though, is the gap-varying coupler that utilizes a set of twin electrostatic actuators in a nano-latch mechanism to fix the moveable waveguide structure after the desired displacement has been achieved and achieves 17 dB port isolation and -0.3 dB IL (**Figure 3.8d**) [109].
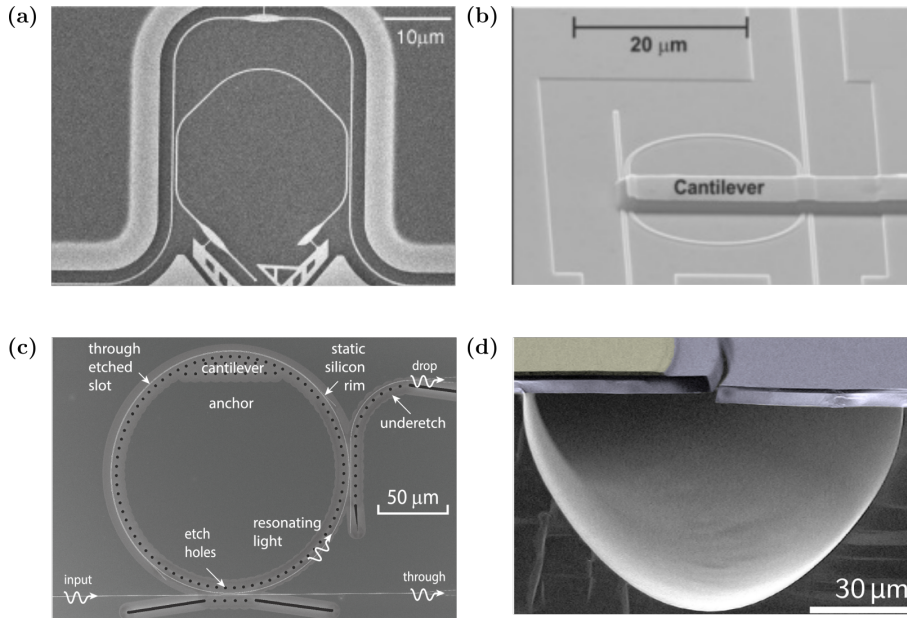
Figure 3.9 – SEM recordings of in-plane and out-of-plane tunable phase shifting approaches (a) Modification of the OPL by waveguide displacement using comb-drives (Reprinted with permission from [113] ©The Optical Society) (b) Out-of-plane displacement of a slab cantilever over a microring for resonance tuning (Reprinted with permission from [114] ©The Optical Society) (c) Alternative out-of-plane resonant tuning approach using deflection of the microring itself (Reprinted with permission from [115] ©The Optical Society) (d) Piezoelectric actuation for out-of-plane displacement to modify the OPL of a microring (Reprinted with permission from [116] ©The Optical Society)

In addition to tunable coupling and switching, there have been numerous realizations of MEMS-enabled phase shifters. Poot and Tang reported a SiN "H-Resonator" that utilizes precisely positioned Cr-Au electrodes between one pair of arms to electrostatically displace waveguides so that the gap in the other pair of arms is modified and hence, n_{eff} (as in **Figure 3.2**), without introducing losses due to absorption [117]. An out-of-plane variant, also implemented in SiN, uses a 150-250 nm thick, 100 µm long suspended beam above a microring that is actuated by gradient electric forces to produce effective index tuning > 0.03 with displacements between 465 and 265 nm [118, 119]. For silicon, an early demonstration of in-plane displacement to electrostatically attract waveguides to one another and decrease gap spacing achieved 60° of phase change for 15 V of applied voltage across a 9 µm slot waveguide [120]. Another variant, using comb-drives instead of the parallel-plate actuation scheme implements phase shifting through modification of the OPL in a moveable waveguide and achieves a larger phase shift (3π) for a voltage of 31 V within a comparatively larger, but still small footprint (50 µm x 85 µm) (**Figure 3.9a**) [113].

Tunable phase shifters have also been incorporated alongside other photonic devices such as ring resonators to provide resonance wavelength tuning. One example includes the 40 µm long cantilever that was suspended 100 nm over a SiN microring resonator to implement 122 pm tuning of the resonance wavelength without additional optical quality factor reduction (**Figure**

3.9b) [114]. A pure silicon implementation of a tunable add-drop filter producing a 530 pm resonance wavelength shift utilizing a different approach wherein the ring itself, and not the waveguide or a slab material, is vertically displaced has also been reported (**Figure 3.9c**) [115]. Although much of the work reported in literature utilizes electrostatic actuation, there have also been some promising, low-power alternatives presented with piezoelectric actuation. Bowers' group demonstrated ultra low-power full 2π-tuning in a SiN ring using lead zirconium titanate (PZT) actuators to effect radial displacement and hence reduction of the OPL (**Figure 3.9d**) [116]. An unreleased AlN piezoelectric actuator for strain-based mechanical tuning has also been shown to be capable of both red and blue tuning of the resonance wavelength under $\pm$ 60 V actuation voltage [121].

Within the last decade or so, an impressive selection of mechanically-tunable PIC devices have been reported, each with a technological or performance advantage over previous demonstrations. Whether it is a more compact footprint and lower IL for enhanced scaling, or a larger operational bandwidth and higher ER for enhanced functionality, the field continues to produce devices that can compete with or even exceed standard tuning and optical modulation approaches. Nonetheless, there remain areas for improvement and obstacles that must be overcome before MEMS-based tuning of PICs becomes a standard technique.

3.4 Open Challenges and Roadmap for MEMS Integration in PICs

Based on the selection of devices presented in the previous section, it becomes manifest that important performance figures-of-merit (FOM) for MEMS-enabled couplers, switches, and phase shifters include IL, response time, actuation voltage, device footprint, and power consumption. As this work presents the design and implementation of MEMS for Silicon Photonics, the ensuing discussion presents issues and opportunities for future work through a lens that focuses on this particular material platform; and yet, many of these points hold broadscale applicability in other material platforms.

With regard to these FOM, MEMS has specific trade-offs inherent to mechanical tuning. In particular because MEMS require suspended, fixed/free structures, there is a tremendous refractive index contrast between waveguide core and cladding materials (i.e., between silicon and air). Transition losses, as would be observed when light passes from an oxide cladded region of the PIC to an exposed, air-cladded portion, where the MEMS modulation takes place, can account for an IL between 0.1 and 1 dB [24]. Additionally, there is always a transition loss associated with the anchor point connecting actuator and waveguide because of the disruption in the cross-section. Such losses can be minimized by, for example, using rib waveguides and having the mechanical connection on the wings, but for devices using small gap variations, strip waveguides with direct anchor connections are unavoidable.

Another primary loss mechanism contributing to IL, irrespective of material platform is scattering loss. The magnitude of this contribution, however, varies between technologies and typically is the result of evanescent field interactions with sidewall roughness produced during

fabrication. Apart from designing new fabrication processes that reduce or mitigate the effect of sidewall roughness, designers of MEMS-tunable devices can leverage the fact that the top and bottom surfaces of unetched thin-films are much smoother than etched sidewalls. Thus, multilayer structures relying on out-of-plane actuation may prove less lossy than standard single-layer, in-plane variants.

The switching or response time of mechanical devices is generally associated with the stiffness of the structure and its mass (Equation 3.7). Typically, MEMS devices fabricated in SOI or similar thin-film technologies are not thick, i.e., only several hundreds of nanometers, so the effect of volume on mass primary arises from the surface area of the device. Accounted for in the surface area are the lengths of any suspensions which combine with the device layer thickness to determine the spring constant, k. Longer, thinner beams are less compliant than shorter thicker beams and thus have a lower resonance frequency. However, there is a balance to be struck between large compliance for quick responsivity and low actuation voltage: driver electronics for sub 20 V operation are easier to design and more easily scaled than those for > 100 V operation. Device geometry also has an impact on the footprint of the device, and configurations that occupy too much chip area cannot be deployed in large numbers.

Finally, the actuation mechanism itself is a deciding factor for the power consumption of the device. Use of electric-fields as in electrostatic and piezoelectric actuation naturally lends itself to low power DC operation, whereas electrothermal and magnetic devices consuming constant, and sometimes large, currents are less power efficient. In this sense, an electrothermally actuated tunable coupler/switch or phase shifter is not fundamentally better or more efficient than an integrated heater. However, a look at **Table 3.1** reveals that electrostatically and electrothermally actuated MEMS currently exhibit the most promise for photonics compatibility. Ranking electrothermal MEMS actuators above piezoelectric devices may be puzzling because the latter are more power efficient and faster than electrothermal devices. This observation introduces the crux of the issue and poses a more fundamental question: what qualities does a technology need to be successful?

History has shown that timing and marketing play a key role in a product's or technology's success, but ultimately, cost drives everything. Whether it is a monetary expenditure or surrendering of the status quo for something new and different, industries and individuals always consider cost. In the field of electronics, silicon has been known to not be the semiconductor of choice and yet it remains "king," why? Silicon is abundant and easy to process, it has a naturally occurring oxide that can be used as an insulator, and for the past 70 years, a multibillion dollar industry has supported its growth and development. One could even posit that the sheer momentum silicon has acquired now sustains its success.

As discussed in Chapter 2, silicon with its indirect bandgap and higher propagation losses diminishes its position in the ranking of material platforms for photonic integration. However, the fact remains that Silicon Photonics is a technology whose material is well understood, whose processing is mature, can be used to make structures small enough to pack tens

of thousands of devices on a single chip, and is the only platform capable of monolithic integration with standard CMOS electronics. It may seem contrived that the success of an integrated photonics platform relies on existing infrastructure and knowledge and not some type of new physics or exotic material, but this is in fact the beauty of Silicon Photonics. The cost of staying with silicon is simply less and for as long as this is true, it will remain the most successful.

Researchers are already addressing the issue of integrating active sources in the platform and the presented state-of-the-art indicates that compact, high-performance devices performing all primary active functions in PICs can be done with physical mechanisms using low power. This efficient method is a topic of interest for reconfigurable and programmable photonics because like a field programmable gate array (FPGA) in electronics, the ability to dynamically reconfigure the connectivity of a PIC through software in the field opens up new opportunities. Such generic field programmable PICs (FP-PICs) would enable rapid prototyping of new PICs without the associated time and cost investment that bars smaller companies and research groups from participating in the field's development.

The next step, and the one demonstrated in this work, is that integration of MEMS into Silicon Photonics need not be done at the small scale of academic research, but can be successfully brought to an established industry platform. It is not only the MEMS-enabled PICs that benefit from large-scale, foundry-quality processing and interfacing with library-standard components. The technology platform too gains a new selection of powerful tunable and functional building blocks from which other users can profit as well.

4 Integration of MEMS into a Silicon Photonics Foundry Platform

Silicon has proven itself a versatile semiconductor for the electronics industry and state-of-the-art research has demonstrated that it can be a suitable material for devices performing the key functions needed in PICs. In particular, Silicon Photonic devices can be made small, low-loss and functionally desirable in terms of high ER, phase tunability, large bandwidth, and quick response times. Furthermore, current limitations in scaling related to high power consumption and losses of conventional tuning approaches can be addressed through the use of power-efficient, physical tuning mechanisms implemented by MEMS.

One of the central tenets underpinning the use of silicon over other materials in integrated photonics has been its compatibility with existing CMOS processing infrastructure. Foundry platforms like IMEC's iSiPP50G platform currently provide access to high-volume, high-performance Silicon Photonic PIC technology for industry and academic customers alike. The selection of passive and active components facilitates the design of next-generation circuits by seamlessly integrating new topologies or structures alongside validated and optimized devices. However, MEMS are currently non-standard components and their integration with Silicon Photonics is typically performed at academic or research cleanrooms and not at foundry-scale, which is necessary for continued growth and widespread adoption of MEMS in PICs. The advantage of a research-scale approach is that development and fabrication times can be kept short and designers have full control over processing. In 2016, a first successful demonstration of a die-level release process in IMEC's iSiPP25G platform as part of a multi project wafer (MPW) indicated the feasibility of merging Silicon Photonics with a foundry process [122]. This early result formed the basis and motivation for this work , whose goal it is to realize wafer-scale silicon photonic MEMS technology.

In order for MEMS to become library-standard photonic components and enable ubiquitous tunability and physical reconfigurability in PICs, they must be vetted in an established foundry platform. This assessment includes evaluation of material compatibilities as well as characterization of the optical performance before and after custom post-processing. Only by demonstrating that the introduction of MEMS does not deleteriously impact the rest of the platform and offers real added value, will foundries adopt mechanical tuning as an alternative

to, or replacement for, existing mechanisms.

4.1   Fabrication Guidelines and Design Principles

When designing and fabricating MEMS in a research environment, one has almost complete control of the material stack and corresponding thicknesses, and it is possible to perform metrology and validation after each processing step. The primary constraints come from the designer's creativity and the physics governing micro-/nanofabrication and electromechanics. Designing in a foundry platform, using the foundry proprietary process design kit (PDK), however, presents additional limitations. One is restricted to a smaller selection of approved materials and optimized thicknesses and the sequence of processing steps is immutable. That which is drawn will be fastidiously fabricated and the library-standard components behave as expected. On the other hand, one cannot reliably leverage specific processing details of the platform to aid in the design of component and so it must be treated as a black box.

Fortunately, there are several aspects of IMEC's iSiPP50G platform that make it amenable to the integration of MEMS. The starting substrate is a 200 mm silicon-on-insulator (SOI) wafer consisting of a thick 725 µm Si handle layer, a 2 µm thermal silicon dioxide layer commonly referred to as the buried oxide (BOX), and a 200 nm thick single crystalline silicon device layer (DL). For standard Silicon Photonics applications, this DL silicon serves as the core material for waveguides and other functional building blocks. Bottom cladding comes from the BOX and top cladding can be realized through the deposition of an additional oxide layer on top of the patterned DL. IMEC then offers a selection of doping levels for creating low-resistivity regions and active electro-optic and electro-thermal modulators, as well as Ge-on-Si epitaxy for integrated photodetectors. Finally, there are Al bondpads and 2-levels of Cu interconnects for electrical connection to the doped silicon and modulators/detectors.

Structurally speaking, only two components are strictly necessary for MEMS, a mechanically deformable layer that can be made anchored or free-standing and a sacrificial layer. The silicon DL of the platform can fulfill the role of the former and the BOX the role of the latter. By timed, selective removal of the BOX below regions of patterned DL, structures can be made free-standing in some regions and anchored in others to produce suspended MEMS. Because this etch process undercuts the devices to release them from the fixed boundary constraint, it is commonly referred to as a "release etch/process" and will hitherto be referred to as such. See **Figure 4.1** for an illustration of a MEMS device before and after the release etch. Electrical contact needed for actuation voltages and currents can be established through the use of doped silicon regions connected to the metallization running through the back-end-of-line (BEOL) stack.

Since the materials under consideration include silicon and silicon dioxide, and the release process requires the BOX to be selectively removed (i.e., only oxide and ideally no silicon), the etchant of choice is hydrofluoric acid (HF). This etching species exhibits almost infinite selectivity to silicon and can hence be used to safely remove oxide. HF can be used in its liquid
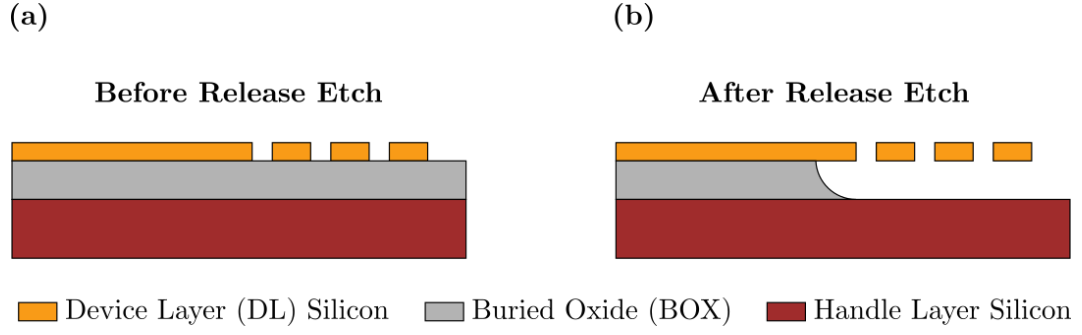
Figure 4.1 – Representative cross-section of a MEMS structure before and after the release etch. (a) Initially, the device layer (DL) silicon is firmly affixed to the BOX layer. (b) Once an etchant is introduced to selectively remove the sacrificial layer, which in this case is the BOX, the structure is undercut to produce suspended regions. Other portions, like that on the left, are only partially undercut, which leaves behind an anchor and produces a fixed-free cantilever structures. Note the isotropic undercut profile characteristic of the etchants typically used in such MEMS release etches.
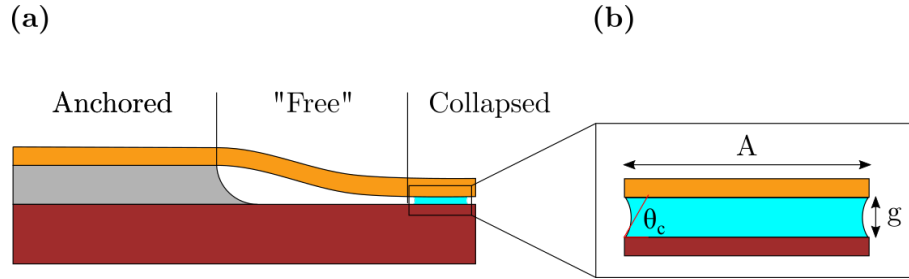
Figure 4.2 – Cross-section of a MEMS cantilever experiencing stiction forces that has caused it to collapse (a) Global view of the full structure depicting the tip that is stuck to the substrate (b) Magnified view of the tip depicting the liquid-air-solid interface and relevant parameters for the capillary force expression in Equation 4.2

phase and proceeds according to the following chemical reaction [123].

$$SiO_2\ (s) + 6HF\ (l) \rightarrow 2H_2O\ (l) + H_2SiF_6\ (aq) \tag{4.1}$$
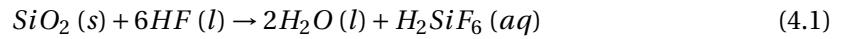
Use of a liquid etchant, however, introduces the risk of stiction (static friction), which impedes motion of objects in contact with one another. This undesirable phenomenon can result when surface micromachined structures are pulled down to the substrate by capillary forces (see **Figure 4.2** and Equation 4.2) during liquid-phase sacrificial layer etching and subsequent drying [124, 125].

$$F_{capillary} = \frac{2A\gamma_{la}cos\,\theta_c}{g} \tag{4.2}$$

Where A is the wetted area, γ_{la} is the surface tension of the liquid-air interface, θ_c is the contact angle between liquid and solid and air, and g is the liquid layer thickness.

Stiction is considered a failure mechanism because the adhesion energy associated with such stiction forces typically counterbalances the restoring spring forces of suspensions, meaning structures that have collapsed stay collapsed [125]. Critical point drying is an approach used to combat stiction in processing that eliminates the direct liquid-gas phase transition generating the detrimental surface tension. The transition does not involve crossing a phase boundary, but instead passes through the supercritical region, where the gas and liquid phases are indistinguishable [126]. This supercritical region can be reached via high-temperature and high-pressure but requires specialized equipment.

An alternative approach is to use vapor phase HF (VHF), which can also be used to remove oxide, albeit by a different mechanism, as anhydrous HF alone is incapable of etching oxide. The vapor phase HF etch proceeds via a slow reaction that is catalyzed by adsorbed moisture on the oxide surface created either by the reaction between HF gas and an alcohol (e.g., methanol or IPA) or directly by the presence of water vapor [127]. The H_2O on the oxide surface initiates ionization of the HF molecules into HF_2^- ions that then etch the oxide and produce silicon tetrafluoride (SiF_4) and more water [128] according to the following chemical reaction:

$$SiO_2 \, (s) + 2HF_2^- \, (ads) + 2MH^+ \, (ads) \rightarrow SiF_4 \, (ads) + 2H_2O \, (ads) + 2M \, (ads) \qquad (4.3)$$
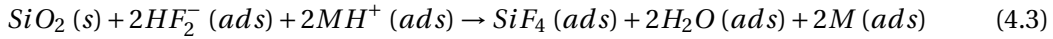
Where M can be either CH_3OH or $CH_3CHOHCH_3$ in the case of methanol and IPA, respectively.

The by-products are then periodically desorbed by heating and pumping so that the etching can proceed, and in the particular case of H_2O, which itself is a catalyst for the reaction, to control the etch rate.

Regardless of its state, HF is aggressive and highly corrosive, meaning any material or region that should not come in contact with it, e.g., the BEOL stack in which the metallization is embedded, should be well protected. One passivation material that satisfies this protective role is the insulator, aluminum oxide (Al_2O_3), also known as alumina/sapphire, which can be conformally deposited by atomic layer deposition (ALD) on a substrate to provide global coverage [129]. Following passivation, one must then open up the regions where one would like to make electrical contact and where in the subsequent step, the HF should have access to the BOX for the release etch, i.e., the MEMS cavities. This selective etching can be performed by either dry or wet etching with chlorine-based chemistry in a plasma etcher or by buffered HF (BHF), respectively. The details of when to use one over the other will be discussed in more detail in the following section.

The material requirements for Silicon Photonic MEMS and one way in which they can be fulfilled through a combination of IMEC's iSiPP50G platform and custom post-processing steps is summarized below:

1. Mechanically deformable, structural layer: DL silicon of an SOI wafer (3 thicknesses from IMEC)

2. Sacrificial layer: BOX layer of an SOI wafer (IMEC)

3. Passivation against HF/VHF: alumina (custom post processing)

4. Selective patterning of alumina to provide electrical contact and access to MEMS cavities for undercut by HF/VHF: plasma etching using chlorine-based chemistry or BHF wet etching (custom post processing)

5. Selective etchant of sacrificial layer: HF/VHF (custom post processing)

Having a material platform and the associated fabrication steps for post-processing of MEMS is necessary but not sufficient. Certain design principles and fabrication guidelines critical for the successful release and operation of devices must also be established.

Areas where the MEMS are designed make use of the EXPO etch module provided by IMEC to remove portions of the BEOL stack and reveal DL silicon and the BOX. Together with the patterned alumina, these openings define the MEMS cavities because here, the alumina is removed making it possible for the VHF to undercut structures. Within each cavity, a silicon rim serves as an anchoring region and also as an additional protective barrier against VHF. In particular, the rim ensures that VHF cannot access the stack laterally, but rather only from below, which can only happen if the underlying BOX is completely removed. It should be noted that such a complete undercut of the silicon rim should never occur as the etching time is controlled to only suspend structures. The rim also accommodates the electrical isolation trenches separating regions at different voltages and the optical transitions needed for low-loss passage between oxide- and air-cladding. A representative sketch from two perspectives of the MEMS cavity is provided in **Figure 4.3**.

Protection of the BEOL stack is a key objective as it not only contains the interconnect metallization, but also oxides and other dielectrics that when exposed to VHF can produce particulate contamination that re-deposit in other regions. If these particles settle on waveguides, losses can dramatically increase and if they land on the MEMS devices themselves, actuation may be hindered or rendered impossible. Etching of the BEOL stack can also lead to structural degradation of MEMS cavities, grating coupler cavities, and contact pads, leaving them unusable. All of these issues related to attack of the BEOL stack constitute process incompatibilities with the iSiPP50G platform and must be prevented. The silicon rim is important in protecting the stack from lateral attack in the MEMS cavities, but the alumina provides the global coverage that passivates all other regions of the sample. In fact, the only vulnerabilities in the alumina arise from its placement (i.e., on top of which material is it deposited?) and its etching, which can lead to cracking in vulnerable regions with large topographical contrast, e.g., MEMS cavities and sealing rings.
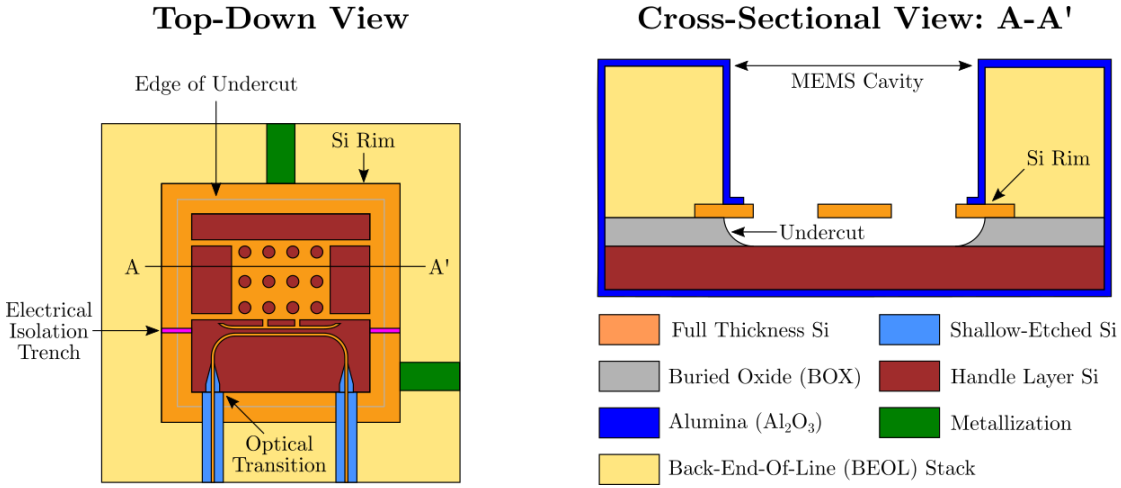
Figure 4.3 – Top-down and cross-sectional view of the MEMS cavity containing a sample photonic MEMS structure and the silicon rim. Salient features include the electrical connection provided by the metallization and the electrical trenches that separate regions at different voltages. The optical transitions form part of the optical I/O and provide low-loss transit of the silicon rim. As indicated in the cross-sectional view, the silicon rim works together with the alumina passivation to restrict the VHF's access to the BOX so that the MEMS are undercut while the BEOL is kept intact.

With respect to alumina's deposition on the material stack, Figure 4.4 depicts a simplified starting cross-section for a MEMS cavity showing an alumina on oxide and an alumina on silicon arrangement. Note the presence of a thin planarization oxide on top of the DL silicon indicated in red, and a pink filler oxide adjacent to the DL silicon. These are chemical-vapor-deposited (CVD) oxides, which as opposed to thermal oxides are less dense and therefore etch more quickly [130]. Used in a planarization process after silicon patterning, these oxides will be attacked and removed by VHF if left unpassivated. As seen in the case where alumina rests on oxide (**Figure 4.4b, c**), the VHF quickly progresses laterally above the DL silicon and attacks the BEOL stack once the planarization oxide is removed. In the case where alumina is deposited on silicon (**Figure 4.4d, e**), VHF has no lateral access to the BEOL stack, thereby ensuring that the only undercut is that of the BOX. Alumina can be deposited directly on silicon by first removing the filler and planarization oxides with a liquid etchant. The additional advantage of performing this step is that any residues related to the precursors in these CVD oxides are washed away and do not redeposit elsewhere.

Once the requisite precautions for protecting the BEOL stack have been implemented, there is one other set of design principle that must be kept in mind. Since VHF is an isotropic etchant that removes the BOX at equal vertical and horizontal rates, one must carefully dimension anchors and suspended structures to ensure that the former remain fixed and the latter free. **Figure 4.5** illustrates the situation graphically: for a BOX of thickness h, and three silicon structures of varying width, $d_1 > 2h, d_2 = 2h, d_3 < 2h$, three distinct scenarios after the VHF etch are possible. In the case where one etches exactly a distance h in the vertical direction to fully remove the BOX and expose the handle layer silicon, one will have etched a distance h
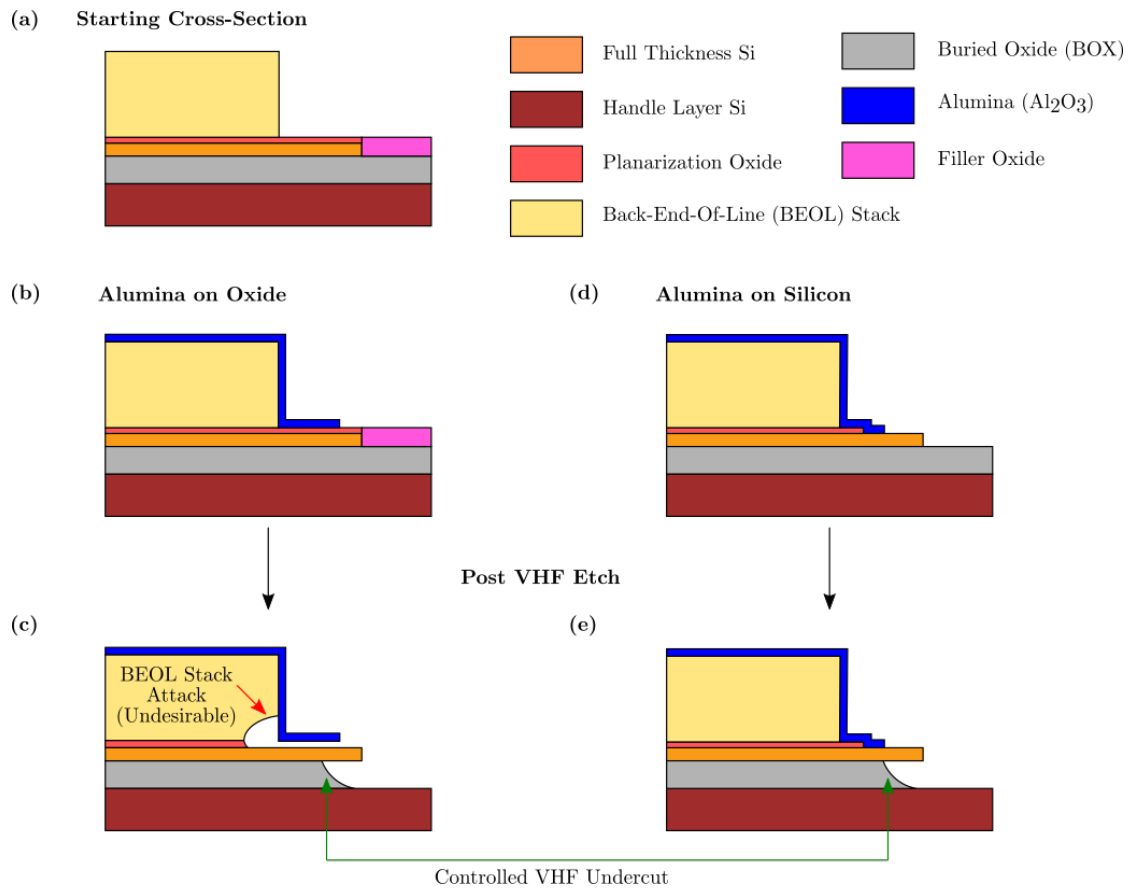
Figure 4.4 – (a) Simplified cross section of a MEMS cavity indicating the CVD oxides present at the start. (b) Alumina deposition directly on these oxides leads to their (c) removal in the final VHF etch step and subsequent attack of the BEOL stack. By (d) first removing these oxides such that alumina is deposited on silicon, (e) the VHF's access is limited to the BOX as desired.

laterally. Note for structures where VHF has access to the BOX on both sides, which is the case here, this undercut distance h is symmetric with respect to the exposed edges. The structure of width d_1, is clearly an anchor because enough BOX remains to fix the DL silicon to the handle layer. For the structure of width d_2, one has reached the limiting case where the DL silicon and BOX are attached at a single point (an oxide pillar) and any subsequent etching makes the structure freestanding. By further decreasing the width to d_3, for example, the height of this pillar reduces until the oxide is fully removed. Although an oxide pillar is generally not a hindrance to in-plane moving MEMS devices, out-of-plane devices will suffer from reduced range of motion and risk of charge-trapping. Consequently, it is good practice to completely remove the oxide pillar.

The minimum value of undercut needed to fully remove the oxide pillar below a structure of width d is given by the hypotenuse of the triangle formed by the BOX height h and half the width, i.e., $d/2$:
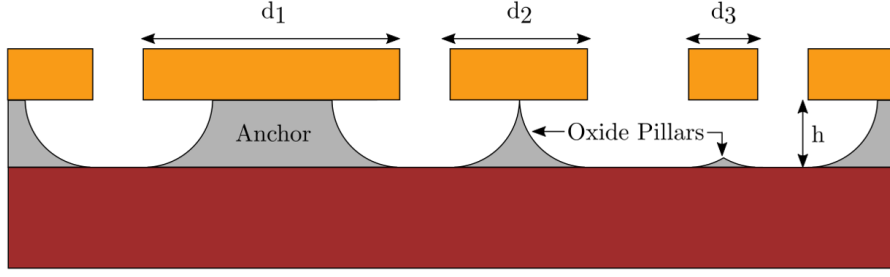
Figure 4.5 – Illustration of the undercut for three structures of varying width, $d_1 > 2h, d_2 = 2h, d_3 < 2h$ and how a release etch targeting a vertical etch distance h produces three distinct characteristics in the remaining oxide. For a width d_1, one is left with an anchor, for width d_2, the structure is in contact with the BOX at a single point of the pillar, and for width d_3, the structure is fully suspended and only a small oxide pillar remains.

$$undercut_{min} = \sqrt{h^2 + \left(\frac{d}{2}\right)^2} \qquad\qquad (4.4)$$

It should be noted that the visualization in **Figure 4.5** is somewhat simplified in that it only takes into account the in-plane dimension (i.e., the width) of a particular cross section. The width could of course vary along the length of the device, which extends out-of-plane, and if one desires the entire structure to be free-standing without underlying oxide pillars, the minimum required undercut would exceed that given in Equation 4.4. However, an often utilized approach to fully undercut large structures is the inclusion of etch holes, which are full-thickness openings in the DL silicon that provide additional access points for the VHF to the BOX. Using these etch holes, one can again use the provided expression for the minimum undercut with the modification that d is replaced with the maximum distance from the edge of an etch hole to another or from an etch hole to an edge/corner of the structure.

It should be noted that this discussion is based off an idealized SOI wafer that has a homogeneous, uniform BOX. Depending on the SOI wafer manufacturing process, the actual undercut etch profiles presented in the previous figures may in fact look quite different. A more complete discussion of this issue is tabled for a later section.

Given the margins between the MEMS cavity openings and silicon rim and worst-case scenario etch propagation in the electrical isolation trenches, this work targets an undercut of approximately 2.5 µm. Consequently, the etch hole-to-etch hole and etch hole-to-edge/corner separation is capped at 3 µm for complete oxide pillar removal as required for out-of-plane moving devices. Larger separations are allowed for in-plane moving devices and even necessary for anchors: in this case, the minimum width/length of an anchor is set to 10 µm so as to ensure a sufficiently large oxide pillar for reliable fixation.

Photonic MEMS designers simulate and draw device topologies that not only respect the design rules of the PDK concerning minimum feature size, for example, but also take into
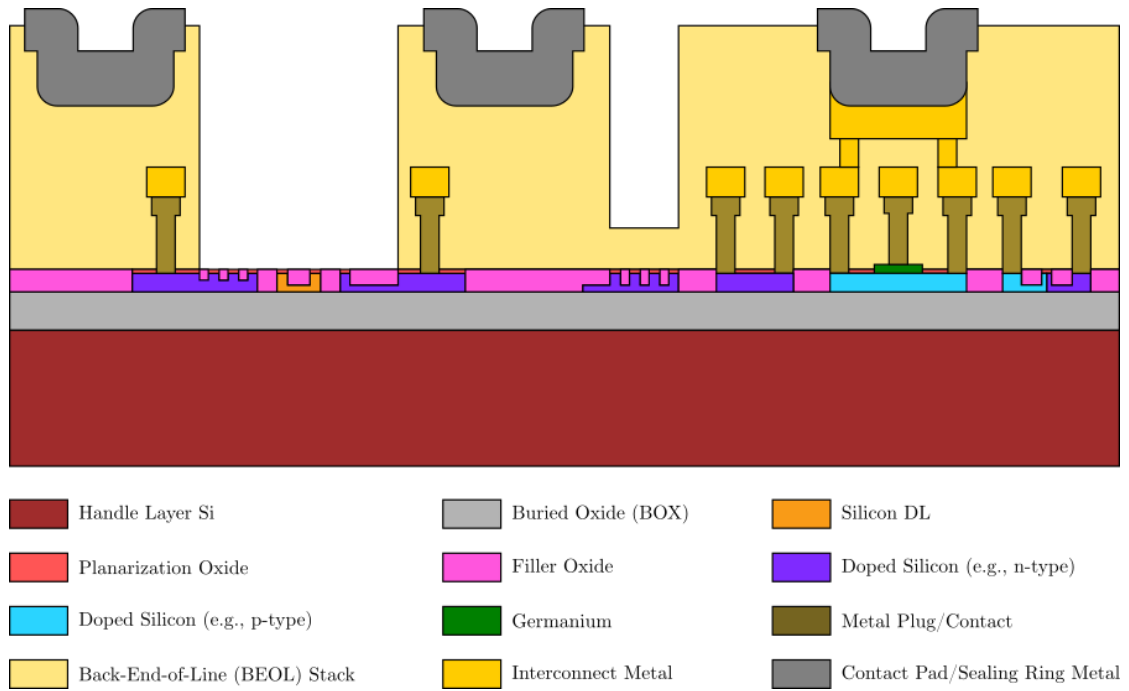
	Handle Layer Si		Buried Oxide (BOX)		Silicon DL
	Planarization Oxide		Filler Oxide		Doped Silicon (e.g., n-type)
	Doped Silicon (e.g., p-type)		Germanium		Metal Plug/Contact
	Back-End-of-Line (BEOL) Stack		Interconnect Metal		Contact Pad/Sealing Ring Metal

Figure 4.6 – Representative cross-section of the starting sample that arrives at EPFL after fabrication at IMEC. Key topographical features include the MEMS cavity that extends through the BEOL stack until the DL silicon, a partial-etch of the stack above the grating coupler, and the openings above the metallization used for bondpads and sealing rings. Relevant materials are color-coded and these colors set a reference for all subsequent cross-sections.

account these presented fabrication guidelines and design principles. Doing so provides the greatest chance of successful photonic MEMS device integration in the iSiPP50G platform. Once designs are submitted and approved, the foundry carries out the fabrication and the next step begins, the custom MEMS post-processing.

4.2   MEMS Post-Processing

Throughout the course of this work, three fabrication runs at IMEC have been carried out, each of which included designs provided by the group at EPFL and from project collaborators. Further details of the IMEC proprietary technology can be found in [86]. The foundry processing is carried out at 200 mm wafer scale, after which the wafers are either diced into coupons consisting of four chips in a 2 x 2 arrangement (total size: 46 mm x 46 mm, chip size: 23 mm x 23 mm) or cored into two 100 mm wafers for wafer-level processing. An additional dicing step can be carried out at any stage in the post-processing to provide individual chips suitable for short-loop experiments and equipment calibration. Samples arrive at EPFL with the following representative cross-section presented in **Figure 4.6**. A simplified process flow illustrating the key steps including planarization and filler oxide removal, alumina passivation, alumina patterning, and the VHF release is provided in **Figure 4.7**.
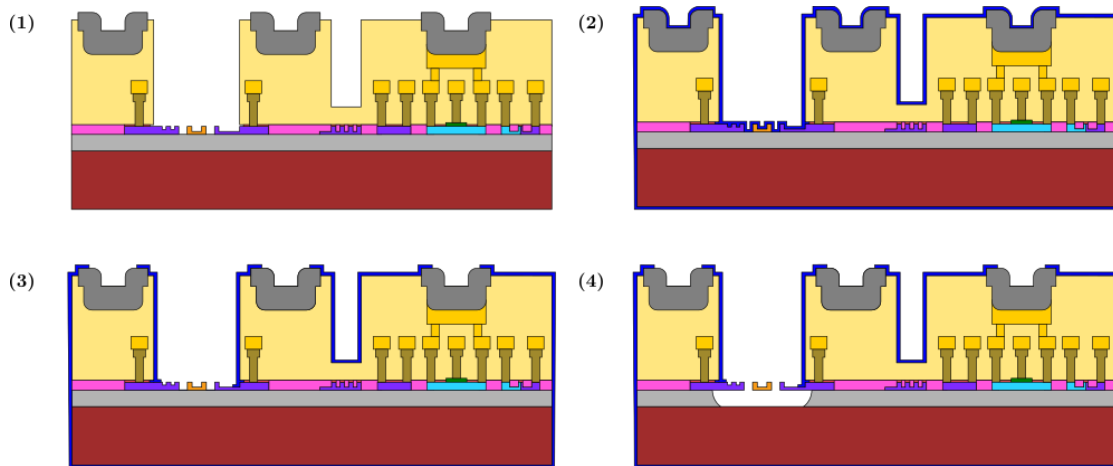
Figure 4.7 – Process flow for the MEMS post-processing detailing the primary steps **(1)** planarization and filler oxide removal by BHF **(2)** alumina passivation **(3)** alumina patterning over the metallization and MEMS cavities by dry and wet etching **(4)** VHF release etching of the BOX

The decision to primarily process at coupon-scale rather than wafer-scale is driven by supply and cost as well as compatibility with equipment for post-processing (e.g., chips > 1 cm x 1 cm can safely be used with all tools). Each fabrication run consists of 24 200 mm wafers, some of which are kept by IMEC for process monitoring, leaving roughly 20 wafers. If each of these were then to be cored into 100 mm wafers and subsequently edge ground for a cumulative cost of several thousand francs per wafer, not only is the leeway for experimentation and error in process development drastically reduced, but one accumulates additional overhead before any MEMS post-processing begins. Nevertheless, wafer-scale processing is necessary for the wafer bonding that takes place after VHF release and provides a protective lid/cap over the MEMS devices.

4.2.1 Planarization and Filler Oxide Clearing

As indicated in the previous section, in order to optimize the protective properties of the alumina passivation such that it lies directly on the silicon ring, the planarization and filler oxides must be first removed. This task is accomplished through the use of BHF, which exhibits good selectivity against the silicon DL (**Figure 4.7a**).

Using a maskless (i.e., direct laser writing) lithography step with alignment, it is possible to write a pattern similar to that of the MEMS cavities already present on the sample. The one modification is that this new "Oxide Clearing" mask is 5 μm smaller than the original MEMS cavity design in all dimensions, i.e., there is a 5 μm margin from the MEMS cavity border to the edge of this new pattern. This value is a compromise between 1) removing enough planarization and filler oxide in the full-etch electrical isolation trenches and shallow-etched optical transitions and 2) providing adequate margin to the MEMS cavity so as to ensure the sidewalls of the cavity are protected by photoresist and to relax alignment accuracy tolerances.

The MEMS cavity presents a vertical step of roughly 6.3 µm in topography and thus, a sufficiently viscous photoresist with adequate thickness is needed to ensure that the sidewalls, as well as the edges and corners of the cavity are covered. A 4.5 µm thick layer of AZ ECI 3027, a chemically amplified i-line positive photoresist satisfies this requirement and can be exposed with 405 nm-wavelength light. CMi's MLA 150 laser writer performs the exposure with an alignment accuracy of better than 500 nm and following manual development in a TMAH-based developer solution (AZ 726 MIF), the sample is ready for liquid BHF etching. It should be noted that the use of a maskless lithography step expedites process development times as it obviates the need for an additional mask-fabrication step. Corrections and additions can be added by simply altering the GDS file in an appropriate layout editor without making any physical changes.

Following an oxygen plasma descum step to ensure that all the photoresist in the exposed regions has been removed, the sample undergoes a 3 minute dip in a BHF bath. BHF's etch rate is oxide-dependent and spans the range from 77 nm/min for thermally grown wet oxide (e.g., the BOX), to 262 nm/min for some CVD oxides. Knowing that the planarization and filler oxides constitute roughly 225 nm of CVD oxide, 3 minutes ensure that even with variations in etch rate, these oxides are completely removed and that enough BOX remains below the 450 nm wide waveguides so that they will not be completely undercut.

Figure 4.8 provides several SEM images of structures where the filler oxide has been completely removed between comb fingers, the structural frames of devices, and between waveguides. The full thickness and shallow-etched DL silicon lie atop BOX pillars, as they have not been fully undercut.

4.2.2 Alumina Passivation

With the planarization and filler oxides removed and the protective photoresist stripped with a combination of wet and dry removal techniques, the next step is the passivation of the entire sample by alumina using atomic layer deposition (ALD) (**Figure 4.7b**).

While alumina can also be deposited by sputtering, the requirement for conformal coverage to protect the MEMS cavity sidewalls limits the usefulness of physical vapor deposition in this step. This work uses a BENEQ TFS200 ALD tool heated to 200 °C to deposit alumina layers ranging from 50 to 70 nm in thickness. As depicted in **Figure 4.9**, the deposited alumina is highly conformal and follows the step in the MEMS cavity. In regions where the planarization and filler oxide have been removed, the alumina rests directly on top of the silicon rim and in the margin where the "Oxide Clearing" mask protected these oxides, alumina rests on top of a filler oxide. The conformality ensures that the oxide sidewalls receive the passivation as well, so that there is no lateral access for the VHF. Furthermore, the subsequent alumina patterning steps in the MEMS cavities also provide a margin to ensure that these "vulnerable" regions do not have their protective alumina coating removed.
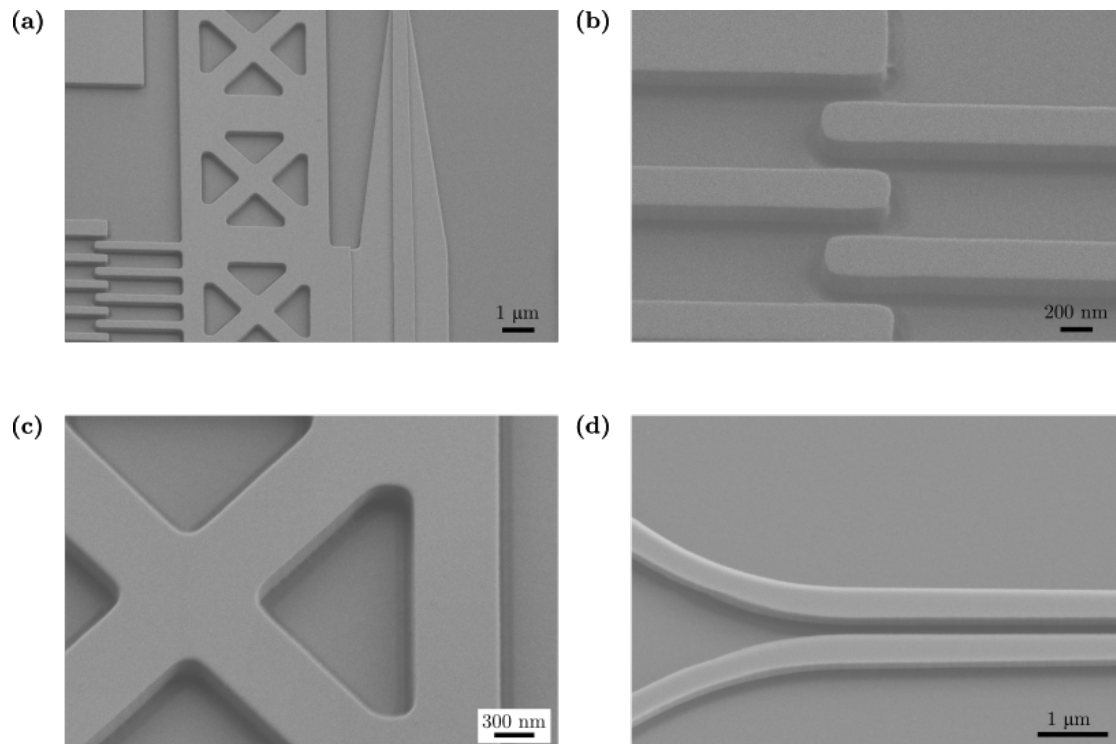
Figure 4.8 – (a) An SEM image of the movable portion of an in-plane, comb-drive based photonic MEMS device that includes comb-fingers, the structure frame, and the attached full thickness and shallow-etched silicon waveguide (b) Magnified view of the comb fingers, showing oxide-free gaps (c) Magnified view of the frame (d) Magnified view of two waveguides in the coupling region of a device indicating a clean gap and slight undercut
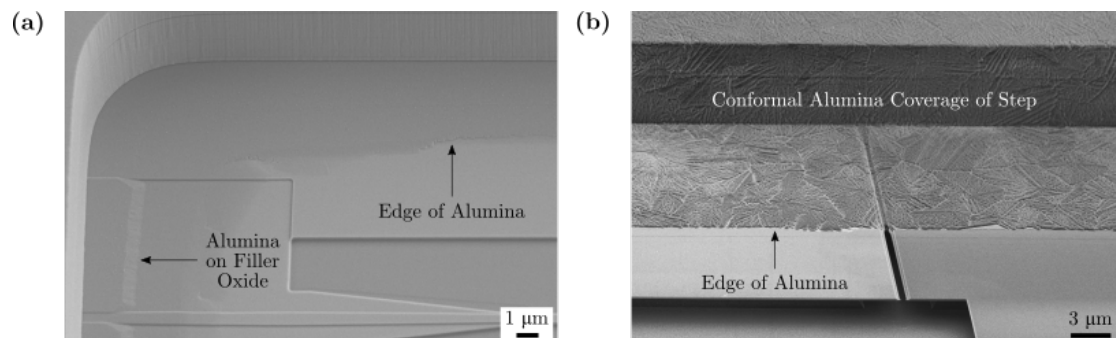

Figure 4.9 – (a) An SEM image of an optical transition in the corner of the MEMS cavity, post alumina patterning, where the wet etch has defined the edges of the alumina. Two distinct regions are visible: one, where alumina lies on top of silicon and another where alumina lies on top of filler oxide (b) An SEM image of an electrical isolation trench after VHF, where the edge of the alumina is clearly visible and the conformality over the step in the MEMS cavity is indicated by a continuity in texture. Note here that the alumina has effectively sealed the electrical isolation trench thereby limiting the VHF's lateral access to the BEOL stack.

Comparing **Figure 4.9a** and **Figure 4.9b**, the alumina in these two samples appear texturally different. The sample from which **Figure4.9b** comes was taken out of the controlled environment of the cleanroom for characterization in the lab and later returned for imaging. Cleanliness aside, the primary difference between the cleanroom and lab setting is the humidity and because samples kept in the cleanroom have not been observed to exhibit this aesthetic, it is likely that these web-like patterns, with some ostensible short-range order, are linked to humidity but would require further investigation. Similar degradation of ALD Al_2O_3 passivated samples has been reported previously, although in 95% to 100% relative humidity [131, 132]. The loss of a smooth alumina layer on top of the optical transition is bound to introduce additional optical scattering losses for the device. If indeed related to humidity, this mutation in alumina morphology can be prevented by hermetic sealing of the MEMS cavities.

4.2.3   Alumina Patterning

Once the sample has been successfully passivated by alumina, the next step is to selectively open up the regions where electrical contact must be made. Alumina must also be removed from the MEMS cavities so as to provide VHF access to the BOX.

Alumina is cited as being "notoriously difficult to dry etch due to its high mechanical hardness and chemical stability" [133]. And in fact, it is the presence of a native aluminum oxide layer that protects aluminum from being etched by pure chlorine and bromine species [134]. Consequently, plasma chemistries using CCl_4 or BCl_3 can be used for ion bombardment to etch the alumina. Unfortunately, this particular chemistry aided by ion bombardment exhibits poor selectivity against silicon, which means that once alumina has been removed, the dry etch will rapidly consume the DL silicon. In waveguides where the physical dimensions are of paramount importance, reduction in waveguide height is deleterious. A reduced DL silicon height is also sub-optimal for the MEMS devices, as their mechanical properties (e.g., stiffness) also depend on these geometric parameters.

If one were to exclusively etch alumina with a dry, chlorine-based chemistry, it is highly probable that either the optical or mechanical portions of the device would suffer. A reduced etch time, on the other hand, runs counter to the common notion that a slight overetch ensures the complete removal of the material to be etched. Even if only a few nanometers of alumina remain, VHF will not have access to the BOX and there will be no undercut of the MEMS devices.

An alternative approach is to use BHF. Unfortunately, but also perhaps unsurprisingly, BHF is known to attack and/or roughen aluminum, the primary constituent element in the metallization for the contact pads and sealing rings. While a roughening of contact pads does not pose a fundamental issue, the surface topography of the sealing rings is critical for wafer-level bonding. In order to prevent unnecessary modification of the metal surfaces, the alumina patterning over the metallization and over the MEMS cavities are decoupled from one another. Etching of alumina over metal is performed using an inductively coupled plasma (ICP) etch
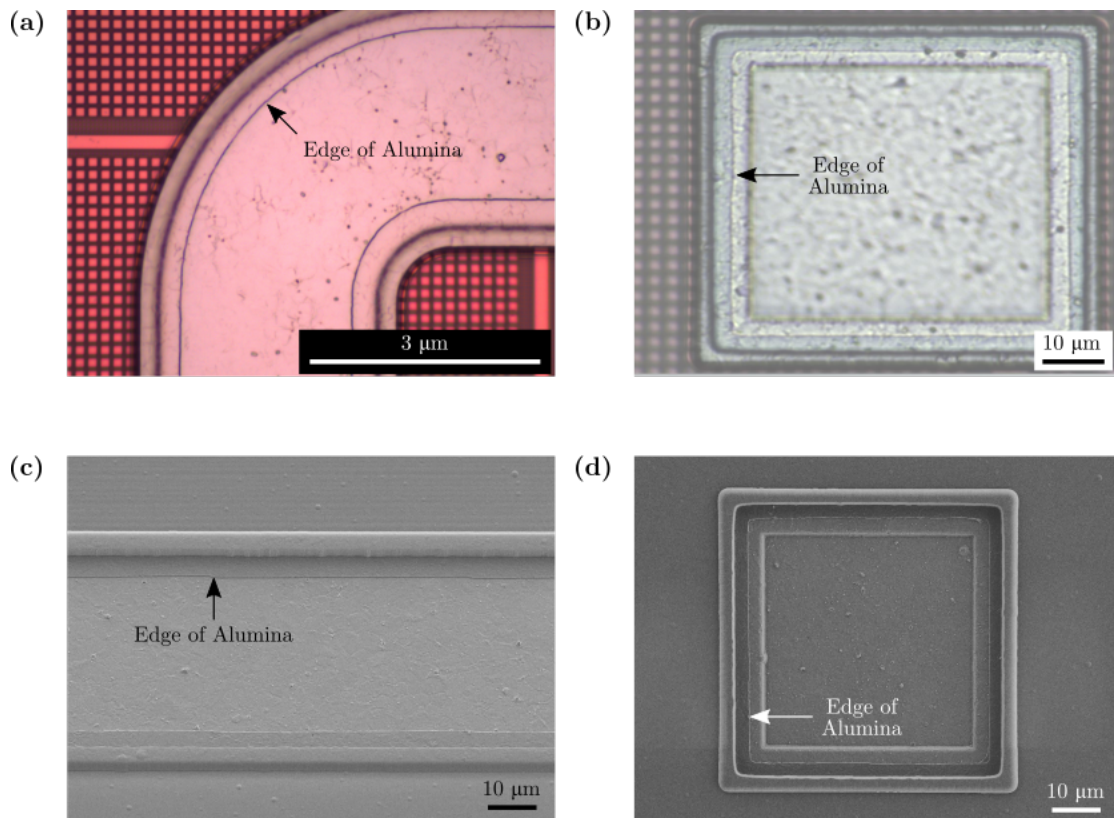
Figure 4.10 – Optical microscope image depicting the patterning of the alumina over the (a) sealing ring and (b) contact pad. The edge is well defined and sharp in both cases because the dry etch is primarily anisotropic. The SEM images provide an alternative visualization of the corresponding alumina etch over (c) the sealing ring and (d) the contact pad.

with Cl_2/BCl_3 chemistry and the corresponding etch over the MEMS cavities is performed using BHF. After these two etches, the sample's cross-section looks as shown in **Figure 4.7c**.

The optical and SEM images in **Figure 4.10** corroborate the ability of the dry etch to successfully open up the alumina over the metallization without disturbing the surface morphology. By using a 2.5 µm margin from the edges of the metallization for the alumina openings, it is possible to ensure that there is continuity of the alumina over the step. Doing so mitigates the risk of cracking or insufficient protection of the BEOL stack at the outer edges. Furthermore, the size of the opening is sufficiently large so as to allow access to probe tips for electrical characterization, but not create excessively tight alignment tolerances.

The alumina opening pattern within the MEMS cavity follows the shape of the cavity itself with a margin of at least 10 µm and maintains a margin from the inside edge of the silicon rim of at least 4 µm (**Figure 4.11**). This characteristic is illustrated in **Figure 4.12**, which presents images of the sample after the alumina patterning in the MEMS cavities. Heuristically determined, these margins secure a safe lateral distance from the BEOL stack in the case that alumina does not completely rest atop silicon, and also guarantees the absence of free-standing alumina
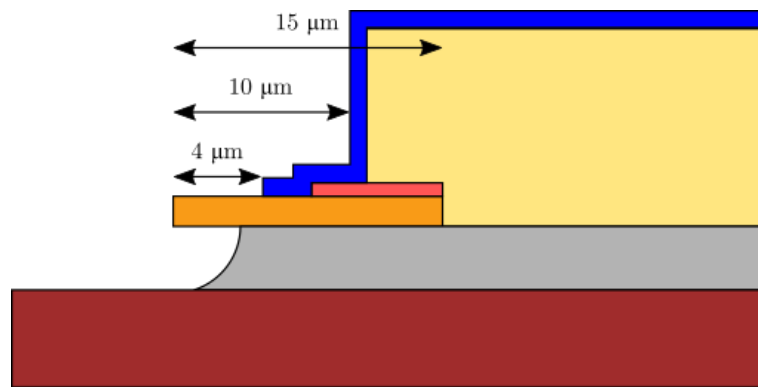
Figure 4.11 – Schematic diagram indicating the various margins for the alumina layer with respect to the inner edge of the silicon rim (4 μm) and the edge of the MEMS cavity (6 μm). An additional 5 μm extension of the silicon rim into the BEOL stack provides an additional fail-safe against VHF propagation into the stack.

cantilevers that could fracture and land elsewhere on the sample.

Smaller margins allow the silicon rim's width to be reduced, effectively decreasing device footprint. On the other hand, margins slightly larger than the minimum and a silicon rim extending beyond the MEMS cavity constitute a hedging technique against unforeseen non-idealities in etching. The compromise between size and safety established in this work is illustrated in **Figure 4.12c**, where the edge of the alumina extends slightly more over the electrical isolation trench. These trenches, while necessary for proper electrical operation, represent a vulnerability in the silicon rim because here, the silicon is fully etched and subsequently filled with CVD oxide. One must then rely on the oxide removal and alumina passivation steps to cover and fill the gap. Thus, any extra margin in these regions is an advantage.

4.2.4   VHF Release Etch

With the BOX in the MEMS cavities exposed and all other regions protected by alumina, the final VHF release step is carried out using an SPTS μEtch tool utilizing anhydrous HF and alcohol. This tool allows users to select from several recipes in which the flow rate of HF, ethanol, and nitrogen can be adjusted to vary the partial pressure of HF to control the etch rate. The chamber pressure, which can be adjusted from high (150 torr) to low (75 torr) can also be used to increase or decrease the etch rate, respectively. In general, the uniformity of the etch degrades with faster etch rates and because the structures designed in this work are rather thin and consequently mechanically fragile, a slow etch rate is employed (90 torr). Using a 900 s etch cycle, repeated 14 to 15 times, it is possible to achieve the targeted undercut of roughly 2.5 μm. A histogram taken over 27 samples (**Figure 4.13**) indicates that using this configuration, the etch rates follow a normal distribution, with the most prevalent values falling between 0.14 μm and 0.17 μm per cycle.

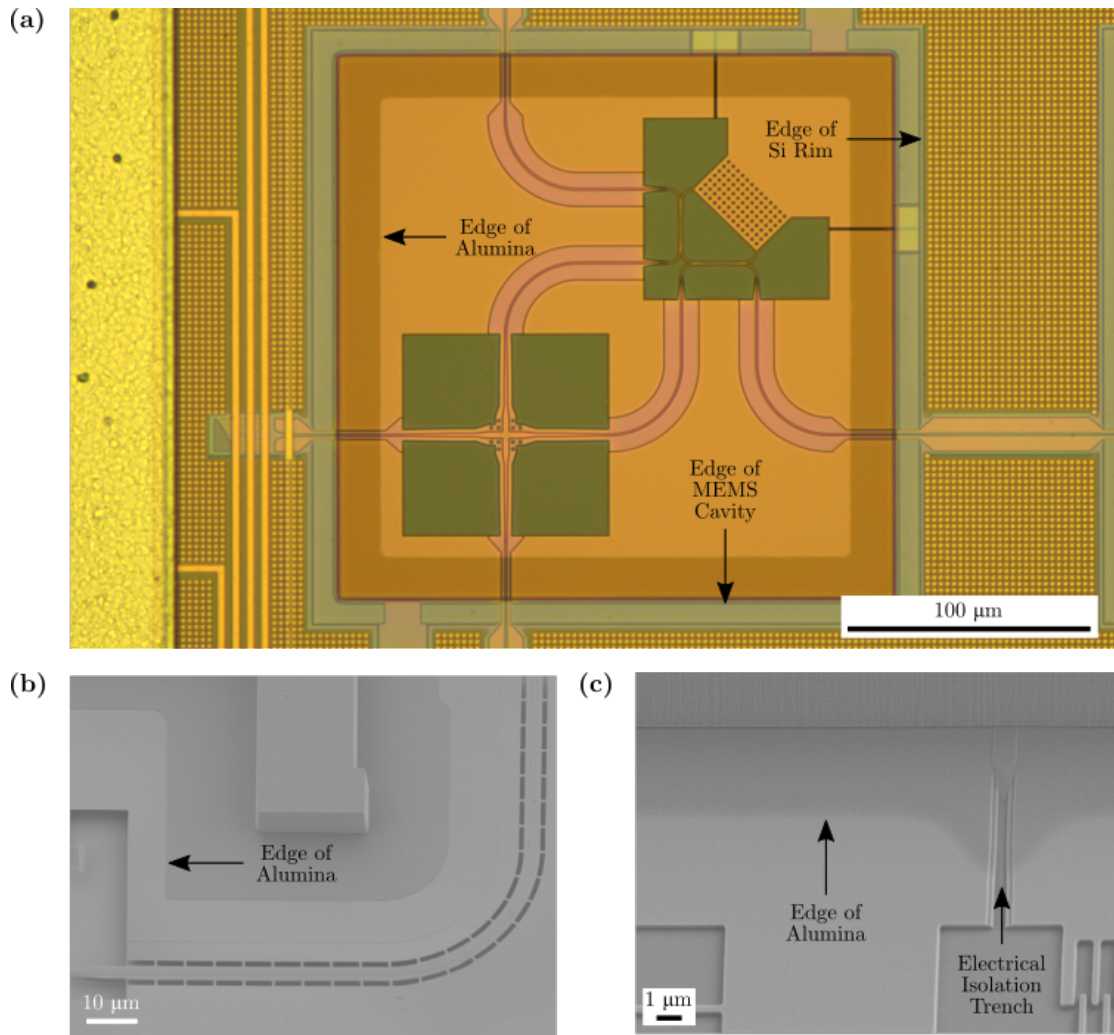Optical inspection of samples after this etch reveals several of the key features of the VHF

Figure 4.12 – (a) Optical microscope image of the alumina patterning within the MEMS cavity. The color contrast between the exposed silicon and the alumina-covered silicon indicates the extents of the etch (b) SEM image depicting the clean alumina and how alumina coverage is preserved in the unexposed regions (c) SEM image of the alumina patterning over an electrical isolation trench.

undercut. **Figure 4.14a** and **Figure 4.14b** capture the etch front and its isotropic characteristic. Anchors can be identified by the oxide pillars that lie below and any out-of-plane deflection or collapse can be identified by variation in the fringing fields on the suspended structures. With the SEM in-lens detector and a high acceleration voltage, one is able to penetrate the thin DL silicon to image the remaining BOX as in **Figure 4.14c**. Furthermore, tilting the sample 30° with respect to the detector and monitoring the backscattered electrons provides a perspective view that captures the free-standing nature of the MEMS shown in **Figure 4.14d**.
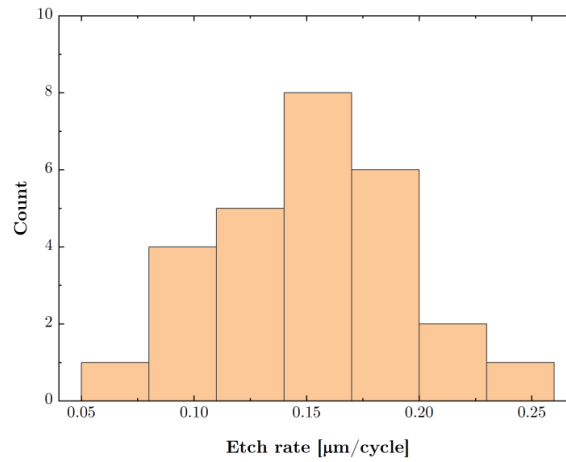
Figure 4.13 – Histogram detailing the normal distribution of etch rates for 27 different samples from RUN2 and RUN3. Samples from RUN1 have been excluded as the SOI wafers utilized in that particular fabrication run exhibited uncontrolled lateral etch rates.
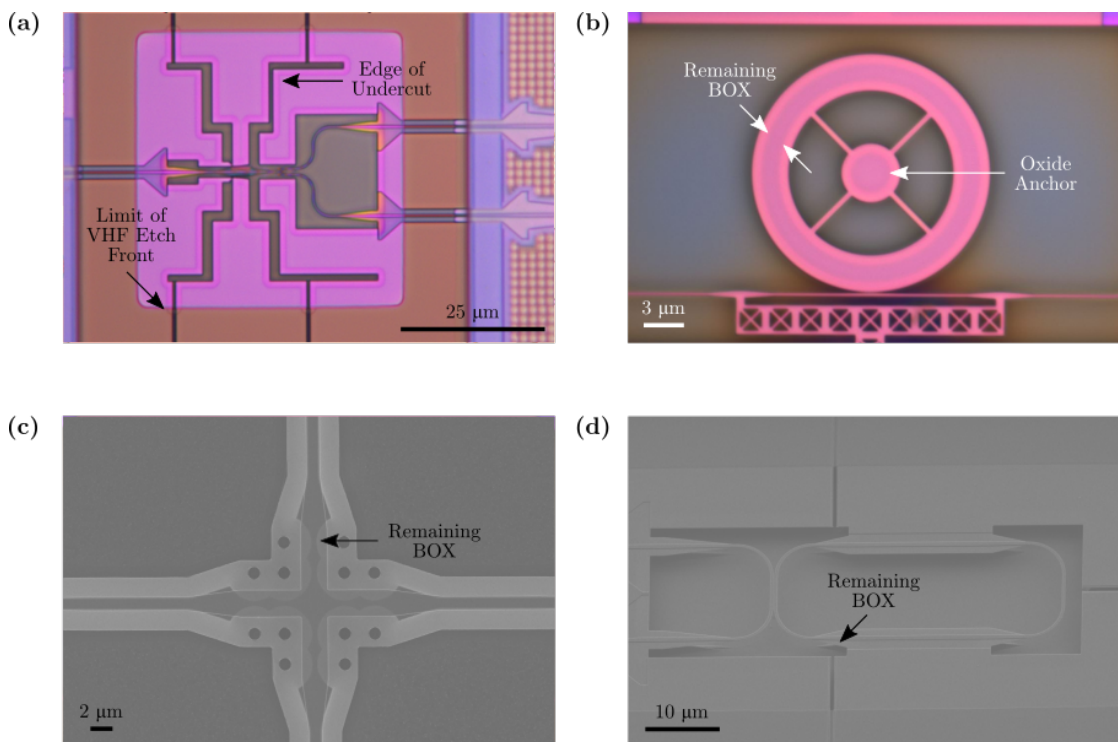

Figure 4.14 – (a) Optical microscope images indicating the extent of the VHF undercut and how the removal of planarization and filler oxide and subsequent alumina deposition limits the extent of the etch front (b) Magnified view of a ring resonator and bus waveguide highlighting the remaining BOX that serves as an anchor (c) SEM image of an optical transition depicting the undercut and remaining BOX through the DL silicon (d) A cleanly suspended tunable resonator structure

65

4.3   Challenges and Solutions

A first challenge arises from substrates used for Silicon Photonic MEMS. Typically, Silicon Photonic wafers are selected with optimal electrical and optical properties. However, when working with photonic MEMS, one has an additional evaluation criterion related to the sacrificial oxide, in this case the BOX, and here, not all SOI wafers are the same.

An SOI wafer can be fabricated either by **S**eparation by **IM**plantation of **OX**ygen (SIMOX), or by wafer bonding. In the SIMOX process, oxygen ions are implanted into a silicon wafer by ion beam implantation and after a high temperature anneal, a BOX layer is created. With wafer bonding on the other hand, an oxidized silicon substrate is directly bonded to another silicon substrate: one substrate is thinned to become the DL, the sandwiched oxide layer becomes the BOX, and the other substrate becomes the handle layer. The exact fabrication method is relevant for this work because if the silicon-oxide interface is defective or the oxide itself is of low-quality, HF-based etching can rapidly propagate in the lateral direction, leading to a purported violation of the isotropic etch characteristic.

An example of this phenomenon can be seen in **Figure 4.15** where a Silicon Photonic MEMS compatible SOI wafer and an SOI wafer incompatible with Silicon Photonic MEMS are compared with one another after the exact same processing and etch time. **Figure 4.15a** shows how a the MEMS-compatible starting substrate exhibits a single etch front, which can be verified by focused ion beam (FIB) etching of the disk in **Figure 4.15c**. The effects of a defective or low-quality BOX can be seen in **Figure 4.15b** and **Figure 4.15d**, where multiple rings in the optical microscope image indicate the presence of the multiple etch fronts seen after a FIB cut. The presence of multiple etch fronts is problematic when designers draw a 10 μm anchor, expecting a 5μm broad oxide pillar to remain after 2.5 μm, undercut only to find that enhanced VHF etch propagation along the bond interface has progressed two to three times farther than expected, collapsing the device. Thus, the first step before any designs are simulated or drawn is to coordinate with the foundry that MEMS-compatible wafers be used.

The presented process flow employs both dry and liquid etching based on material compatibility. Dry plasma etching is compatible with metals, liquid etching by BHF is suitable for the MEMS structures, and dry VHF etching does not negatively influence either: it simply removes the BOX and provides the undercut. Use of BHF has the added advantage of being able to cleanly remove oxide, independent of its type (e.g., CVD, PECVD, thermal, etc.). For example, if a low-quality oxide is present and only dry etching is used to remove it, particles can be observed to redeposit on the handle layer (**Figure 4.16**) and potentially on the waveguides and MEMS structures as well. A liquid etchant like BHF on the other hand, removes the oxide and washes away any embedded particles.

Non-idealities in the alumina passivation and patterning insufficient thickness of the deposited layer and modified boundaries of the photoresist at high temperatures, which can lead to a cracking failure mechanism only evident after the VHF release etch. Alumina that cracks or delaminates is discernable without need for magnification, as evidenced in **Figure**
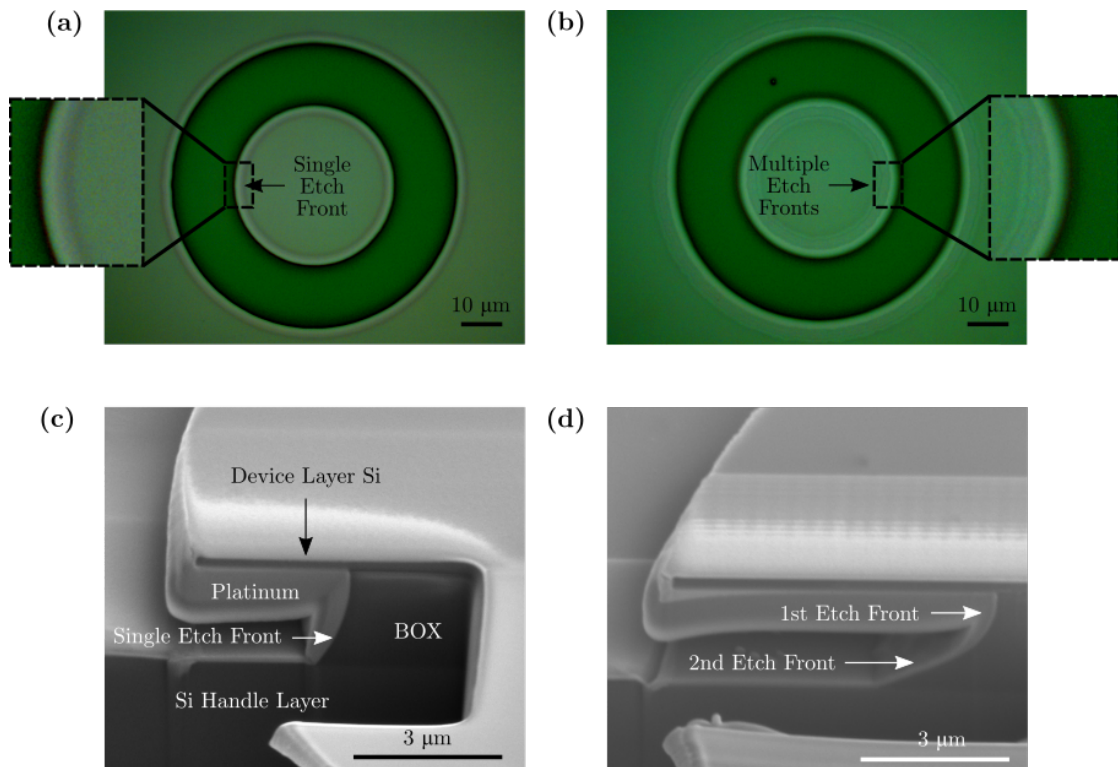
Figure 4.15 – Comparison of the undercut/etch front characteristics of Silicon Photonic MEMS compatible and Silicon Photonic MEMS incompatible SOI wafers that have undergone identical processing. Optical microscope images of a (a) single etch front after versus (b) multiple etch fronts can be confirmed in the FIB cuts in (c) and (d).
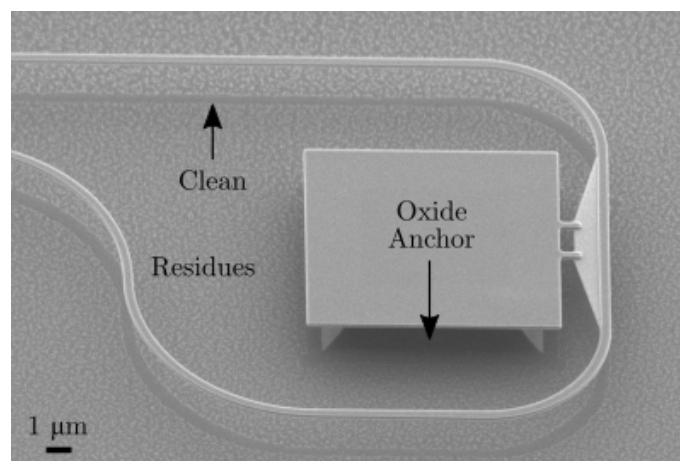

Figure 4.16 – SEM image capturing a clean region on the handle layer silicon below the suspended structure because there was not any planarization/filler oxide present there. These "shadows" contrast with the other regions where CVD oxide remained on top of BOX and any embedded residues redeposited on the substrate during the dry etching
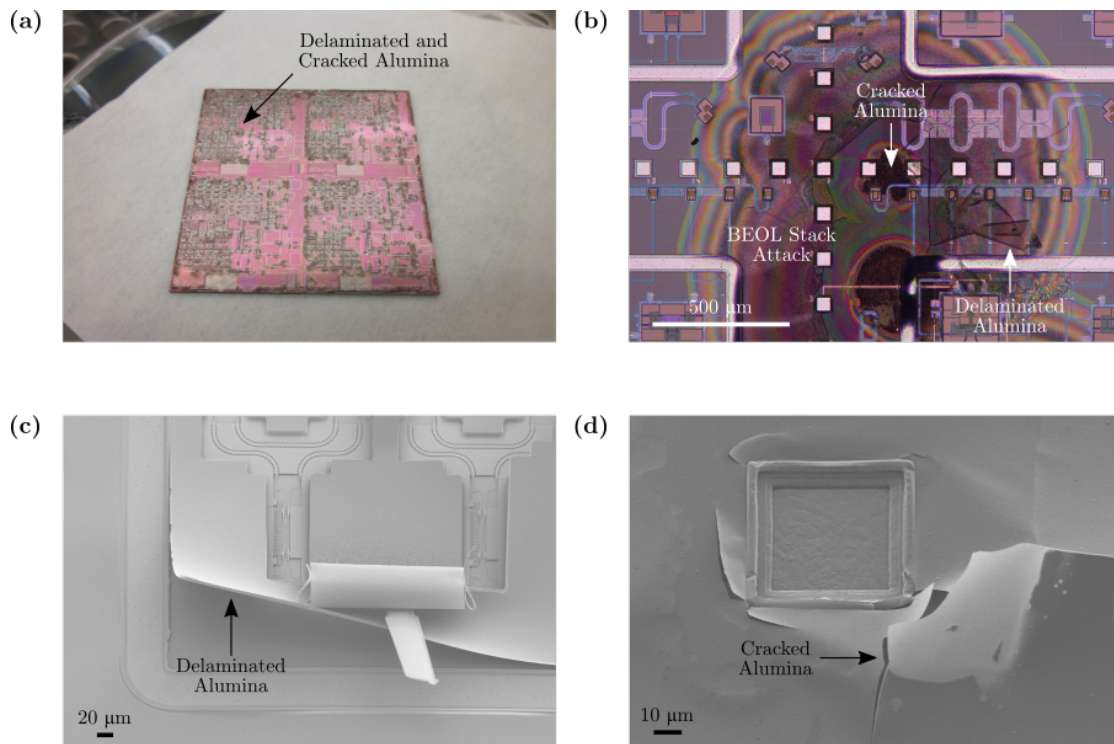
Figure 4.17 – (a) Photo of a post-VHF sample where the cracked and delaminated regions of alumina are visible on the surface (b) Optical microscope image more closely indicating from where the alumina failure points originate and how the BEOL stack looks (c) and (d) SEM images of the delaminated and cracked alumina around the sealing ring and contact pads, respectively

4.17a because the underlying oxide in the BEOL stack is consumed, leading to a rupturing or deformation around the failure epicenter. A closer look under the optical microscope (**Figure 4.17b**) helps to identify the origins of the issue as the corners and edges of sealing rings and contact pads (**Figure 4.17c** and **Figure 4.17d**, respectively) and the corresponding regions in the MEMS cavities, all locations with a high contrast in topography. Thus, in order to preserve integrity of the alumina, priority is placed on having a sufficiently thick layer that is mechanically robust and ensuring complete coverage of topographical steps by photoresist when etching with BHF. With regard to this second point, because BHF is an isotropic liquid etchant, the photoresist at the corners and edges of the MEMS cavities and metallization should not expose any alumina because it will be etched away, leaving behind an access point for VHF to the BEOL stack.

Unfortunately, there are some regions of the sample that will always be exposed to VHF attack using this passivation scheme. In particular, the edges of chips, coupons, and even wafers suffer from an "edge attack" that is characteristic of any region that has come in contact with a dicing blade (**Figure 4.18**). Edge chipping is a documented and well-understood phenomenon originating from the dicing step post-fabrication resulting from brittle cracks and damage to the wafer when using a diamond saw [135, 136]. The end result, particularly for Silicon Photonics SOI wafer with a multi-layer BEOL stack, is an edge that resembles a mille-feuille
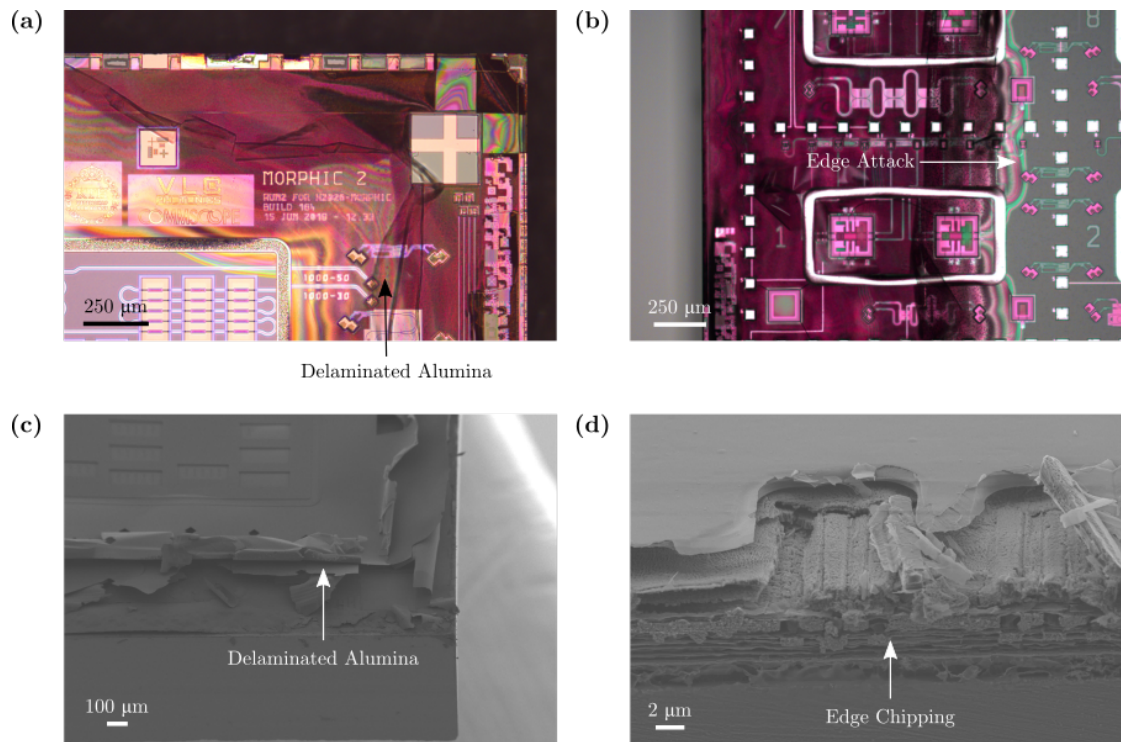
Figure 4.18 – (a) and (b) Optical microscope images of a sample corner and edge, respectively, where VHF propagation in the chipping regions has attacked the BEOL stack and delaminated alumina (c) and (d) SEM images of these same regions providing a perspective view detailing the edge attack.

of cantilever-like structures. These individual, fragile layers exposed by the dicing blade are particularly brittle and even with a thick alumina passivation greater than 60 nm, can break off and expose the BEOL stack, leading to an edge attack.

This edge attack, while inconvenient for samples at the chip- and coupon-level because devices at the edges cannot be characterized, is not considered an impasse. This issue is also present in wafers, but chips along these edge regions are typically discarded and not packaged because they are either incomplete or suffer from the edge non-uniformity inherent to wafer-scale processing. If this process were to be adopted by a foundry, one would simply perform the packaging step and discard the chips at the peripheries where the edge attack exists.

It was alluded to earlier that protection of the edges and corners of cavities and metallization required a sufficiently thick alumina layer (e.g., 60 nm), but what happens when the thickness is increased even further to 70 nm and above? **Figure 4.19a** and **Figure 4.19b** show how designed dimensions for waveguide gap and comb finger separation can be modified by the filling-in of the conformal alumina deposition. The desired dimensions can typically be recovered using the designated BHF etch, but in cases where there is actual bridging or small gaps in alumina hindering access to the etchant, or an insufficient etch time is employed, residues will remain in the gaps and along the sidewalls. The sidewall roughness that these
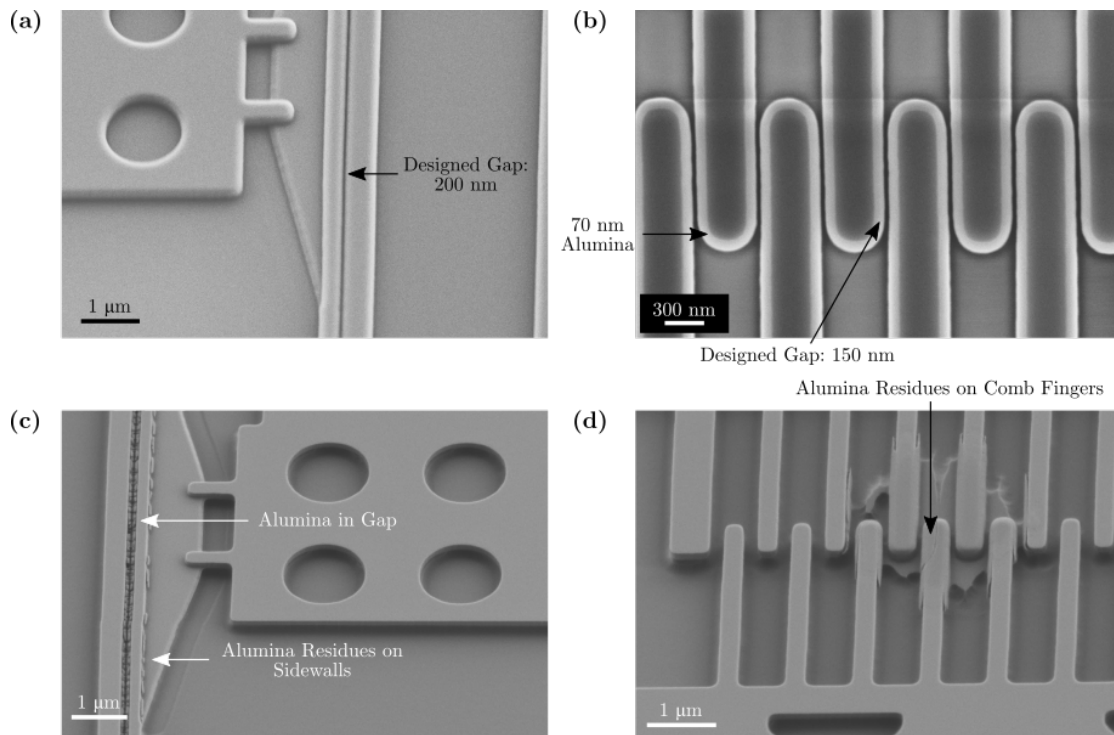
Figure 4.19 – SEM images indicating how an alumina passivation layer > 70 nm in thickness can lead to near complete sealing of (a) waveguide gaps and (b) comb drive finger separation that in the worst case, causes bridging that is difficult to fully remove. SEM imaging after etching reveals that alumina was incompletely removed from (c) the waveguide gap and shows where residues remain on the waveguide sidewalls and (d) on the sidewalls of comb fingers

residues produce introduces additional optical losses and in terms of operation, can prevent the MEMS from being actuated properly. Thus, it is prudent to deposit an alumina layer with thickness less than half the minimum gap separation between structures and to perform a 50% overetch to guarantee its removal in the MEMS cavity.

Some issues do not manifest themselves until characterization. One example is that of the instability of the applied voltage found when actuating devices. As seen in **Figure 4.20a**, when designers do not extend the edge of the electrical isolation trench sufficiently far past the silicon rim, it is possible that a form of bridging occurs in the silicon rim, which implies that regions of different voltage are not entirely isolated from one another. Although the bridging itself may be on the nanometer scale, the fluctuations observed warrant an auxiliary silicon etch just in these regions. Following these "patch-etches" imaged in **Figure 4.20a** and **Figure 4.20b**, the devices could be actuated as designed.

As with any new process development, there are challenges to be addressed and overcome, and at this point, the MEMS post processing is mature enough that it can be reliably repeated with good yield. Devices released according to the outlined process flow can already be individually characterized in the lab, but the pursuit of robust and dense, PICs necessitates additional
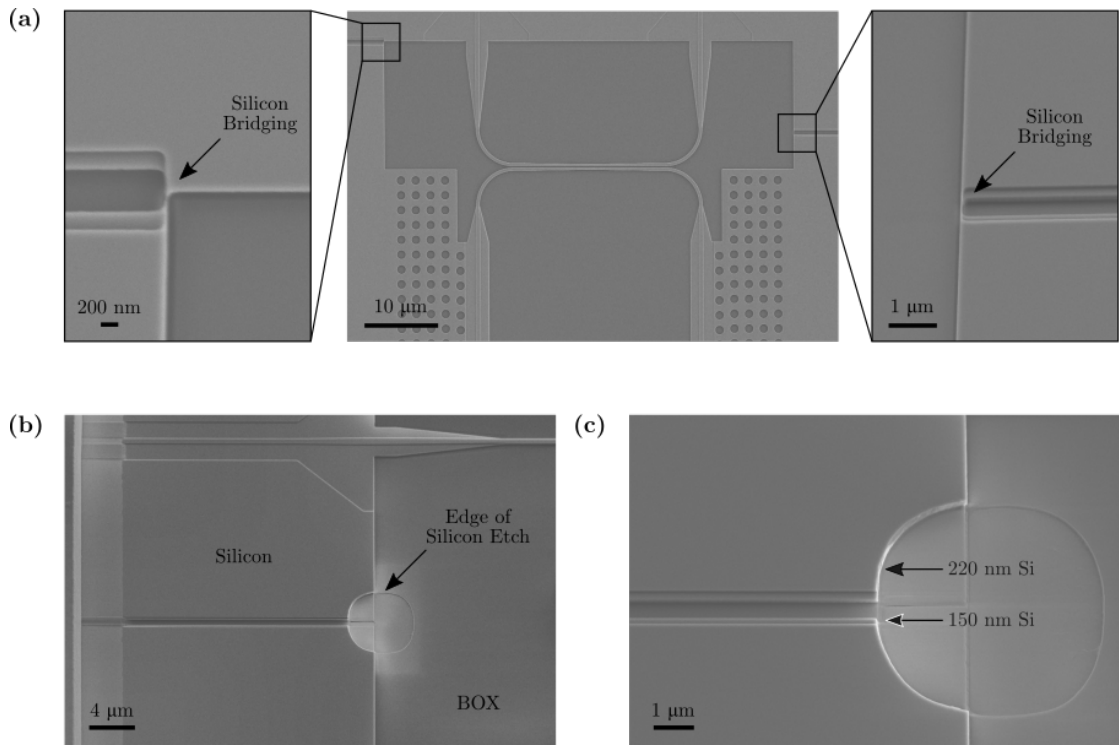
Figure 4.20 – (a) SEM image of an out-of-plane tunable ring resonator where the electrical isolation trenches on the left and right, separating the grounded region from those carrying a voltage exhibit silicon bridging. By using a targeted silicon etch as in (b) and (c), it is possible to locally remove the excess silicon and ensure proper electrical isolation.

steps including a wafer-level sealing process and electrical packaging.

4.4   Sealing and Electrical & Optical I/O

In order to maintain an optimal operating environment, semiconductor devices require packaging. This packaging distributes the electrical and optical connections from chip to circuit board and provides mechanical and chemical protection from the environment, as well as thermal management [137]. As electrostatic MEMS typically do not consume much power and hence generate little heat, the role of thermal management is less important than the first two functions. In the field of photonic MEMS and opto-mechanics, a vacuum environment is crucial for the encapsulation of active, moving devices and wafer-level packaging with thin sealing caps is the most cost-effective approach to accomplish this task.

The MEMS release process performed at wafer-scale is coordinated with project collaborators at the Royal Institute of Technology in Stockholm (KTH), who carry out the wafer-level hermetic sealing, which is described in detail in [138]. We here summarize the main process steps for completeness. Visually described in brief in **Figure 4.21**, the sealing lids are fabricated on a separate SOI wafer whose sealing ring pillars are patterned by a partial etch in the silicon
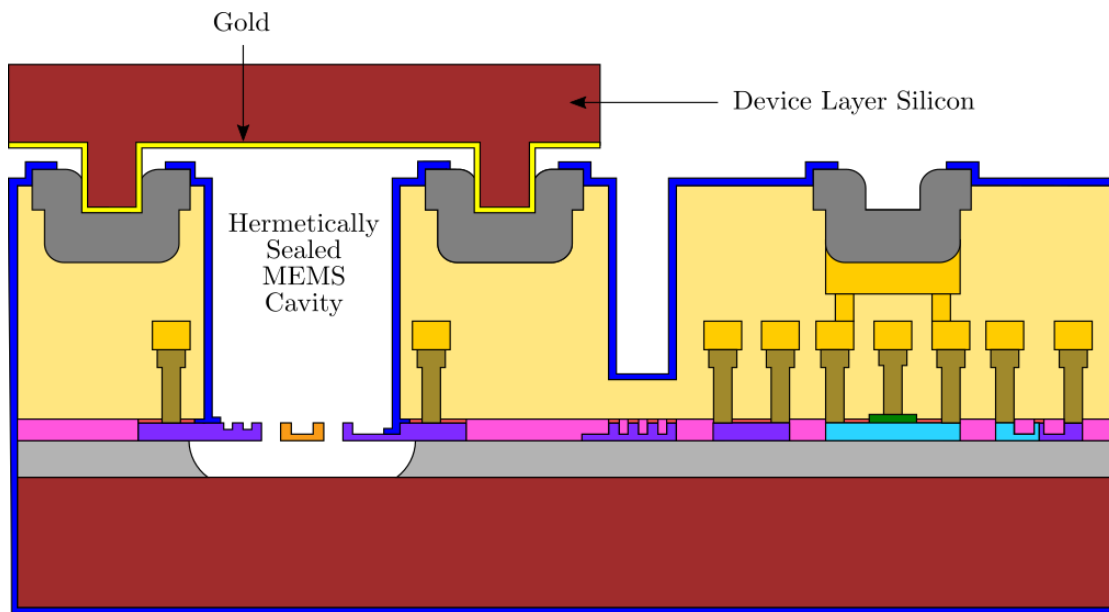
Figure 4.21 – Schematic cross-section of a released Silicon Photonic MEMS sample, complete with hermetic sealing of the MEMS cavity by a sealing lid. Lids consist of a patterned SOI wafer, whose handle layer has been thinned down and whose DL is patterned and covered by a gold contact layer. The patterns on the sealing wafer DL is aligned and then bonded to the aluminum-copper sealing rings already present on the sample by thermocompression. Schematic based on [138]

DL and then covered in gold. Individual lids are separated by a full silicon, full BOX etch to the handle layer silicon and then the sealing wafer is bonded to the released Silicon Photonic MEMS wafer by thermocompression. After successful bonding, the sealing wafer handle layer is thinned down such that the overall sealing cap is only 30 μm in height [138].

The optical microscope images in **Figure 4.22a** and **Figure 4.22b** compare a sample before and after the sealing process. Note that because the metallization and waveguides lie within the BEOL stack, they are able to pass below the sealing lid and are accessible by externally located grating couplers and contact pads for electrical and optical I/O. These sealing lids are firmly secured and robust as confirmed by their ability to stay in place after close-proximity dicing, i.e., within 100 μm.

Figure 4.22b draws attention to the contact pads that have been gold stud-bumped and makes reference to an electrical interposer. While individual device characterization can be performed with a multi-probe setup where the probe tips directly contact the aluminum-copper contact pads, such an approach is neither scalable, nor a permanent option for large-scale circuits with numerous devices and potentially hundreds of connections. A common approach employed in electronic packaging to make these connections is wire bonding to pads on a printed circuit board (PCB). However, when the density of connections becomes too large or a smaller packaged assembly is desired, one turns to flip-chip bonding. In this process, solder bumps are deposited on the contact pads (sample top surface) and then the entire sample is flipped over onto an external circuit with matching pad configuration so that
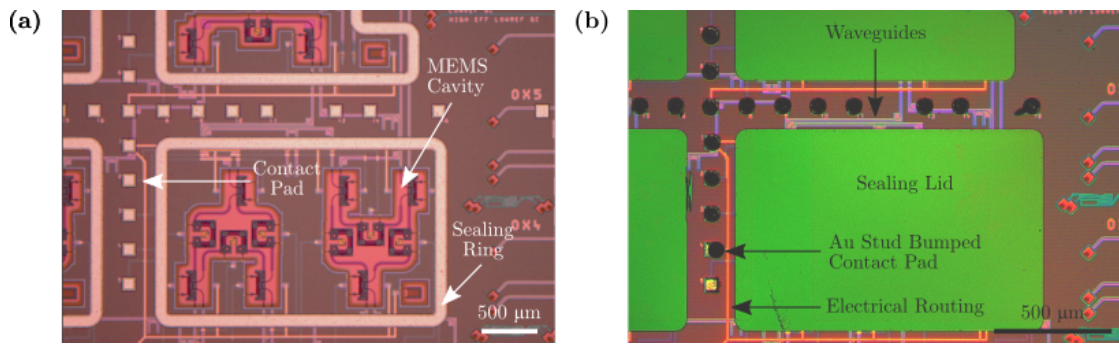
Figure 4.22 – Optical microscope images comparing the same region on a sample (a) without the sealing lids where the MEMS cavity and encompassing sealing ring are indicated (b) Optical microscope image of a sample with the sealing lids. Note that in (b), several contact pads have also been gold stud-bumped in preparation for the flip-chip bonding process to the electrical interposer needed for dense electrical connectivity. Waveguides and electrical routing running through the BEOL stack pass below the sealing lid.

it is face down. The solder is then reflowed to ensure a proper electrical connection.

It should be noted that this first step of solder bumping takes place at wafer-scale and is consequently unsuitable for chip-scale process development of the electronic packaging [139]. An attractive alternative is gold stud-bumping, which utilizes the same equipment used for wire bonding and is therefore compatible with chip-scale development, but where the wire is snapped off after the ball is deposited on the contact pad. What is left behind is a gold stud bump with a sharp peak where the wire is broken off, and this peak is flattened during a process known as "coining" to define a planar surface with good conductivity to the second surface (e.g., interposer or PCB) [139]. In this work, the second surface is an electrical interposer, whose role it is to spread the electrical connections to a wider pitch and/or provide additional routing from the small, densely packed flip-chip bond pads to the larger, more evenly spaced wirebond pads.

The effort involved in gold-stud bumping and performing the electrical and optical packaging has been performed by project collaborators at Tyndall National Institute. The new challenge is the sheer number of electrical contacts and the presence of sealed MEMS cavities that reduce vertical clearance between the stud-bumped sample and the interposer. Design and fabrication of several interposers for a selection of mini-demonstrators, smaller photonic MEMS sub-circuits, has been carried out as part of this work. A simplified process flow for the interposer fabrication is detailed in **Figure 4.23**. Here, a glass starting substrate undergoes a chrome (15 nm) - gold (150 nm) - titanium (10 nm) deposition and is later patterned to form the flip-chip contact pads, wire bond pads, and electrical traces between the two. The use of chrome improves adhesion between the gold and the substrate and the titanium promotes adhesion between the patterned gold and a subsequent oxide layer that is deposited to provide electrical isolation preventing any shorts between traces. Once openings in this overlying oxide layer are created, the underlying titanium can be removed so that the gold is once again exposed and the sample is ready for gold or solder stud-bumping.
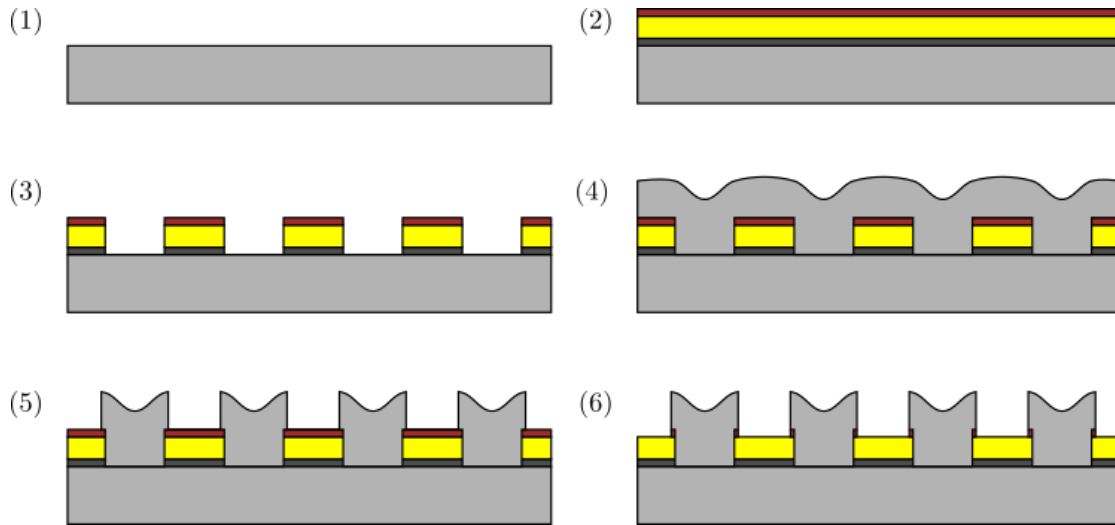
Figure 4.23 – Cross-sectional images of the interposer fabrication process flow. (1) A starting glass substrate is first cleaned in a piranha solution and then (2) sputtered with a Cr-Au-Ti metal stack 15 nm - 150 nm - 10 nm in thickness. Next, the samples are (3) patterned with maskless lithography and etched with ion beam etching (IBE). In (4), a 300 nm passivation oxide is sputtered over the sample and subsequently (5) etched to expose metal. A final (6) titanium etch exposes the gold.

Figure 4.24 provides several visualizations photo of a finished interposer with the photo in **Figure 4.24a** providing a generalized overview of the various regions (e.g., flip chip bond pads, dense traces, and regularly spaced wirebond pads). **Figure 4.24b** shows an optical microscope image focusing on the connectivity between pads and traces, while **Figures 4.24c - d** look closely at the structure of the exposed gold pads and oxide-covered traces.

The approaches outlined thus far describe the packaging techniques use for wafer-level processes and large scale connectivity. For individual photonic MEMS devices, whose characterization will be discussed in the following two chapters, a slightly different approach is employed. Samples are taken directly from the cleanroom to the lab after the VHF release etch and are characterized in the setup schematically described in **Figure 4.25**.

Light within the infrared optical communication range of wavelengths (C-band) from 1530 to 1565 nm is injected into a fiber array from an Agilent 81682A tunable laser (1460 to 1580 nm) after passing through a fiber polarization controller. A six degrees of freedom alignment procedure is then performed to position the fiber array above a 1 x 10 array of on-chip grating couplers. The x-, y-position are adjusted with the 2-axis, long-travel stage and the fiber-array holder mounted on a stage is capable of adjusting the z-position, as well as roll, pitch, and yaw. Proper alignment is verified by optimizing the power transmission through a shunt connection. The procedure is as follows: light is coupled from one fiber into a grating coupler at one end of the array; it then follows a waveguide connected to a grating coupler at the opposite end, where it is coupled out of the chip into a separate fiber connected to a photodetector. If the alignment is poor, the measured power at the photodetector will be low, and the chip must be repositioned, or the fiber array raised/lowered.
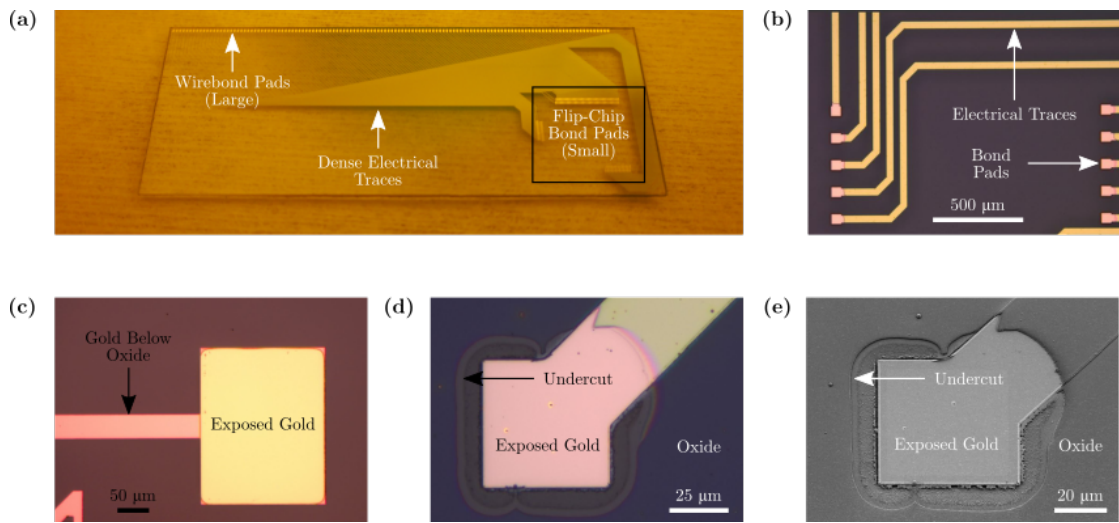
Figure 4.24 – (a) Photo of a sample interposer with exposed gold flip-chip bond pads, traces, and wirebond pads (b) Optical microscope image focusing on the bond pads and the electrical traces (c) Optical microscope image of a wirebond pad exhibiting a color difference between exposed gold and gold below oxide (d) Optical microscope image of a bond pad indicating the various materials and the undercut resulting from the use of BHF to remove the oxide (e) The corresponding SEM image to (d) showing topographical features that mirror the color differences of various materials and features in the optical microscope image

This approach takes into account the fiber-to-grating coupler alignment; however, there is another aspect to be considered. The manufacturer of the fiber array specifies a $\pm 5\mu$m absolute spacing accuracy between adjacent fibers, which can be interpreted as a fiber-to-fiber alignment. Ideally, there would be no offset between fibers, so maximum power transmission in the shunt configuration would ensure that the other eight grating couplers in between are also perfectly aligned to the fiber array. This, is not the case, and according to Taillaert et al., who examined lateral fiber-to-grating alignment tolerances, for $\pm 5\mu$m offsets, one can expect an additional 0.5 dB of coupling loss [140].

Following the optical alignment procedure, the electronic probe tips are carefully positioned over the aluminum-copper contact pads that are arranged in a grid pattern across the chip and brought into contact. The applied voltage at each tip can be tuned and activated using a custom-designed voltage control board that can be either connected to a DC power supply or a waveform generator. Actuation of the photonic MEMS devices and the effect it has on the optical output is then monitored by the photodetectors, which have been connected to the corresponding fibers and grating couplers. For AC measurements, an oscilloscope can be connected to the output of a high-speed photodetector to provide the opto-electronic transduction needed to observe switching times. A direct visualization of the setup, mapping functional blocks in the schematic to physical components is provided in **Figure 4.26**.

The methods and results presented in this chapter give insight into the various steps and challenges associated with bringing MEMS to an established integrated photonics platform.
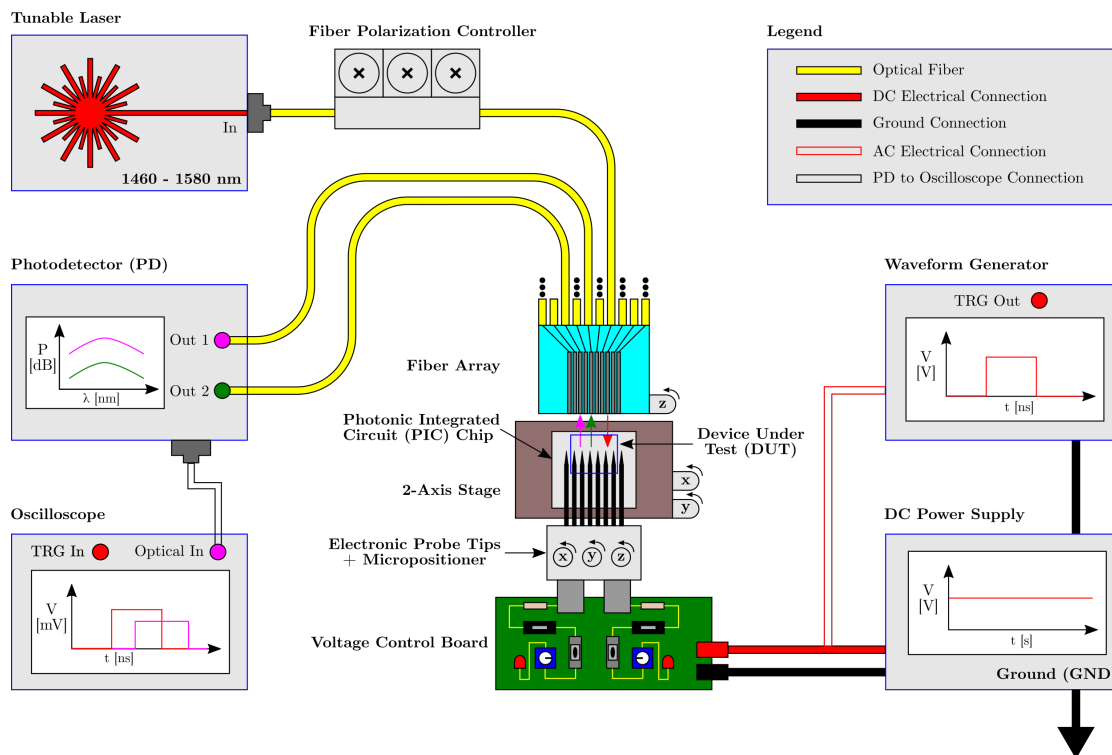
Figure 4.25 – Schematic diagram indicating the primary components of the characterization setup. Light from a tunable laser passes through a fiber polarization controller and into a fiber array, where it is coupled into the PIC. The PIC itself is mounted on a 2-axis stage that can move in the x- and y-directions, while the fiber array provides tuning in the z-direction. Electrical connectivity is provided by probe tips mounted on micropositioners with three degrees of freedom. The probe tips are in turn connected to a voltage control board that controls and distributes voltage from a DC power supply or a waveform generator for steady-state and AC measurements, respectively. With the MEMS actuated, light passing through the output ports of the device is monitored through a separate set of fibers in the fiber array, connected to the photodetectors. In the case of transient (e.g., switching time measurements), the output can be fed into an oscilloscope that is triggered by the output of the waveform generator.
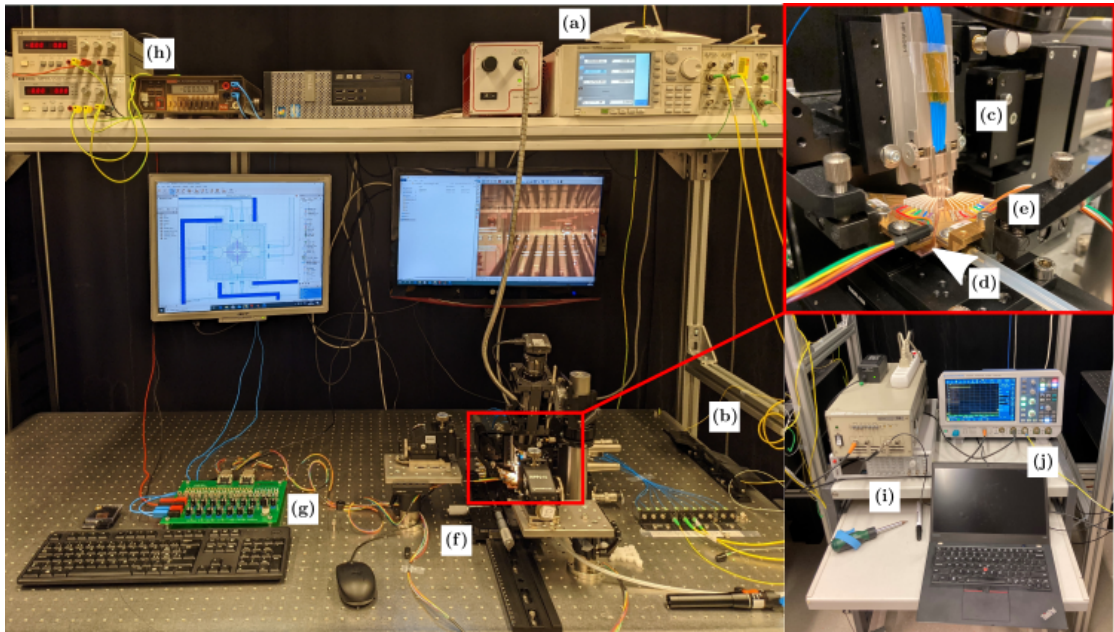
Figure 4.26 – Photographs of the characterization setup with elements in the schematic of Figure 4.25 labeled: (a) tunable laser (b) fiber polarization controller (c) fiber array and holder (d) PIC (e) electronic probes and micropositioner (f) 2-axis stage (g) voltage control board (h) DC power supply (i) waveform generator (j) photodetectors (k) oscilloscope

One cannot simply toss the samples into a VHF chamber with the hopes that the result are residue-free, suspended structures, capable of reliable actuation. Planning for success begins with the selection of the proper SOI wafers and a shrewd strategy for passivating regions of the chip, especially the particularly vulnerable BEOL stack. Within the fabrication itself, one must monitor the effects of various etchants in patterning steps and find solutions to non-idealities and unexpected behavior, like cracking of alumina and edge attacks.

Released devices are either sealed at wafer-level and then packaged or proceed directly to the lab where they undergo electro-optic characterization. It is this last step, the measurement of photonic MEMS devices that completes the picture and shows how well they work.

5 MEMS-Enabled Tunable Couplers

The directional coupler, as discussed in Chapter 2 on integrated photonics, is one of the most widely used devices in PICs. This versatile building block finds extensive use in passive wavelength-selective power dividers and in active light switches and modulators [141][142]. Furthermore, being that they are the prevalent constituent photonic component in the devices presented in this chapter, it is instructive to elaborate on their behavior and design. Since any directional couplers integrated with a MEMS actuator must be made free-standing, the discussion begins with the suspended directional coupler designed as part of this work.

5.1   Suspended Directional Coupler

The directional coupler is a two input, two output device consisting of two well-separated waveguides commonly used to divide power in arbitrary proportions. Specifically, light injected at one of the input ports can either continue along the same input waveguide to one output, or it can partially/fully couple over to the other output (**Figure 5.1**). In the configuration where light is injected at input 1, light can continue to output 1 without coupling over; thus, this port is commonly referred to as the "Through" port. Output 2 receives light that couples to the second waveguide and is referred to as the "Drop" port.
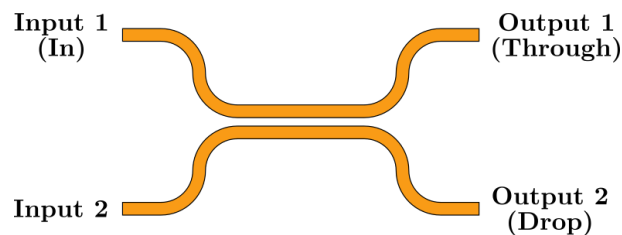

Figure 5.1 – Schematic diagram indicating the input-output relationship of a directional coupler. In the presented configuration, light injected at the input 1 port passes to either the output 1 ("Through") or output 2 ("Drop") port in varying proportions depending on the geometrical design of the device.

In PICs, directional couplers are implemented by 2 photonic waveguide sections brought together in close vicinity, leading to a field coupling between the waveguides. Coupled mode

theory describes the total effective mode propagating in a directional coupler and when the waveguide branches are identical, this effective mode can be decomposed into an even and odd supermode (**Figure 5.2**). It is the coupling between their evanescent fields that leads to power transfer between the waveguides [143]. Because these supermodes have different propagation constants, they accumulate a phase difference whilst propagating, and it is their constructive/destructive interference that determines in which waveguide the effective mode is localized, i.e., where the optical power is concentrated. In this manner, light introduced in one waveguide, e.g., the top waveguide in **Figure 5.2b**, gradually becomes transferred to the bottom waveguide.

Optical power is fully transferred to the second waveguide once a phase difference of π has accumulated. This condition of power exchange to another waveguide (i.e., switching) is often used in directional coupler design, and the distance over which this phase difference accumulates is referred to as the beat-length, L_{beat}. The exchange of power is periodic in that if the supermodes are allowed to propagate further, their phase difference continues to increase until it reaches 2π. Here, the optical power distribution has returned to its initial state and is focused in the input waveguide.

Consequently, the length of the directional coupler can then be designed for 0% or 100% power transfer, or also any fractional amount, e.g., $L_{beat}/2$ for a 50% (3-dB) coupling, to obtain a coupling ratio in between.
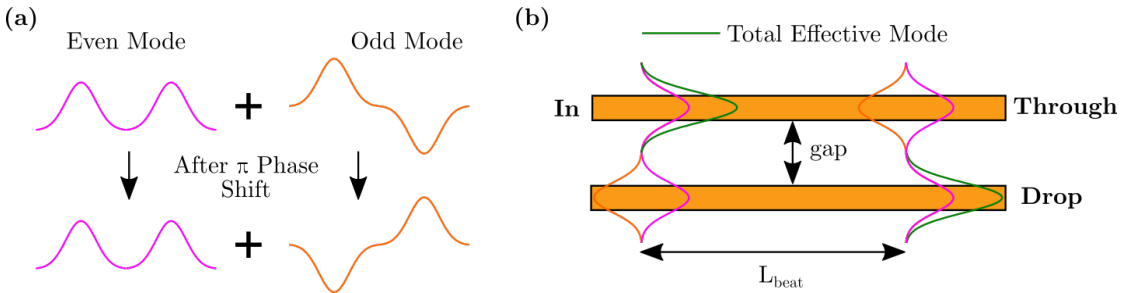

Figure 5.2 – (a) Visualization of the even and odd supermodes with zero phase difference and after travelling a distance equal to the beat-length, L_{beat}, at which point they have accumulated a phase difference of π (b) Depiction of a directional coupler where the total effective mode is initially localized in the top input waveguide and after travelling an integer multiple of the beat-length, is transferred in the lower waveguide

The quantitative relation describing the coupling behavior in a directional coupler as a ratio of power coupled to the second waveguide ($P_{coupled}$), to power injected into the input waveguide (P_0), is repeated here as:

$$\kappa^2 = \frac{P_{coupled}}{P_0} = sin^2(C \cdot L) \tag{5.1}$$

Where C represents a coupling coefficient and L is the length of the coupler.

C in turn is given by:

$$C = \frac{\pi \Delta n}{\lambda} \tag{5.2}$$

Where Δn is the difference in effective indices of the even and odd supermodes.

The beat-length can be determined by evaluating for what distance, L_{beat}, the phase difference between the two modes equals π:

$$L_{beat} = \frac{\lambda}{2\left(n_{eff} - n_0\right)} = \frac{\lambda}{2\Delta n} \tag{5.3}$$

As illustrated in Equation 5.1 and Equation 5.3, both the coupling coefficient C and the beat-length L_{beat} exhibit a dependence on the effective refractive index difference between supermodes. With a higher refractive index contrast, the coupling between waveguides can be made strong and correspondingly, the beat-length, small.

The coupling behavior can also be influenced by geometric parameters such as the gap separation between waveguides and their shape. Qualitatively, if the gap is reduced, the evanescent field interaction between the modes increases, which leads to stronger coupling and subsequently, a decrease in beat-length [144]. Conversely, longer geometry-induced beat-lengths (e.g., larger gaps) indicate, by proxy, that the waveguide coupling is weaker. This gap-dependence can be corroborated using waveguide mode solvers to show that the beat-length exponentially increases with larger gaps [145].

This observation that coupling strength is gap-dependent motivates the operation of the directional coupler employed in this work. Relevant details and results are summarized below, and a complete discussion of the design, simulation, and characterization, has been published in [146]. The designed directional coupler is schematically depicted in **Figure 5.3a**. Also included are a pair of cross-sectional electric field profiles and a plot of the normalized optical power distribution in the coupler obtained from a waveguide mode solver (**Figure 5.3b**). The corresponding values for all parameters in **Figure 5.3a** are provided in **Table 5.1**.

Parameter	L	W	L_c	L_s	w_1	w_2	$g_{lat,0}$	$g_{ver,0}$
Value	30 μm	20 μm	21 μm	1 μm	450 nm	300 nm	150 nm	0 nm

Table 5.1 – Parameters for Suspended Directional Coupler

The design methodology can be outlined as follows:

1. Almost all PICs need directional couplers to distribute and divide light amongst the various other photonic components, and scaling considerations dictate they must be
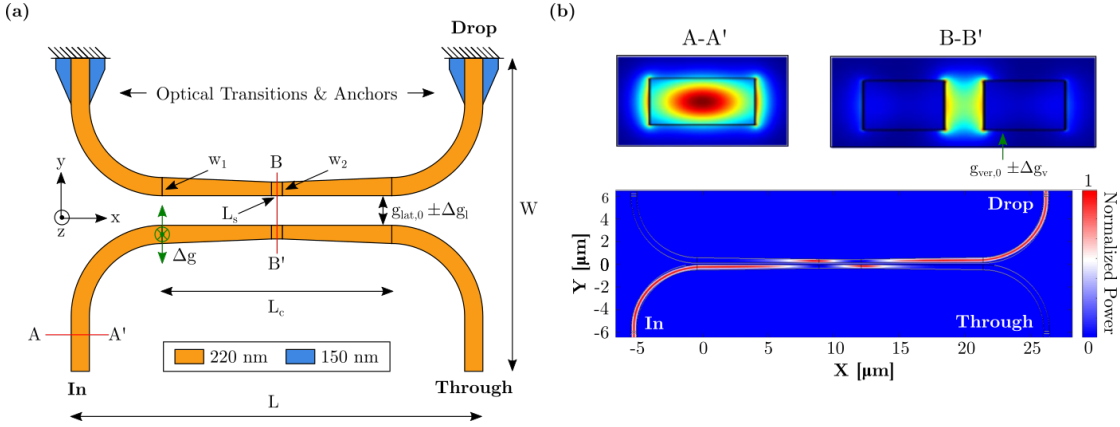
Figure 5.3 – (a) Schematic of the designed directional coupler indicating the key geometric parameters listed in **Table 5.1**. The top waveguide is anchored while the bottom one is free to move both in-plane in the y-direction, as well as out-of-plane in the z-direction. These degrees of freedom are indicated by the green arrow and serve to modify the initial gap configurations by an amount Δg. (b) Cross-sectional electric field profiles indicating that the mode is initially well confined and that in the coupling region, the evanescent fields of the supermodes extend beyond the core to enhance coupling. The full normalized power distribution for the directional coupler is shown in the bottom plot wherein light is completely coupled from the "In" port to the "Drop" port.

made **compact** and **low-loss**.

- For a fixed waveguide gap, directional couplers can be made compact by using **narrow waveguides** that allow for enhanced evanescent field interaction and consequently stronger coupling and **shorter beat-lengths**.

2. Narrow waveguides enhance coupling, but guided light also becomes prone to **sidewall scattering losses**, as a larger fraction of the mode extends beyond the waveguide core.

- The lossy, narrow waveguide region can be limited by using wider waveguides at the beginning of the coupling region and **tapering** them to a short narrow region in the center. Doing so provides a smooth mode transition with minimal loss.

3. If the initial waveguide gap, as well as the core and cladding material are fixed, tuning of the coupling ratio is implemented through modification of the coupler length.

- A coupling length exactly matching a single beat-length, $L = L_{beat}$, ensures **full power transfer** to the second waveguide branch of the directional coupler.

- A coupling length such that $L = n \cdot L_{beat}$, where n is an integer, means the **full optical power alternates** between the first and second waveguides with even and odd n, respectively.

- A coupling length of $L \neq L_{beat}$ leads to **fractional power transfer**.

Conventional directional coupler design ends at Step 3 because once a physical coupler length has been selected, it cannot be modified post-fabrication. Although this also holds true for

the couplers designed in this work, the MEMS post-fabrication steps re-introduce a degree of freedom post-release. With the BOX etched away, the directional couplers are suspended in air. Fixing one waveguide while allowing the second to move enables gap tuning and thus, the beat-length can be adjusted with respect to the coupling length post-fabrication.

The combination of a 150 nm lateral gap and the tapering of the initial waveguide width from 450 nm to 300 nm yields a beat-length of approximately 7 μm. This value is roughly a third of the value required by a comparable, straight, suspended directional coupler simulated with a 150 nm air gap [146]. Note, however, that the length of the coupling region L_c is roughly three times the beat-length (see the characteristic beating pattern in the bottom plot of **Figure 5.3b**), which means the waveguides are in a sense overcoupled. The device can be made more compact by matching the coupler length with a single beat-length, but this overcoupled condition is an intentional design choice as it enables the bi-directional physical tuning that is desired.

In particular, by adjusting the gap between waveguides, one controls the ratio of power transfer through modification of the beat-length. For example, the initial gap conditions enable a full transfer of power from the "In" port to the second waveguide in a single beat-length of 7 μm. After two beat-lengths (14 μm), power has returned to the input waveguide, and finally after one more beat-length (21 μm, which is the length of the coupling region), power is completely transferred to the "Drop" port.

The interesting behavior develops when increasing or decreasing the gap alters the beat-length. With the physical length of the coupling region fixed at 21 μm, if the gap is reduced/increased so that the beat-length correspondingly decreases/increases, one observes the behavior seen in **Table 5.2**.

n	$n \cdot L_{beat}$				Waveguide with Full Optical Power
	$L_{beat} = 3.5\,\mu m$	$L_{beat} = 7.0\,\mu m$	$L_{beat} = 10.5\,\mu m$	$L_{beat} = 21.0\,\mu m$	
0	0	0	0	0	**1**
1	3.5	7.0	10.5	21.0	**2**
2	7.0	14.0	21.0	-	**1**
3	10.5	21.0	-	-	**2**
4	14.0	-	-	-	-
5	17.5	-	-	-	-
6	21.0	-	-	-	**1**

Table 5.2 – Alternating power transfer between waveguide branches due to gap-induced variation in beat-length in a 21 μm long coupler. Waveguide 1 indicates the input waveguide with the "Through" port and waveguide 2 indicates the waveguide with the "Drop" port. Note: Highlighted cells indicate the physical extent of the coupling length: beat-lengths whose multiples do not match this length lead to fractional power transfer.

Each time the physical coupling length is an integer multiple of the beat-length, the full optical power is transferred between waveguides. This switching behavior is demarcated by the color-coded values in the last column, where a red "1" indicates power staying in the input waveguide and continuing to the "Through" port, and a blue "2" indicates power transfer to the "Drop" port. Intermediary lengths, e.g., for $n = 4, 5$ correspond to incomplete coupling.

The proposed coupler employs an initial gap of $g = 150$ nm, which corresponds to a beat-length of 7 μm. As seen in **Table 5.2**, this situation means that after three beating cycles, power exits the "Drop" port. By increasing/decreasing this gap, one can obtain beat-lengths of 3.5 μm or 10.5 μm, both of which correspond to a complete switch in output power to the "Through" port. This is the desirable bi-directional tuning motivating the selection of the initial gap spacing. A configuration with larger initial gap corresponding to a beat-length of 21 μm, for example, can only provide efficient switching in one direction, i.e., by decreasing the gap to obtain a beat-length of 10.5 μm.

A complete picture of the coupling sensitivity to in-plane and out-of-plane gap variation can be extracted from three-dimensional finite difference time domain (FDTD) simulations, the results of which are provided in **Figure 5.4**. In these simulations the initial lateral gap is set to 150 nm, the initial vertical gap to 0 nm, and the wavelength to 1550 nm.
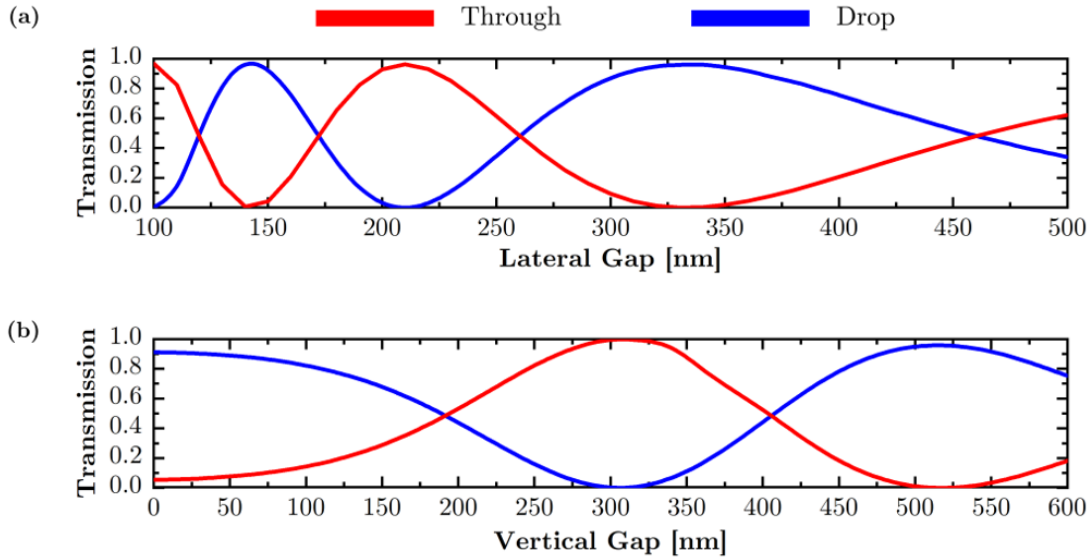

Figure 5.4 – FDTD simulations of the (a) lateral and (b) vertical gap-dependence on power transmission between waveguides in a tunable directional coupler. The "Drop" port curve in (a) indicates that for an initial gap of 150 nm, the full power can be transmitted back to the "Through" port by decreasing the lateral gap towards 0 nm or increasing it towards 215 nm. Power can be returned to the "Drop" port by further increasing the gap from 215 nm to 330 nm.

Figure 5.4a illustrates 100% to 0% tuning capability when the initial lateral gap decreases from 150 nm towards 100 nm or increases towards 215 nm. The beat-length associated with larger gaps continues to increase until it eventually matches the full length of the coupler, which

explains the second power swap to the "Drop" port at 330 nm. After this point, the coupling efficiency gradually decreases until it becomes negligible. In general, the small displacements between 50 and 100 nm required to implement this switching behavior are easily obtained by compact electrostatic MEMS devices, such as comb drive actuators.

A similar behavior can be observed when the movable waveguide is displaced out-of-plane to increase the vertical gap. The sensitivity to vertical gap variation is noticeably less than in the case of lateral gap variation, but **Figure 5.4b** shows that the full exchange of power can be accomplished within 300 nm of displacement. This amount is safely within the stable operating range of out-of-plane electrostatic MEMS actuators.

Given this behavior, when determining the quiescent point of the design, the following considerations had to be taken to account:

- The minimum feature size allowed by the PDK is 150 nm

- The transmission v. lateral gap spacing curve exhibits a steeper slope in the regions between 100 nm < g_{lat} < 210 nm than for 210 nm < g_{lat} < 320 nm, which translates to improved tuning sensitivity

- Relying on a minimum feature size gap can lead to silicon bridging as seen in Chapter 5, which would render the device non-operational even after release

- A 200 nm to 210 nm initial gap starts with the full optical power being completely transferred to the "Drop" port and requires more displacement to switch, which may necessitate the use of a stronger and perhaps larger MEMS actuator

- The coupling behavior is less sensitive to variation in the vertical-gap, but out-of-plane MEMS actuators tend to be more compact than their in-plane counterparts, making them capable of faster switching speeds

An additional design consideration is the bandwidth of the coupler because in order to function properly over a wide range of wavelengths, the device must be broadband. This low sensitivity to the operating wavelength is implemented in this design by the waveguide tapering sections, which not only help reduce insertion loss, but also simulate an adiabatic transition. In an adiabatic transition, the waveguide sidewalls (i.e., width) spread slower than the diffraction of the single, guided first-order mode, which means there is no conversion to higher-order modes or radiation modes, and couplers using such geometries can be remarkably broadband [147, 148].

Before delving into the full tunable photonic MEMS devices employing this suspended coupler, the results from the static, proof-of-concept device in the first fabrication run are presented. The structure is drawn with the geometry and dimensions provided in **Figure 5.3** and **Table 5.1** and undergoes the MEMS release post-processing detailed in Chapter 5. Optical microscope and SEM images depicting the suspended directional coupler are provided in **Figure 5.5**.
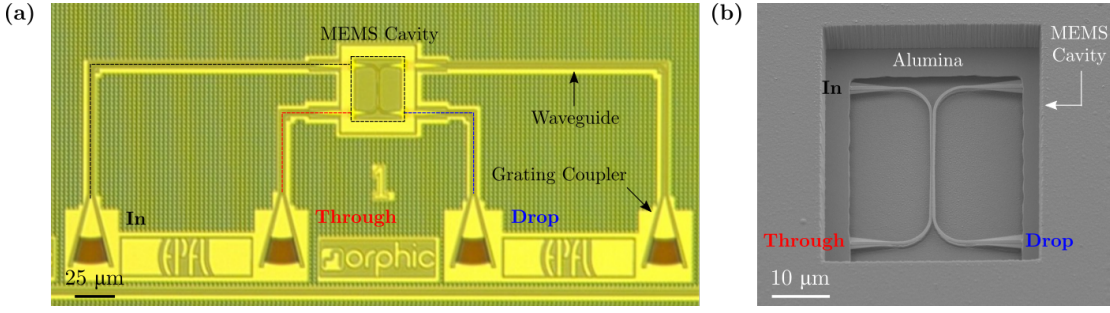
Figure 5.5 – (a) Optical microscope image of the suspended directional coupler within the MEMS cavity alongside the waveguides and grating couplers for the input/output ports (b) Corresponding SEM image of the device showing the two suspended waveguides and the alumina passivation within the MEMS cavity

The characterization results of the coupler are provided in **Figure 5.6** and they exhibit a strong correspondence with the 3D FDTD simulated power spectrum that has been superimposed upon the measurement curves. The measured extinction ratio (ER) of 25 dB at λ= 1550 nm is less than simulated and this is attributed to sidewall roughness that modulates the supermode indices and coupling length at the central designed wavelength [146]. Consequently, a residual amount of light leaks to the "Through" port thereby decreasing the ER at this wavelength. This same sidewall roughness, whose effect is typically masked by an oxide cladding but is now exposed through the enhanced refractive index contrast of an air cladding, is responsible for the insertion loss (IL) of 0.5 dB at λ= 1560 nm. However, by limiting the length of the narrow waveguide region where this phenomena is exacerbated, this excess loss is minimized. The device is relatively broadband with a 1-dB spectral bandwidth of 35 nm at λ= 1550 nm.

With an overall footprint of 20 µm x 30 µm, this suspended directional coupler is quite compact. Combined with its high ER, low IL, and broadband behavior, it is an attractive candidate for integration with MEMS to make its optical characteristics mechanically tunable.

5.2 Continuously Tunable Silicon Photonic MEMS 2 x 2 Directional Coupler

Having introduced the standalone structure serving as the basis photonic component in this work, it is now possible to discuss the full photonic MEMS devices. The first device is a continuously tunable 2 x 2 directional coupler. The results presented in this section are partially published in [91].

This device consists of three parts, one suspended and fixed arm of a directional coupler, a second directional coupler arm that is suspended and attached to the movable portion of a comb-drive, and a fixed comb-drive aligned to its movable counterpart. All optical ports are anchored to the silicon rim through an optical transition, consisting of a shallow-etched rib waveguide. By using such a structure, one can minimize transition losses associated with light
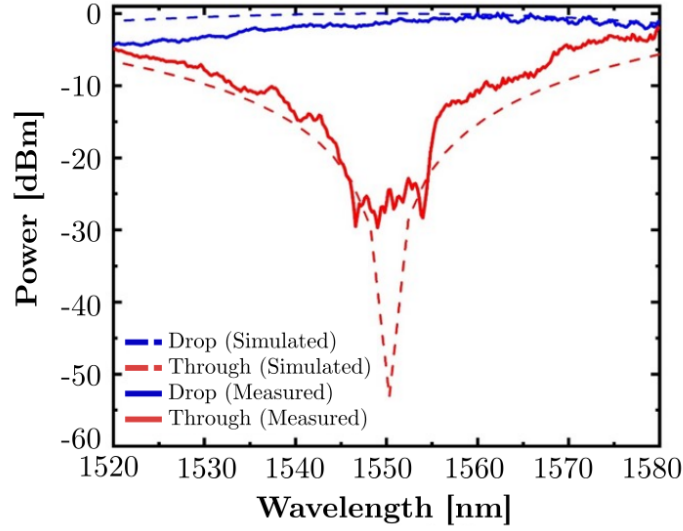
Figure 5.6 – Characterization results comparing the simulated and measured spectral behavior for the "Drop" and "Through" ports of the suspended directional coupler. The insertion loss (IL) of this device is 0.5 dB at λ= 1560 nm and the extinction ratio (ER) is roughly 25 dB at λ= 1550 nm. The broadband characteristics of the device can be seen in the 1-dB bandwidth of 35 nm at λ= 1550 nm

moving from an oxide clad region in the BEOL stack to the air-cladded region of the MEMS cavity. Anchor points for the mechanical suspension and the fixed part of the comb-drive come from pillars in the BOX that remain after the timed VHF release etch.

A top-down schematic view of the device indicating the waveguide and comb-drive suspensions, the direction of displacement, and the various optical I/O ports is presented in **Figure 5.7a**. A corresponding 3D perspective view is provided in **Figure 5.7b** and shows how the actuation voltage is applied between the fixed and movable portions of the comb-drive. The device footprint is 60 μm x 130 μm.
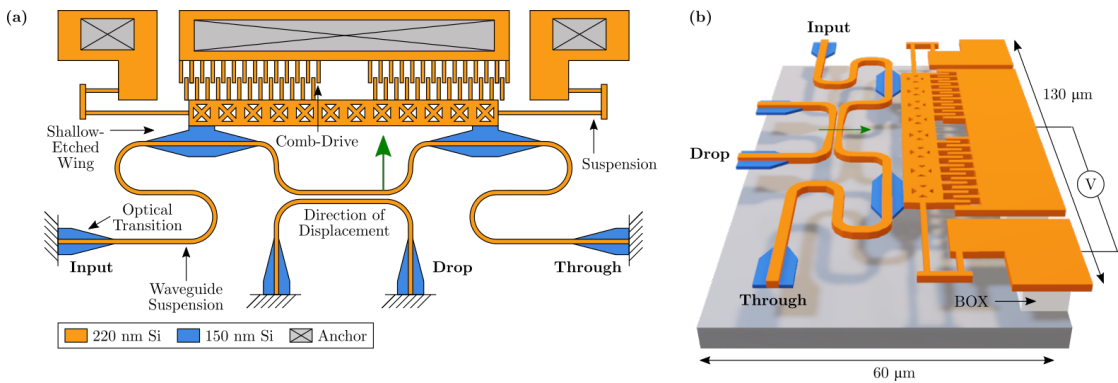

Figure 5.7 – (a) Top-down schematic view of the continuously tunable 2 x 2 directional coupler indicating the fixed arm and the movable arm, which is attached to the electrostatic comb-drive (b) 3D perspective view of the device showing dimensions, the BOX anchors, and how the voltage is applied between the fixed and movable portions of the comb-drive.

The connection between the movable waveguide and movable portion of the comb-drive is through wide regions of shallow-etched silicon (blue region in **Figure 5.7**) so as to prevent coupling losses to the mechanical structure.

In its initial, unactuated state, the gap spacing between waveguides is, as before, 150 nm. By applying a voltage between the fixed and movable portion of the comb-drive, an electrostatic force is generated that pulls the former towards the latter, thereby increasing the gap spacing. Note that both the substrate and movable portion of the waveguide are grounded so as to prevent a downward attractive electrostatic force from being generated that would lead to unwanted out-of-plane displacement.

The amount by which the movable waveguide is displaced is determined by the balance between this attractive electrostatic force and the restoring spring force from the combined waveguide and comb-drive suspensions. Schematic diagrams indicating the various states in which power is initially coupled entirely to the "Drop" port (gap: 150 nm), split evenly between the "Drop" and "Through" ports (gap: ≈ 175 nm), and eventually transferred completely to the "Through" port (gap ≈ 210 nm) are provided in **Figure 5.8** alongside correspondingly labeled regions of the optical simulation. Further increases in the gap beyond 210 nm lead to longer beat-lengths and a subsequent increase in power back to the "Drop" port.
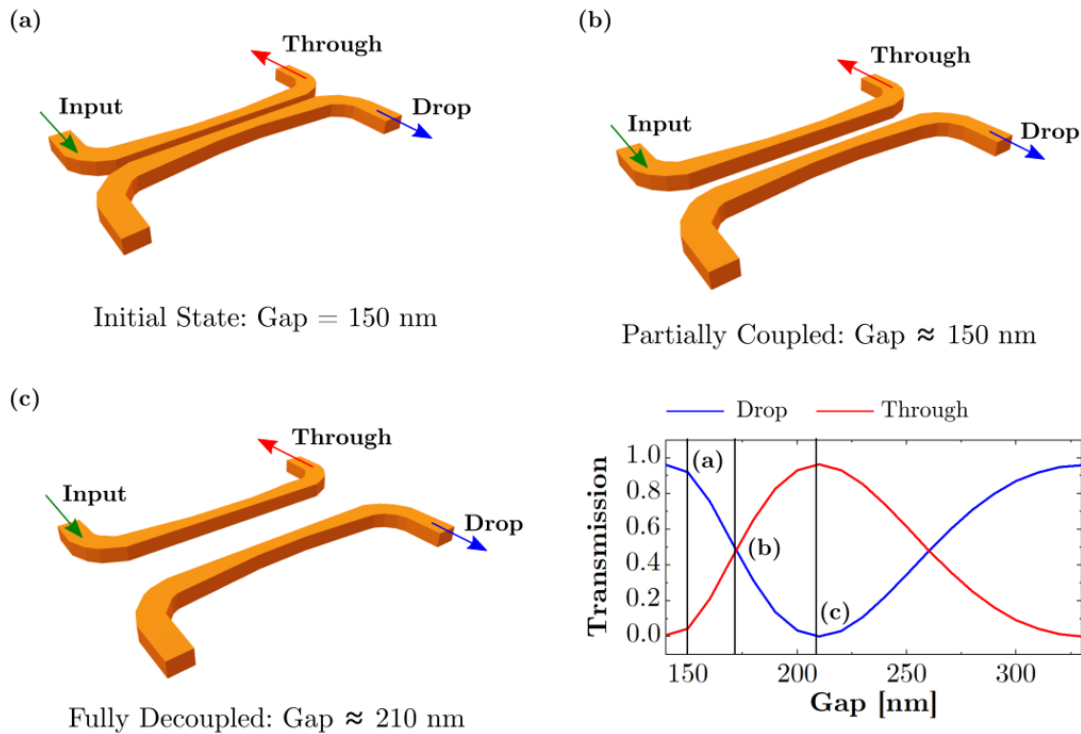

Figure 5.8 – (a) Initial, unactuated state with a gap spacing of 150 nm where all power is coupled to the "Drop" port (b) 3-dB coupling state where the approximately 175 nm gap allows for even power sharing between the "Drop" and "Through" ports (c) Switched state where the gap is 210 nm and power is fully transferred to the "Through" port

With the optical behavior defined by the directional coupler, the next step is to obtain the in-plane displacements given by the desired gap spacing in **Figure 5.8**'s transmission v. gap plot. In order to minimize computation time, the design flow first focuses exclusively on the MEMS and then integrates the photonic components, i.e., suspended waveguide, only changing the mechanical or electrical aspects as needed. As such, the discussion of this device's design continues with an analysis of the actuator.

The comb-drive is perhaps one of the most commonly used MEMS actuators and from the time it was originally proposed, there has been a preponderance of literature detailing its operation and optimization for large displacements, small footprint, etc. For example, Legtenberg et al. presented a large-displacement comb-drive actuator capable of achieving up to 30 μm of displacement under 20 V of actuation voltage [149]. Although notable in its ability to overcome the electromechanical side instability characteristic of large-stroke comb-drive actuators, it is readily discernable that this amount of displacement far exceeds what is necessary for tunable directional couplers. In general, because the entire tuning range of the designed directional coupler can be accessed within a 500 nm range of displacement, photonic MEMS devices can be made compact, which is beneficial to the scaling aspect of MEMS-enabled PICs.

A generalized unit cell of a comb drive is shown in the schematic of **Figure 5.9** where one set of fingers has a spring force boundary condition and is hence moveable, while the other has a fixed boundary condition. The former is sometimes referred to as the rotor and the latter, the stator. The capacitance between the rotator and stator can be split into a parallel component and a perpendicular component which are given by the following two equations:
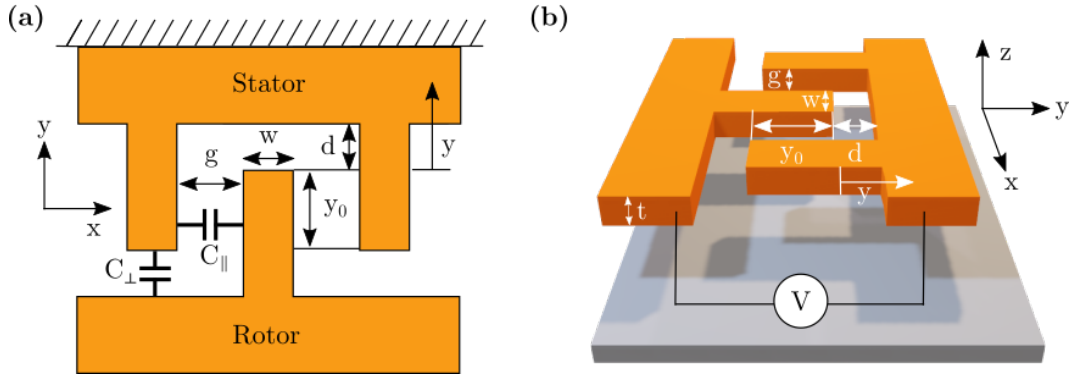

Figure 5.9 – (a) Top down and (b) 3D perspective view of a generalized comb drive unit cell ($n = 1$) indicating the relevant parameters, t = thickness of the layer, y = rotor displacement, y_0 = initial finger overlap between rotor and stator, g = gap spacing between fingers, w = finger width, d = distance between finger tip and stator, and V = actuation voltage. NOTE: dimensions are NOT drawn to scale; in particular, g should be much smaller than d

$$C_\parallel = \frac{2n\epsilon_0 t(y + y_0)}{g} \tag{5.4}$$

$$C_\perp = \frac{\epsilon_0 w t}{d - y} \tag{5.5}$$

Where n = the number of comb-drive unit cells (counted on the rotor side), ϵ_0 = permittivity of free-space, t = thickness of the comb-drive, y = rotor displacement, y_0 = initial finger overlap between rotor and stator, g = gap spacing between fingers, w is the width of a finger, and d is the perpendicular distance between the movable finger tips and the stator.

For small to moderate displacements (e.g., $d - y > 4g$), the parallel capacitance dominates the electrostatic behavior of the comb-drive and the perpendicular component can be neglected. This simplification comes from the fact that in this operating range, the vertical capacitance is much smaller than the parallel capacitance. At larger displacements, though, $C_\perp$ is no longer negligible and must be taken into account.

It can be shown that under a voltage-control actuation scheme, the electrostatic force between the rotor and stator is given by the following expression [149]:

$$F_{el} = \frac{n\epsilon_0 t}{g} V^2 \tag{5.6}$$

Where all parameters are as in Equation 5.5 and V is the actuation voltage.

This electrostatic force is balanced by the mechanical restoring force of the suspensions, which for small displacements within the elastic deformation region (i.e., stress is linearly proportional to strain), can be approximated by a linear spring given by Hooke's law:

$$F_{mech} = k y \tag{5.7}$$

Where k is the spring constant of the suspension in the direction of displacement and y is the rotor displacement.

The suspension can take on multiple geometries, varying from simple clamped-clamped beams to more mechanically robust crab-leg flexures and folded flexures (**Figure 5.10**). However, in all cases, one dimension of the beam (i.e., the length) must be significantly larger than the other two. The two flexure variants reduce extensional axial forces that can produce non-linear force v. displacement characteristics and effectively increase the suspensions' stiffness as the deflection increases [149].

In general, small deflection theory is valid for in-plane displacements up to a quarter of the structure thickness, which is a functional generalization of the more specific Euler-Bernoulli assumptions that (1) the cross section of a deflected beam does not significantly deform under transverse/axial loads and (2) during deflection, the beam cross section remains planar and normal to the axis in which the load is applied.
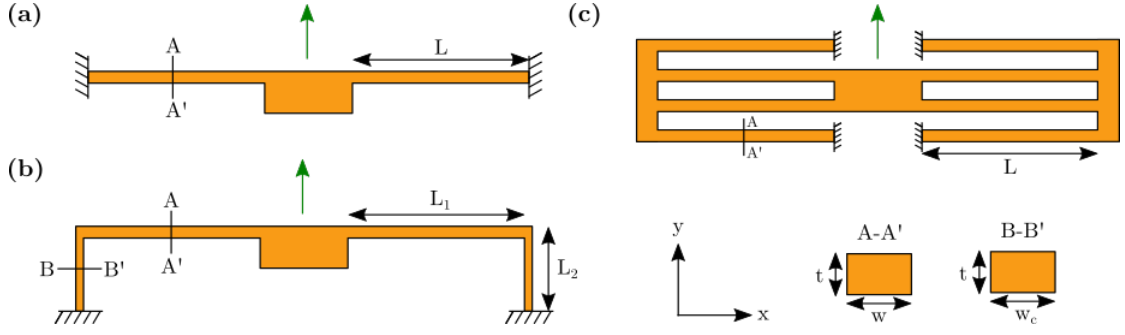
Figure 5.10 – Schematic views of the (a) Clamped-Clamped (b) Crab-Leg Flexure and (c) Folded Flexure suspensions along with the key geometric parameters and a green arrow indicating the deflection direction

Given this mechanical framework and the validity assumptions for linear beam bending theory, one obtains the following spring constants in the x- and y-directions for three common suspension geometries [149].

Suspension Type	k_x	k_y
Clamped-Clamped	$\dfrac{2Ehw}{L}$	$\dfrac{2Ehw^3}{L^3}$
Crab-Leg Flexure	$\dfrac{12E_y I_2}{L_2^3}\left(\dfrac{L_1 I_2 + 2L_2 I_1}{2L_1 I_2 + L_2 I_1}\right)$	$\dfrac{24EI_1}{L_1^3}\left(\dfrac{L_1 I_2 + L_2 I_1}{L_1 I_2 + 4L_2 I_1}\right)$
Folded Flexure	$\dfrac{2Ehw}{L}$	$\dfrac{2Ehw^3}{L^3}$

Table 5.3 – Spring Constants for Various Suspension Geometries

Where E is the Young's modulus of the suspension material and h, w, and L correspond to the height/thickness, width, and length of the suspension, respectively. Parameters with subscripts are specific to the crab-leg flexure suspension and are indicated in **Figure 5.10b**. Additionally, I_1 and I_2 correspond to the second moment of inertia of the two segments in the crab-leg flexure and are given by:

$$I_1 = \frac{1}{12}\frac{tw^3}{L_1^3} \tag{5.8}$$

$$I_2 = \frac{1}{12}\frac{tw_c^3}{L_2^3} \tag{5.9}$$

Consolidating these physical relationships and equating the electrostatic and mechanical forces (for the clamped-clamped and folded flexure suspensions), one obtains the following expression for the in-plane displacement of the comb-drive as a function of geometric parameters and the actuation voltage:

$$y = \frac{n\epsilon_0 t}{k_y g} V^2 = \frac{n\epsilon_0 t}{g} \left(\frac{L^3}{2Ehw^3} \right) V^2 = \frac{n\epsilon_0 L^3}{2Eg w^3} V^2 \qquad (5.10)$$

Here, it has been assumed that the comb-drive and suspension have the same height/thickness, so the values t and h cancel out. The final result is a simple analytical expression that can provide an upper bound on the expected in-plane displacement for a given comb-drive/suspension configuration.

As this device is intended for modification of the lateral gap spacing in the attached directional coupler, one must also take into consideration its resilience against out-of-plane displacement, which could result from mechanical shock during handling. Responsible design address this issue by making the device sufficiently stiff in the out-of-plane or z-direction:

$$k_z = \frac{2Ewh^3}{L^3} \qquad (5.11)$$

While this model does not capture all aspects of device operation (e.g., non-linear deflections where $y > t, h$, side instability at higher voltages, or fringing field effects), it is sufficient for hand calculations.

Given Equation 5.10 and Equation 5.11, one must consider the following points:

1. A complete switch in optical power from the "Drop" to the "Through" port requires a minimum achievable displacement of 210 nm. Thus, the electromechanical design should be able to provide at least this amount of displacement using an actuation voltage below 25 V so as to facilitate the design of the driver electronics, which will distribute voltages to the individual devices in larger-scale circuits

2. Scaling-considerations dictate that the comb-drive actuator should be made as compact as possible with the following considerations taken into account:

   - Structure thickness' such as t and h are restricted to the available silicon thicknesses of the PDK (i.e., 70 nm, 150 nm, and 220 nm)

   - The minimum feature size in the PDK is 150 nm, so $g > 150$ nm to ensure that the gap is free of silicon-bridging or other residues

   - A smaller n means the device can be made narrower but also reduces the electrostatic force

3. Integration of the directional coupler necessitates that one of its arms be attached to the comb-drive body, which effectively increases the device's in-plane spring stiffness. Specifically, the waveguide is a clamped-clamped beam (i.e., it is anchored to the silicon rim by the optical transitions) that appears in parallel with the comb-drive suspen-

sion, meaning the achievable in-plane displacements will be less than that provided in Equation 5.10

- In general, for the same applied electrostatic force, a smaller in-plane spring stiffness allows for greater displacements

- It is desirable to operate the device at high-frequencies, with quick response times, meaning the device should in fact not have a prohibitively small in-plane spring stiffness, as the mechanical resonance frequency scales with $\sqrt{k_y}$

4. The device should be robust against mechanical shock during handling and/or shipping and other out-of-plane forces like stictional forces, which means k_z should not be too small

- The best way to increase k_z without negatively affecting the in-plane displacement is to use a thick suspension, i.e., large h; thus, one should use the maximum allowed thickness of 220 nm

- k_z can also be varied by increasing the beam width, w, or decreasing its length, L (Note: that varying either of these two parameters to increase k_z will reduce the maximum achievable in-plane displacement

Given these design guidelines and trade-offs, the utilized comb-drive uses a mechanical suspension with folded springs and a truss and has the following parameters:

Parameter	# of Comb Fingers (n)	Suspension Length (L)	Finger Gap Spacing (g)	Beam Width (w)
Value	76	20 µm	200 nm	300 nm

Table 5.4 – Initial comb drive specifications to achieve a minimum displacement of 210 nm

Using these parameters, one expects approximately 600 nm of displacement at 13 V of actuation voltage. However, nonlinear effects, such as spring hardening start to arise when the relative displacement is comparable to the beam thickness in the displacement direction (e.g., 600 nm displacement for a 300 nm wide beam) [150]. Thus, the results from Equation 5.10 may in fact be an overestimate for the achievable displacement. Moreover, when the waveguide suspension is added, k_y increases, and if its geometry is designed such that its stiffness matches that of the mechanical suspension, the total expected displacement further drops by a factor of two to approximately 300 nm.

As an alternative to using the non-linear formulations, the design process continues by including the additional elements such as the anchors and waveguides in the directional coupler to the as-designed comb-drive. This composite structure is then modeled in COMSOL, which is a finite element method (FEM) software. The computational advantage of simulation is that

the electromagnetic and mechanical fields in this complex composite structure can be more accurately and quickly evaluated than if done by hand. That being said, the model is only as accurate as its boundary conditions and meshing, which necessitates a solid understanding of the underlying physics and device operation.

As 2D simulations are computationally more efficient than their 3D counterparts, the device is first simulated in this environment for actuation voltages between 0 to 15 V to extract the voltage-displacement curve. The mechanical deformation for one symmetric half of the device and the associated displacement v. voltage curve obtained from the FEM simulation are provided in **Figure 5.11a** and **Figure 5.11b**, respectively.
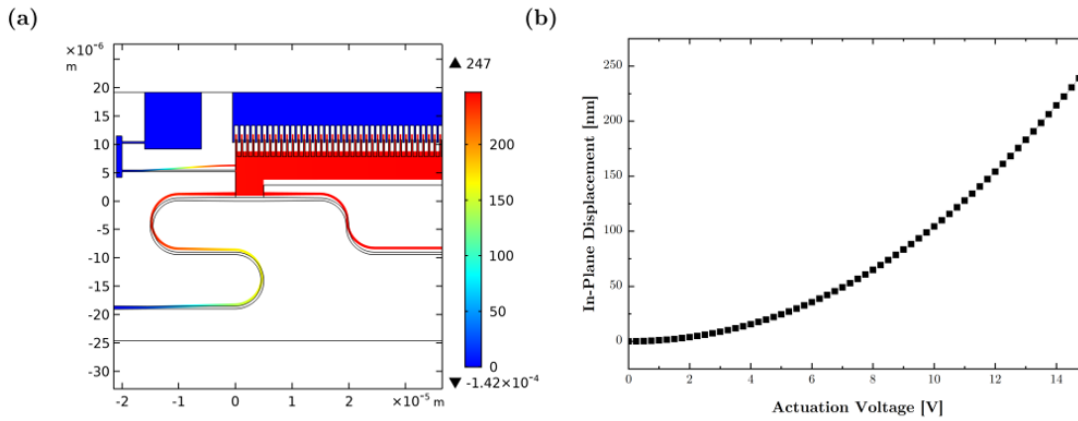

Figure 5.11 – (a) Visualization of the structural deformation given in nanometers in the device for one half of the device; note that the deformation has been scaled by a factor of 5 to highlight the displacement (b) Simulated Displacement v. Voltage plot for the geometry presented in Table 5.4

Following fabrication and the MEMS release process described in Chapter 4, the device is imaged using an optical microscope (**Figure 5.12a**). Although the maximum achievable magnification of this approach does not allow for a close-up examination of the structure, it does enable the device to be put in context alongside ancillary components. For example, the MEMS cavity with its metallization and waveguides serving as electrical and optical I/O, respectively, can be seen transiting below the MEMS sealing ring to the grating couplers and contact pads. Scanning electron microscopy (SEM) uses an electron beam to image devices, so there is a risk that during observation, the beam sufficiently charges the suspended device and/or surrounding regions such that the MEMS device collapses, rendering it non-functional. Thus, this metrology step, the result of which is presented in **Figure 5.12b**, takes place after the device has been fully characterized and if it were to collapse, would not be detrimental.

Characterization of this 2 x 2 continuously tunable coupler begins with alignment of the 1 x 10 fiber array to a corresponding array of on-chip grating couplers. Proper alignment is obtained by using the outer two grating couplers (i.e., 1 and 10) that have been connected in a shunt configuration to position the chip such that maximum power transmission is recorded when light is injected in grating coupler 1 and extracted from grating coupler 10. This
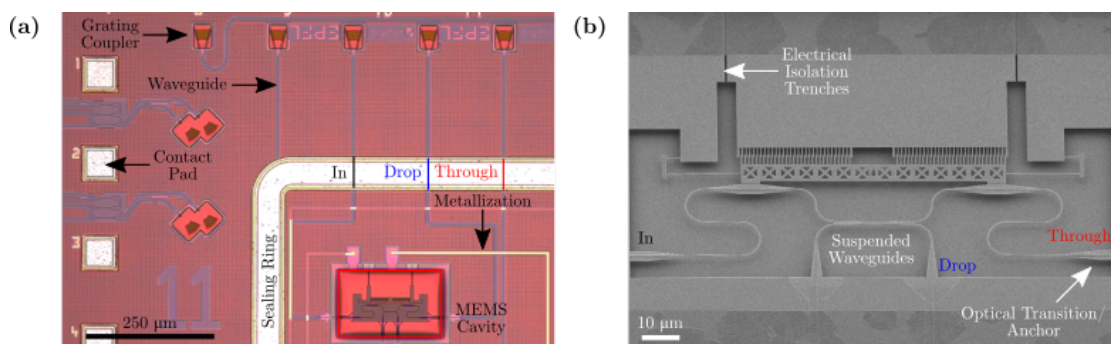
Figure 5.12 – (a) Optical microscope image of the 2 x 2 continuously tunable directional coupler indicating the MEMS cavity, the waveguides and grating couplers for carrying light into and out of the device, as well as the metallization and contact pads that provide the actuation voltage (b) Corresponding SEM recording that provides a more detailed view of the suspended device and shows the electrical isolation trenches and optical transitions/anchors

procedure sets the reference transmission characteristics for normalization of subsequent measurements thereby allowing the optical behavior of the device under test to be isolated. Next, the probe tips are brought in contact with the electrical contact pads and a wavelength sweep from 1500 nm to 1580 nm at 0 dBm input power is carried for 0 V of actuation voltage. The spectral characteristic is recorded and then this procedure is repeated for 1 V increments in the actuation voltage until the coupler switches power between ports or collapses. A plot of the transmission as a function of wavelength for five selected actuation voltages is presented in **Figure 5.13** and indicates a 3-dB bandwidth of approximately 30 nm.

Focusing on a single wavelength, e.g., the central wavelength of 1550 nm for which the directional coupler has been designed, provides the transmitted power v. actuation curve that characterizes the MEMS-tunability of the device. A side-by-side comparison of the measurement results with those from simulation is provided in **Figure 5.14** and **Figure 5.14a** reveals a large extinction ratio (ER) > 27 dB at 6.5 V, which produces the state in which all optical power is transmitted to the "Through" port. However, comparing with **Figure 5.14b** reveals that this large extinction ratio is neither obtained for the initial unactuated state nor for the fully actuated state (11 V for measurement, 13 V for simulation) in which the full optical power should return to the "Drop" port. Ideally, there should be a clear separation in power levels between the two output ports in these switching states and the discrepancy is attributed to in-plane or out-of-plane misalignment of the suspended waveguides due, for example to residual in-plane stress. Such skewing from the nominal parallel arrangement can lead to additional unwanted coupling between branches at specific wavelengths, leading to enhanced transmission back to the "Through" port. Additionally, the asymmetry in the suspension lengths can cause the electrostatic force to generate undesirable torques that rotate the device out-of-plane instead of purely translating it in-plane. This unwanted additional modification of the directional coupler gap is not controlled for in the design and the device can be improved.
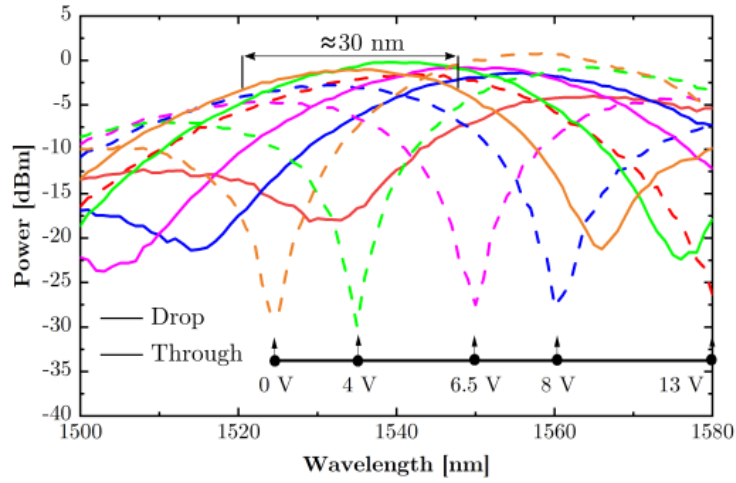
Figure 5.13 – Measured spectral response of the device for five different actuation voltages indicating a 3-dB bandwidth of approximately 30 nm. The input power is 0 dBm and power transmission is normalized to the power characteristics of the shunt grating coupler connection to remove the effects of grating coupler insertion loss, misalignment, and other losses in the measurement setup.
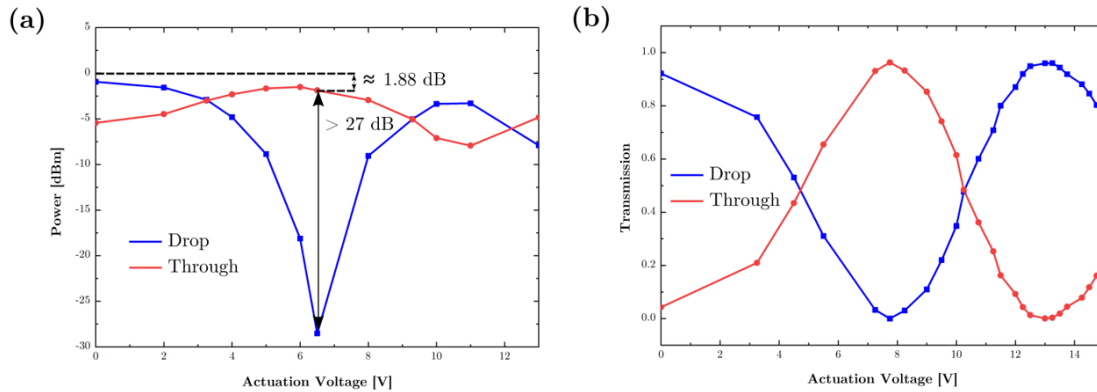

Figure 5.14 – (a) Measured transmitted power v. actuation voltage for the device at 1550 nm and for 0 dBm input power. Indicated in the plot are the ER > 27 dB at 6.5 V actuation voltage and the corresponding IL in this state of approximately 1.88 dB (b) Simulated transmitted power v. actuation voltage characteristic based on the displacement simulation results in **Figure 5.11b** and the lateral gap sensitivity of the power transmission in the designed directional coupler presented in Figure 5.4a.

However, as a proof-of-concept that MEMS can be successfully integrated into an established Silicon Photonics technology enabling continuous optical power tuning, this device is a success. It demonstrates that the proposed mechanical tuning mechanism can provide analog power coupling in a compact form factor (60 μm x 130 μm) and with low actuation voltage (6.5 V for switching state). The ER > 27 dB in the switching state is respectably high and the optical bandwidth of approximately 30 nm is sufficiently broadband for most PIC applications.

5.3 Symmetric Continuously Tunable Silicon Photonic MEMS 2 x 2 Directional Coupler

If the device of the preceding section can be considered a prototype, then the device presented here is the improved version suitable for use in large-scale circuits. In fact, this symmetric variant of the continuously tunable 2 x 2 directional coupler has been replicated over 100 times in the field-programmable PIC (FP-PIC) that has been designed in parallel by project partners as part of this work' parent-project, MORPHIC (**M**EMS-Based Zer**O**-Power **R**econfigurable **PH**otonic **IC**s), whose goal it is to demonstrate software-reconfigurable PICs in an established Silicon Photonics platform [151].

As the name suggests, the primary point under consideration for this improved device is rectifying the "asymmetry" in the ER in the initial unactuated and switched states. The ER in this first state should be equal, i.e., symmetric, to that in the switched state. Note, that the identification of ports receiving the full optical power in a particular state will be omitted for now, as the initial lateral gap spacing in the suspended directional coupler is not the same as before.

The proposed hypothesis regarding the asymmetric ER of the previous device posited that the initial anti-parallel and/or out-of-plane arrangement of waveguides due to residual in-plane stress could be a key contributing factor. It was also suggested that the length mismatch in the comb-drive suspension could lead to a rotation of the device under actuation, which would also contribute to non-planar displacement of the waveguide. The first condition is not easily confirmed visually, e.g., by optical or SEM imaging, because of the respective lack of resolution or risk of charging at enhanced magnification. However, it can be inferred from the optical microscope and SEM images of other structures in **Figure 5.15** that the out-of-focus regions in the former indicate out-of-plane deflection and that in the latter, stiff clamped-clamped beams can buckle upwards.
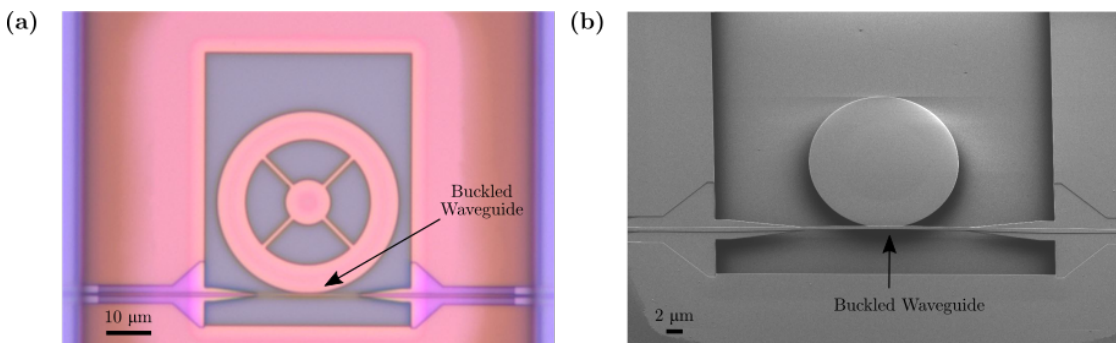

Figure 5.15 – (a) Optical microscope image showing that the bus waveguide to a ring resonator is slightly out of focus with respect to the other structures, indicating out-of-plane deflection (b) Tilted-view SEM recording of a bus waveguide to a disk resonator confirming slight upward buckling of the waveguide

It is also possible to confirm this stress-related buckling using another form of metrology such as optical profilometry. From optical profiler measurements carried out by project partners

at KTH on dedicated test structures, residual stress leading to out-of-plane deflection was observed. Depending on the sample, for clamped-clamped beams 50 μm long, the center deflection was recorded to be as much as ± 400 to 500 nm. Although the suspended directional coupler arms are not quite as long as the test-structures, these findings indicate that there is non-negligible, in-plane residual stress causing out-of-plane deflection.

The second point concerning a device rotation can be linked to a force imbalance between the lower and upper surfaces of the device, similar to the phenomenon reported in [152]. Like the device presented by Tang et al., in the presented actuation scheme, the movable device layer and movable part of the comb drive are grounded while the fixed portion of the comb drive receives the actuation voltage. The substrate layer is grounded and serves as a grounding plane. However, because of the inherent asymmetry in the structure, e.g., a 2 μm air gap separating the device layer and substrate and an effectively "infinite" expanse of air above the device, there is an imbalance in the field distribution that results in a net vertical force. This force, when applied to the length-mismatched suspensions can create a torque that rotates the device out-of-plane. This behavior is readily verified by the full electromechanical FEM simulation seen in **Figure 5.16**, which provides an image of the deformed 3D model capturing the out-of-plane deflection.
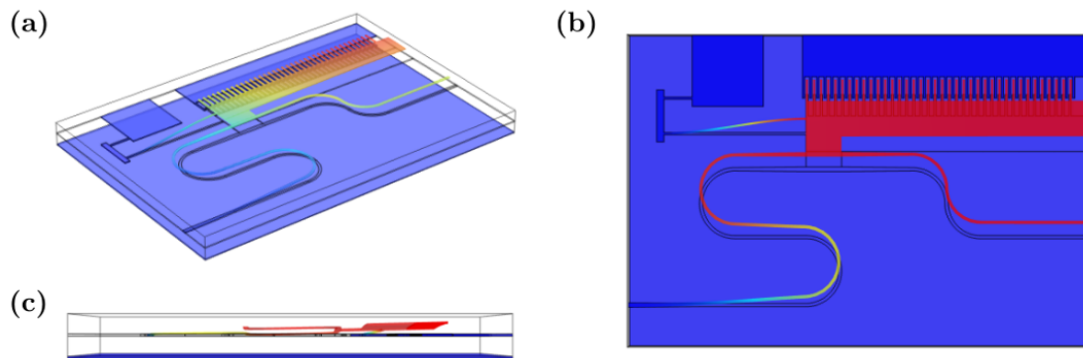

Figure 5.16 – (a) Full perspective view of the 3D FEM simulation results of the device from the previous section where the effect of a length mismatch in the mechanical suspension manifests itself as an out-of-plane rotation of the device (b) Top-down view of the device indicating the in-plane component of the displacement (roughly 40 nm) (c) Side-view of the device capturing the out-of-plane component of the displacement (roughly 20 nm)

Having confirmed out-of-plane deflection caused by residual stress and rotation from length-mismatched suspensions, it is possible to modify the original design to address these issues. The first and perhaps most straightforward change is to simply match the lengths of the beams in the mechanical suspension. Concurrently, one can also reduce their lengths to provide additional stiffness in the out-of-plane direction, making the structure more robust to out-of-plane forces. The second key change is to replace the 90° U-shaped bends in the movable waveguide suspension with shallow S-shaped bends and to utilize this new geometry for the fixed waveguide as well. S-shaped bends allow for smooth stress-relaxation in the suspended regions when their fixed boundary constraints are removed during the VHF release

etch. Consequently, the released structure in its initial unactuated state is less likely to exhibit residual out-of-plane misalignment. It should be noted that while this type of waveguide suspension takes up more space in the long dimension of the device, by using the same geometry in the fixed waveguide, the dimensions in the orthogonal directional can in fact be reduced. Furthermore, by limiting the extents of the straight region after the S-bend and before the anchored optical transition, the waveguide stiffness can be more easily tuned than before.

An additional change not related to the performance of the progenitor device is the use of a 200 nm initial waveguide gap spacing rather than 150 nm. The decision to increase the waveguide gap stems from the fabrication non-idealities encountered during the MEMS post-processing wherein structures utilizing the minimum allowed feature sizes of the PDK suffered from silicon- and alumina-bridging and could not be separated. All other physical aspects of the directional coupler, e.g., the coupling length remain the same. With this in mind, the optical power transfer characteristics from the previous two sections are flipped in that for the initial, unactuated state, all the power stays in the waveguide branch with the "Through" port and only after increasing the gap separation, is light localized in the waveguide branch with the "Drop" port.

A schematic diagram of the final device and its 3D perspective view are presented in **Figure 5.17** and the relevant parameters of the updated comb-drive are listed in **Table 5.5**. The device has a footprint of 25 μm x 150 μm, which represents almost a 50% reduction from the original geometry.
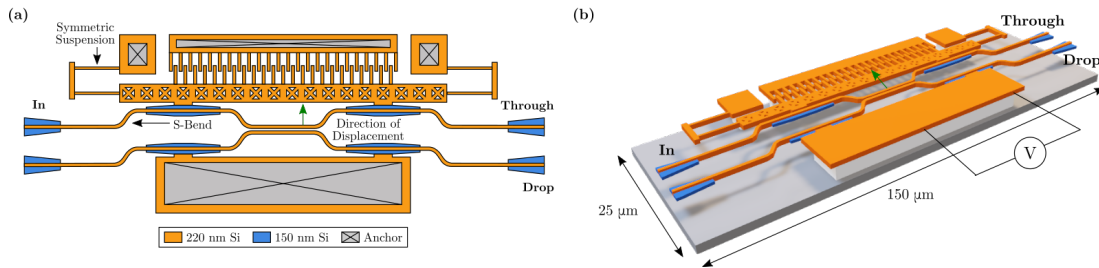

Figure 5.17 – (a) Schematic view of the symmetric 2 x 2 continuously tunable directional coupler where the 90° U-bends have been replaced by softer S-bends and the input and output waveguide share the same geometry (b) 3D perspective view of the device indicating the new dimensions

Parameter	# of Comb Fingers (n)	Suspension Length (L)	Finger Gap Spacing (g)	Beam Width (w)
Value	70	10 μm	200 nm	300 nm

Table 5.5 – Updated Comb Drive Specifications

As before, following MEMS-release post-processing, the device is imaged under an optical

microscope (**Figure 5.18a**) to verify the absence of any blatant defects (e.g., collapse to the substrate or particulate contamination on the optical structures) and is then characterized in the lab, outside the cleanroom. The prudence of this protocol in which device characterization occurs before SEM imaging reveals itself in **Figure 5.18b** where one can observe that despite all other components being nicely suspended, the suspended waveguide has collapsed in the coupling region presumably due to charging. This conjecture is supported by the fact that the following characterization data was taken from this exact device, and that such a collapse would lead to incomplete or "noisy" coupling.
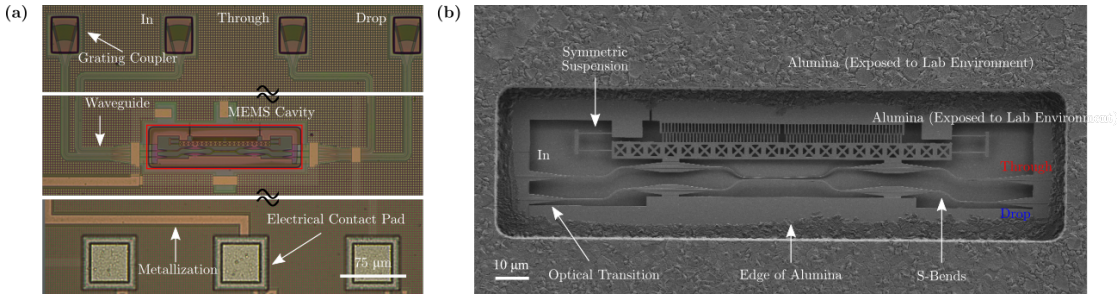

Figure 5.18 – (a) Optical microscope image of the released device within the MEMS cavity alongside the various supporting optical and electrical components (b) SEM image of the device indicating the key structural improvements to the original design; the rough texture of the alumina, which is believed to be due to the change in environmental conditions outside the cleanroom is also visible
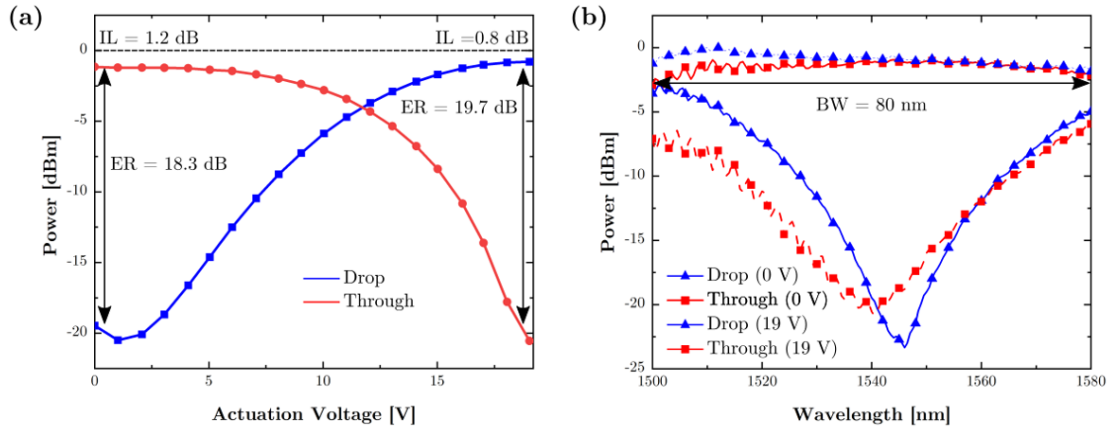

Figure 5.19 – (a) Power Transmission v. Actuation Voltage plot for 0 dBm input power at 1540 nm where the symmetric ER > 18 dB in both the idle and actuated states has been labeled, as well as the corresponding IL of 1.2 dB and 0.8 dB (b) Spectral response of the symmetric 2 x 2 tunable directional coupler for 0 dBm input power in the 0 V and 19 V states. Broadband behavior of the device is indicated by an almost flat response over the entire wavelength sweep in the active port (3-dB bandwidth > 80 nm)

Figure 5.19a presents the power transmission v. actuation voltage of this device for 1540 nm and validates the modifier "symmetric" in the name "Symmetric Continuously Tunable Photonic MEMS 2 x 2 Directional Coupler." The actuation curve exhibits a well-matched > 18 dB ER in both the idle and actuated states and reaches the switching point in power

transmission at 19 V, which is larger than the 6.5 V of the asymmetric design. However, the difference can be attributed to two properties:

1. The larger initial gap spacing (200 nm), which according to **Figure 5.4a** requires the movable waveguide to be displaced an additional 100 nm more to achieve a transfer of power between output ports than if it were only (150 nm). The larger displacement necessitates a greater electrostatic force and hence, a greater actuation voltage

2. Although the new waveguide suspension is more robust against out-of-plane displacement, it is also stiffer than the original design. Combined with a shorter mechanical suspension in the comb-drive, the restoring spring force is stronger and consequently, the actuation voltage generating the electrostatic force must also be stronger/larger to obtain the same displacements as before

The directional coupler is designed for a central wavelength of 1550 nm, but since the best optical performance can be found at 1540 nm, this is the selected wavelength for which the measurement results are presented. This shift of 10 nm can be attributed to fabrication variation of the designed device dimensions and since the device still performs well within the C-band, this deviation is deemed acceptable. **Figure 5.4a** also presents the insertion loss (IL) in the idle (1.2 dB) and actuated states (0.87 dB), both of which are less than that of the original device. Sources of the excess insertion loss include propagation, scattering, and transition losses within the MEMS cavity. With regard to the latter two, the SEM recording of **Figure 5.18** indicates that the visibly rough alumina lies on top of the waveguide in the optical transition, which can contribute to scattering losses.

A wavelength sweep for the idle (0 V) state and the actuated state of 19 V, where the switch in optical power between waveguides has occurred, is shown in **Figure 5.19a**. One of the prominent features of this spectral response is its remarkably flat (i.e., broadband) response in the active port across the wavelength range from 1500 to 1580 nm, which covers the entire C-band. The measured 3-dB bandwidth > 80 nm, far exceeds that of the original device and even that of the standalone suspended directional coupler presented in the first section of this chapter. This enhanced congruity between measurement and simulation is attributed to the improved waveguide suspensions that have been included in this device. Note that in both **Figure 5.3** and **Figure 5.7**, the fixed waveguide makes a 90° bend after the coupling region and is immediately anchored to the optical transitions after a short distance. This geometry contrasts with the updated approach of allowing the fixed waveguide branch to mirror the movable branch by including S-bends, and distributing the anchor points in shallow etched silicon along its length. By virtue of the improved residual stress relaxation discussed previously, this configuration also makes the fixed portion of the directional coupler more robust against out-of-plane displacement. The advantage of this design is that it also allows for better initial in-plane alignment of waveguide branches.

Because this updated design is mechanically more robust than its predecessor, it is also

possible to perform a transient characterization of the device. Here, the DC actuation voltage is replaced by a rectangular pulse from a waveform generator and the power sent to the output grating coupler is collected by the fiber array and sent to a high-speed, amplified photodetector. The amplitude of the actuation voltage is set to 12 V, which is where the cross-over point in which power in the "Through" and "Drop" ports are equal to one another occurs. Using a slightly lower voltage than the full 19 V needed for the full optical power to appear in the "Drop" port is a safety precaution against operating the device at its limit where it could electrically collapse. The additional 5 dB one obtains at this fully actuated state can be compensated for by increasing the input power by this amount, and in fact, this provides the added advantage of boosting the output signal recorded in the photodetector response.
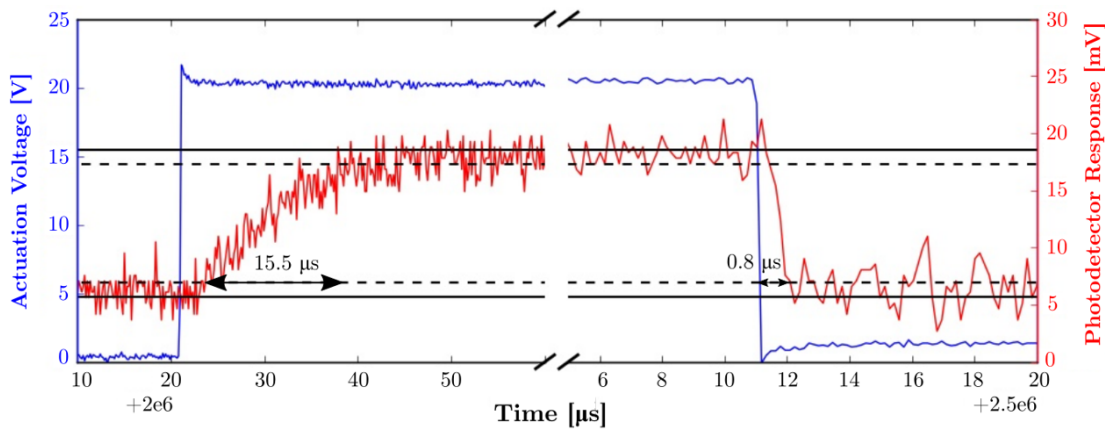

Figure 5.20 – Transient measurement showing a close-up view of the on- and off-switching transitions where the rise-time is recorded to be 15.5 μs and the fall-time, 0.8 μs

The results of the transient measurement are shown in **Figure 5.20** which shows a close-up view of the on- and off-switching events. The device exhibits relatively quick response-times, with a 15.5 μs rise-time and a 0.8 μs fall-time. This asymmetry in the switching time response can be explained by a difference in the magnitude of the forces present at the on- and off-state instances. At time t = 0, when the voltage reaches its maximum value, it is only the fast-acting electrostatic force that accelerates the device towards the fixed comb drive. And at time t = 0⁺ the slower restoring mechanical force is able to respond to the resulting displacement and the device finds an equilibrium position. Recall that the magnitude of the electrostatic force is dependent on the energy stored in the capacitor, which in the initial state is not particularly large because of the small overlap area between comb fingers. In the ON state now, though, there is a larger overlap area and hence more stored capacitive energy, which means both the electrostatic and complementary mechanical restoring force are larger than in the initial configuration when there was only a small overlap. Now, when the voltage goes low, the electrostatic force responds almost instantaneously compared to its mechanical counterpart and goes to zero, leaving behind a rather large restoring force to push the device away from the fixed comb drive. Thus, the force associated with the ON-OFF state transition is initially larger than that associated with that of the OFF-ON state transition, which explains the faster

off-switching time.

Overall, this device presents a large improvement over the initial design with a 50% smaller footprint, symmetric extinction ratio > 18 dB for both idle and actuated states at 19 V with < 1.3 dB IL. The tunable directional coupler is remarkably broadband (> 80 nm of bandwidth) thanks to the robust waveguide suspension and is responsive, as seen by the fast on-/off-state switching times of 15.5 µs and 0.8 µs, respectively. Given these performance metrics, this device fulfills the requirements for fast and efficient optical power tuning in PICs. Variations on this improved design can be made to further optimize the design with respect to other figures of merit and two such examples targeting lower actuation voltage to reach the switch in power are briefly summarized in the next section.

5.4 Variations on a Theme: Low Actuation Voltage MEMS-Enabled Tunable Couplers

Although 19 V is not a particularly large voltage for obtaining a > 18 dB ER in a fully switched-state in an electrostatic device, as in transistor design, one always looks towards reducing the supply, or in this case, actuation voltage.

All devices presented in this work utilize electrostatic actuation and as such, in an ideal situation do not consume steady-state power. However, in addition to the transient flow of electrons needed to establish voltage differences, there are ever present leakage currents, which do contribute to DC power consumption. Minimizing the actuation voltage reduces the power consumption penalty to be paid, thereby bolstering the advantage MEMS-based optical tuning holds over its established thermoelectric counterpart.

Using the updated waveguide suspensions from the symmetric 2 x 2 tunable directional coupler from the preceding section, there are two simple approaches for reducing the required actuation voltage. The first approach is to simply increase the length of the mechanical suspensions on the comb-drive to make them softer. This approach will not increase the overall footprint as long as it is the waveguide suspensions that determine the full length of the device. The reduction in actuation voltage can be seen in the plot presented in **Figure 5.21** where the actuation voltage to reach full power transmission in the "Drop" port has been reduced to 17 V. For this device, the mechanical suspension has been increased from 10 µm to 15 µm.

Using a slightly longer suspension successfully reduces the voltage needed to reach the fully actuated state by 2 V (19 V versus 17 V). The 50% increase in length reduces the stiffness of the suspension by roughly 80% of its original value. Consequently, the device becomes more susceptible to in-plane and out-of-plane deformation during the stress relaxation associated with the removal of the fixed boundary condition during the release process. The modified waveguide suspension has been primarily designed to combat the out-of-plane deformation, but it is still possible that in-plane asymmetries still cause the waveguides to align in a skewed,
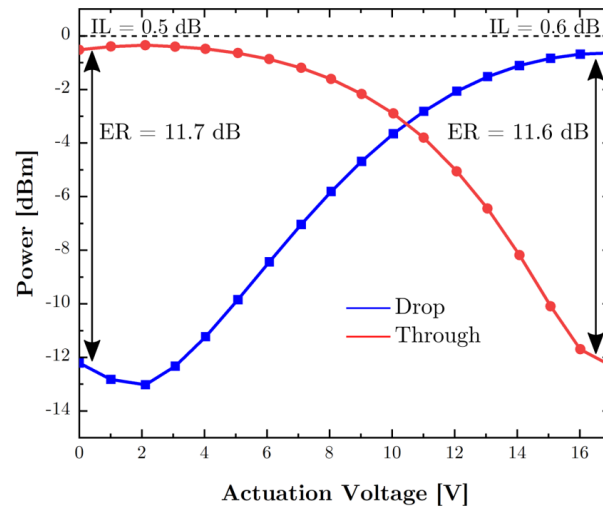
Figure 5.21 – Power Transmission v. Actuation Voltage characteristic for a symmetric, continuously tunable 2 x 2 directional coupler at 1550 nm and 0 dBm input power where the mechanical suspension has been is 15 μm long. The voltage for the fully-actuated state is 17 V, and the ER and IL in the idle and fully actuated states are > 11.5 dB and < 0.7 dB, respectively.

rather than parallel arrangement. It is these geometric and fabrication-related non-idealities to which the 6 dB reduction in ER from the previous design is attributed.
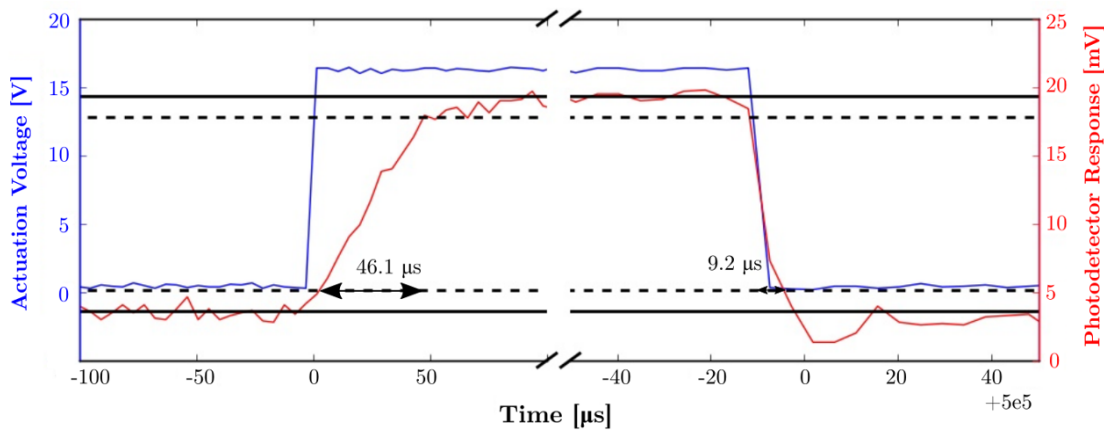

Figure 5.22 – Transient measurement showing a close-up view of the on- and off-switching transitions for the tunable 2 x 2 directional coupler with mechanically softer suspension, where the rise-time is recorded to be 46.1 μs and the fall-time, 9.2 μs. Like the previous variant, the asymmetry in switching times is attributed to the difference in switching forces present in the OFF-ON and ON-OFF transitions.

In any case, the primary effect of a softer mechanical suspension is verified by a reduction in switched-state actuation voltage. This benefit, however, is offset by a slower response time, as can be observed in **Figure 5.22**, where the on-state and off-state switching times are characterized by a 46.1 μs rise-time and a 9.2 μs fall-time.

A more elegant solution for reducing the actuation voltage, which leaves the length of the
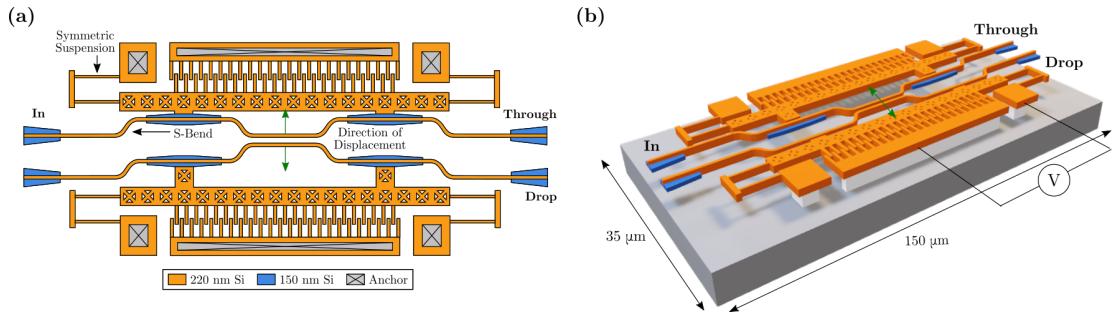
Figure 5.23 – (a) Schematic view of the double-sided comb-drive 2 x 2 continuously tunable directional coupler (b) 3D perspective view
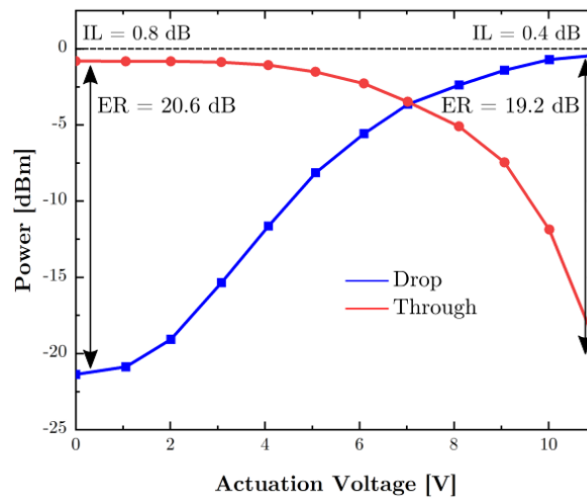

Figure 5.24 – Power v. Actuation Voltage characteristic for the double-sided comb-drive 2 x 2 continuously tunable directional coupler revealing an 8 V reduction in the voltage required to obtain the fully actuated state (11 V). The device exhibits remarkably high ER in the idle and fully actuated states, 20.6 dB and 19.2 dB, respectively, and low IL for both states, < 0.9 dB

mechanical suspension unaltered, is to mirror the movable waveguide and comb-drive along the long dimension of the device. Doing so replaces the fixed arm of the directional coupler with a symmetric version of the movable arm and allows the waveguide gap separation to be increased through a "pulling" action on both sides. This adjustment pays a paltry penalty in footprint by contributing additional width (35 µm instead of 25 µm), but the increase is hardly significant when compared to the other devices that have already been demonstrated. A 2D schematic view of the device is presented in **Figure 5.23a** and a 3D perspective view is shown in **Figure 5.23b**.

The characterization results for this device are presented in **Figure 5.24** and indicate the advantage of using a double-sided comb-drive topology: the state in which all the optical power is transferred to the other waveguide occurs for 11 V. This 8 V reduction in the nominal actuation voltage required by the symmetric variant is a much more efficient solution than

simply increasing the length of the mechanical suspension. Further benefits of preserving the mechanical design can be seen in the respectably large ER obtained in both the idle and fully actuated states. An ER > 19 dB and IL < 0.9 dB for both states more closely mirrors, the original characterization data of the original improved symmetric design. The benefit here now is that these values are obtained for a lower actuation voltage.

This double-sided comb-drive variant of the symmetric, continuously tunable 2 x 2 directional coupler is the culmination of the design process carried out in this work in demonstrating MEMS-enabled directional coupler tuning. The final device is compact (35 μm x 150 μm), operates under low actuation voltage (11 V), and achieves high ER (> 19 dB) and low IL (< 0.9 dB) for both the idle and fully actuated states. For this configuration, the two movable waveguides need to travel a shorter distance than in the case for the single movable waveguide to obtain the same increase in gap separation.

5.5   Concluding Remarks on MEMS-Tunable Power Couplers

With tunable power couplers constituting an important element in PICs, there are a selection of key device parameters including IL, ER, BW, switching speed, footprint, and actuation voltage that determine system scalability and performance. The IL and footprint are two parameters critical for scaling because they determine how many devices can be connected to one another in a given area. Too high IL results in the signal losing significant optical power after traversing only a few devices, and if the devices themselves are too big, not many can be included in a single circuit. Use of rib waveguides to connect mechanical and optical portions of a photonic MEMS device together and including smooth S-bends helps reduce both metrics. The devices presented in this chapter do an excellent job of fulfilling the criteria of low IL and small footprint, with an average IL below 1 dB for the fully optimized design and a minimum footprint of 25 μm x 150 μm.

ER, BW, and switching speed are parameters contributing to the optical performance of the system and dictate the port isolation, spectral window of operation, and responsivity, respectively. A complete separation of power levels between the "Through" and "Drop" is desirable and if this characteristic can be switched back and forth quickly over the entire telecom C-band, one has successfully fulfilled all the optical requirements for an effective Silicon Photonic power coupler. Short, rigid suspensions combined with the smooth S-bends in the waveguides enable the coupling regions of the device to be displaced parallel to one another with good alignment and also enable the switching to be abrupt for good ER and fast switching speeds. The broadband behavior of the device is dictated by the optical behavior of the coupler, which if it includes tapers mimicking adiabatic transitions, drastically its reduce wavelength-sensitivity. All presented devices include such a compact, broadband coupler and the symmetric, continuously tunable power coupler achieves an impressive 80 nm of optical bandwidth while offering > 18 dB ER and on-/off-state switching faster than 16 μs.

Actuation voltage, the final metric represents not only the power consumption but also a

general compatibility with MEMS-enabled photonics integrated alongside electronic systems. Static power consumption is linked to leakage current in electrostatic devices, so the actuation voltage should be minimized; this decision also translates favorably to the driver electronics, which typically operate at voltages less than 25 V.

In summary this chapter has provided a selection of in-plane actuated devices employing a common optical design for effective, scalable, fast, and power-efficient optical power tuning. However, other designs are possible that can further boost performance. For example, one can imagine turning to out-of-plane electrostatic actuation schemes, which not only provide a potential savings in footprint because the relatively long comb finger arrays are replaced by a single electrode, but also by virtue of a smaller size, promise faster switching times. Furthermore, by careful design of the suspension to make the out-of-plane stiffness sufficiently soft, one can imagine power couplers with very low actuation voltage. One can also imagine multi-layer power couplers where instead of having waveguides initially separated by a lateral gap, are initially offset by a vertical gap. The advantage of this approach is that one can take advantage of the near atomic smoothness of waveguide top surfaces, thereby reducing scattering losses associated with light interactions at waveguide sidewalls.

The next category of devices is that of the integrated Silicon Photonic MEMS switch, which like the tunable directional coupler relies on a transfer of optical power between waveguide branches. And while it can be argued that the Silicon Photonic MEMS switch is simply a different end-application of a tunable coupler, the distinction that will be demonstrated in this work is either additional routing between input and output ports beyond the standard 2 x 2 arrangement, or a stronger and faster transfer of power in a more compact form-factor.

6 Silicon Photonic MEMS Switches

Depending on their port count and the respective connectivity of these ports, optical or photonic switches take on a variety of roles. At smaller scale, in 1 x 2 (1 input, 2 outputs), or 2 x 2 (2 inputs, 2 outputs), photonic switches can be used for testing and measurement of small systems. And at larger scales, e.g., 1 x N or N x N port configurations, it becomes possible to implement sensor networks (N < 16), or communication networks (N >> 16). With 75% of data traffic occurring within datacenters and a desire to continuously scaling-up capacity without a proportional increases in power consumption, it is such networks that are the primary technology driver for photonic switches [153]. With an N x N number of components in such a communication network, there is a clear need for integrated photonic switching solutions whose constituent devices can provide high port ER (proper ON/OFF functionality), low IL (< 3 dB), broadband behavior, and fast switching speed (ns - ms), all while occupying a minimal amount of space and consuming little to no power.

As seen in the previous chapter, the physical displacement of waveguides to increase the gap separation between the arms of a directional coupler enables powerful, compact, efficient, and fast optical modulation. Specifically, using in-plane, electrostatic actuation mechanisms provides a continuum of optical power distributions needed for analog tuning and does so with minimal power consumption and within a small form-factor. This electrical-mechanical-optical effect in photonic MEMS can also be used to provide dynamic reconfiguration of information flow, i.e., switching. Like the switchboard operators of yore, Silicon Photonic MEMS switches can be used to reroute information in the modern optical cross-connects (OXC) found in the telecommunication systems and datacenters discussed above. The 2 x 2 arrangement of the tunable directional couplers in the previous section are capable of routing a substantial amount of information, particularly when using a wavelength division multiplexing (WDM) scheme, but the number of input and output ports is still limiting. Adding additional ports introduces new input-output configurations that can be operated in parallel, and hence such devices can be seen as taking on the role of switching hubs or sub-units. When connected to one another, these devices can help implement the desired N x N switching functionality implemented in communication networks, for example.

6.1 Low Voltage Vertically Movable Silicon Photonic MEMS Switch

This work has presented a selection of devices that operate based on the modification of the lateral, or in-plane gap, separation between waveguides. However, 3D FDTD simulations characterizing the gap dependence of power transmission in a directional coupler indicate that the vertical, or out-of-plane gap, can also be varied. An implementation of the vertically tunable mechanism using an extremely low actuation voltage MEMS is presented here. Note that this device has been presented before and that details and descriptions complementary to those presented here can be found in [154].

Figure 6.1a presents the schematic diagram of the device and **Figure 6.1b** shows the corresponding 3D perspective view. Indicated are the six optical I/O ports, which are connected through three suspended directional couplers, whose optical design has been discussed in the previous chapter, but whose mechanical design makes the arrangement unique from what has previously been demonstrated. In particular, both arms of the directional coupler connecting ports 3 and 4 and those of the coupler connecting ports 5 and 6 have been made "stiff" so that they are fixed and maintain a 100% cross-coupling ratio. Only one arm of the coupler at the bottom is made tunable and this is accomplished through the use of a mechanically "soft" (in the out-of-plane direction) suspension. Together, these couplers enable four different switching configurations. Also included are the optical terminations whose role it is to attenuate any excess non-coupled light so that it does not cause back-reflections.
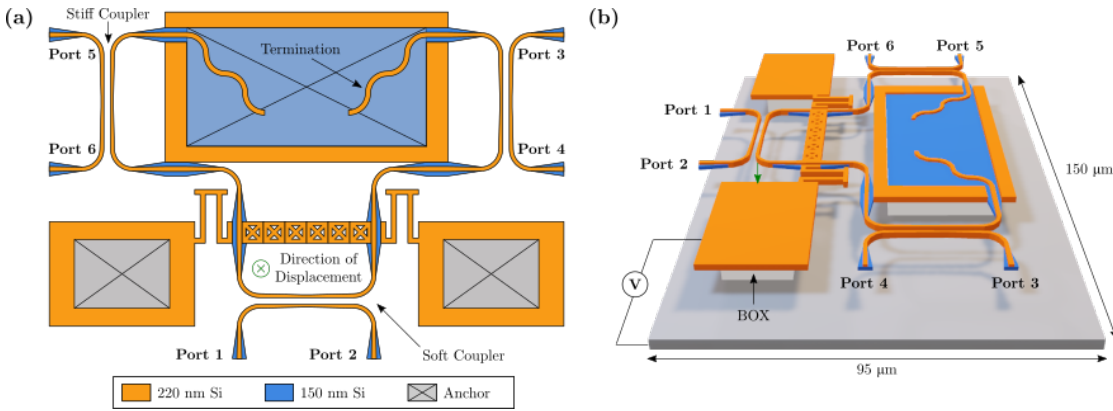

Figure 6.1 – (a) 2D schematic view of the vertically moving Silicon Photonic MEMS switch indicating I/O ports, the soft, movable couplers and the stiff, fixed couplers, and optical terminations to reduce back-reflections (b) 3D perspective view showing the overall dimensions of the device, 95 μm x 150 μm and how the actuation voltage is applied between the suspended device layer silicon and substrate

Unlike in-plane electrostatic actuation, where the movable structure and substrate are typically both grounded and voltage is applied to the fixed regions, here, voltage is applied to the movable structure while the substrate is grounded. The resulting electrostatic force attracts all suspended portions of the device to the substrate, but because only one coupler arm is "soft", only it is pulled down, thereby increasing the vertical waveguide gap separation in the bottom coupler. Because voltage is now applied to optically active waveguides (i.e., waveguides

carrying light), a more elaborate electrical isolation scheme is necessary. In addition to the electrical isolation trenches in the silicon rim separating regions at different voltages, the movable structure carrying voltage must now also be isolated from the optical inputs and outputs. Not doing so presents the risk of electrical crosstalk with other components that are optically and electrically connected to this switching device through the waveguides.

The full eight, six unique, switching configurations for the OFF- and ON-states of the device, complete with input and corresponding "Drop" and "Through" ports are presented in **Table 6.1**. Because the device is intended to be operated as a switch, the "Drop" port should receive the full optical power and is therefore highlighted to easily identify the possible output ports.

	OFF-State				**ON-State**		
Configuration	**Input**	**Drop**	**Through**	**Configuration**	**Input**	**Drop**	**Through**
1	Port 1	Port 3	Port 2	**5**	Port 1	-	Port 2
2	Port 2	Port 5	Port 1	**6**	Port 2	-	Port 1
3	Port 3	Port 1	Port 4	**7**	Port 3	Port 5	Port 4
4	Port 5	Port 2	Port 6	**8**	Port 5	Port 3	Port 6

Table 6.1 – Switching Configurations for Vertically Movable Silicon Photonic MEMS Switch

It should be noted that although the overall footprint of the device is 95 μm by 150 μm, roughly three times that of the double-sided comb drive tunable coupler, most of this area is consumed by the waveguide routing needed for electrical isolation: the actuator itself is quite compact. In fact, this out-of-plane electrostatic geometry is roughly 40 μm x 50 μm, which is a distinct size-reduction over the comb-drive actuator geometry.

In order to determine the actuation voltage required to trigger the switching event, a 3D FEM simulation is performed on a simplified actuator geometry that includes only the suspended waveguide, the structural lattice spanning the movable waveguide arm, the mechanical suspension, and the fixed portion attached to the central anchor. Combined with a single waveguide thickness (220 nm) for all components, e.g., no shallow-etched silicon rib connections, the resulting structure will be stiffer than reality, but the computational savings enabled a quicker convergence on a suitable geometry. The results of the FEM simulation are presented as an actuation curve indicating the out-of-pane displacement v. actuation voltage characteristic of the device in **Figure 6.2a**. These values can be compared with a concatenated version of the power transmission v. vertical gap (only indicating one beat-length) in a tunable directional coupler (**Figure 6.2b**) to reveal that the full switch in optical power between "Input" and "Drop" ports can be obtained for roughly 5 V of actuation voltage. The corresponding displacement is 300 nm, well within the stability criterion before pull-in occurs at one-third of the initial vertical gap (2 μm dictated by the thickness of the BOX). This remarkably low actuation voltage is a significant improvement over the comb-drive actuator-based designs of the previous chapter despite having to travel a greater distance.

The standard optical microscopy (**Figure 6.3a**) following the MEMS post-processing indicates
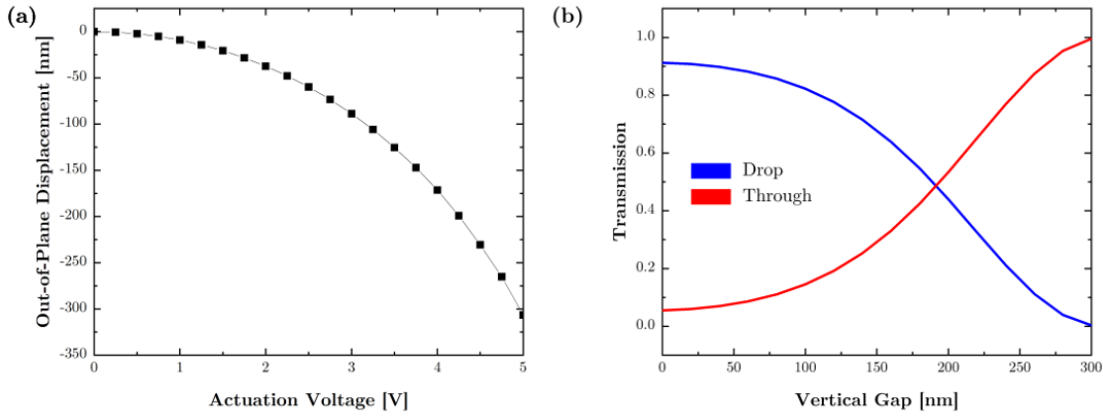
Figure 6.2 – (a) FEM simulation results on the actuation characteristics of the vertically movable device (b) FDTD-simulated power transmission v. vertical gap characteristic of the tunable directional coupler designed in Chapter 5. Presented here is a close-up view on the displacement range of interest, indicating that the full transfer of power occurs at 300 nm of vertical displacement and that this can be achieved, according to (a) at roughly 5 V of actuation voltage

that no serious particulate contamination or readily observed mechanical failure (e.g,. anchor collapse or stiction of waveguides to the substrate) has occurred and that the device is ready for characterization. A tilted-view SEM recording of the device (**Figure 6.3b**) reveals how accurately the drawn design is replicated in the foundry and how the MEMS release process produces cleanly suspended structure. It is not visible whether the stiff couplers exhibit the same characteristic, but it appears as though that the movable waveguide in the directional coupler is slightly misaligned out-of-plane with respect to the fixed one. This situation, however, is not serious as the waveguides can be brought back into alignment as the movable waveguide is pulled down by the electrostatic force once the actuation voltage is applied. All optical I/O ports have been labeled and the edges of the alumina passivation on the silicon rim are clearly defined.

Measurement of this device follows the same procedure as that used for in-plane actuated devices. Performing a wavelength sweep reveals the spectral behavior of the device for a particular actuation voltage and this process is repeated until the device reaches its maximum ER, which serves as an indicator of the port isolation between "Drop" and "Through" ports, or how strong the switching effect is. As predicted by simulation, this vertically actuated device achieves maximum port isolation in the switched state below 5 V, 3.75 V to be exact. The difference in actuation voltage can be attributed to the use of a single waveguide thickness (220 nm) for the entire structure instead of including the shallow-etched (150 nm) rib waveguides for the FEM simulation and a potential out-of-plane misalignment of the coupler after MEMS release. The first modification results in a slightly stiffer design, which increases the expected actuation voltage, and the second can lead to lower measured actuation voltages if the movable coupler arm is already slightly bent down towards the substrate in some regions along its length. This switching-state actuation voltage and the ER for both the OFF- and ON-states is
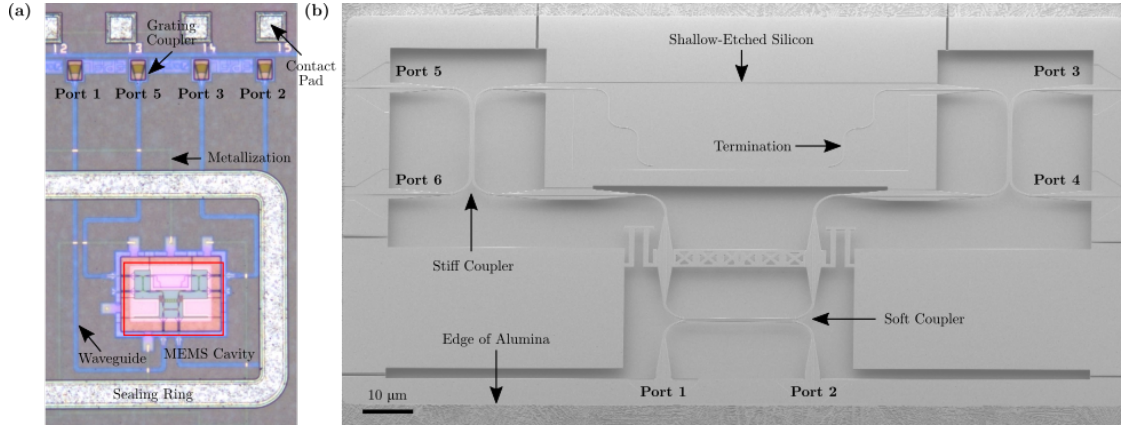
Figure 6.3 – (a) Optical microscope image of the released, vertically moving photonic MEMS switch. Note that ports 4 and 6 have been left unconnected; this is done intentionally because injecting light into these ports with the presence of termination structures would not produce meaningful or measurable behavior (b) Corresponding SEM recording of the device depicting the residue-free suspended structures

graphically depicted in **Figure 6.4** for the switching configuration in which light is injected into Port 1, so that the "Drop" port is Port 3 and the "Through" port is Port 2.
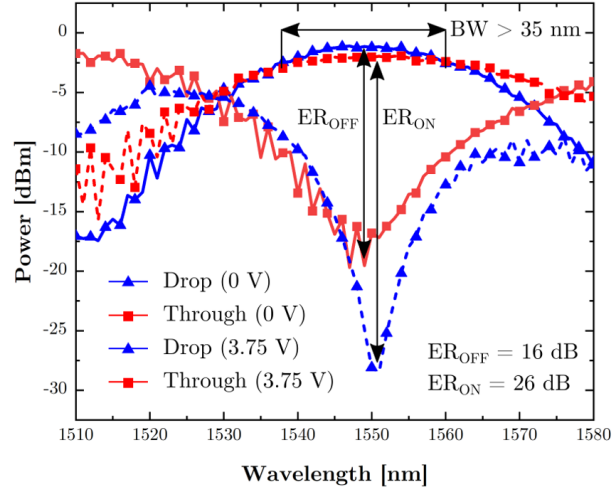

Figure 6.4 – Spectral characterization of the device for an input power of 0 dBm indicating a 16 dB ER in the OFF-state and a 26 dB in the ON-state. The device is also observed to be reasonably broadband with an optical 3-dB bandwidth > 35 nm and exhibits an IL < 2 dB

The central wavelength of the device is 1550 nm, which corresponds well with the simulated value of the directional coupler design. Additionally, the broadband behavior of this device can also be attributed to the optical design, where tapering of the waveguides in the coupling region, mimics an adiabatic transition, thereby reducing wavelength-sensitivity. Although the ERs between the OFF- and ON-state differ by 7 dB, this behavior is not unexpected. In fact, by following the light path, one observes that for the OFF-state, light from Port 1 is coupled

across two directional couplers, both of which are engaged in the cross-state, before reaching output Port 3. Fabrication imperfections and residual stress potentially influence the gap spacing between waveguides in a way that allows light to leak to the "Through" ports. In the ON-state, light passes directly from the input at Port 1 to the "Through" port at Port 3 with minimal evanescent field interactions with the movable directional coupler arm because the latter has been spatially removed. Consequently, there is little to no leakage to the "Drop" port and the ON-state ER is larger.

Identifying the origins of the comparatively large IL, less than 2 B, but still greater than that observed for the in-plane moving tunable directional couplers, is not trivial. This excess loss includes the same contributions from optical transitions, propagation, bending, and scattering losses, and optical peripherals like grating couplers seen before. The additional directional coupler in the OFF-state path would suggest that the IL in this state would be larger than that in the ON-state, but this is not the case. This discrepancy suggests that something in the path of the "Through" port in the fixed directional coupler arm is sub-optimal. Whether it is a fabrication-induced imperfection that can be evaded by coupling to the movable arm in the OFF-state or whether the grating coupler at the output is damaged or obstructed would require additional investigation or a dedicated test structure in a future experiment.

In general, this device demonstrates that variation of the vertical gap separation in a tunable directional coupler can be used to implement a suitable switching mechanism in PICs. The device is reasonably compact (95 μm x 150 μm), the ER in the OFF- and ON-states of 16 dB and 26 dB are suitably high, and the transition between the two states is achieved with very low voltage (< 4 V). Broadband behavior (> 35 nm BW) is attributed to the optical design of the directional coupler and although the IL is larger than desired, it does not appear to be fundamentally connected to the design. With regard to the asymmetry of ER in the OFF- and ON-states, one could imagine replacing the two stiff, fixed couplers with soft, movable couplers. Doing so enables additional tuning at the output ports to reduce leakage in the "Through" ports. Additionally, by making these couplers movable, one enables additional port-connectivity, i.e., in the current design, because light is always transferred between the fixed couplers, it is not possible to efficiently transfer light between Ports 3 and 4, and Ports 5 and 6. If these couplers are displaced downward, these connections are made possible. This approach of course hinges on the assumption that any sources of misalignment in the coupler arms is uniform and can be resolved with a single actuation voltage. Another design modification worth considering is adding a fourth vertically tunable directional coupler pair at the top of the device to make use of Ports 4 and 6, which currently end in terminations and are effectively non-functional.

Having presented a switch that doubles the number of I/O port connections, the next section presents a device that reduces the number of switching connections to two, but is more broadband and much smaller.

6.2 Broadband Compact Singe-Pole Double-Throw Silicon Photonic MEMS Switch

Drawing inspiration from the field of electronics, the photonic switch presented in this section is the optical analog of the electrical single-pole double-throw (SPDT) switch. The name "single-pole double-throw" indicates that a single input, i.e., the pole, can be directed to one of two outputs, the throws. For top-of-rack optical switch boxes handling data rates on the order of 400-GB/s per link, the switches must not only be small and power-thrifty, but they should also be fast [155]. Furthermore, in order to preserve data integrity and avoid logistically and financially expensive amplification, the switches must exhibit high port isolation (large ER) and low IL, respectively. The work reported in this section has been published partly in [92].

The schematic view of this Silicon Photonic SPDT is provided in **Figure 6.5a** alongside its 3D perspective counterpart in **Figure 6.5b**. Key features include the single-sided suspended input waveguide, which is free to move in-plane and the two single-sided suspended, but fixed output waveguides. The middle region of the input waveguide has a rib section, at the edges of which are a pair of raised shuttle "wings." Also included is a pair of stoppers limiting the maximum displacement of the waveguide. **Table 6.2** provides the corresponding values for all parameters indicated in **Figure 6.5a** and the device has an overall footprint of 65 µm by 62 µm.
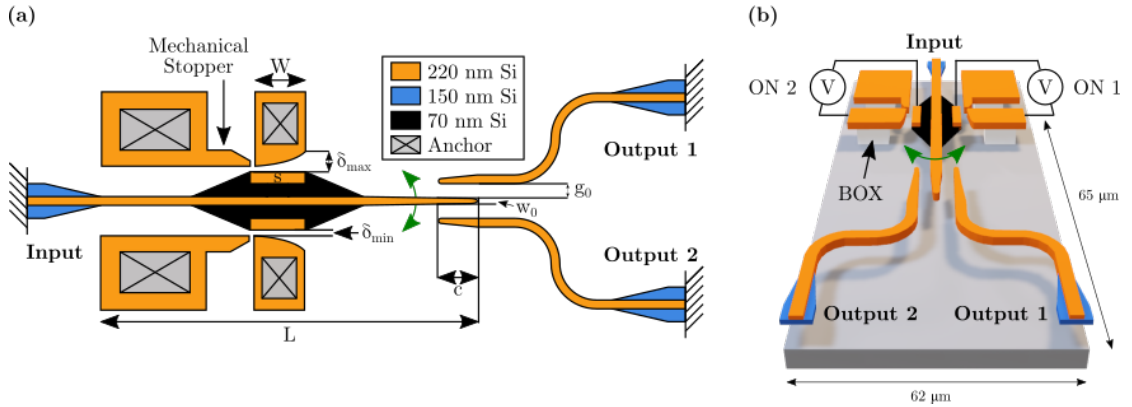

Figure 6.5 – (a) Schematic diagram of the SPDT photonic MEMS switch showing the various components of the device, the input waveguide, two output waveguides, two electrodes, and stoppers. Key geometric parameters are also indicated and summarized in **Table 6.2** (b) 3D perspective view showing how the actuation voltage can be applied either between electrode 1 and the shuttle wing or between electrode 2 and the shuttle wing

Using **Figure 6.5** as reference, the operating principle of the device is outlined as follows:

- The input is a single-sided suspended strip waveguide, fixed at one end, which gradually transitions into a rib waveguide and then back into a strip waveguide at its free end; in this sense, it is an in-plane cantilever-like structure

- In the region of the rib waveguide, a pair of raised shuttle "wings" are placed at the edges;

Symbol	Quantity	Value
g_0	Initial coupling gap	400 nm
w_0	Waveguide width	450 nm
C	Coupling length	2.7 µm
W	Electrode width	5 µm
δ_{max}	Maximum electrode-shuttle distance	700 nm
δ_{min}	Minimum electrode-shuttle distance	200 nm
s	Shuttle wing length	5.8 µm
z	Length of input waveguide	23.4 µm

Table 6.2 – SPDT Photonic MEMS Switch Parameters

these structures serve as the counter-electrodes to a pair of fixed, curved electrodes on either side

- Flanking both sides of the free end of the input waveguide and separated by a well-defined initial gap spacing (g_0), are two single-sided suspended output waveguides

- By grounding the input waveguide and applying a voltage to one of the fixed electrodes (e.g., electrode 1), an attractive electrostatic force develops between the raised shuttle wings and the electrode, pulling the waveguide preferentially up towards output 1

- Displacing the input waveguide towards electrode 1 correspondingly decreases the waveguide gap separation to output 1's waveguide

- A smaller gap separation means injected light in the input waveguide has a stronger evanescent field interaction with the waveguide of output 1 than that of output 2, meaning light is preferentially coupled to this branch; this behavior corresponds to the ON1 state

- If the actuation voltage is instead applied to electrode 2, the input waveguide is pulled towards the waveguide of output 2 and light is shuttled to this port, resulting in the ON2 state

- When no actuation voltage is applied, the input waveguide should be perfectly centered (i.e., equal gap separation) between the two output waveguides so that only equal amounts of residual light are coupled to the two output branches; this is referred to as the IDLE state

- The mechanical stoppers limit the maximum displacement of the input waveguide to the point when the gap separation is effectively zero so that it does not continue to push against the active output waveguide, therein presenting the risk of bending or deformation

The behavior described above is substantiated by the optical simulations presented in **Figure 6.6**, which visually confirm the distribution of optical power between input and output waveguides. **Figure 6.6a** depicts the IDLE state where only a negligible amount of residual power couples to the two outputs and **Figure 6.6b** depicts the ON1 state where all the optical power is switched to output 1.
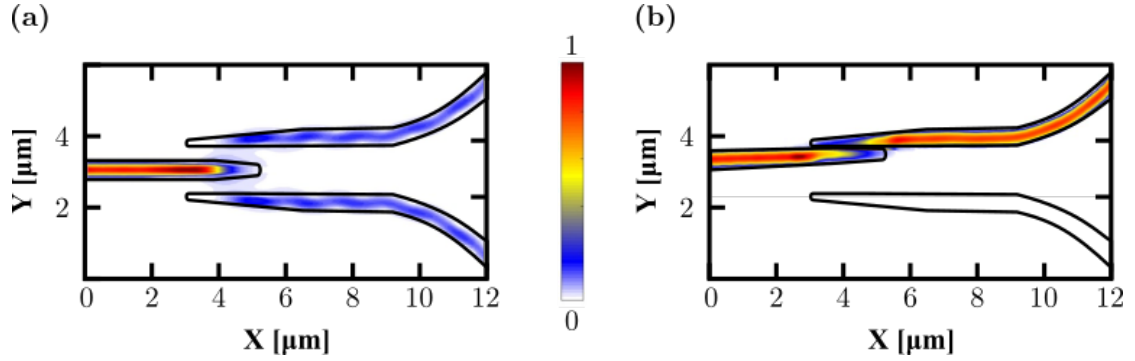

Figure 6.6 – Simulation of the optical power distribution between input and output waveguides for the (a) IDLE and (b) ON1 state. In the former, because the input waveguide rests evenly between the two output waveguides with gap spacing g = 400 nm, little optical power is recorded at the outputs. In the latter case, the input waveguide has been displaced completely towards output 1, so that the gap spacing is effectively 0 and all the power is routed here

As this device does not employ the standard tunable directional coupler design used in all other previously demonstrated devices, a brief explanation of the optical design is needed. The principles of MEMS-based optical modulation discussed in Chapter 3 indicate that the amount of cross-coupled power in a directional coupler through evanescent field interaction is primarily a function of the gap separation or amount of overlap length in the coupling region. Nowhere was it imposed that the input-output relationship must take on a 2 x 2 configuration. Thus, it is possible to utilize the same guiding principles for the optical design of this device as was used previously.

In particular, because the switch is designed for single-mode operation in the C-band using IMEC's iSiPP50G PDK, the cross-sectional dimensions in the coupling region are more or less fixed to a 220 nm thickness and 450 nm width. This combination enables low-loss propagation of light, and while strip waveguides are used in the coupling region, the portion of the input waveguide between the electrodes is a rib configuration (70 nm thick Si). Using a wider waveguide topology to create a shuttle allows the raised, full thickness silicon (220 nm) needed to maximize the effective area for the electrostatic force, to be placed at the edges of the wings. This approach optically isolates the light-carrying region in the center from the electric effects needed for actuation. However, in order to minimize the transition losses associated with going from a strip waveguide to a rib waveguide, the shuttle is gradually tapered to the desired width. Regarding the shape of the input and output waveguides in the coupling region, the waveguide width is tapered down from 450 nm to 200 nm to allow for short coupling lengths and to decrease the coupling wavelength sensitivity (i.e., to improve the optical bandwidth).

Although the optical coupling mechanism is dictated by evanescent field interactions, the exact relationship for this non-standard and somewhat complex geometry is not easily described by simple analytical models. Consequently, it is more time-efficient to use numerical simulation of coupled waveguide modes in 3D FDTD software to extract the coupling dependence on gap separation. Although brute force methods of exhaustively exploring the entire parameter space is possible, in order to efficiently converge to an optimal geometry, a proper design methodology is required.

Optical design begins with simulating an ON state that provides maximum coupling to one output with minimal losses. Strong optical coupling can be achieved using a standard geometry employing two long (> 5 μm), 450 nm wide, 220 nm thick, rectangular slab waveguides that are close to one another (e.g., $g_0 \approx 0$ nm). However, the abrupt termination at the tip of such a generic topology introduces excess losses and neither the bandwidth nor the length are optimized. A solution to reduce losses and broaden the bandwidth is to round the tip and introduce adiabatic tapering on both sides of the input waveguide such that its width decreases from $w_0 = 450$ nm to 200 nm, while keeping the inner edges of the output waveguide straight. This modification provides a smooth transition in geometry-induced effective refractive index to reduce losses and also decreases wavelength-sensitivity. In order to obtain symmetric behavior in the output waveguides, the tips are also rounded and the outer edges are tapered such that their width increases from 200 nm to 450 nm. Now, along the coupling region, the input waveguide gradually decreases in width while the output waveguides gradually becomes wider and the result is a strong coupling with a smooth transition until the termination of the input waveguide. The length over which this tapering occurs is also the coupling length, and this distance can be adjusted to match a single beat-length for full power transmission. If the coupling length is made longer or shorter, less power is transferred, which translates to a reduction in the ER. Finally, the gap between input and output waveguides at the beginning of the coupling/tapered region where $w_0 = 450nm$ is increased to ensure an IDLE state with < -5 dB transmission to either outputs.

Using this sequential approach, one obtains the finalized geometry outlined in **Figure 6.5** and parameterized in **Table 6.2**. **Figure 6.7a** illustrates the simulated power distribution between output ports as a function of the tip displacement from the initial gap position for the ON1 state in which the actuation voltage is applied to electrode 1. As can be evinced, equal power to the outputs is transmitted for zero tip displacement and when the tip is displaced 400 nm (i.e., $g = 0$ nm) for the ON1 state, all the power is transferred to output 1 because of the enhanced coupling. The complementary gap between input waveguide and that of output 2 simultaneously increases by 400 nm leading to weaker coupling in this branch and a transmitted power in output 2 that is effectively zero.

Optical simulation of the spectral behavior of this device in the IDLE and ON1 states confirms the broadband characteristics related to the adiabatic tapering of the waveguides. The relative absence of wavelength-dependence on the output characteristics is presented in **Figure 6.7b**.
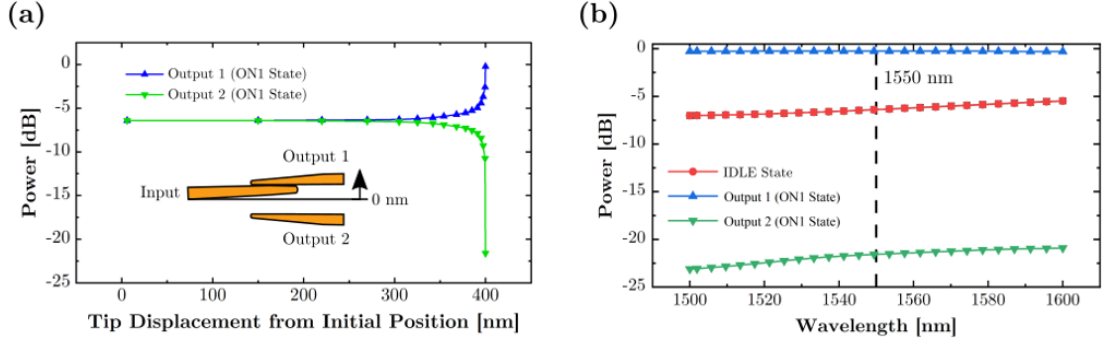
Figure 6.7 – (a) Simulated power transmission in the output waveguides as a function of the tip displacement for the case in which voltage is applied to electrode 1 and the displacement goes from zero ($g = g_0 = 400$ nm) in the IDLE state to 400 nm ($g = 0$ nm) in the ON1 state. Here, power is completely transferred to output 1 and at the same time, because the gap between input waveguide and that of output 2 has increased by 400 nm, there is negligible power coupling to this second output (b) Simulation of the spectral characteristics of the SPDT photonic switch for the ON1 state. The relatively flat response over the entire wavelength range indicates a broadband characteristic

With the optical design of the device fixed, the next task is to determine a suitable electrostatic actuator with mechanical suspension capable of displacing the input waveguide 400 nm to obtain full optical power transfer. As was the case for the in-plane tunable directional couplers, consideration for the driver electronics design imposes an upperbound on the maximum actuation voltage of 25 V. The next step is to establish the boundaries of the initial design parameter space by using simplified analytical models coupling the electrical and mechanical behavior to displacements. Like comb-drive actuators, which have a set of well-established analytical equations, there are a corresponding set of relations for parallel-plate electrostatic actuators. Because the raised wings of the shuttle, the corresponding surface of the electrode, and the air gap between them constitutes a parallel-plate capacitor of sorts, this simplified model is a good starting point for the electromechanical design.

In addition to the actuation voltage, the simplest parallel plate electrostatic actuator model consists of three key design parameters, the initial gap distance, d_0, the spring constant of the suspension, k, and the electrode area A. The device demonstrated here operates in the pull-in mode wherein a force imbalance between the attractive electrostatic force pulling the input waveguide to the electrode and the restoring mechanical force of the waveguide itself (i.e., the suspension) causes the waveguide to rapidly "snap" to an output. This behavior occurs at roughly one-third the initial gap spacing and results in a sudden decrease in gap separation between waveguides that enhances coupling. Ignoring fringing fields and employing a 1D electric field distribution, one can derive an expression for the pull-in voltage, for which this phenomenon occurs.

$$V_{pull-in} = \sqrt{\frac{8kd_0^3}{27\epsilon_0 A}} \qquad (6.1)$$

119

Because the input waveguide is a cantilever-like structure, it exhibits a lever effect, where for a particular electrostatic force, a point at the tip of the input waveguide is displaced more than a point near the shuttle. What this means is that if the start of the coupling region in the input waveguide, which has a initial gap separation g_0 from either output waveguide, must be displaced 400 nm to achieve full power switching, a point closer to the axis of rotation (i.e., the anchor of the optical transition) need not travel as far. Quantitatively, the farthest edge of the counter-electrode on the shuttle is 13 µm from the axis of rotation whereas the beginning of the coupling region is 20 µm away. Using similar triangles, one can determine that if the start of the coupling region must be displaced 400 nm, the counter-electrode must only be displaced 260 nm. This value of 260 nm is then the initial gap distance, d_0.

With this in mind, one can begin exploring different electrode areas A and the geometry of the input waveguide itself, which will determine the spring constant of the suspension, k. Together, with the now "fixed" initial gap distance, these parameters determine the pull-in voltage and it is this value that will undergo optimization. One would like the smallest pull-in voltage possible subject to the constraints of fabrication limits and the desire for a compact footprint. For a clamped-free, transversely loaded beam of rectangular cross-section (220 nm x 450 nm), Equation 6.1 predicts a pull-in voltage of 34.3 V for a 13 µm beam.

This first calculation does not bode well for the 25 V upper limit set for the maximum actuation voltage. And the situation looks less promising when one recognizes that the parallel plate model in fact underestimates the pull-in voltage because by construction, the model decouples the geometries of the mechanical portion, the spring, and the electrical portion, the capacitor. A more refined analysis of the device models the device as it is, a cantilever-electrode arrangement, where the geometry of the cantilever defines both the electrical and mechanical behavior. The distributed electrostatic force acting on the raised wings of the shuttle can be represented as a net bending moment applied at the cantilever tip rather than the less accurate transverse point load, or the deflection of the beam can be derived using the derivative of the system capacitance function [156]. Unfortunately, but not unexpectedly, both more refined models predict a pull-in voltage at a slightly larger gap.

While it would seem as though the actuator design must be completely overhauled, this is not necessary. The design efforts up to this point have been focused on the movable input waveguide, when in fact, one has one more degree of freedom, the fixed electrode. **Figure 6.8** indicates that the fixed electrode can either be flat or it can be curved, and this subtle difference endows the second geometry with a large advantage.

For a flat electrode, the electrostatic force is initially constant along the length of the movable structure and at one third of the initial spacing δ_0, pull-in occurs. For a curved electrode, the situation is slightly different in that the electrostatic force is strongest at one end where the gap is smallest (δ_0) and gradually decreases with increasing gap. What this means is that the electrostatic force is not constant: it is initially stronger at one end and as the movable structure is pulled towards the electrode to decrease the gap, the force becomes noticeable
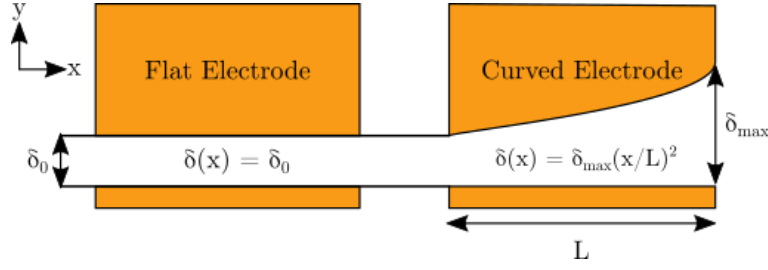
Figure 6.8 – Comparison between a standard, flat electrode geometry and a curved electrode geometry. In the flat configuration, the initial gap separation is maintained between the electrode and movable structure, whereas in the curved topology, the gap exhibits a gradual increase from left to right

over a greater length [157]. Consequently, pull-in occurs first at one end, at one third of δ_0, and only after some additional displacement at the other end, at one third of $\delta_{max} > \delta_0$. Thus, with a curved electrode δ_0 need not be equal to the desired displacement, it can be smaller. For the proposed design, this means that δ_0 can be made smaller than 260 nm, e.g., the 200 nm minimum feature size that is safe against silicon- and alumina-bridging. Using the basic formulation of Equation 6.1, one now predicts a pull-in voltage of 23.2 V, which is now within specifications. As such, the curved electrode provides a better performance when it comes to pull-in characteristics compared to the standard flat electrode.

Figure 6.8 indicates that the curvature of the electrode as a function of position along the movable structure is defined by the order of the polynomial (n = 2 for this design). Modifying this value enables tuning of the displacement sensitivity with respect to voltage. A second order polynomial yields a device that can be used as a digital switch with abrupt transitions, while higher order polynomials provide a more gradual transition suitable for continuous modulation of optical power transmission [157].

The proposed device is not an idealized cantilever of uniform rectangular cross-section, nor does the distributed load from the electrostatic force act along the entire length. Instead, the initial strip waveguide expands into a rib waveguide with raised wings, where the electrostatic force is applied, and then it tapers down again to a strip waveguide. Because the final structure has a composite cross-section consisting of several discrete and unique cross-sections and the position-dependent force is only applied over a portion of the moveable structure, one ends up with the following form of the Euler-Bernoulli equation:

$$\frac{d^4 w}{dx^3} = \frac{q(x)}{EI(x)} \tag{6.2}$$

Where w is the displacement, x is the position along the length of the movable structure, $q(x)$ is the position-dependent load, E is the Young's modulus of the material, and $I(x)$ is the the area moment of inertia, which depends on the position along the movable structure.

A full closed-form solution to Equation 6.2 for the presented geometry becomes computation-

ally untenable and it is more efficient to segment the structure into smaller slices to which Equation 6.2 can be applied. Because this is precisely the motivation behind the finite element method (FEM), the device is simulated using FEM software (COMSOL), where the applied voltage in a particular geometry is increased until the simulation fails to converge. This non-convergence signifies pull-in and it can then be verified whether the desired 400 nm of displacement at the tip of the input waveguide has occurred for an actuation voltage below 25 V. The results of these simulations are presented in **Figure 6.9** which shows the displacement along the length of the input waveguide for gradually increasing actuation voltages.
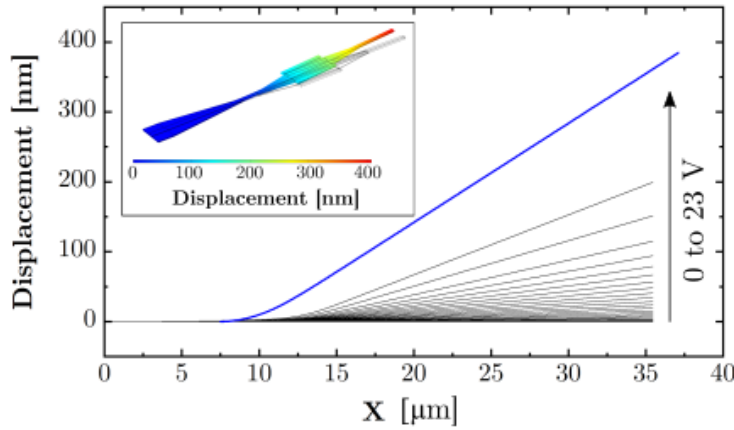

Figure 6.9 – FEM electromechanical simulation result indicating the displacement as a function of distance along the input waveguide for actuation voltages ranging from 0 to 23 V

Having confirmed that the 400 nm of displacement should be achievable below 25 V of actuation voltage with this particular geometry, the design is sent for fabrication at IMEC and returns to EPFL for the MEMS release process at CMi. The optical microscope image of **Figure 6.10a** and SEM recording in **Figure 6.10b** confirm that the release process was a success and that all components are fully suspended. The curved electrodes and mechanical stoppers are nicely defined and the input waveguide appears to be well centered between the two output waveguides as desired for the IDLE state.

Different from the characterization approach used for the other MEMS-enabled photonic devices of this work, functionality of the SPDT photonic MEMS switch is demonstrated by first tuning the laser to an input wavelength of 1550 nm and observing the power transmission in each output as a function of actuation voltage. The waveguide gap spacing should decrease with increasing actuation voltage for the active output and this should be reflected in an increase in power transmission. **Figure 6.11a** confirms this behavior as can be seen in the increase in power to output 1 and corresponding decrease in power to output 2 for the ON1 state. Similar behavior with the ports reversed is observed for the ON2 state as well. The ON1 state is fully achieved at roughly 22 V and the corresponding ER between output 1 and output 2 is approximately 25 dB. By applying this same 22 V to electrode 2, one achieves the ON2 state which has a symmetric ER.
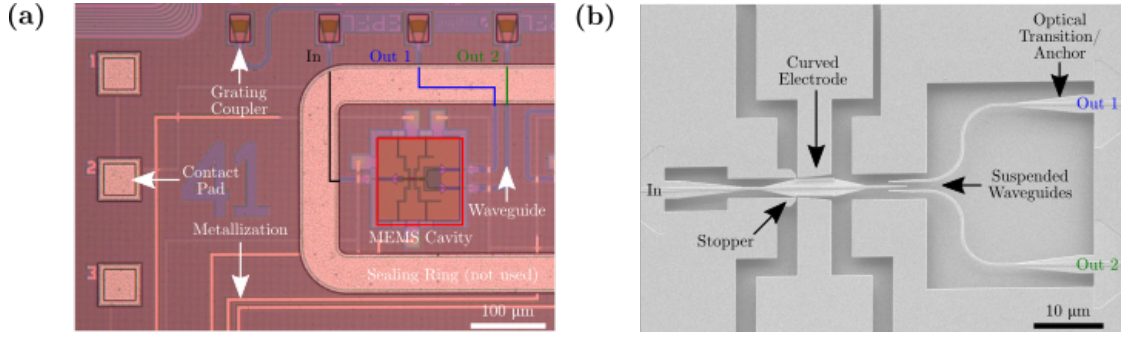
Figure 6.10 – (a) Optical microscope image of the release SPDT photonic MEMS switch with metallization, waveguide routing, and the corresponding electrical and optical I/O structures (b) SEM recording indicating well-suspended and well-aligned structures
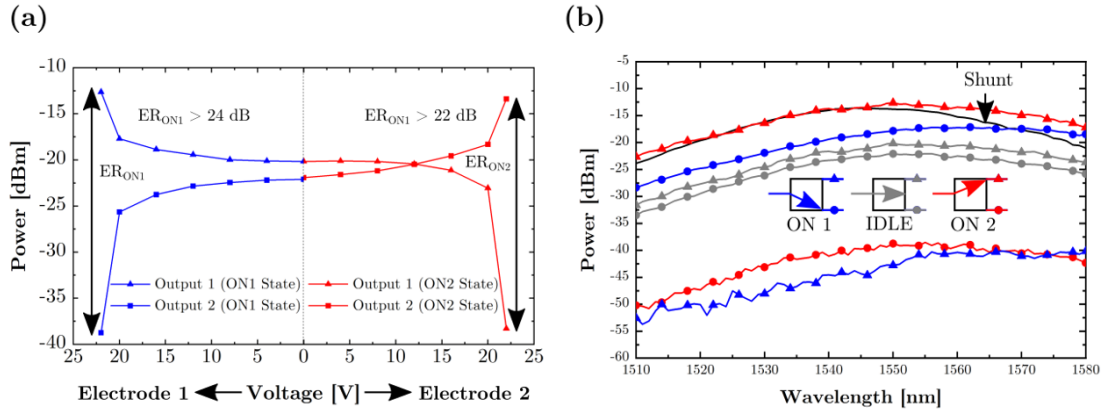

Figure 6.11 – (a) DC voltage sweep presenting the optical power to each output as a function of the actuation voltage for a wavelength of 1550 nm and 0 dBm input power. The blue curves indicate the ON1 state when the actuation voltage is applied to electrode 1 and the red curves correspond to the ON2 state when electrode 2 is active. ERs > 24 dB and > 22 dB for the ON1 and ON2 states, respectively, have been indicated (b) Spectral characteristics of the device for the ON1 and ON2 states showing how an ER > 23 dB is maintained over the full 70 nm wavelength range

One feature that is immediately obvious in **Figure 6.11a** is that when no voltage is applied to either electrode (the IDLE state), the observed power distribution is not symmetric as designed. Rather, the power transmission to output 1 is initially 3 dB larger than that for output 2 and the crossing point indicating a 0 dB difference in transmission is shifted to the right by approximately 12 V. This discrepancy between simulation and characterization can be attributed to a combination of the following:

1. Asymmetric relaxation of the mechanical boundary conditions of the anchored and free regions of the input waveguide during the VHF release, which can cause the input to bend preferentially toward output 1; such behavior has also been observed for the continuously tunable 2 x 2 directional couplers

2. Loss variation in the optical path between the two outputs originating from differences

in the optical transitions, grating couplers, and waveguide routing

Despite this non-ideality, the shift in a balanced zero-difference state can be compensated for by applying a systematic offset voltage. Additional comparison of **Figure 6.11a** with the simulation results in **Figure 6.7a** indicates a difference of roughly 12 dB in the maximum achievable power transmission. This offset comes from the fact that the losses in the passive devices are also included in the plot, i.e., the measurements are not normalized. The alignment procedure for the fiber array utilizes a shunt connection to determine the chip position with maximum power transmission. For the device under test, a different set of grating couplers is used to inject and sense light, but ideally, the measurements can be normalized to those of the initial shunt connection, thereby allowing the IL of the device to be extracted. However, deviation of the fiber cores from their ideal positions over the grating couplers leads to variation in coupling efficiency, peak wavelength, and symmetry in power transmission. There is already one contribution of error in the fiber-grating coupler pair used for alignment, and each subsequent pair between the ones used for alignment and those used for device I/O contributes additional errors. Because no means of isolating the misalignment error for each device is present, it is only possible to provide an estimate of the IL, which has been determined to be < 0.4 dB between 1520 nm and 1545 nm.

With the switching voltage identified, it is now possible to perform a wavelength sweep in the three states, ON1, IDLE, and ON2 to determine the spectral behavior. **Figure 6.11b** presents these results and indicates that an ER > 22 dB is maintained over the entire wavelength range. For the tunable coupler design, the 3-dB bandwidth of the device corresponds to the wavelength range over which the power transmission in the active output port stayed within 3 dB of its maximum value. Here, the bandwidth metric is determined slightly differently. In particular, because this device is intended to be used as a switch, it is important that the port isolation, or ER, be maintained for both ON states across a broad range of wavelengths. If there is dispersive behavior, as long as it is consistent between the two output ports, the strong switching behavior is maintained. Consequently, another look at **Figure 6.11b**, shows that an ER > 22 (smaller of the two ON states) is actually maintained over the full 70 nm sweep and this is the reported bandwidth of the device.

That being said, the dispersion characteristics of this device are slightly stronger in the measurements than those predicted by the FDTD simulation and this is attributed to variations in the grating couplers due to fabrication and misalignment. Despite the closest process control, each grating coupler exhibits its own peak transmission and dispersion characteristic, which is then superimposed on top of the device's nominally flat, but in reality wavelength-dependent, output characteristics.

The transient response of the switch is the final performance metric to be evaluated and is extracted using a rectangular pulse with an amplitude of 22 V as the actuation signal and converting the output optical signal to the electrical domain using a high-speed photodiode (PD). This signal is then fed to an oscilloscope, where it is possible to visualize the delay

between the triggered step in the actuation voltage and the optical response during switching. **Figure 6.11** presents the switching times from the IDLE state to the ON1 state and back to the IDLE state. The rise-time and fall-time are measured to be 822 ns and 736 ns, respectively, which is quite fast and the speed can be attributed to both the steep, non-linear behavior of the device in the pull-in regime and the low-resistance, doped silicon used for electrical contact. Stiffer geometries using a shorter input waveguide would have even faster switching times, but there would be a trade-off in larger pull-in voltage.
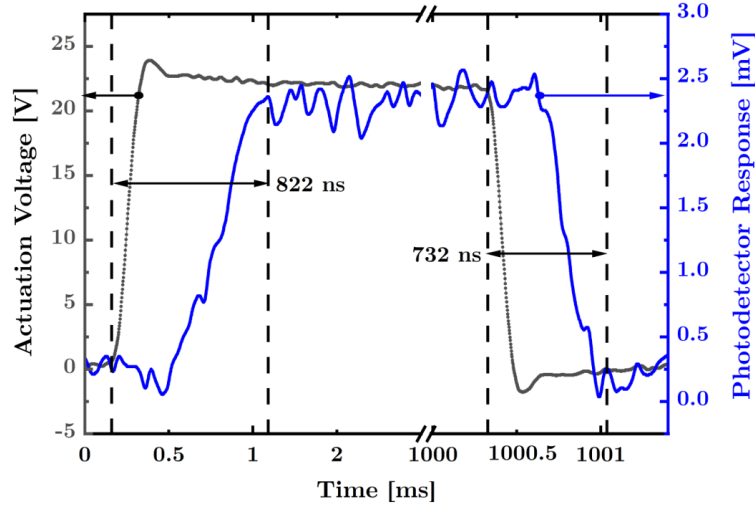

Figure 6.12 – Switching time measurement presenting the 22 V rectangular pulse applied to electrode 1 to trigger the ON1 state and the subsequent optical response, which is recorded as an electrical signal from the PD by the oscilloscope. 822 ns after the driving voltage goes high, the SPDT switch responds, and following a transition to a low state in the actuation voltage, the optical signal in the device follows 732 ns later

The combination of the SPDT topology and a curved electrode geometry is a novel approach for implementing switching with photonic MEMS, and the device demonstrates strong port isolation (ER > 22 dB) over a wide range of wavelengths (BW > 70 nm) and exhibits fast switching below 1 μfor an applied voltage of 23 V. Combined with a compact footprint of 65 μm x 62 μm, this optical performance make this device an attractive candidate for use in dense switch networks.

6.3   Final Remarks on Silicon Photonic MEMS Switches

The two devices presented in this chapter address the performance needs in large-scale photonic switching from two different approaches. By expanding the I/O port count from four to six and using a mechanically soft suspension for the optical component, the low-voltage (< 4 V), vertically actuated switch enables additional port configurations using low-voltages. In this manner, this switch takes on the role of a mini switching hub that can route additional I/O streams with near-negligible power consumption. As discussed previously, the device can be improved for better utilization of chip area, by replacing the terminations with an

additional directional coupler to increase the number of ports to eight, enabling a true 4 x 4 switching element. This modification would need to be implemented alongside a change in the "stiff" directional couplers to "soft" ones in order to enable additional control of the switching configurations.

On the other hand, the presented SPDT photonic switch, with its three ports in a 1 x 2 port configuration, focuses on the following performance metrics, a high ER, broadband behavior, and small footprint. With a nearly symmetric ER > 22 dB between output ports for both switching states that is maintained over 70 nm, this device fulfills the first two criteria. Its 65 µm x 62 µm footprint meet the third criterion for compactness and one can imagine connecting several of these 1 x 2 devices in series in a tree-like network to route a single input to 8 or more unique outputs. Like its vertically-actuated counterpart, the electrostatic actuator for the SPDT photonic switch is in fact quite small, and further reductions in the overall footprint can be achieved by reducing the anchoring and fixed electrode areas or integrating them with the silicon rim. One limitation associated with continued size-reduction of only the switches, though, is that eventually the electrical isolation and contact regions needed for actuation will be packed too closely to one another and may not offer sufficient clearance to the optical I/O. The electrical I/O must be scaled in parallel with the devices themselves in order to efficiently utilize space.

Although the SPDT photonic switch offers faster switching times than any of the demonstrated tunable power couplers, there is another MEMS-based actuation mechanism that can potentially improve upon this speed performance. Piezoelectric actuation in particular offers a fast, compact, and power-efficient approach to effecting the mechanical displacements needed for waveguide-gap modulation. The challenge here is the material compatibility of piezoelectric thin films with foundries for potential large-scale production in the future. If the electrical-mechanical-optical principle behind MEMS-enabled tuning can be demonstrated after a similar form of post-processing as that shown here, though, piezoelectric photonic switches would provide a robust addition to the portfolio of MEMS-enabled photonics and lend additional credibility to the efficacy of this modulation approach.

7 MEMS-Enabled Silicon Photonic Devices

Chapter 5 demonstrated electrostatic MEMS-enabled, continuous tunability of optical power transmission, which is the first milestone in realizing larger-scale PICs because it provides a power-efficient alternative to standard thermo-optic tuning. Not only can these MEMS tunable directional couplers finely adjust for the as-designed power distribution, but they are also strong enough to induce a full transfer of optical power between branches. Devices specifically designed for switching functionality, though, can be made to handle additional ports with low-voltage operation and extremely broadband and compact. This class of MEMS-enabled photonic switches can be used in lieu of lossier, albeit faster plasma dispersion-based switches and was the focus of Chapter 6.

The devices presented and described here represent other classes of specialized, higher-function building blocks. These additional MEMS-enabled Silicon Photonic devices can be integrated alongside the components demonstrated in this work to reduce the footprint of PICs while improving their optical performance.

7.1 Vertically Movable Add-Drop Filter

For most fields, the need to efficiently maximize usage of limited resources is a fundamental requirement for continued growth. In telecommunications systems, this resource is the transmission media (e.g., electrical wires/cables, antenna elements, and, waveguides) because it is not scalable to dedicate a separate medium for each network node. This desire to reduce redundancy led to the development of multiplexing schemes that combine multiple digital or analog data inputs into a single transmitted signal.

Examples include space-division multiplexing, where one uses separate physical elements for each transmission channel; time-division multiplexing, where segments of information are sent sequentially and distinguished by their temporal segregation; and frequency-division multiplexing, where information streams are separated by their transmission frequency. The optical analog of this last form of multiplexing is wavelength-division multiplexing (WDM) and

it is one of the key technologies/schemes enabling the exponential growth of data transmission today. In fact, WDM and now dense WDM (DWDM) is one of the reasons why the operational bandwidth of integrated photonic devices is important. The optical C-band (1530 nm to 1565 nm) is segmented into individual wavelengths separated by fixed spatial or temporal frequencies. Information sent in channels allocated to wavelengths at 1530 nm, for example, should be optically modulated in the same manner as those travelling in channels dedicated 1565 nm. Thus, a tunable coupler or switch that cannot provide a bandwidth over > 30 nm is bandwidth-limited and not an ideal candidate for use in a large-scale circuit.

Being able to transmit and switch/tune a wide range of signals in a PIC is a good basis. However, sometimes it is also necessary to manipulate the information en route with a fine degree of granularity. A concrete example would be a wavelength-selective switch that can remove a single channel from the composite signal travelling in a WDM system and route it elsewhere. Likewise, perhaps one would later like to add back in this channel with different information. Such functionality can be implemented by an add-drop filter, which as its name suggests, filters or selects a particular wavelength that should be added or dropped (i.e., removed) from a transmitted spectrum. One commonly utilized topology of the add-drop filter employs micro-ring resonators (RR) because of their ability to precisely and efficiently isolate individual wavelengths thanks to their resonant-mode operation. These devices also have relatively small footprints, making them suitable for large-scale integration.

Given a broadband input signal travelling in the input bus waveguide of a RR, only wavelengths satisfying the resonance condition of the RR will be coupled to the structure:

$$m\lambda_m = 2\pi r n_{eff} \tag{7.1}$$

Where λ_m is the mth resonant mode of the structure, r is the radius of the RR, and n_{eff} is the effective refractive index of the guided mode.

For a fixed r and n_{eff}, one observes the higher-order modes $m > 1$ at evenly spaced intervals in the wavelength. This interval is known as the free spectral range (FSR) and is given by

$$FSR = \frac{\lambda^2}{n_g L} \tag{7.2}$$

Where λ is the wavelength under consideration, n_g is the group index, and L is the roundtrip length of the cavity.

By adding a second bus waveguide next to the RR, one can then extract this wavelength to route it elsewhere; this is the "drop" operation. One can reverse the direction of this process by injecting light at the resonant wavelength from the second bus waveguide to "add" information to the composite signal travelling down the input bus waveguide. Thus, the RR add-drop filter

offers one method of providing the desired wavelength-selectivity. The next step is to provide wavelength tunability, as it is not viable to create a separate device for every wavelength that will be used.

Consequently, a large selection of tunable RRs have been developed for use in integration of large-scale WDM and DWDM systems. For the fundamental mode $m = 1$, Equation 7.1 indicates that there are two primary means of tuning the resonant wavelength λ_1:

1. Modify the physical radius of the RR, r

2. Modify the effective refractive index, n_{eff} through thermal, electrical, or mechanical means

Modifying the radius of a RR can be accomplished using pure mechanical deformation. In one demonstration, this approach involved the contraction of a SiN RR using a piezoelectric thin film, which effected a blue-shift in the resonant wavelength by 412 pm for 16 V of applied voltage [116]. Furthermore, because of the piezoelectric nature of this mechanism, the power consumption can be made quite low.

As was the case for tunable directional couplers and photonic switches, using the thermo-optic effect to modify n_{eff} is a commonly employed technique. Here, the change in n_{eff} shifts the resonance frequency and previously demonstrated works have achieved relatively large shifts, up to a full FSR (19 nm) using 27 mW of power [158]. Although the resonance shift is significant, this amount of power consumption is also quite large, especially when one considers that this was for a single device. Additional considerations prohibiting the widespread use of such a tuning mechanism is the risk of thermal crosstalk between neighboring devices.

Tuning of the resonance frequency through modification of n_{eff} has also been demonstrated using the plasma-dispersion (free-carrier injection) effect. One particular example showed a 1 nm shift in the resonance frequency with nanosecond responsivity, but a 4.7 dB optical IL for a single element [159]. Although the magnitude of the shift could be larger, the speed and power-efficiency of this approach exceed that of thermo-optic tuning. However, as is the case for plasma-dispersion based tunable couplers and switches, the limiting factor when it comes to scaling are the inherently higher losses due to photon-carrier scattering.

A resonance tuning approach that provides a similarly fast response time without the associated optical losses found in plasma-dispersion tuning is through the use of electrooptic (EO) materials. One demonstration presented resonance shifters over 0.1 nm with 9 V of applied voltage and a response time on the order of tens of picoseconds [160]. Here the disadvantage is related to the use of a pure lithium niobate material platform, which is notoriously difficult to process (e.g., dry etching does not work well and produces waveguides with high optical loss) .

The final approach, and the one utilized in the device presented here, is MEMS-based tuning.

As seen before, the physical mechanism produces strong optical effects and when combined with an electrostatic actuator can be made both power-efficient and compact. Losses are primarily limited to the alignment of waveguide structures and the quality of the processing, which can be optimized. A common approach towards mechanically modification of n_{eff} is to displace an initially air-clad RR with respect to a slab material, or vice versa. The presence of an absorptive slab media within the proximity of the resonant mode leads to a leak in optical power and an increase in the effective refractive index. The increase in n_{eff} induces a red-shift, or increase in the resonance frequency. If on the other hand, the RR is initially aligned with a slab material, and the two are brought out of alignment, the effective refractive index decreases, and the result is a blue-shift, or decrease in the resonance frequency.

An example where the RR is displaced with respect to an absorptive silicon rim achieved a 0.52 nm shift for 100 nW of power consumption [115]. The displacement of slab material on the other hand, e.g., a MEMS cantilever suspended above a RR, presumably produces a weaker effect, as one demonstration reported tuning of only 0.12 pm **??**. A third MEMS-based approach, not relying on the displacement of RR or slab material to change n_{eff}, but rather a displacement of the internal RR structure to increase the roundtrip length of the cavity, L, showed an impressive 10 nm of tuning [161].

The device presented here consists of a conventional racetrack RR architecture where the RR is initially well-aligned and coupled to two bus waveguides, yielding four ports, "In", "Through", "Drop" and "Add". A schematic diagram of the device is presented in **Figure 7.1a** and shows the resonant-mode operation of the device when the RR is initially well aligned with respect to the two fixed bus waveguides. The 3D perspective view in **Figure 7.1b** shows that the device is relatively compact with footprint of 45 μm x 75 μm.
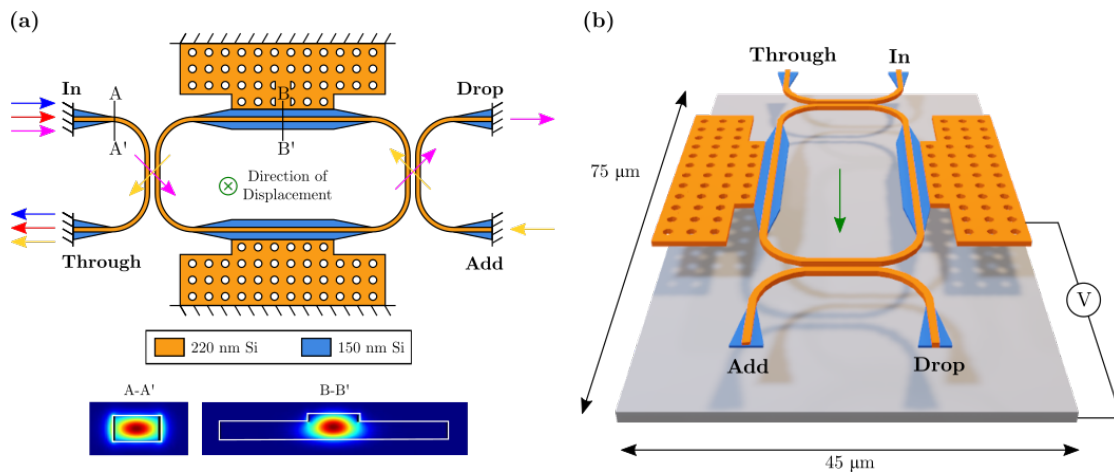

Figure 7.1 – (a) Schematic diagram of the MEMS-tunable add-drop filter indicating the optical I/O ports and the resonant-mode operation, which is illustrated by the cross-coupling of yellow and pink arrows into/out of the RR. Also shown are the cross-sectional electric field profiles within the strip (A-A') and rib (B-B') waveguides (b) 3D Schematic diagram indicating out of plane displacement of the RR with respect to the fixed bus waveguides to

Light of blue, red, and pink wavelengths enter from the "In" port. The pink wavelength, which satisfies the resonance condition of the RR then couples into the RR, circulates, and then is coupled out at the second bus waveguide, where it is routed to the "Drop" port. Adding wavelengths operates in an analogous fashion with yellow wavelength light being injected from the "Add" port, coupling into the RR, and then coupling out to the "Through" port alongside the original red and blue wavelength light. Off-resonance wavelengths (i.e., blue and red light) do not couple strongly to the RR resonator and pass directly to the "Through" port.

The RR is anchored to the electrodes by shallow-etched silicon, which is a part of the rib waveguide structure used in this region of the device. When a voltage difference is applied between the electrodes and the substrate, the electrodes and connected RR are pulled downwards and the RR is brought out of alignment with the fixed bus waveguide, i.e., the vertical gap separation in the coupling region increases. Consequently, the coupling efficiency and fraction of power transmitted to the "Drop" port reduces. As an additional consequence of the reduced evanescent field interaction of the coupled mode with the bus waveguide, the effective refractive index of the coupled mode decreases.

Specific optical design features include the following:

- The 10 μm long suspended strip bus waveguide and 150 nm gap in the coupling region allows for overcoupling to the RR so that transmission to the drop port at the resonant wavelength can be tuned

- Use of straight rib waveguides to connect the RR to the electrodes at the wings isolates the rib core by keeping it at a safe distance from the actuator structure (see cross-sectional E-field profiles in **Figure 7.1**). This waveguide topology reduces propagation losses and has the added benefit of providing structural rigidity during actuation

- Tapered waveguide transitions into the electrode anchoring regions of the RR enable a smooth mode transition (i.e., low transition loss) without a penalty in device footprint

An estimate of the FSR for this RR structure can be obtained by modifying the standard form presented in Equation 7.1. In particular, because the proposed structure does not match the conventional, perfectly circular, strip waveguide topology, there is not one unique group index, n_g for the RR. Instead, one must obtain the group index in various sections, including the straight strip waveguide in the coupling regions, the strip waveguide bends, the tapered waveguide sections leading to the electrode anchoring region, and the rib waveguides. One must then multiply them by their corresponding lengths and add them together to obtain a new nL product. Thus, Equation 7.1 can be rewritten as follows for the presented geometry:

$$FSR = \frac{\lambda^2}{n_s L_s + n_b L_b + n_t L_t + n_r L_r} \tag{7.3}$$

Where the group index n and length L of each region has a subscript s, b, t, r referring to the strip, bend, taper, and rib, regions respectively.

Extraction of the group index for the given waveguide sections is performed using FDTD simulation and provides the values presented in **Table 7.1**. It should be noted that in the case of the waveguide taper, because the cross-sectional geometry evolves along its 5 µm length, the contribution to the denominator of Equation 7.3 is obtained by piecewise linear approximation of the group index obtained at 1 µm steps.

Parameter	n_s	n_b	n_t	n_r
Value	4.5272	4.5158	3.7073	3.7035

Table 7.1 – Extracted Group Indices of Vertically Movable RR

Combined with the corresponding lengths, L_s = 10 µm, L_b = 7.85 µm, n_t = 5 µm, and L_r = 20 µm yields an FSR of approximately 5.28 nm for λ = 1550 nm.

Simulation of this device begins in the optical domain where FDTD modeling allows for the extraction of the group indices presented in **Table 7.1** to calculate the expected FSR. Next, a light propagation simulation is performed for the initial, unactuated state where the RR is aligned with the two bus waveguides: here, the MEMS actuator is not active, but the filter is engaged. Because the focus of this device is on the filter behavior, this state is henceforth referred to as the Filter-ON state. It should be noted that due to the resonant-nature of the device, performing a full 3D FDTD simulation is neither time nor memory efficient and hence, a truncated simulation is performed. The consequence of this reduced simulation is uncertainty with regards to ER and the resonance bandwidth.

Simulation results for the spectral behavior in the Filter-ON state are presented in **Figure 7.2**. In the Transmission v. Wavelength plot, the resonance behavior is characterized by sharp dips in the "Through" port transmission at the resonant wavelengths and corresponding peaks in the "Drop" port transmission. From this plot one can also extract an FSR of approximately 5.2 nm, which is consistent with the analytical calculation of 5.28 nm. The same Filter-ON state behavior is visualized in the two figures depicting normalized power distribution in the add-drop RR: off-resonance wavelengths are preferentially sent to the "Through" port, while resonant wavelengths circulate with some portion getting sent to the "Drop" port.

It can be observed in **Figure 7.2** that the "Through" port does not exhibit near-unity transmission for the off-resonance wavelengths, and correspondingly, the peak transmission in the "Drop" port at resonance peaks at around 50% transmission. This behavior is a consequence of the overcoupled OFF state and the nature of the RR: both resonant and off-resonance wavelengths incompletely couple into the RR, but only the former persist, so the "Through" port exhibits a loss in transmission. The resonant wavelengths further decrease in power because the RR is also overcoupled to the second bus waveguide, and these wavelengths incompletely couple out to the "Drop" port.
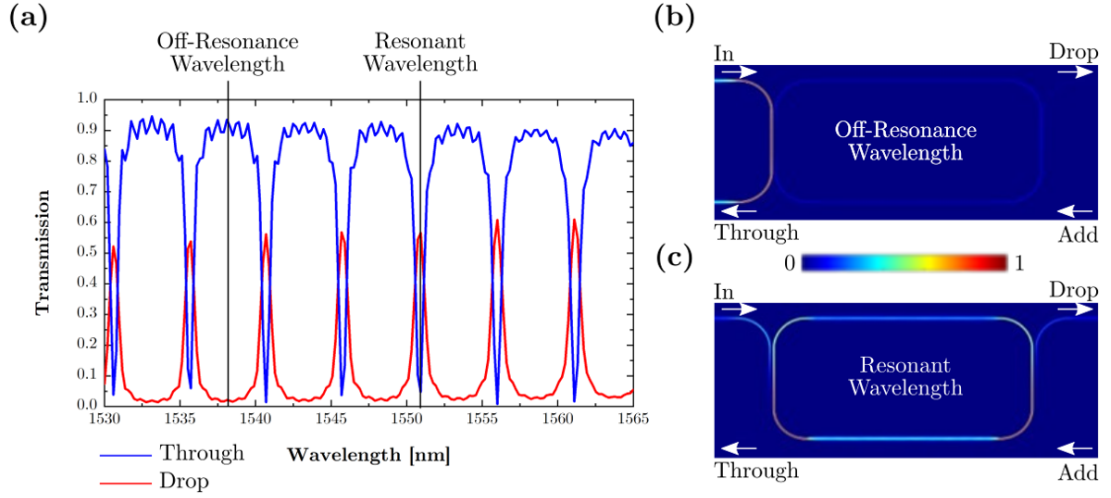
Figure 7.2 – (a) Simulation results depicting the spectral characteristics of the optical power transmission in the add-drop RR. Local minima and maxima in the "Through" and "Drop" ports, respectively, at the specific wavelengths reflect the expected resonant behavior. These extrema are supported by the two E-field plots on the right providing a color-coded visualization of the normalized power transmission in the structure for (b) off-resonance wavelengths and (c) resonant wavelengths

When an actuation voltage is applied to the electrodes, the RR is displaced downwards due to the attractive electrostatic force pulling the attached electrodes to the substrate. This action causes the device to become vertically misaligned with the bus guides, and with sufficient vertical displacement, ultimately results in an undercoupled state. Simulations indicate that at roughly 350 nm of vertical displacement, one has reached the Filter-OFF state, which is well within the stable operating region of this electrostatic actuator. Here, only residual optical power couples to the RR and from that meager amount, only a portion of the resonant wavelengths show up at the "Drop" port. By actuating the RR, one has effectively deactivated the "Drop" port and brought back the resonant wavelength to the "Through" port. As such, the behavior of this device can be summarized as an add-drop filter that functions as intended in the Filter-ON state and in the Filter-OFF state becomes an all-pass filter.

In the FEM electromechanical simulations, the actuation voltage applied to the electrodes is increased from 0 V until the 300 nm required for the Filter-OFF state of the device is reached. The vertical displacement of the ring is tracked as a function of this voltage to obtain an actuation curve. These results are shown in **Figure 7.3** with **Figure 7.3a** showing the deformation profile and **Figure 7.3b** providing the actuation curve.

It can be noted that deformation of the RR is not uniform and that the bends and thin straight portions in the coupling region bend down more than the other portions. This behavior can be explained by the RR geometry and its deformation during actuation. The RR consists of two electrodes, which by themselves constitute relatively stiff cantilevers; they are connected to one another by the rib waveguides and subsequently the 90° waveguide bends and straight sections in the coupling region to produce a closed ring. When these electrodes are pulled

to the substrate by the electrostatic force, they do not move down parallel to the substrate. Instead, they pivot around the anchor point located along the silicon rim, like a hinge, and the displacements at their "free" edges trace out circular arcs. However, because the electrode edges are not truly "free," but rather attached to the waveguide bends and straight waveguide sections, this motion produces tensile stress in the connecting regions. This tensile stress is released by an additional elongation/strain in the bends and straight regions down towards the substrate.
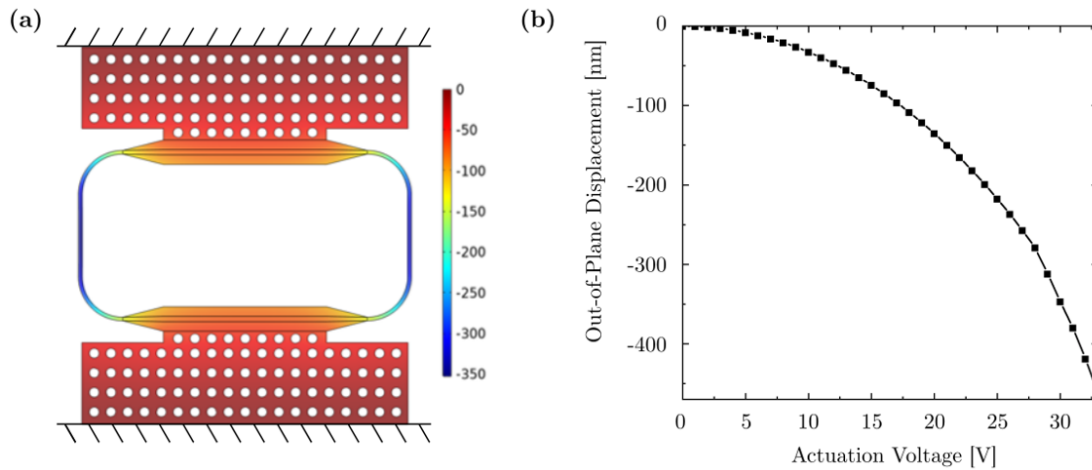

Figure 7.3 – (a) Visualization of the simulated out-of-plane deformation for the device at 30 V. Here, the coupling regions are displaced downward by roughly 350 nm (b) Actuation curve depicting out-of-plane displacement as a function of the actuation voltage. The required 350 nm of displacement is achieved at 30 V

Following MEMS post-processing and characterization, the devices are imaged using optical and SEM microscopy (**Figure 7.4**). Of noteworthy interest in the SEM recording of **Figure 7.4b** are the oxide pillars that remain and are visible below the rib-waveguides. Although the height of these pillars is not easily discernible from the image, their presence does not limit the displacement needed for the Filter-OFF state.

Optical characterization of this device begins with a coarse wavelength sweep over the entire operating range of the tunable laser to identify the location of resonance peaks and troughs. Next, a series of finer wavelength sweeps using intervals in the range of tens of picometers is carried out around these peaks to more clearly resolve the resonant behavior. One such sweep from 1545 nm to 1560 nm is presented in **Figure 7.5**. Here, the power transmission to the "Drop" and "Through" ports for the Filter-ON (0 V) and Filter-OFF (27 V) state are indicated by solid and dashed lines, respectively.

One of the first key parameters that can be identified for the Filter-ON state is the position of the resonant wavelength at 1552 nm instead of 1550 nm. This shift can be attributed to fabrication-induced geometry variation of the ring radius. Next, one observes that the FSR is roughly 5 nm which agrees well with both the analytical and simulated value. The port isolation for resonant wavelengths is an appreciable 20.4 dB and 13.2 dB for off-resonance wavelengths
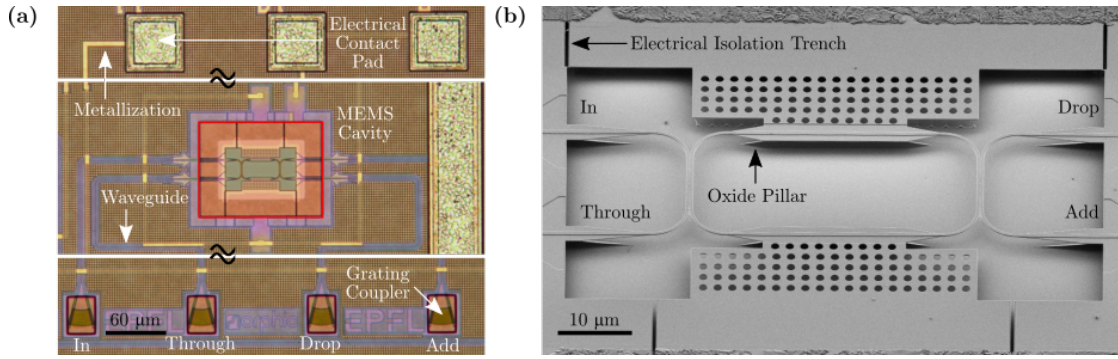
Figure 7.4 – (a) Optical microscope image of the released add-drop filter (b) SEM recording of the released device indicating a nicely suspended RR structure that is well aligned to the bus waveguides. Also indicated are the electrical isolation trenches and the oxide pillars that remain below the rib waveguides

and the bandwidth is quantitatively described by the full-width at half maximum (FWHM), which is approximately 1.4 nm. This somewhat less narrowband operation can be explained by the fact that when the filter is engaged, the RR has been designed to be overcoupled, thereby enabling maximum peak rejection [162]. In the context of this design, maximum peak rejection corresponds to low resonant wavelength transmission to the "Through" port so that most of their optical power is transmitted to the "Drop" port. For conventional resonant filters such as this one, there is a fundamental trade-off between the resolution (e.g., minimum achievable FWHM) and the peak rejection [163]. This particular design has prioritized the power levels at the output port, but one could modify the coupling length and/or initial lateral gap spacing in the coupling region to obtain a critically coupled condition. In that case, the wavelength-selectivity in the Filter-ON state would be improved, but the device would be more sensitive to the initial alignment of the RR to the bus waveguides.

The Filter-OFF state reveals some distinct changes from the Filter-ON state. First, the "Through" port transmission is almost flat, indicating near-complete all-pass behavior of all wavelengths, as expected. Because of the logarithmic scale, though, it is possible to still see how the undercoupling affects the transmission to the "Drop" port. A 0.5 nm decrease (blue-shift) in the resonance frequency in the Filter-OFF state curves can also be observed. Recalling Equation 7.1, there are two ways in which the resonance frequency can be modified, and that is either through modification of the effective refractive index, n_{eff}, or altering the roundtrip length of the cavity, L. A first analysis identifies the out-of-plane displacement of the RR with respect to the bus waveguides as indicative of the first tuning mechanism. The bus waveguides made of silicon are "replaced" by air in the Filter-OFF state so that there is little evanescent field interference with the resonant mode. Because the effective mode index decreases for this situation, one expects the resonance frequency to also decrease, which it does. It is likely that there is also some mechanical deformation in the RR taking place during its downward displacement, but presumably the effect is not as strong as was observed in [116].

Given this new resonant wavelength of 1551.5 nm, one can identify the corresponding port
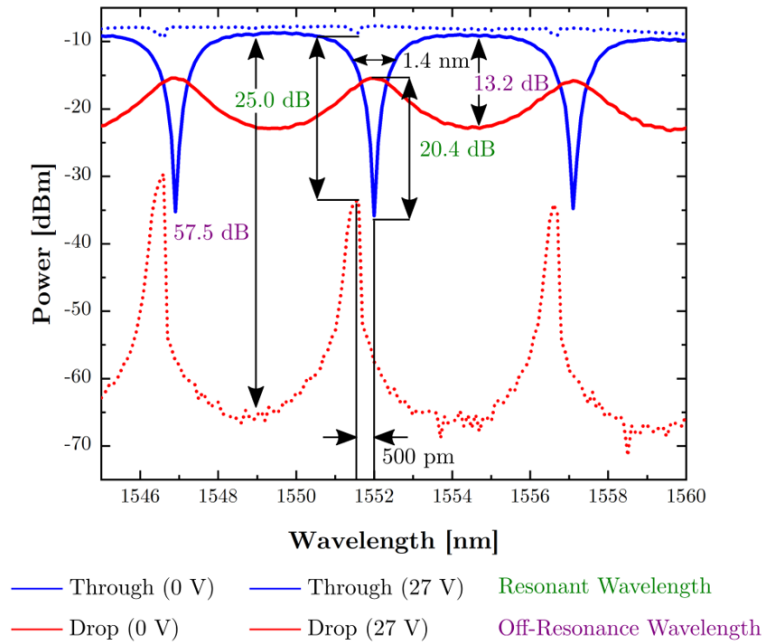
Figure 7.5 – Wavelength sweep capturing three resonances of the add-drop RR device. Power transmission in the "Through" and "Drop" ports for the OFF state are indicated by solid lines and those in the ON state are given by dotted lines. Port isolations for two selected resonant and off-resonance wavelengths are also indicated for the OFF and ON states

isolations for resonant wavelengths, 25.0 dB, and for off-resonance wavelengths (57.5 dB). The evolution of the port isolation is more easily discerned in **Figure 7.6**, which plots the power in the "Through" and "Drop" ports for the new resonant wavelength (1552 nm) and an off-resonance wavelength (1549 nm) as a function of actuation voltage.

Figure 7.6 illustrates that behavior that was described in the operating description of the device. Here, it is manifest that at 0 V actuation voltage, the "Drop" port receives more power from resonant wavelengths than it does off-resonance wavelengths. Relatedly, the "Through" port in this Filter-ON state receives much of the off-resonance wavelength power and little of the resonant wavelength power. As the device is actuated and the RR brought out of the coupling region, the amount of resonant wavelength power appearing in the "Through" port increases leaving little for the "Drop" port, which receives neither the resonance, nor the off-resonance wavelength power. Looking at **Figure 7.6** reveals that this device exhibits an impressive 50 dB of port isolation for resonant wavelengths and even larger 57 dB of port isolation for off-resonance wavelengths.

One characteristic that is common to both **Figure 7.5** and **Figure 7.6** is the presence of a 9 dB IL. This level of excess loss is uncharacteristically high and not part of the design. One possible source of loss is an asymmetric coupling of the RR to the input and output bus waveguides, which could be caused by a tilt in the displacement of the RR during actuation. Additionally, as has been the case for all the other devices demonstrated in this work, the background loss
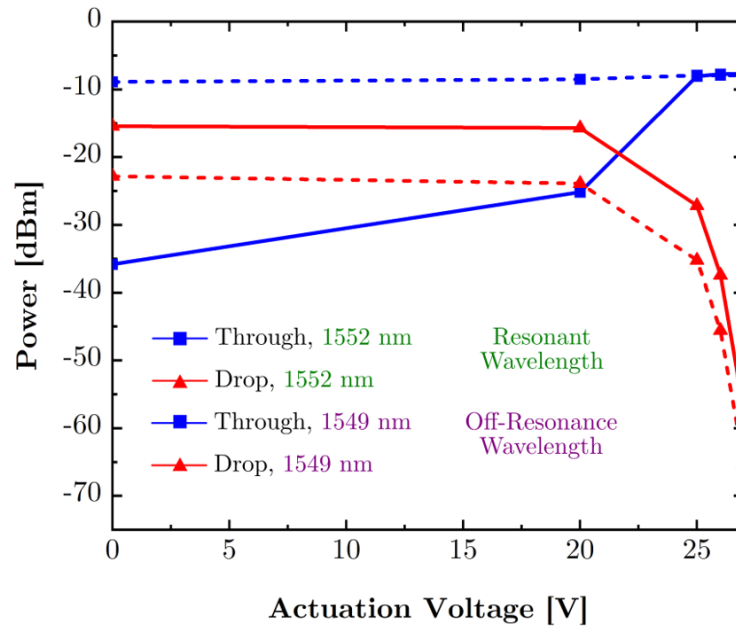
Figure 7.6 – Power transmission to the "Through" and "Drop" ports as a function of actuation voltage. Power in the "Through" port for off-resonance wavelengths is more or less constant as a function of voltage, while the "Drop" port gradually receives less and less power as the RR is brought into an undercoupled state with the input bus waveguide.

from the grating couplers cannot fully be removed from the measurements. It is estimated that in a perfectly symmetric setup with no additional grating coupler losses, the IL in the Filter-OFF state would be less than 1 dB. A more precise characterization requires dedicated monitoring structures and would be recommended for inclusion in follow-up work.

In summary, the device presented here is a compact (45 μm x 75 μm) tunable add-drop filter consisting of an electrostic MEMS-actuated RR with an FSR of approximately 5 nm. The initial unactuated (Filter-ON) state has a resonance frequency of $\lambda = 1550$ nm and provides a port isolation > 20 dB for resonant wavelengths and > 13 dB for off-resonance wavelengths. A 0.5 nm resonance frequency shift is observed for the Filter-OFF state and the port extinction for the resonant and off-resonance wavelengths increase to 25 dB and > 57 dB for a modest actuation voltage of 27 V. Experimental results agree closely with analytical calculations as well as with FDTD and FEM simulations. With a 1.4 nm bandwidth, low power consumption and small footprint, this MEMS-enabled add-drop filter is a suitable candidate for integration in coarse WDM applications.

7.2 Silicon Photonic MEMS Phase Shifters

Another key functionality in a linear optical system is the ability to control and modify the phase information of an optical carrier, which is the role of a phase shifter. Project partners at KTH performed the simulation and design of the MORPHIC phase-shifters and because

these devices constitute another key MEMS-enabled Silicon Photonic building block, they have been included here for completeness. A generalized summary of the theoretical background, operating principles of several devices, and a qualitative reporting of key results is provided here. For a complete review of these designs and their characterization, please see the references listed in **Table 7.2** later in this section.

The phase delay acquired by a guided mode with wavelength λ and effective refractive index n_{eff} over a distance L is given by:

$$\phi = \frac{n_{eff}L}{\lambda} \tag{7.4}$$

This expression indicates that a phase shift can be effected by a variation in either n_{eff} or L. Both of these parameters can be physically tuned with MEMS, as was demonstrated in Chapter 3, by the displacement of slab material into the evanescent field of a guided mode, or by modifying the overlap length in the coupling region. A full 2π phase shift covers the entire phase space, thereby allowing one to control the exact position (i.e., interference) of an optical signal with respect to one travelling in a different branch.

Figure 7.7a provides a schematic diagram of one of the KTH-designed phase shifters. Combined with the corresponding 3D perspective view in **Figure 7.7b**, the operating principle of slab waveguide displacement into the evanescent field of the guided mode by electrostatic actuation to modify n_{eff} is made clear. An optical microscope image and a corresponding SEM recording taken after the post processing at EPFL are also provided in **Figure 7.8**. **Figure 7.8a** captures the difference in grating couplers and contact pad layout compatible with KTH's characterization setup and **Figure 7.8b** confirms that the MEMS release process also works well for the phase shifters.
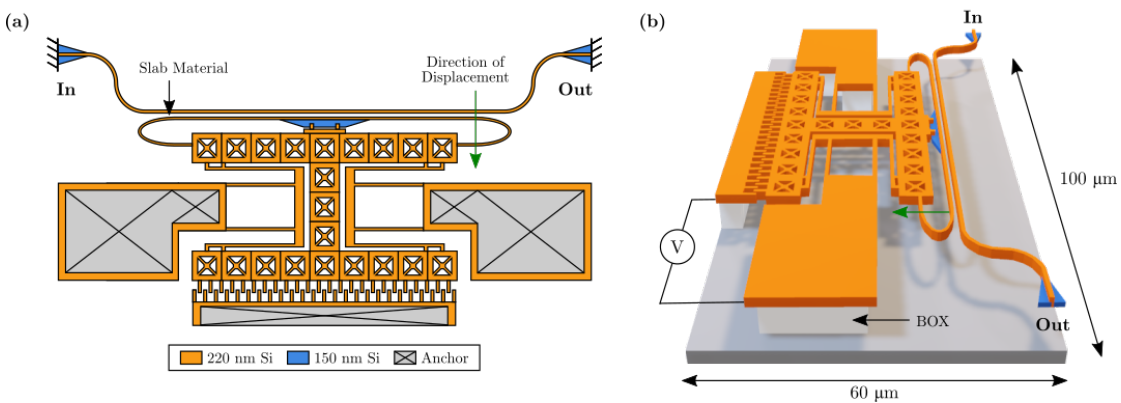

Figure 7.7 – (a) Schematic diagram of one of the MEMS-enabled phase shifters demonstrated by KTH; indicated are input and output ports and the direction of displacement for the slab material (b) 3D perspective view of the suspended phase shifter

Phase shifters find use, for example, in reconfigurable optical circuits and photonic radiofre-
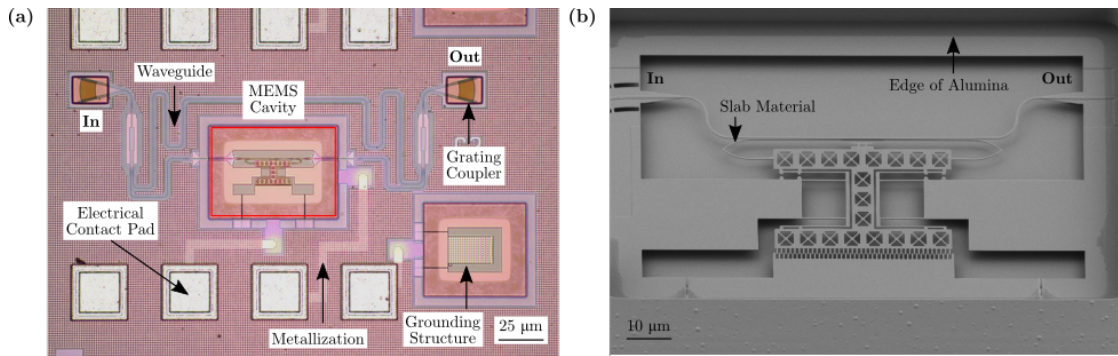
Figure 7.8 – (a) Optical microscope image of the released MEMS phase shifter from KTH; a noticeable difference from this layout compared to those previously shown is the use of two grating couplers on the left and right, instead of a 1 x 10 array on top and a narrow pitch for the electrical contact pads. A dedicated grounding structure has is also included and is indicated on the bottom right (b) Corresponding SEM recording of the released device indicating nicely suspended regions. Note that due to the orientation in which the image was captured, the "In" and "Out" ports are reversed with respect to the schematic diagram

quency waveform generation, as well as in beam steering for free-space communication [164, 165, 166]. Alternatives to MEMS-enabled phase shifting include those utilizing the thermo-optic and plasma dispersion (free-carrier injection) effects to change n_{eff}, but the common theme throughout this work is the relative power-inefficiency, excessive loss, or prohibitively large footprint associated with these other approaches.

A series of performance metrics can be used to compare MEMS-enabled phase shifters and they include, the maximum achievable phase shift in a single stage, the actuation voltage required to obtain a π phase-shift, the IL, and the device footprint. As discussed previously, the ideal phase-shifter obtains a full 2π phase-shift, and it would do so with minimal actuation voltage and insertion loss within a compact form factor. **Table 7.2** lists KTH's work on MEMS-enabled phase shifters that was carried out in parallel with this work and summarizes the performance metrics, as well as the novelty of each contribution. From KTH's first demonstration of a comb-drive based phase shifter consuming 10^5 less power than traditional thermal phase shifters, to improvements in the linearity of actuation, and reduction in footprint, IL, and response time, these MEMS-enabled phase shifters have progressed tremendously. The continuous improvement in the optical performance and reduction in size present key steps towards the realization of large-scale programmable, PICs.

7.3 Concluding Remarks on MEMS-Enabled Devices and Outlook for MEMS-Enabled PICs

Based off their low power consumption due to electrostatic actuation, good optical qualities (e.g., low IL, high ER, large BW), and small form factor, there is little difficult arguing that one-to-one, the devices presented here can compete with or even exceed the performance of

Design Feature	Shift	Voltage [V]	IL [dB]	Footprint [μm^2]	Reference
Comb Drive	1.2π	20	0.3	50 x 70	[167]*
Linearized	-	-	-	-	[168]†
Compact	π	20	0.2	40 x 30	[169]‡
Fast	$> 2\pi$	25	0.5	-	[170]§
Low-Loss	2.9π	10.7	0.33	-	(To be published) ‖

* Comb-drive based MEMS-enabled phase shifter with low IL

† Reduction of actuation nonlinearity in MEMS-enabled phase shifters

‡ Footprint and IL reduction of MEMS-enabled phase shifter

§ Fast, μs time constant MEMS-enabled phase shifter

‖ Low-loss, low-power MEMS-enabled phase shifter for scalable programmable PICs

Table 7.2 – Summary of MORPHIC MEMS-Enabled Phase Shifters

standard modulation schemes. That being said, every device demonstrated in this chapter and the preceding ones has made use of a single actuator.

Large-scale PICs are promising for application areas ranging from next-generation optical networks, wavelength division multiplexing, and lab-on-chip [171]. The case for MEMS enabling such applications, to truly realize MEMS-enabled PICs, can further be reinforced by demonstrating multiple devices working in parallel to achieve better or novel functionality. In fact, larger-scale integration is the next step in the MORPHIC project, and the goal is to confirm that individual MEMS-enabled devices can be connected to one another to implement circuit-level functionality. Once this milestone has been achieved, the devices will be placed in programmable meshes to implement programmable PICs.

Even a comparatively "small" circuit, like a 4 x 4 switch network requiring 16 electrical contacts for the MEMS actuators plus additional ones for the substrate grounding is beyond the capabilities of the characterization setup presented in Chapter 2. Such a system must already be electrically and optically packaged in order to be testable in an efficient manner. Thus, the evaluation of these "demonstrator" sub-circuits is assigned to other project partners with the requisite testing infrastructure. There are, however, certain composite devices consisting of multiple independently-actuated actuators, such as the 4 x 4 power divider that could be used to show multi-MEMS functionality.

It should be prefaced that the following class of devices has not yet been experimentally characterized, but whose design and fabrication promise proof of scalability beyond a single device. The 4 x 4 power divider, unlike the 4 x 4 switch network does not consist of 16 individual photonic MEMS switches, but rather four as indicated in **Figure 7.9**.

As indicated in **Figure 7.9**, the 4 x 4 power divider consists of four directional coupler pairs
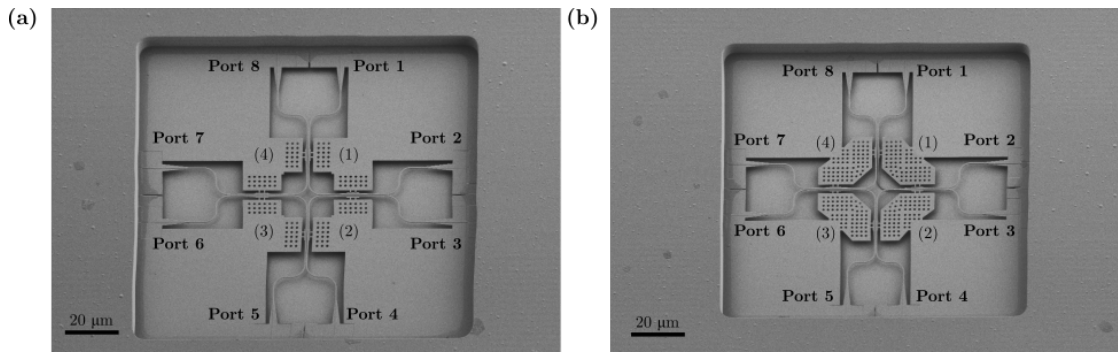
Figure 7.9 – (a) SEM recording of one variant of 4 x 4 power divider indicating the eight I/O ports and the four actuators (indicated by a number in parenthesis) capable of out-of-plane displacement towards the substrate (b) SEM recording of another 4 x 4 power divider where the density and placement of etch holes results in a structure that is mechanically "softer" and should be capable of lower-voltage actuation

attached to a matching set of four actuators. In the initial, unactuated state, the couplers are perfectly aligned with one another, allowing for a complete transfer of power between branches. Thus, if light is injected from port 1, for example, it will couple over to the branch attached to actuator 4 and then again to the branch attached to actuator 3, where it is ultimately routed to port 6. When actuator 1 is activated such that it is displaced downwards, there no longer is strong coupling into the first directional coupler and light from port 1 passes directly to port 2. If, however, actuator 1 is left untouched and actuator 3 is activated instead, the guided mode will only cross-couple once and exits at port 7. By similar reasoning, if actuator 4 is activated, light injected at port 1 is routed to port 3.

Table 7.3 lists the complete input-output routing of the 4 x 4 power divider and indicates how four inputs can be routed to four unique outputs. Only four inputs are considered because unidirectional transmission of light means that the symmetric connections, e.g., light travelling either from port 1 to port 6 or vice versa in the OFF state, are only counted once. Note that non-unique connections, i.e., those achievable with a previously demonstrated active actuator, are indicated by a hyphen.

		Input Port							
	State*	1	2	3	4	5	6	7	8
	OFF	6	5	8	7	2	1	4	3
	ON: 1	2	1	5	-	3	8	-	6
Output Port	**ON: 2**	-	8	4	3	7	-	5	2
	ON: 3	7	4	-	2	6	5	1	-
	ON: 4	3	-	1	6	-	4	8	7

*Numbers indicate active ON state actuators

Table 7.3 – Switching Configuration for 4 x 4 Power Divider

A closer look at this 4 x 4 power divider reveals that it constitutes a design improvement on the vertically movable Silicon Photonic MEMS switch presented in Chapter 6. Specifically, with this topology, one is able to access 16 unique switching combinations, whereas the other topology was effectively a 3 x 2 switch with only six possible switching combinations. This modification is made possible through the use of 90° turn waveguide-actuator combinations allowing for the integration of two orthogonal directional coupler arms in a single unit. Furthermore, there are no "dummy" connections ending in terminations with this design, so the entire footprint (approximately 145 µm x 145 µm, roughly 50% larger than the previous design) consists of active, usable space. Because of the ever-present trade-off between structural robustness and low-voltage actuation, the actuator design has been varied though differences in etch-hole patterns, as can be seen by comparing **Figure 7.9a** and **Figure 7.9b**.

This device will demonstrate the feasibility of controlling multiple MEMS actuators in parallel in a single switch to enhance port connectivity and demonstrates local-scalability within individual devices. The next step towards providing a compelling vision for the future of circuit-level scalability offered by MEMS in Silicon Photonics is to combine individual switches/devices to adjust the connectivity of a network. Of all the silicon photonic devices presented in this work, the SPDT photonic MEMS switch, by virtue of its small footprint, broadband behavior, and excellent ER, is one of the most promising candidates for demonstrating a circuit utilizing multiple devices. **Figure 7.10** presents the layout of a 1 x 8 switch circuit utilizing seven individual SPDT photonic MEMS switches.
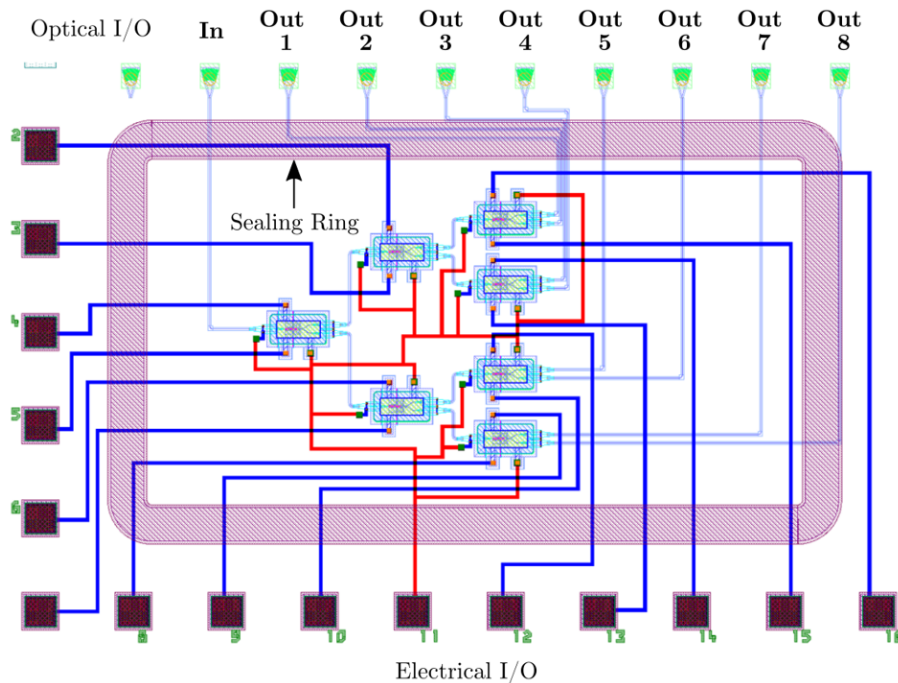

Figure 7.10 – Layout of a 1 x 8 switch network consisting of seven SPDT photonic MEMS switches. The input and eight unique outputs are labeled at the top of the figure as well as the sealing ring, grating coupler array for the optical I/O, and the electrical contact pads for providing actuation voltage.

By electrostatically actuating the individual switches to one of their respective output 1 or output 2 ports, it is possible to route a single input to one of eight unique outputs. As can be seen, the network is relatively compact and fits within a single sealing lid with dimensions 1.2 mm x 0.7 mm. Characterization of this switch configuration is still possible without specialized packaging and the overall optical performance is expected to be comparable to that of the single demonstrated device except for the additional losses due to additional per-unit IL.

Looking beyond pure switch networks, the combination of other MEMS-enabled photonic devices that exhibit similarly advanced function-specific optical performance at low-power, such as the add-drop filter and phase shifters, will constitute a leap forward in realizing scalable MEMS-enabled PICs.

8 Conclusion and Outlook

Silicon Photonics provides a promising complement to electronics, which for decades sustained itself on a continuous reduction in device size but now faces physical limits and thermal bottlenecks hindering continued scaling. However, in order to effectively leverage photonics' greater bandwidth and lower power consumption, truly large-scale photonic integrated circuits (PICs) must be developed. More devices enable additional connectivity, and greater connectivity begets enhanced functionality, such as dense, on-chip switching networks and fully-integrated optical beam-forming circuits. The current issue plaguing existing larger-scale silicon-based PICs is non-trivial power consumption and excessive loss from active devices. Silicon Photonic MEMS is an attractive low-power solution to this issue because the redistribution of physical media has a strong optical effect. Individual MEMS-enabled photonic devices can be made compact and desirable in terms of optical performance, and some larger scale circuits utilizing thousands of such devices have been demonstrated. The next step is to bring the technology to an established foundry platform and make MEMS-based functionality library-standard and accessible to all.

This thesis began with the integration of MEMS in a standard Silicon Photonics technology. The first step was establishing a set of design rules and guidelines regarding minimum margins between layers, dimensions, and geometries to foster successful MEMS post-processing that yielded residue-free, suspended devices. Next, the process development of the MEMS release process (i.e., removal of the sacrificial buried oxide) was presented with a careful examination of each step to identify vulnerabilities and provide solutions. Alumina must cover all regions of the sample that should not come in contact with the aggressive vapor phase hydrofluoric acid (VHF) used to remove the buried oxide, and its placement directly on top of silicon is a vital aspect of this passivation strategy. Failure to do so can lead to etch propagation into undesired regions leading not only to structural failure, but also degraded optical/electrical performance. Selective removal of the alumina over the electrical contact pads and over the MEMS cavities also needs careful consideration as a single etching strategy is not compatible with both regions. Finally, the VHF etch must be controlled so as to enable sufficient removal of the sacrificial oxide while mitigating attacks at the sample edges or in regions where the alumina

has cracked/failed. From a fabrication-perspective the presented process flow exhibits a high-yield with minimal particulate contamination and/or residues on waveguide and MEMS structures, firmly anchored and suspended devices with good alignment, and a VHF attack that has been limited to the edges of the sample. The success of this custom post-processing illustrates the viability of MEMS integration with the foundry platform.

With successful MEMS fabrication and release having been demonstrated, the focus of this work shifted towards the individual components themselves. In particular, large-scale production is only meaningful insofar as each device behaves as designed and that the optical performance includes broadband behavior, high extinction ratio, and low optical loss. Thus, the hierarchy of needs stipulates that the optical design of Photonic MEMS components takes highest priority. As such, the design, simulation, and characterization of a broadband suspended directional coupler, included as part of each of the presented tunable couplers, has been described in detail. This device indicated an attractive candidacy for integration with an actuator and the demonstrated in-plane tunable directional coupler implemented this mechanical-photonic combination. The structure consisted of a fixed and suspended directional coupler arm positioned across from another suspended arm that has been made movable through attachment to a comb-drive. An interplay of the electrostatic force from the comb drive and the restoring forces of the suspensions dictated the modulation of the waveguide gap spacing in the directional coupler arm, thereby providing continuous tunability of optical power. As the first variant exhibited an asymmetry in the power transfer characteristics, improvements in the mechanical design to bolster robustness against out-of-plane displacement from residual stress were implemented. The resulting device was symmetric and exhibited high ER (> 20 dB), low IL (< 1 dB), and a broadband response (> 80 nm). Additional optimization for lower actuation voltages entailed further changes to the suspension geometry and inclusion of a second comb-drive.

Two photonic MEMS switches capable of complete power transfer were also demonstrated, with the first exhibiting a more intricate switching configuration than previously shown and a very compact out-of-plane actuator design. The device achieved a large ER (> 16 dB) with low actuation voltage (< 4 V) but exhibited a slightly larger footprint than the tunable directional couplers. Next, a different type of device, the single-pole double-throw photonic MEMS switch was presented and because the optical, mechanical, and electrical design varied from those of the other devices, a complete discussion of the design and operating principles was included. Characterization of this switch showed high ER (> 22 dB), a broadband response (> 70 nm), and a sub-microsecond response time. Paired with its small size, this device is a prime candidate for dense integration in larger scale circuits.

Having demonstrated two basic functionalities, continuous tunable power coupling and near-digital 100% optical power switching, a discussion of other MEMS-enabled photonic devices was included. An add-drop filter capable of narrow wavelength-selective filtering and strong switching was demonstrated with a theoretical background to substantiate the measured behavior. This device provided a complement to the demonstrated spectrally broadband
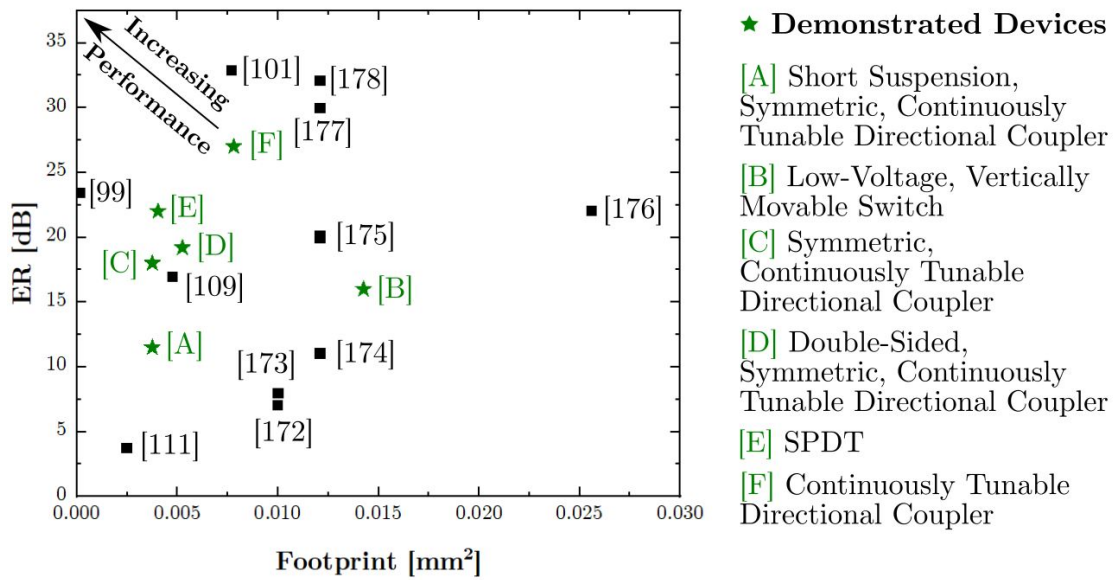
Figure 8.1 – Comparison of the demonstrated MEMS-enabled photonic components with other state-of-the-art devices with regard to footprint and extinction ratio. Components with a large "modulation-strength density" desired for enhanced component density lie in the upper left-hand corner of the plot.

devices, and paired with the phase shifters designed by project partners, adds phase shifting to the selection of MEMS-enabled photonic functions. A preview of a device containing multiple actuators working in parallel was also included to discuss the next steps in MEMS-enabled PICs.

Context for this work's contribution to the field of Silicon Photonics is provided by an evaluation of the presented devices' performance against those of other active components. This comparison can be performed specifically with other state-of-the-art MEMS-enabled devices, as well as more generally, with other optical modulation schemes. One basis of comparison for MEMS-based approaches considers "modulation-strength density," which takes into account a device's ability to effect large extinction ratio, i.e., strong optical modulation, in a compact form factor. Such devices can be desirable for dense optical networks, for example, where an abundance of strong switching/optical isolation connections are needed for efficient and extensive routing. Figure 8.1 illustrates the comparison and reveals that the devices realized in this work occupy a desirable region of the plot. These couplers and switches are among the smallest devices and still offer strong optical modulation.

The attractiveness of this physical modulation scheme for certain PIC applications increases when it is compared with other approaches. Table 8.1 lists the four primary methods available for optical modulation in Silicon Photonics: MEMS, thermal tuning, free-carrier/plasma dispersion, and electro-optic effects (e.g., Pockels effect). The criteria by which these solutions are evaluated include the strength of the effect, fabrication complexity/ease of integration with standard technologies, device size, optical loss, power consumption, and speed.

147

Technology	Strength	Fabrication	Size	Loss	Power	Speed
Thermal	+ +	+	+	+ +	- -	-
Plasma Dispersion	+ +	+ +	- -	- -	+	+ +
Pockels Effect	-/+	- -	+ +	+	+ +	+ +
MEMS	+	+	+ +	+	+ +	+

+ + Excellent, + Good, - Medium, - - Poor

Table 8.1 – Comparison of Optical Modulation Approaches

Conventional thermal tuning is moderately effective and not difficult to implement in standard Silicon Photonic platforms as it relies on resistive heating, which simply requires doped regions or metallization. The resulting devices can be made relatively compact and low-loss. However, the need for large amounts of DC current resulting in mW-level power consumption, and the µs switching times limits thermal-tuning in large-scale PICs. Plasma dispersion-based modulation can also be easily implemented in standard technologies (e.g., as p-n/p-i-n diodes or MOS capacitors) and enables very compact and fast (ps - ns) devices requiring little DC power (µW). On the other hand, the optical effect of this approach is relatively weak and the associated optical insertion losses can be up to 10 dB.

Electro-optic modulation via the Pockels effect is not available in pure silicon due to its centrosymmetry. However, progress on the epitaxial growth and wafer-bonding of ferroelectric materials such as lithium niobate and barium titanate on top of silicon introduces this functionality. The resulting devices can operate at ps - ns speeds and not only have lower loss than their plasma dispersion-based counterparts, but also consume less power because they operate using field-effects and not charge flow. On the other hand, devices for electro-optic modulation tend to be rather large with mm-long effective lengths requiring coils hundreds of microns in diameter. And although the difficulty in processing these ferroelectrics has historically been a limiting factor in their integration with Silicon Photonics, recent developments on wafer-scale processes have lowered this barrier.

The introduction of suspended, movable structures to perform optical modulation is unconventional in a field dominated by solid-state devices. Yet, the properties summarized in Table 8.1 and embodied by the demonstrated tunable couplers, switches, and add-drop filter provide a compelling argument for the inclusion of MEMS-enabled photonic devices in PICs. Their successful integration in an established platform confirms compatibility with the established technology. Furthermore, despite their ns - µs response times precluding them from competing with electro-optic-based modulators, they produce impressively strong optical effects with minimal power consumption (nW-level). As such, mechanical-based

optical modulation is more a natural complement or alternative to thermal tuning, where efficient, sub-microsecond adjustments are desired.

In this manner, MEMS-enabled devices help Silicon Photonics overcome the scaling limitations imposed by power budgets and loss figures. The groundwork for establishing a means of high-density integration has been achieved by careful design of compact devices and development of a MEMS release process that is compatible with an established foundry platform. The next step is to connect numerous such devices, more than was previously possible, in a circuit architecture where the low-loss routing of light can be physically adjusted to pass through other functional units of the platform or those of custom design. This co-integration of tunable photonic devices alongside library standard components and user designs ushers in the possibility to realize truly large scale and reliable systems as well as reconfigurable PICs.
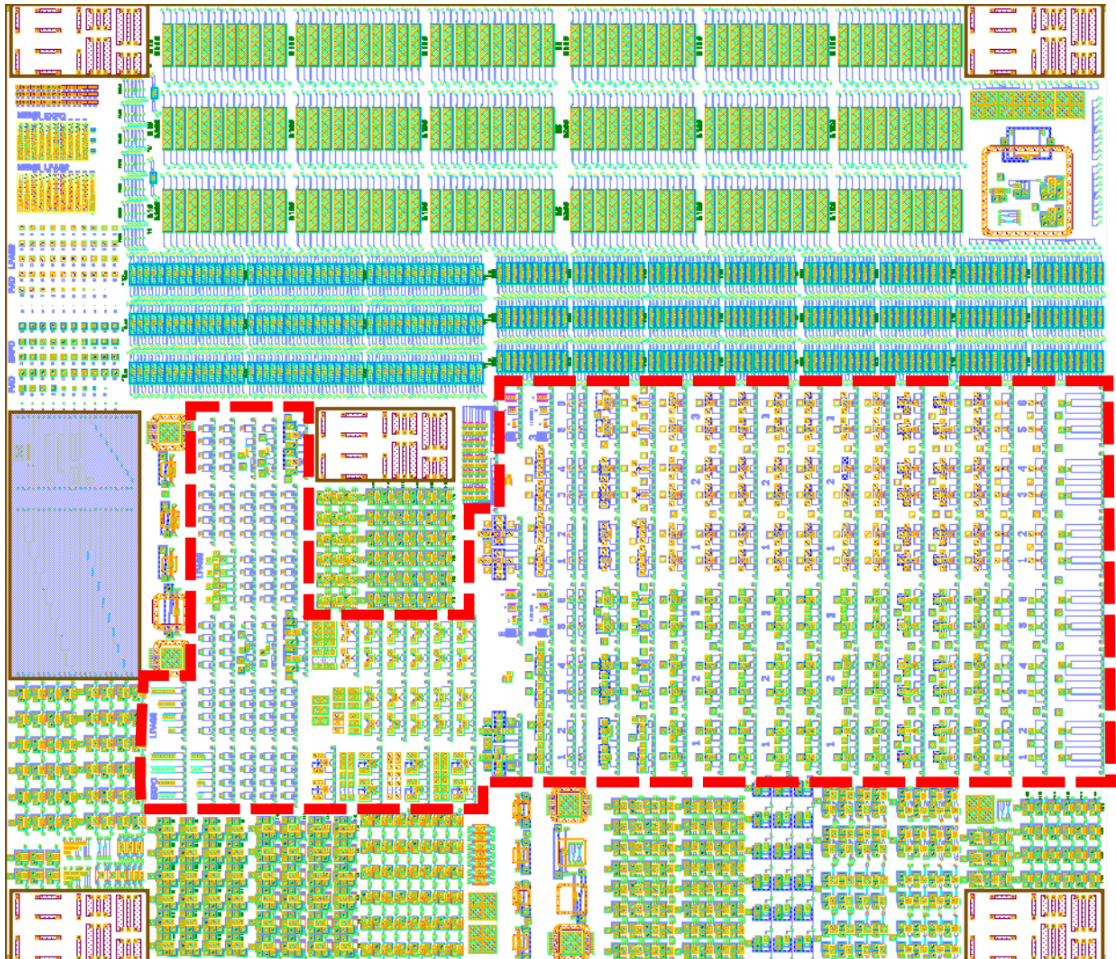
A Layouts

Figure A.1 – RUN1 chip layout where the EPFL contributions are indicated by the red-dashed boundary. As the first fabrication run, this layout included a variety of different couplers and switches, as well as test structures needed for process development. Note that because MEMS-incompatible SOI wafers were used, many of the active structures could in fact not be tested as they had collapsed to the substrate during the VHF release step.
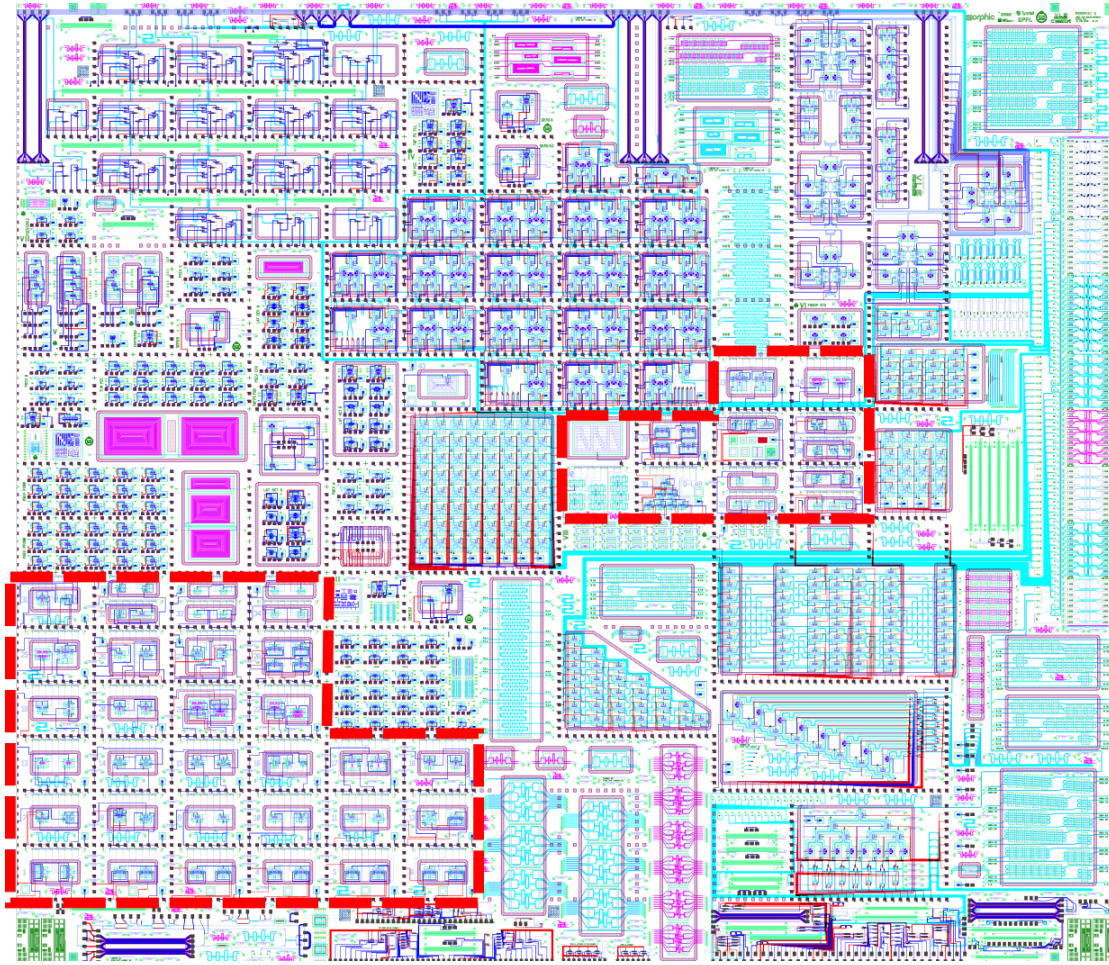
Figure A.2 – RUN2 chip layout where the EPFL contributions are indicated by the red-dashed boundary. This fabrication run not only included some of the designs from RUN1 that were not testable but also some larger scale mini-demonstrator circuits using several MEMS-enabled couplers, switches, and phase shifters connected to one another. Another noticeable feature in this layout is the use of unit cells that have been placed on a regular grid and contain metal sealing rings and contact pads.
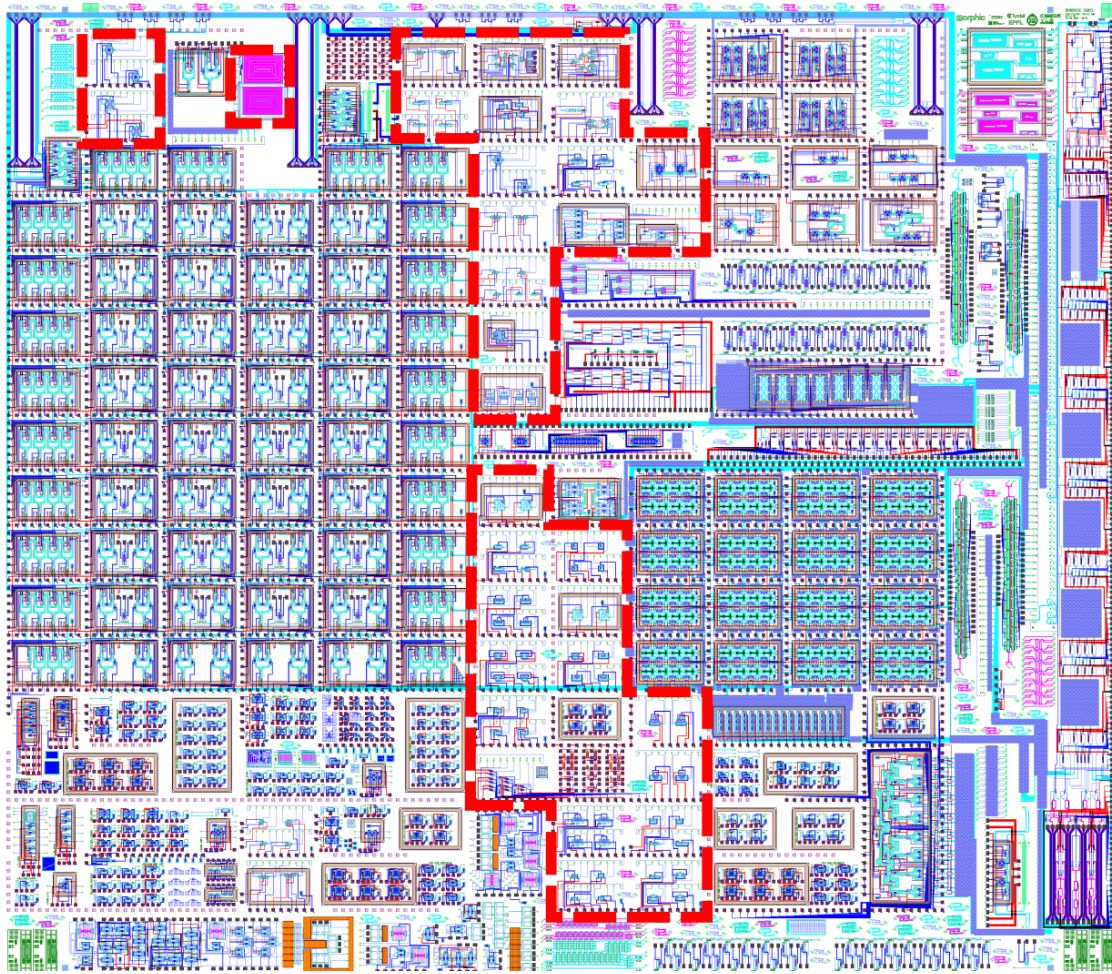
Figure A.3 – RUN3 chip layout where the EPFL contributions are indicated by the red-dashed boundary. This was the final fabrication run and included the optimized designs from RUN2 as well as the full scale field-programmable PIC (FP-PIC) (see large block on the left). In addition to mature couplers, switches, and phase shifters, more experimental devices, such as an optical microphone and optical gyroscope have been included as well. The characterization of these components was not included as part of this work, but is planned in the future.

B List of Publications

Journal Contributions

J01 **A. Y. Takabayashi**, H. Sattari, P. Edinger, P. Verheyen, K. B. Gylfason, W. Bogaerts, and N. Quack, "Broadband Compact Single-Pole Double-Throw Silicon Photonic MEMS Switch," Journal of Microelectromechanical Systems, vol. 30, pp. 322–329, Apr. 2021.

J02 P. Edinger, **A. Y. Takabayashi**, C. Errando-Herranz, U. Khan, H. Sattari, P. Verheyen, W. Bogaerts, N. Quack, and K. B. Gylfason, "Silicon photonic MEMS phase shifters for scalable programmable photonic circuits," Optics Letters, 46, 5674-5674, 2021.

J03 G. Jo, P. Edinger, S. J. Bleiker, X. Wang, **A. Y. Takabayashi**, H. Sattari, N. Quack, M. Jezzini, P. Verheyen, I. Zand, U. Khan, W. Bogaerts, G. Stemme, K. B. Gylfason, and F. Niklaus, "Wafer-level hermetic sealing of silicon photonic MEMS," Photonics Research, Under Review 2021.

J04 H. Sattari, **A. Y. Takabayashi**, Y. Zhang, P. Verheyen, W. Bogaerts, and N. Quack, "Compact broadband suspended silicon photonic directional coupler," Optics Letters, vol. 45, pp. 2997–3000, June 2020.

J05 C. Errando-Herranz, **A. Y. Takabayashi**, P. Edinger, H. Sattari, K. B. Gylfason, and N. Quack, "MEMS for Photonic Integrated Circuits," IEEE Journal of Selected Topics in Quantum Electronics, vol. 26, pp. 1–16, Mar. 2020.

J06 N. Quack, H. Sattari, **A. Y. Takabayashi**, Y. Zhang, P. Verheyen, W. Bogaerts, P. Edinger, C. Errando-Herranz, and K. B. Gylfason, "MEMS-Enabled Silicon Photonic Integrated Devices and Circuits," IEEE Journal of Quantum Electronics, vol. 56, pp. 1–10, Feb. 2020.

Conference Proceedings and Contributions

C01 **A. Y. Takabayashi**, H. Sattari, P. Edinger, P. Verheyen, K. B. Gylfason, W. Bogaerts, and N. Quack, "Compact Integrated Silicon Photonic MEMS Power Coupler for Programmable

Photonics," in 35th IEEE International Conference on Micro Electro Mecahnical Systems (MEMS 2022), Accepted 2021.

C02 **A. Y. Takabayashi**, H. Sattari, P. Edinger, P. Verheyen, K. B. Gylfason, W. Bogaerts, and N. Quack, "Continuously Tunable Silicon Photonic MEMS 2×2 Power Coupler," in 21st International Conference on Solid-State Sensors, Actuators and Microsystems (Transducers), pp. 447–450, June 2021.

C03 **A. Y. Takabayashi**, H. Sattari, P. Edinger, P. Verheyen, K. B. Gylfason, W. Bogaerts, and N. Quack, "Broadband Compact Single-Pole Double-Throw SIlicon Photonic MEMS Switch," in 22nd European Conference on Integrated Optics (ECIO), June 2020.

C04 W. Bogaerts, **A. Y. Takabayashi**, P. Edinger, I. Zand, G. Jo, H. Sattari, P. Verheyen, M. A. Jezzini, C. Antony, G. Talli, M. Saei, S. Kumar, C. L. Arce, M. G. Porcel, N. Quack, K. B. Gylfason, F. Niklaus, and U. Khan, "Programmable Photonic Circuits using Silicon Photonic MEMS," in OSA Advanced Photonics Congress 2021., Optical Society of America, July 2021.

C05 D. U. Kim, M. S. Hong, D. Y. Kim, Y. J. Park, **A. Y. Takabayashi**, Y. Jeong, J. Park, S. Han, N. Quack, K. Yu, and S. Han, "8×8 Programmable Multi-Beam Pattern Projection Based on Multicast Silicon Photonic MEMS Switches," in Optical Fiber Communication Conference (OFC) 2021 (2021), paper F4A.3, Optical Society of America, June 2021.

C06 P. Edinger, K. Kristinsson, C. Errando-Herranz, **A. Y. Takabayashi**, H. Sattari, N. Quack, P. Verheyen, W. Bogaerts, and K. B. Gylfason, "Silicon photonic MEMS phase shifter with μs time constant built on a foundry platform," in Conference on Lasers and Electro-Optics, (San Jose, California), Optical Society of America, May 2021.

C07 W. Bogaerts, L. V. Iseghem, L. V. Iseghem, P. Edinger, H. Sattari, **A. Y. Takabayashi**, X. Chen, X. Chen, H. Deng, H. Deng, P. Verheyen, A. Ribeiro, A. Ribeiro, U. Khan, U. Khan, N. Quack, and K. B. Gylfason, "Low-Power Electro-Optic Actuators for Large-Scale Programmable Photonic Circuits," in Conference on Lasers and Electro-Optics (2021), Optical Society of America, May 2021.

C08 Y. J. Park, D. U. Kim, D. Y. Kim, M. S. Hong, **A. Y. Takabayashi**, Y. Jeong, J. Park, S. Han, N. Quack, K. Yu, and S. Han, "Fully Reconfigurable Coupled-Resonator Optical Waveguides (CROWs) with 10 nW Static Power MEMS," in Conference on Lasers and Electro Optics (2021), paper STh1Q.5, Optical Society of America, May 2021.

C09 D. Y. Kim, Y. J. Park, D. U. Kim, M. S. Hong, **A. Y. Takabayashi**, Y. Jeong, J. Park, S. Han, N. Quack, K. Yu, and S. Han, "16-Core Recirculating Programmable Si Photonic MEMS," in Conference on Lasers and Electro-Optics (2021), paper STh1Q.6, Optical Society of America, May 2021.

C10 G. Jo, P. Edinger, S. J. Bleiker, X. Wang, **A. Y. Takabayashi**, H. Sattari, N. Quack, M. Jezzini, P. Verheyen, G. Stemme, W. Bogaerts, K. B. Gylfason, and F. Niklaus, "Wafer-level vacuum

sealing for packaging of silicon photonic MEMS," in Silicon Photonics XVI, vol. 11691, International Society for Optics and Photonics, Mar. 2021.

C11 K. B. Gylfason, P. Edinger, C. Errando-Herranz, **A. Y. Takabayashi**, H. Sattari, N. Quack, P. Verheyen, and W. Bogaerts, "Compact and low power silicon photonic components based on MEMS," in MOEMS and Miniaturized Systems XX, vol. 11697, SPIE, Mar. 2021.

C12 H. Sattari, **A. Y. Takabayashi**, P. Edinger, P. Verheyen, K. B. Gylfason, W. Bogaerts, and N. Quack, "Low-Voltage Silicon Photonic MEMS Switch with Vertical Actuation," in 34th IEEE International Conference on Micro Electro Mechanical Systems (MEMS 2021), pp. 298–301, Jan. 2021.

C13 H. Sattari, **A. Y. Takabayashi**, P. Edinger, P. Verheyen, K. B. Gylfason, W. Bogaerts, and N. Quack, "Silicon Photonic MEMS Add-Drop Filter," in 2020 European Conference on Optical Communications (ECOC), pp. 1–4, Dec. 2020.

C14 W. Bogaerts, P. Edinger, **A. Y. Takabayashi**, I. Zand, X. Chen, X. Wang, H. Sattari, P. Verheyen, M. A. Jezzini, G. Talli, S. Kumar, M. G. Porcel, A. Ribeiro, G. Jo, N. Quack, K. B. Gylfason, F. Niklaus, and U. Khan, "Building Large-Scale Programmable Photonic Circuits Using Silicon Photonic MEMS," in OSA Advanced Photonics Congress (AP) 2020, paper PsTh1F.1, Optical Society of America, July 2020.

C15 L. V. Iseghem, U. Khan, P. Edinger, C. Errando-Herranz, **A. Y. Takabayashi**, H. Sattari, K. B. Gylfason, N. Quack, J. Beeckman, and W. Bogaerts, "Liquid crystal phase shifter integrated in a silicon photonics platform," in 22nd European Conference on Integrated Optics (ECIO), June 2020.

C16 P. Edinger, C. Errando-Herranz, **A. Y. Takabayashi**, H. Sattari, N. Quack, P. Verheyen, W. Bogaerts, and K. B. Gylfason, "Compact low loss MEMS phase shifters for scalable field-programmable silicon photonics," in Conference on Lasers and Electro-Optics, (Washington, DC), OSA, May 2020.

C17 W. Bogaerts, H. Sattari, P. Edinger, **A. Y. Takabayashi**, I. Zand, X. Wang, A. Ribeiro, M. Jezzini, C. Errando-Herranz, G. Talli, K. Saurav, M. G. Porcel, P. Verheyen, B. Abasahl, F. Niklaus, N. Quack, K. B. Gylfason, P. O'Brien, and U. Khan, "MORPHIC: programmable photonic circuits enabled by silicon photonic MEMS," in Silicon Photonics XV, vol. 11285, p. 1128503, International Society for Optics and Photonics, Feb. 2020.

C18 N. Quack, H. Sattari, **A. Y. Takabayashi**, Y. Zhang, P. Edinger, C. Errando-Herranz, and K. B. Gylfason, "MEMS-based Silicon Photonic Integrated Devices and Circuits," in 21st European Conference on Integrated Optics (ECIO), Feb. 2020.

C19 N. Quack, H. Sattari, **A. Y. Takabayashi**, Y. Zhang, C. Errando-Herranz, P. Edinger, and K. B. Gylfason, "Photonic MEMS: Exploiting Mechanics at the Micro- and Nanoscale for Efficient Reconfiguration of Photonic Integrated Circuits," in 2019 IEEE Photonics Society Summer Topical Meeting Series (SUM), pp. 1–1, July 2019.

C20 Y. Zhang, **A. Y. Takabayashi**, H. Sattari, and N. Quack, "Freestanding Silicon Photonic Ring and Disk Resonators," in 2019 International Conference on Optical MEMS and Nanophotonics (OMN), pp. 212–213, July 2019.

C21 H. Sattari, **A. Y. Takabayashi**, Y. Zhang, and N. Quack, "Silicon Photonic Broadband Suspended Directional Coupler," in 2019 International Conference on Optical MEMS and Nanophotonics (OMN), pp. 214–215, July 2019.

C22 N. Quack, H. Sattari, **A. Y. Takabayashi**, Y. Zhang, P. Edinger, C. Errando-Herranz, K. B. Gylfason, X. Wang, F. Niklaus, M. A. Jezzini, H. Y. Hwang, P. O'Brien, M. A. G. Porcel, C. L. Arce, S. Kumar, B. Abasahl, P. Verheyen, and W. Bogaerts, "Silicon Photonic MEMS: Exploiting Mechanics at the Nanoscale to Enhance Photonic Integrated Circuits," in 2019 Optical Fiber Communications Conference and Exhibition (OFC), pp. 1–3, Mar. 2019.

C Copyright Licenses

Figure 1.1a "Classic shot of the ENIAC" by unidentified U.S. Army photographer, 1946, Public Domain

Figure 1.1b "Person Holding Black and Gray Audio Mixer" by IT services EU, 2021, Pexels License

Figure 1.3a Reproduced from "CALIENTs S320 Optical Switch front and center @Super-computing SCinet last week in Dallas," 2018 with permission from Calient Technologies

Figure 3.7a Reproduced from C. Papon, X. Zhou, H. Thyrrestrup, Z. Liu, S. Stobbe, R. Schott, A. D. Wieck, A. Ludwig, P. Lodahl, and L. Midolo, "Nanomechanical single-photon routing," Optica, vol. 6, pp. 524–530, Apr. 2019. with permission of the Optical Society

Figure 3.7b Reproduced from M.-C. M. Lee and M. C. Wu, "Tunable coupling regimes of silicon microdisk resonators using MEMS actuators," Optics Express, vol. 14, pp. 4703–4712, May 2006. with permission of the Optical Society

Figure 3.7c Reproduced from T. Ikeda and K. Hane, "A tunable notch filter using micro-electromechanical microring with gap-variable busline coupler," Optics Express, vol. 21, pp. 22034–22042, Sept. 2013. with permission of the Optical Society

Figure 3.7d Reproduced from X. Chew, G. Zhou, F. S. Chau, J. Deng, X. Tang, and Y. C. Loke, "Dynamic tuning of an optical resonator through MEMS-driven coupled photonic crystal nanocavities," Optics Letters, vol. 35, pp. 2517–2519, Aug. 2010. with permission of the Optical Society

Figure 3.8a Reproduced from E. Bulgan, Y. Kanamori, and K. Hane, "Submicron silicon waveguide optical switch driven by microelectromechanical actuator," Applied Physics Letters, vol. 92, p. 101110, Mar. 2008. with permission of AIP Publishing

Figure 3.8b Reproduced from M.-C. Lee, D. Hah, E. Lau, H. Toshiyoshi, and M. Wu, "MEMS-actuated photonic crystal switches," IEEE Photonics Technology Letters, vol. 18, pp. 358–360, Jan. 2006. with permission of the Optical Society

Bibliography

[1] G. P. Agrawal, "Optical Communication: Its History and Recent Progress," in *Optics in Our Time* (M. D. Al-Amri, M. El-Gomati, and M. S. Zubairy, eds.), pp. 177–199, Cham: Springer International Publishing, 2016.

[2] A. Huurdeman, *The Worldwide History of Telecommunications*. John Wiley & Sons, Inc, July 2003.

[3] G. E. Moore, "Cramming more components onto integrated circuits, Reprinted from Electronics, volume 38, number 8, April 19, 1965, pp.114 ff.," *IEEE Solid-State Circuits Society Newsletter*, vol. 11, pp. 33–35, Sept. 2006.

[4] A. Burks, "Electronic Computing Circuits of the ENIAC," *Proceedings of the IRE*, vol. 35, pp. 756–767, Aug. 1947.

[5] W. Commons, "File:classic shot of the eniac.jpg — wikimedia commons, the free media repository," 2021.

[6] I. services EU, "Person holding black and gray audio mixer," 2021.

[7] W. Arden, M. Brillouët, P. Cogez, M. Graef, B. Huizing, and R. Mahnkopf, ""More-than-Moore" White Paper," p. 31, 2010.

[8] Q. Cheng, M. Bahadori, M. Glick, S. Rumley, and K. Bergman, "Recent advances in optical technologies for data centers: a review," *Optica*, vol. 5, p. 1354, Nov. 2018.

[9] D. J. Blumenthal, "Photonic integration for UV to IR applications," *APL Photonics*, vol. 5, p. 020903, Feb. 2020.

[10] @CalientTech, "Calient's s320 optical switch front and center at @supercomputing scinet last week in dallas," 2018.

[11] M. Glick, L. C. Kimmerling, and R. C. Pfahl, "A Roadmap for Integrated Photonics," 2018.

[12] W. Bogaerts, D. Pérez, J. Capmany, D. A. B. Miller, J. Poon, D. Englund, F. Morichetti, and A. Melloni, "Programmable photonic circuits," *Nature*, vol. 586, pp. 207–216, Oct. 2020.

Bibliography

[13] M. Wirz, T. Franke, D. Roggen, E. Mitleton-Kelly, P. Lukowicz, and G. Tröster, "Probing crowd density through smartphones in city-scale mass gatherings," *EPJ Data Science*, vol. 2, pp. 1–24, Dec. 2013.

[14] Y. Luo, C. Zhang, Y. Zhang, C. Zuo, D. Xuan, Z. Lin, A. C. Champion, and N. Shroff, "ACOUSTIC-TURF: Acoustic-based Privacy-Preserving COVID-19 Contact Tracing," *arXiv:2006.13362 [cs, eess]*, June 2020.

[15] J. Kilby, "Invention of the integrated circuit," *IEEE Transactions on Electron Devices*, vol. 23, pp. 648–654, July 1976.

[16] S. E. Miller, "Integrated optics: An introduction," *The Bell System Technical Journal*, vol. 48, pp. 2059–2069, Sept. 1969.

[17] P. K. Tien, "Integrated optics and new wave phenomena in optical waveguides," *Reviews of Modern Physics*, vol. 49, pp. 361–420, Apr. 1977.

[18] N. Jones, "How to stop data centres from gobbling up the world's electricity," *Nature*, vol. 561, pp. 163–166, Sept. 2018.

[19] C. Kachris and I. Tomkos, "A Survey on Optical Interconnects for Data Centers," *IEEE Communications Surveys Tutorials*, vol. 14, no. 4, pp. 1021–1036, 2012.

[20] G. Carpintero, R. C. Guzmán, C. Gordón, G. Kervella, M. Chitoui, and F. Van Dijk, "Photonic Integrated Circuits for Radio-Frequency Signal Generation," *Journal of Lightwave Technology*, vol. 34, pp. 508–515, Jan. 2016.

[21] E. Luan, H. Shoman, D. M. Ratner, K. C. Cheung, and L. Chrostowski, "Silicon Photonic Biosensors Using Label-Free Detection," *Sensors*, vol. 18, p. 3519, Oct. 2018.

[22] A. Martin, D. Dodane, L. Leviandier, D. Dolfi, A. Naughton, P. O'Brien, T. Spuessens, R. Baets, G. Lepage, P. Verheyen, P. De Heyn, P. Absil, P. Feneyrou, and J. Bourderionnet, "Photonic Integrated Circuit-Based FMCW Coherent LiDAR," *Journal of Lightwave Technology*, vol. 36, pp. 4640–4645, Oct. 2018.

[23] H.-S. Zhong, H. Wang, Y.-H. Deng, M.-C. Chen, L.-C. Peng, Y.-H. Luo, J. Qin, D. Wu, X. Ding, Y. Hu, P. Hu, X.-Y. Yang, W.-J. Zhang, H. Li, Y. Li, X. Jiang, L. Gan, G. Yang, L. You, Z. Wang, L. Li, N.-L. Liu, C.-Y. Lu, and J.-W. Pan, "Quantum computational advantage using photons," *Science*, vol. 370, pp. 1460–1463, Dec. 2020.

[24] C. Errando-Herranz, A. Y. Takabayashi, P. Edinger, H. Sattari, K. B. Gylfason, and N. Quack, "MEMS for Photonic Integrated Circuits," *IEEE Journal of Selected Topics in Quantum Electronics*, vol. 26, pp. 1–16, Mar. 2020.

[25] D. H. Geuzebroek and A. Driessen, "Ring-Resonator-Based Wavelength Filters," in *Wavelength Filters in Fibre Optics* (H. Venghaus, ed.), Springer Series in Optical Sciences, pp. 341–379, Berlin, Heidelberg: Springer, 2006.

[26] D. Rafizadeh, J. P. Zhang, S. C. Hagness, A. Taflove, K. A. Stair, S. T. Ho, and R. C. Tiberio, "Waveguide-coupled AlGaAs/GaAs microcavity ring and disk resonators with high finesse and 21.6-nm free spectral range," *Optics Letters*, vol. 22, pp. 1244–1246, Aug. 1997.

[27] J. Cai, Y. Ishikawa, and K. Wada, "Strain induced bandgap and refractive index variation of silicon," *Optics Express*, vol. 21, p. 7162, Mar. 2013.

[28] A. Melloni, R. Costa, G. Cusmai, and F. Morichetti, "The role of index contrast in dielectric optical waveguides," *International Journal of Materials and Product Technology*, vol. 34, no. 4, p. 421, 2009.

[29] M. H. P. Pfeiffer, J. Liu, A. S. Raja, T. Morais, B. Ghadiani, and T. J. Kippenberg, "Ultra-smooth silicon nitride waveguides based on the Damascene reflow process: fabrication and loss origins," *Optica*, vol. 5, pp. 884–892, July 2018.

[30] J. F. Bauters, M. J. R. Heck, D. D. John, J. S. Barton, C. M. Bruinink, A. Leinse, R. G. Heideman, D. J. Blumenthal, and J. E. Bowers, "Planar waveguides with less than 0.1 dB/m propagation loss fabricated with wafer bonding," *Optics Express*, vol. 19, pp. 24090–24101, Nov. 2011.

[31] G. Bourdon, G. Alibert, A. Beguin, B. Bellman, and E. Guiot, "Ultralow loss ring resonators using 3.5% index-contrast Ge-doped silica waveguides," *IEEE Photonics Technology Letters*, vol. 15, pp. 709–711, May 2003.

[32] C. R. Doerr and K. Okamoto, "Advances in Silica Planar Lightwave Circuits," *Journal of Lightwave Technology*, vol. 24, pp. 4763–4789, Dec. 2006.

[33] J. Klamkin, H. Zhao, B. Song, Y. Liu, B. Isaac, S. Pinna, F. Sang, and L. Coldren, "Indium Phosphide Photonic Integrated Circuits: Technology and Applications," in *2018 IEEE BiCMOS and Compound Semiconductor Integrated Circuits and Technology Symposium (BCICTS)*, pp. 8–13, Oct. 2018.

[34] T.-M. Shih, *Indium phosphide based integrated photonic devices for telecommunications and sensing applications*. Thesis, Massachusetts Institute of Technology, 2012.

[35] M. Takenaka and Y. Nakano, "InP photonic wire waveguide using InAlAs oxide cladding layer," *Optics Express*, vol. 15, pp. 8422–8427, June 2007.

[36] M. Takenaka and S. Takagi, "InP-based photonic integrated circuit platform on SiC wafer," *Optics Express*, vol. 25, p. 29993, Nov. 2017.

[37] D. D'Agostino, G. Carnicella, C. Ciminelli, P. Thijs, P. J. Veldhoven, H. Ambrosius, and M. Smit, "Low-loss passive waveguides in a generic InP foundry process via local diffusion of zinc," *Optics Express*, vol. 23, pp. 25143–25157, Sept. 2015.

[38] L. Li, G. Nordin, J. English, and J. Jiang, "Small-area bends and beamsplitters for lowindex-contrast waveguides," *Optics Express*, vol. 11, p. 282, Feb. 2003.

[39] S. K. Selvaraja, P. D. Heyn, G. Winroth, P. Ong, G. Lepage, C. Cailler, A. Rigny, K. K. Bourdelle, W. Bogaerts, D. V. Thourhout, J. V. Campenhout, and P. Absil, "Highly uniform and low-loss passive silicon photonics devices using a 300mm CMOS platform," in *Optical Fiber Communication Conference (2014), paper Th2A.33*, p. Th2A.33, Optical Society of America, Mar. 2014.

[40] R. Soref and B. Bennett, "Electrooptical effects in silicon," *IEEE Journal of Quantum Electronics*, vol. 23, pp. 123–129, Jan. 1987.

[41] T. Komljenovic, M. Davenport, J. Hulme, A. Y. Liu, C. T. Santis, A. Spott, S. Srinivasan, E. J. Stanton, C. Zhang, and J. E. Bowers, "Heterogeneous Silicon Photonic Integrated Circuits," *Journal of Lightwave Technology*, vol. 34, pp. 20–35, Jan. 2016.

[42] P. Neutens, A. Subramanian, M. Ul Hasan, C. Chen, R. Jansen, T. Claes, X. Rottenberg, B. Du Bois, K. Leyssens, P. Helin, S. Severi, A. Dhakal, F. Peyskens, L. Lagae, P. Deshpande, R. Baets, and P. Van Dorpe, "Characterization of PECVD silicon nitride photonic components at 532 and 900 nm wavelength," (Brussels, Belgium), p. 91331F, May 2014.

[43] A. Z. Subramanian, E. Ryckeboer, A. Dhakal, F. Peyskens, A. Malik, B. Kuyken, H. Zhao, S. Pathak, A. Ruocco, A. De Groote, P. Wuytens, D. Martens, F. Leo, W. Xie, U. D. Dave, M. Muneeb, P. Van Dorpe, J. Van Campenhout, W. Bogaerts, P. Bienstman, N. Le Thomas, D. Van Thourhout, Z. Hens, G. Roelkens, and R. Baets, "Silicon and silicon nitride photonic circuits for spectroscopic sensing on-a-chip [Invited]," *Photonics Research*, vol. 3, p. B47, Oct. 2015.

[44] A. H. Hosseinnia, A. H. Atabaki, A. A. Eftekhar, and A. Adibi, "High-quality silicon on silicon nitride integrated optical platform with an octave-spanning adiabatic interlayer coupler," *Optics Express*, vol. 23, p. 30297, Nov. 2015.

[45] J. F. Bauters, M. L. Davenport, M. J. R. Heck, J. K. Doylend, A. Chen, A. W. Fang, and J. E. Bowers, "Silicon on ultra-low-loss waveguide photonic integration platform," *Optics Express*, vol. 21, pp. 544–555, Jan. 2013.

[46] D. Zhu, L. Shao, M. Yu, R. Cheng, B. Desiatov, C. J. Xin, Y. Hu, J. Holzgrafe, S. Ghosh, A. Shams-Ansari, E. Puma, N. Sinclair, C. Reimer, M. Zhang, and M. Lončar, "Integrated photonics on thin-film lithium niobate," *Advances in Optics and Photonics*, vol. 13, p. 242, June 2021.

[47] R. Wu, M. Wang, J. Xu, J. Qi, W. Chu, Z. Fang, J. Zhang, J. Zhou, L. Qiao, Z. Chai, J. Lin, and Y. Cheng, "Long Low-Loss-Litium Niobate on Insulator Waveguides with Sub-Nanometer Surface Roughness," *Nanomaterials*, vol. 8, Nov. 2018.

[48] L. Arizmendi, "Photonic applications of lithium niobate crystals," *physica status solidi (a)*, vol. 201, no. 2, pp. 253–283, 2004.

[49] Y. Qi and Y. Li, "Integrated lithium niobate photonics," *Nanophotonics*, vol. 9, pp. 1287–1320, June 2020.

[50] T.-J. Lu, M. Fanto, H. Choi, P. Thomas, J. Steidle, S. Mouradian, W. Kong, D. Zhu, H. Moon, K. Berggren, J. Kim, M. Soltani, S. Preble, and D. Englund, "Aluminum nitride integrated photonics platform for the ultraviolet to visible spectrum," *Optics Express*, vol. 26, pp. 11147–11160, Apr. 2018.

[51] C. Xiong, W. H. P. Pernice, and H. X. Tang, "Low-Loss, Silicon Integrated, Aluminum Nitride Photonic Circuits and Their Use for Electro-Optic Signal Processing," *Nano Letters*, vol. 12, pp. 3562–3568, July 2012.

[52] G. N. West, W. Loh, D. Kharas, C. Sorace-Agaskar, K. K. Mehta, J. Sage, J. Chiaverini, and R. J. Ram, "Low-loss integrated photonics for the blue and ultraviolet regime," *APL Photonics*, vol. 4, p. 026101, Feb. 2019.

[53] M. K. Kiss, *Advanced Diamond Microfabrication for Microoptics and Photonics.* PhD thesis, EPFL, Lausanne, 2019.

[54] S. Mi, M. Kiss, T. Graziosi, and N. Quack, "Integrated photonic devices in single crystal diamond," *Journal of Physics: Photonics*, vol. 2, p. 042001, Aug. 2020.

[55] M. J. Burek, Y. Chu, M. S. Z. Liddy, P. Patel, J. Rochman, S. Meesala, W. Hong, Q. Quan, M. D. Lukin, and M. Lončar, "High quality-factor optical nanocavities in bulk single-crystal diamond," *Nature Communications*, vol. 5, p. 5718, Dec. 2014.

[56] P. Hill, E. Gu, M. D. Dawson, and M. J. Strain, "Thin film diamond membranes bonded on-demand with SOI ring resonators," *Diamond and Related Materials*, vol. 88, pp. 215–221, Sept. 2018.

[57] R. Kitamura, L. Pilon, and M. Jonasz, "Optical constants of silica glass from extreme ultraviolet to far infrared at near room temperature," *Applied Optics*, vol. 46, pp. 8118–8133, Nov. 2007.

[58] J. F. Bauters, M. J. R. Heck, D. John, M.-C. Tien, A. Leinse, R. G. Heideman, D. J. Blumenthal, and J. E. Bowers, "Ultra-low loss silica-based waveguides with millimeter bend radius," in *36th European Conference and Exhibition on Optical Communication*, pp. 1–3, Sept. 2010.

[59] R. Baets, R. Baets, A. Z. Subramanian, A. Z. Subramanian, S. Clemmen, S. Clemmen, B. Kuyken, B. Kuyken, P. Bienstman, P. Bienstman, N. L. Thomas, N. L. Thomas, G. Roelkens, G. Roelkens, D. V. Thourhout, D. V. Thourhout, P. Helin, and S. Severi, "Silicon Photonics: silicon nitride versus silicon-on-insulator," in *Optical Fiber Communication Conference (2016), paper Th3J.1*, p. Th3J.1, Optical Society of America, Mar. 2016.

[60] W. Bogaerts and S. K. Selvaraja, "Compact Single-Mode Silicon Hybrid Rib/Strip Waveguide With Adiabatic Bends," *IEEE Photonics Journal*, vol. 3, pp. 422–432, June 2011.

[61] S. T. Ilie, T. D. Bucio, T. Rutirawut, L. Mastronardi, I. Skandalos, H. Chong, and F. Y. Gardes, "Silicon-rich silicon nitride CMOS platform for integrated optical phased arrays," in *Smart Photonic and Optoelectronic Integrated Circuits XXIII*, vol. 11690, p. 1169005, International Society for Optics and Photonics, Mar. 2021.

[62] M. Leidinger, S. Fieberg, N. Waasem, F. Kühnemann, K. Buse, and I. Breunig, "Comparative study on three highly sensitive absorption measurement techniques characterizing lithium niobate over its entire transparent spectral range," *Optics Express*, vol. 23, p. 21690, Aug. 2015.

[63] X. P. Li, K. X. Chen, and Z. F. Hu, "Low-loss bent channel waveguides in lithium niobate thin film by proton exchange and dry etching," *Optical Materials Express*, vol. 8, pp. 1322–1327, May 2018.

[64] A. Majkić, U. Puc, A. Franke, R. Kirste, R. Collazo, Z. Sitar, and M. Zgonik, "Optical properties of aluminum nitride single crystals in the THz region," *Optical Materials Express*, vol. 5, p. 2106, Oct. 2015.

[65] C. Xiong, W. H. P. Pernice, X. Sun, C. Schuck, K. Y. Fong, and H. X. Tang, "Aluminum nitride as a new material for chip-scale optomechanics and nonlinear optics," *New Journal of Physics*, vol. 14, p. 095014, Sept. 2012.

[66] W. Bogaerts, D. Taillaert, B. Luyssaert, P. Dumon, J. V. Campenhout, P. Bienstman, D. V. Thourhout, R. Baets, V. Wiaux, and S. Beckx, "Basic structures for photonic integrated circuits in Silicon-on-insulator," *Optics Express*, vol. 12, p. 1583, Apr. 2004.

[67] Q. Wilmart, S. Brision, J.-M. Hartmann, A. Myko, K. Ribaud, C. Petit-Etienne, L. Youssef, D. Fowler, B. Charbonnier, C. Sciancalepore, E. Pargon, S. Bernabe, and B. Szelag, "A Complete Si Photonics Platform Embedding Ultra-Low Loss Waveguides for O- and C-Band," *Journal of Lightwave Technology*, vol. 39, pp. 532–538, Jan. 2021.

[68] D. Taillaert, W. Bogaerts, P. Bienstman, T. Krauss, P. Van Daele, I. Moerman, S. Verstuyft, K. De Mesel, and R. Baets, "An out-of-plane grating coupler for efficient butt-coupling between compact planar waveguides and single-mode fibers," *IEEE Journal of Quantum Electronics*, vol. 38, pp. 949–955, July 2002.

[69] D. Vermeulen, S. Selvaraja, P. Verheyen, G. Lepage, W. Bogaerts, P. Absil, D. V. Thourhout, and G. Roelkens, "High-efficiency fiber-to-chip grating couplers realized using an advanced CMOS-compatible Silicon-On-Insulator platform," *Optics Express*, vol. 18, pp. 18278–18283, Aug. 2010.

[70] R. K. Gupta, S. Chandran, and B. K. Das, "Wavelength-Independent Directional Couplers for Integrated Silicon Photonics," *Journal of Lightwave Technology*, vol. 35, pp. 4916–4923, Nov. 2017.

[71] Z. Lu, H. Yun, Y. Wang, Z. Chen, F. Zhang, N. A. F. Jaeger, and L. Chrostowski, "Broadband silicon photonic directional coupler using asymmetric-waveguide based phase control," *Optics Express*, vol. 23, pp. 3795–3808, Feb. 2015.

[72] W. Bogaerts, P. De Heyn, T. Van Vaerenbergh, K. De Vos, S. Kumar Selvaraja, T. Claes, P. Dumon, P. Bienstman, D. Van Thourhout, and R. Baets, "Silicon microring resonators," *Laser & Photonics Reviews*, vol. 6, pp. 47–73, Jan. 2012.

[73] G. Brunetti, F. Dell'Olio, D. Conteduca, M. N. Armenise, and C. Ciminelli, "Ultra-Compact Tuneable Notch Filter Using Silicon Photonic Crystal Ring Resonator," *Journal of Lightwave Technology*, vol. 37, pp. 2970–2980, July 2019.

[74] J. D. Orlet and R. C. Bailey, "Silicon Photonic Microring Resonator Arrays as a Universal Detector for Capillary Electrophoresis," *Analytical Chemistry*, vol. 92, pp. 2331–2338, Jan. 2020.

[75] L. Pavesi, L. Dal Negro, C. Mazzoleni, G. Franzò, and F. Priolo, "Optical gain in silicon nanocrystals," *Nature*, vol. 408, pp. 440–444, Nov. 2000.

[76] O. Boyraz and B. Jalali, "Demonstration of a silicon Raman laser," *Optics Express*, vol. 12, pp. 5269–5273, Oct. 2004.

[77] D.-C. Wang, C. Zhang, P. Zeng, W.-J. Zhou, L. Ma, H.-T. Wang, Z.-Q. Zhou, F. Hu, S.-Y. Zhang, M. Lu, and X. Wu, "An all-silicon laser based on silicon nanocrystals with high optical gains," *Science Bulletin*, vol. 63, pp. 75–77, Jan. 2018.

[78] A. W. Fang, H. Park, O. Cohen, R. Jones, M. J. Paniccia, and J. E. Bowers, "Electrically pumped hybrid AlGaInAs-silicon evanescent laser," *Optics Express*, vol. 14, pp. 9203–9210, Oct. 2006.

[79] M. Sakib, J. Sun, R. Kumar, J. Driscoll, K. Yeung, and H. Rong, "Demonstration of a 50 Gb/s all-silicon waveguide photodetector for photonic integration," in *Conference on Lasers and Electro-Optics (2018), paper JTh5A.7*, p. JTh5A.7, Optical Society of America, May 2018.

[80] M. Ziebell, D. Marris-Morini, G. Rasigade, J.-M. Fédéli, P. Crozat, E. Cassan, D. Bouville, and L. Vivien, "40 Gbit/s low-loss silicon optical modulator based on a pipin diode," *Optics Express*, vol. 20, pp. 10591–10596, May 2012.

[81] D. Patel, S. Ghosh, M. Chagnon, A. Samani, V. Veerasubramanian, M. Osman, and D. V. Plant, "Design, analysis, and transmission system performance of a 41 GHz silicon photonic modulator," *Optics Express*, vol. 23, pp. 14263–14287, June 2015.

[82] S. Chung, M. Nakai, and H. Hashemi, "Low-power thermo-optic silicon modulator for large-scale photonic integrated systems," *Optics Express*, vol. 27, pp. 13430–13459, Apr. 2019.

[83] J. Sun, E. Timurdogan, A. Yaacobi, Z. Su, E. S. Hosseini, D. B. Cole, and M. R. Watts, "Large-Scale Silicon Photonic Circuits for Optical Phased Arrays," *IEEE Journal of Selected Topics in Quantum Electronics*, vol. 20, pp. 264–278, July 2014.

[84] N. C. Harris, D. Bunandar, M. Pant, G. R. Steinbrecher, J. Mower, M. Prabhu, T. Baehr-Jones, M. Hochberg, and D. Englund, "Large-scale quantum photonic circuits in silicon," *Nanophotonics*, vol. 5, pp. 456–468, Aug. 2016.

[85] M. J. Collins, C. Xiong, I. H. Rey, T. D. Vo, J. He, S. Shahnia, C. Reardon, T. F. Krauss, M. J. Steel, A. S. Clark, and B. J. Eggleton, "Integrated spatial multiplexing of heralded single-photon sources," *Nature Communications*, vol. 4, p. 2582, Oct. 2013.

[86] M. Pantouvaki, S. A. Srinivasan, Y. Ban, P. De Heyn, P. Verheyen, G. Lepage, H. Chen, J. De Coster, N. Golshani, S. Balakrishnan, P. Absil, and J. Van Campenhout, "Active Components for 50 Gb/s NRZ-OOK Optical Interconnects in a Silicon Photonics Platform," *Journal of Lightwave Technology*, vol. 35, pp. 631–638, Feb. 2017.

[87] P. O'Brien, L. Carrol, C. Eason, and J. S. Lee, "Packaging of Silicon Photonic Devices," in *Silicon Photonics III: Systems and Applications* (L. Pavesi and D. J. Lockwood, eds.), Topics in Applied Physics, pp. 217–236, Berlin, Heidelberg: Springer, 2016.

[88] R. Marchetti, C. Lacava, L. Carroll, K. Gradkowski, and P. Minzioni, "Coupling strategies for silicon photonics integrated chips [Invited]," *Photonics Research*, vol. 7, pp. 201–239, Feb. 2019.

[89] D. A. B. Miller, "Perfect optics with imperfect components," *Optica*, vol. 2, pp. 747–750, Aug. 2015.

[90] Y. Kim, M. Takenaka, T. Osada, M. Hata, and S. Takagi, "Strain-induced enhancement of plasma dispersion effect and free-carrier absorption in SiGe optical modulators," *Scientific Reports*, vol. 4, p. 4683, Apr. 2014.

[91] A. Y. Takabayashi, H. Sattari, P. Edinger, P. Verheyen, K. B. Gylfason, W. Bogaerts, and N. Quack, "Continuously Tunable Silicon Photonic MEMS 2 x 2 Power Coupler," in *2021 21st International Conference on Solid-State Sensors, Actuators and Microsystems (Transducers)*, pp. 447–450, June 2021.

[92] A. Y. Takabayashi, H. Sattari, P. Edinger, P. Verheyen, K. B. Gylfason, W. Bogaerts, and N. Quack, "Broadband Compact Single-Pole Double-Throw Silicon Photonic MEMS Switch," *Journal of Microelectromechanical Systems*, vol. 30, pp. 322–329, Apr. 2021.

[93] A. Kheyraddini Mousavi and Z. C. Leseman, "Basic MEMS Actuators," in *Encyclopedia of Nanotechnology* (B. Bhushan, ed.), pp. 173–185, Dordrecht: Springer Netherlands, 2012.

[94] C. R. Knick, *Optimization of MEMS Actuator Driven by Shape Memory Alloy Thin Film Phase Change*. IntechOpen, May 2020.

[95] S. Rastjoo, R. Fechner, L. Bumke, M. Kötz, E. Quandt, and M. Kohl, "Development and co-integration of a SMA/Si bimorph nanoactuator for Si photonic circuits," *Microelectronic Engineering*, vol. 225, p. 111257, Mar. 2020.

[96] L. Lin, A. Pisano, and A. Lee, "Microbubble powered actuator," in *TRANSDUCERS '91: 1991 International Conference on Solid-State Sensors and Actuators. Digest of Technical Papers*, pp. 1041–1044, June 1991.

[97] J.-L. Pouchairet and C. Rossi, "PyroMEMS as Future Technological Building Blocks for Advanced Microenergetic Systems," *Micromachines*, vol. 12, p. 118, Jan. 2021.

[98] Z. K. Bishop, A. P. Foster, B. Royall, C. Bentham, E. Clarke, M. S. Skolnick, and L. R. Wilson, "Electro-mechanical control of an on-chip optical beam splitter containing an embedded quantum emitter," *Optics Letters*, vol. 43, pp. 2142–2145, May 2018.

[99] C. Papon, X. Zhou, H. Thyrrestrup, Z. Liu, S. Stobbe, R. Schott, A. D. Wieck, A. Ludwig, P. Lodahl, and L. Midolo, "Nanomechanical single-photon routing," *Optica*, vol. 6, pp. 524–530, Apr. 2019.

[100] Y. Akihama, Y. Kanamori, and K. Hane, "Ultra-small silicon waveguide coupler switch using gap-variable mechanism," *Optics Express*, vol. 19, pp. 23658–23663, Nov. 2011.

[101] K. Takahashi, Y. Kanamori, Y. Kokubun, and K. Hane, "A wavelength-selective add-drop switch using silicon microring resonator with a submicron-comb electrostatic actuator," *Optics Express*, vol. 16, pp. 14421–14428, Sept. 2008.

[102] T. Nagai and K. Hane, "Silicon photonic microelectromechanical switch using lateral adiabatic waveguide couplers," *Optics Express*, vol. 26, pp. 33906–33917, Dec. 2018.

[103] M.-C. M. Lee and M. C. Wu, "Tunable coupling regimes of silicon microdisk resonators using MEMS actuators," *Optics Express*, vol. 14, pp. 4703–4712, May 2006.

[104] T. Ikeda and K. Hane, "A tunable notch filter using microelectromechanical microring with gap-variable busline coupler," *Optics Express*, vol. 21, pp. 22034–22042, Sept. 2013.

[105] X. Chew, G. Zhou, F. S. Chau, J. Deng, X. Tang, and Y. C. Loke, "Dynamic tuning of an optical resonator through MEMS-driven coupled photonic crystal nanocavities," *Optics Letters*, vol. 35, pp. 2517–2519, Aug. 2010.

[106] E. Bulgan, Y. Kanamori, and K. Hane, "Submicron silicon waveguide optical switch driven by microelectromechanical actuator," *Applied Physics Letters*, vol. 92, p. 101110, Mar. 2008.

[107] M.-C. Lee, D. Hah, E. Lau, H. Toshiyoshi, and M. Wu, "MEMS-actuated photonic crystal switches," *IEEE Photonics Technology Letters*, vol. 18, pp. 358–360, Jan. 2006.

[108] T. J. Seok, N. Quack, S. Han, R. S. Muller, and M. C. Wu, "Highly Scalable Digital Silicon Photonic MEMS Switches," *Journal of Lightwave Technology*, vol. 34, pp. 365–371, Jan. 2016.

[109] S. Abe and K. Hane, "Variable-Gap Silicon Photonic Waveguide Coupler Switch With a Nanolatch Mechanism," *IEEE Photonics Technology Letters*, vol. 25, pp. 675–677, Apr. 2013.

[110] G. Nielson, D. Seneviratne, F. Lopez-Royo, P. Rakich, Y. Avrahami, M. Watts, H. Haus, H. Tuller, and G. Barbastathis, "Integrated wavelength-selective optical MEMS switching using ring resonator filters," *IEEE Photonics Technology Letters*, vol. 17, pp. 1190–1192, June 2005.

[111] M. Pruessner, K. Amarnath, M. Datta, D. Kelly, S. Kanakaraju, P.-T. Ho, and R. Ghodssi, "InP-based optical waveguide MEMS switches with evanescent coupling mechanism," *Journal of Microelectromechanical Systems*, vol. 14, pp. 1070–1081, Oct. 2005.

[112] S. Han, T. J. Seok, N. Quack, B.-w. Yoo, and M. C. Wu, "Monolithic 50×50 MEMS Silicon Photonic Switches with Microsecond Response Time," in *Optical Fiber Communication Conference (2014), paper M2K.2*, p. M2K.2, Optical Society of America, Mar. 2014.

[113] T. Ikeda, K. Takahashi, Y. Kanamori, and K. Hane, "Phase-shifter using submicron silicon waveguide couplers with ultra-small electro-mechanical actuator," *Optics Express*, vol. 18, pp. 7031–7037, Mar. 2010.

[114] S. M. C. Abdulla, L. J. Kauppinen, M. Dijkstra, M. J. d. Boer, E. Berenschot, H. V. Jansen, R. M. d. Ridder, and G. J. M. Krijnen, "Tuning a racetrack ring resonator by an integrated dielectric MEMS cantilever," *Optics Express*, vol. 19, pp. 15864–15878, Aug. 2011.

[115] C. Errando-Herranz, F. Niklaus, G. Stemme, and K. B. Gylfason, "Low-power microelectromechanically tunable silicon photonic ring resonator add-drop filter," *Optics Letters*, vol. 40, pp. 3556–3559, Aug. 2015.

[116] W. Jin, R. G. Polcawich, P. A. Morton, and J. E. Bowers, "Piezoelectrically tuned silicon nitride ring resonator," *Optics Express*, vol. 26, pp. 3174–3187, Feb. 2018.

[117] M. Poot and H. X. Tang, "Broadband nanoelectromechanical phase shifting of light on a chip," *Applied Physics Letters*, vol. 104, p. 061101, Feb. 2014.

[118] M. W. Pruessner, D. Park, T. H. Stievater, D. A. Kozak, and W. S. Rabinovich, "Broadband opto-electro-mechanical effective refractive index tuning on a chip," *Optics Express*, vol. 24, pp. 13917–13930, June 2016.

[119] M. W. Pruessner, D. Park, B. J. Roxworthy, D. A. Kozak, T. H. Stievater, N. F. Tyndall, and W. S. Rabinovich, "Loss reduction in electromechanically tunable microring cavities," *Optics Letters*, vol. 44, pp. 3346–3349, July 2019.

[120] K. Van Acoleyen, J. Roels, T. Claes, D. Van Thourhout, and R. Baets, "NEMS-based optical phase modulator fabricated on Silicon-On-Insulator," in *8th IEEE International Conference on Group IV Photonics*, pp. 371–373, Sept. 2011.

[121] H. Tian, B. Dong, M. Zervas, T. J. Kippenberg, and S. A. Bhave, "An unreleased MEMS actuated silicon nitride resonator with bidirectional tuning," in *Conference on Lasers and Electro-Optics (2018), paper SW4B.3*, p. SW4B.3, Optical Society of America, May 2018.

[122] J. Jacobs, T. Graziosi, M. Kiss, S. Han, T. J. Seok, M. C. Wu, and N. Quack, "Die level release of silicon photonic MEMS," in *2016 International Conference on Optical MEMS and Nanophotonics (OMN)*, pp. 1–2, July 2016.

[123] D. J. Monk, D. S. Soane, and R. T. Howe, "A review of the chemical reaction mechanism and kinetics for hydrofluoric acid etching of silicon dioxide for surface micromachining applications," *Thin Solid Films*, vol. 232, pp. 1–12, Sept. 1993.

[124] C. Mastrangelo and C. Hsu, "Mechanical stability and adhesion of microstructures under capillary forces. I. Basic theory," *Journal of Microelectromechanical Systems*, vol. 2, pp. 33–43, Mar. 1993.

[125] N. Tas, T. Sonnenberg, H. Jansen, R. Legtenberg, and M. Elwenspoek, "Stiction in surface micromachining," *Journal of Micromechanics and Microengineering*, vol. 6, pp. 385–397, Dec. 1996.

[126] E. Tsotsas and A. S. Mujumdar, *Modern Drying Technology, Volume 3: Product Quality and Formulation.* John Wiley & Sons, Aug. 2011. Google-Books-ID: 5210HQIwxzsC.

[127] C. S. Lee, J. T. Baek, H. J. Yoo, and S. I. Woo, "Modeling and Characterization of Gas-Phase Etching of Thermal Oxide and TEOS Oxide Using Anhydrous HF and CH 3 OH," *Journal of The Electrochemical Society*, vol. 143, p. 1099, Mar. 1996.

[128] W. I. Jang, C. A. Choi, M. L. Lee, C. H. Jun, and Y. T. Kim, "Fabrication of MEMS devices by using anhydrous HF gas-phase etching with alcoholic vapor," *Journal of Micromechanics and Microengineering*, vol. 12, pp. 297–306, May 2002.

[129] M. Winterkorn, A. Dadlani, Y. Kim, T. English, K. Harrison, J. Provine, and F. Prinz, "ATOMIC LAYER DEPOSITED ETCH STOP LAYERS FOR HYDROFLUORIC ACID," in *2016 Solid-State, Actuators, and Microsystems Workshop Technical Digest*, (Hilton Head, South Carolina, USA), pp. 133–136, Transducer Research Foundation, May 2016.

[130] K. Williams, K. Gupta, and M. Wasilik, "Etch rates for micromachining processing-part II," *Journal of Microelectromechanical Systems*, vol. 12, pp. 761–778, Dec. 2003.

[131] W. Liang, D. Suh, J. Yu, J. Bullock, and K. J. Weber, "Degradation of the surface passivation of plasma-assisted ALD Al2O3 under damp-heat exposure," *physica status solidi (a)*, vol. 212, no. 2, pp. 274–281, 2015.

Bibliography

[132] A. Rückerl, R. Zeisel, M. Mandl, I. Costina, T. Schroeder, and M. H. Zoellner, "Characterization and prevention of humidity related degradation of atomic layer deposited Al2O3," *Journal of Applied Physics*, vol. 121, p. 025306, Jan. 2017.

[133] Y.-A. Chen, I.-T. Chen, and C.-H. Chang, "Increasing etching depth of sapphire nanostructures using multilayer etching mask," *Journal of Vacuum Science & Technology B*, vol. 37, p. 061606, Nov. 2019.

[134] D. W. Hess, "Plasma etch chemistry of aluminum and aluminum alloy films," *Plasma Chemistry and Plasma Processing*, vol. 2, pp. 141–155, June 1982.

[135] U. Efrat, "Optimizing the wafer dicing process," in *Proceedings of 15th IEEE/CHMT International Electronic Manufacturing Technology Symposium*, pp. 245–253, Oct. 1993.

[136] J. Shen, X. Zhu, J. Chen, P. Tao, and X. Wu, "Investigation on the Edge Chipping in Ultrasonic Assisted Sawing of Monocrystalline Silicon," *Micromachines*, vol. 10, p. 616, Sept. 2019.

[137] B. Kim and W.-T. Park, "MEMS Packaging," in *Encyclopedia of Nanotechnology* (B. Bhushan, ed.), pp. 1351–1359, Dordrecht: Springer Netherlands, 2012.

[138] G. Jo, P. Edinger, S. J. Bleiker, X. Wang, A. Y. Takabayashi, H. Sattari, N. Quack, M. Jezzini, P. Verheyen, G. Stemme, W. Bogaerts, K. B. Gylfason, and F. Niklaus, "Wafer-level vacuum sealing for packaging of silicon photonic MEMS," in *Silicon Photonics XVI*, vol. 11691, p. 116910E, International Society for Optics and Photonics, Mar. 2021.

[139] J. Jordan, "Gold stud bump in flip-chip applications," in *27th Annual IEEE/SEMI International Electronics Manufacturing Technology Symposium*, pp. 110–114, July 2002.

[140] D. Taillaert, F. V. Laere, M. Ayre, W. Bogaerts, D. V. Thourhout, P. Bienstman, and R. Baets, "Grating Couplers for Coupling between Optical Fibers and Nanophotonic Waveguides," *Japanese Journal of Applied Physics*, vol. 45, p. 6071, Aug. 2006.

[141] S. Boscolo, M. Midrio, and C. Someda, "Coupling and decoupling of electromagnetic waves in parallel 2D photonic crystal waveguides," *IEEE Journal of Quantum Electronics*, vol. 38, pp. 47–53, Jan. 2002.

[142] Y. Xing, U. Khan, A. Riberio, and W. Bogaerts, "Behavior Model for Directional Coupler," p. 4, 2017.

[143] W.-P. Huang, "Coupled-mode theory for optical waveguides: an overview," *JOSA A*, vol. 11, pp. 963–983, Mar. 1994.

[144] M. G. Kuzyk, *Polymer Fiber Optics: Materials, Physics, and Applications.* CRC Press, Oct. 2018.

[145] L. Chrostowski and M. Hochberg, *Silicon Photonics Design.* Cambridge: Cambridge University Press, 2015.

[146] H. Sattari, A. Y. Takabayashi, Y. Zhang, P. Verheyen, W. Bogaerts, W. Bogaerts, and N. Quack, "Compact broadband suspended silicon photonic directional coupler," *Optics Letters*, vol. 45, pp. 2997–3000, June 2020.

[147] Y. Fu, T. Ye, W. Tang, and T. Chu, "Efficient adiabatic silicon-on-insulator waveguide taper," *Photonics Research*, vol. 2, pp. A41–A44, June 2014.

[148] H. Yun, W. Shi, Y. Wang, L. Chrostowski, and N. A. F. Jaeger, "2x2 adiabatic 3-dB coupler on silicon-on-insulator rib waveguides," in *Photonics North 2013*, vol. 8915, pp. 251–256, SPIE, Oct. 2013.

[149] R. Legtenberg, A. W. Groeneveld, and M. Elwenspoek, "Comb-drive actuators for large displacements," *Journal of Micromechanics and Microengineering*, vol. 6, pp. 320–329, Sept. 1996.

[150] S. Boisseau, G. Despesse, and B. A. Seddik, "Adjustable Nonlinear Springs to Improve Efficiency of Vibration Energy Harvesters," *Journal of Applied Mechanics*, vol. 80, p. 061013, Nov. 2013.

[151] W. Bogaerts, H. Sattari, P. Edinger, A. Y. Takabayashi, I. Zand, X. Wang, A. Ribeiro, M. Jezzini, C. Errando-Herranz, G. Talli, K. Saurav, M. G. Porcel, P. Verheyen, B. Abasahl, F. Niklaus, N. Quack, K. B. Gylfason, P. O'Brien, and U. Khan, "MORPHIC: programmable photonic circuits enabled by silicon photonic MEMS," in *Silicon Photonics XV*, vol. 11285, p. 1128503, International Society for Optics and Photonics, Feb. 2020.

[152] W. Tang, M. Lim, and R. Howe, "Electrostatic Comb Drive Levitation And Control Method," *Journal of Microelectromechanical Systems*, vol. 1, pp. 170–178, Dec. 1992.

[153] "Cisco Global Cloud Index: Forecast and Methodology 2013–2018 White Paper," p. 41, 2014.

[154] H. Sattari, A. Y. Takabayashi, P. Edinger, P. Verheyen, K. B. Gylfason, W. Bogaerts, and N. Quack, "Low-Voltage Silicon Photonic MEMS Switch with Vertical Actuation," in *2021 IEEE 34th International Conference on Micro Electro Mechanical Systems (MEMS)*, pp. 298–301, Jan. 2021.

[155] B. G. Lee, N. Dupuis, P. Pepeljugoski, L. Schares, R. Budd, J. R. Bickford, and C. L. Schow, "Silicon Photonic Switch Fabrics in Computer Communications Systems," *Journal of Lightwave Technology*, vol. 33, pp. 768–777, Feb. 2015.

[156] G. O'Brien, D. J. Monk, and L. Lin, "MEMS cantilever beam electrostatic pull-in model," in *Design, Characterization, and Packaging for MEMS and Microelectronics II*, vol. 4593, pp. 31–41, SPIE, Nov. 2001.

[157] R. Legtenberg, J. Gilbert, S. Senturia, and M. Elwenspoek, "Electrostatic curved electrode actuators," *Journal of Microelectromechanical Systems*, vol. 6, pp. 257–265, Sept. 1997.

[158] P. Dong, W. Qian, S. Liao, H. Liang, C.-C. Kung, N.-N. Feng, R. Shafiiha, J. Fong, D. Feng, A. V. Krishnamoorthy, and M. Asghari, "Low loss shallow-ridge silicon waveguides," *Optics Express*, vol. 18, p. 14474, July 2010.

[159] A. W. Poon, X. Luo, F. Xu, and H. Chen, "Cascaded Microresonator-Based Matrix Switch for Silicon On-Chip Optical Interconnection," *Proceedings of the IEEE*, vol. 97, pp. 1216–1238, July 2009.

[160] C. Wang, M. Zhang, B. Stern, M. Lipson, and M. Lončar, "Nanophotonic lithium niobate electro-optic modulators," *Optics Express*, vol. 26, pp. 1547–1555, Jan. 2018.

[161] T. Ikeda and K. Hane, "A microelectromechanically tunable microring resonator composed of freestanding silicon photonic waveguide couplers," *Applied Physics Letters*, vol. 102, p. 221113, June 2013.

[162] M. Mancinelli, R. Guider, P. Bettotti, M. Masi, M. R. Vanacharla, J.-M. Fédéli, D. V. Thourhout, and L. Pavesi, "Optical characterization of silicon-on-insulator-based single and coupled racetrack resonators," *Journal of Nanophotonics*, vol. 5, p. 051705, Jan. 2011.

[163] D. Marpaung, B. Morrison, R. Pant, C. Roeloffzen, A. Leinse, M. Hoekman, R. Heideman, and B. J. Eggleton, "Si$_3$N$_4$ ring resonator-based microwave photonic notch filter with an ultrahigh peak rejection," *Optics Express*, vol. 21, pp. 23286–23294, Oct. 2013.

[164] J. Carolan, C. Harrold, C. Sparrow, E. Martín-López, N. J. Russell, J. W. Silverstone, P. J. Shadbolt, N. Matsuda, M. Oguma, M. Itoh, G. D. Marshall, M. G. Thompson, J. C. F. Matthews, T. Hashimoto, J. L. O'Brien, and A. Laing, "Universal linear optics," *Science*, vol. 349, pp. 711–716, Aug. 2015.

[165] M. H. Khan, H. Shen, Y. Xuan, L. Zhao, S. Xiao, D. E. Leaird, A. M. Weiner, and M. Qi, "Ultrabroad-bandwidth arbitrary radiofrequency waveform generation with a silicon photonic chip-based spectral shaper," *Nature Photonics*, vol. 4, pp. 117–122, Feb. 2010.

[166] J. Sun, E. Timurdogan, A. Yaacobi, E. S. Hosseini, and M. R. Watts, "Large-scale nanophotonic phased array," *Nature*, vol. 493, Jan. 2013.

[167] P. Edinger, C. Errando-Herranz, and K. B. Gylfason, "Low-Loss MEMS Phase Shifter for Large Scale Reconfigurable Silicon Photonics," in *2019 IEEE 32nd International Conference on Micro Electro Mechanical Systems (MEMS)*, pp. 919–921, Jan. 2019.

[168] P. Edinger, C. Errando-Herranz, and K. B. Gylfason, "Reducing Actuation Nonlinearity of MEMS Phase Shifters for Reconfigurable Photonic Circuits," in *Conference on Lasers and Electro-Optics*, (San Jose, California), p. SF2H.3, OSA, 2019.

[169] P. Edinger, C. Errando-Herranz, A. Y. Takabayashi, H. Sattari, N. Quack, P. Verheyen, W. Bogaerts, and K. B. Gylfason, "Compact low loss MEMS phase shifters for scalable field-programmable silicon photonics," in *Conference on Lasers and Electro-Optics*, (Washington, DC), p. SM3J.2, OSA, 2020.

[170] P. Edinger, K. Kristinsson, C. Errando-Herranz, A. Y. Takabayashi, H. Sattari, N. Quack, P. Verheyen, W. Bogaerts, and K. B. Gylfason, "Silicon photonic MEMS phase shifter with µs time constant built on a foundry platform," in *Conference on Lasers and Electro-Optics*, (San Jose, California), p. STu2Q.1, OSA, 2021.

[171] D. Dai, J. Bauters, and J. E. Bowers, "Passive technologies for future large-scale photonic integrated circuits on silicon: polarization handling, light non-reciprocity and loss reduction," *Light: Science & Applications*, vol. 1, pp. e1–e1, Mar. 2012.

[172] Y. Akihama and K. Hane, "Single and multiple optical switches that use freestanding silicon nanowire waveguide couplers," *Light: Science & Applications*, vol. 1, pp. e16–e16, June 2012.

[173] R. Chatterjee and Chee Wei Wong, "Nanomechanical Proximity Perturbation for Switching in Silicon-Based Directional Couplers for High-Density Photonic Integrated Circuits," *Journal of Microelectromechanical Systems*, vol. 19, pp. 657–662, June 2010.

[174] T. J. Seok, N. Quack, S. Han, W. Zhang, R. S. Muller, and M. C. Wu, "64×64 Low-loss and broadband digital silicon photonic MEMS switches," in *2015 European Conference on Optical Communication (ECOC)*, pp. 1–3, Sept. 2015.

[175] T. J. Seok, N. Quack, S. Han, R. S. Muller, and M. C. Wu, "Large-scale broadband digital silicon photonic switches with vertical adiabatic couplers," *Optica*, vol. 3, pp. 64–70, Jan. 2016.

[176] S. Han, T. J. Seok, N. Quack, B.-W. Yoo, and M. C. Wu, "Large-scale silicon photonic switches with movable directional couplers," *Optica*, vol. 2, pp. 370–375, Apr. 2015.

[177] T. J. Seok, T. J. Seok, J. Luo, Z. Huang, K. Kwon, J. Henriksson, J. Jacobs, L. Ochikubo, R. S. Muller, and M. C. Wu, "MEMS-Actuated 8×8 Silicon Photonic Wavelength-Selective Switches with 8 Wavelength Channels," in *Conference on Lasers and Electro-Optics (2018), paper STu4B.1*, p. STu4B.1, Optical Society of America, May 2018.

[178] T. J. Seok, N. Quack, S. Han, and M. C. Wu, "50×50 Digital Silicon Photonic Switches with MEMS-Actuated Adiabatic Couplers," in *Optical Fiber Communication Conference (2015), paper M2B.4*, p. M2B.4, Optical Society of America, Mar. 2015.

Alain Yuji Takabayashi

Chemin d'Éterpy 73
1020 Renens
℡ +41 76 295 70 97
✉ alain.takabayashi@epfl.ch
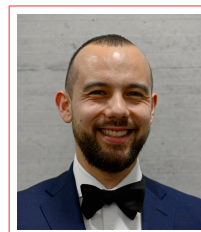
Education

2018 - Present	**PhD**, *École Polytechnique Fédérale de Lausanne (EPFL)*, *Electrical and Micro Engineering*
Thesis	Integration of MEMS in Silicon Photonics
2015 - 2017	**MSc**, *Eidgenössische Technische Hochschule, Zürich (ETHZ)*, *Electrical Engineering and Information Technology*
Thesis	Continuous Time Delta Sigma Modulator Based ADC
2011 - 2015	**BSc**, *University of California, Berkeley (UCB)*, *Electrical Engineering and Computer Science*

Employment

2018 - Present	**Research Assistant**, *École Polytechnique Fédérale de Lausanne*
Fall 2017	**Research Intern**, *Swiss Federal Institute of Technology, Zurich, Institute of Electronics*
Fall 2015	**Teaching Assistant for Microfabrication Technology (EE143)**, *University of California, Berkeley*
Fall 2014	**Course Reader for Microfabrication Technology (EE143) and Linear Integrated Circuits (EE140)**, *University of California, Berkeley*

Selected Publications

A. Y. Takabayashi et al., *Broadband Compact Single-Pole Double-Throw Silicon Photonic MEMS Switch*, Journal of Microelectromechanical Systems (2021)

C. Errando-Herranz, A. Y. Takabayashi, P. Edinger, H. Sattari, K. B. Gylfason and N. Quack, *MEMS for Photonic Integrated Circuits* IEEE Journal of Selected Topics in Quantum Electronics (2020)

N. Quack, H. Sattari, A .Y. Takabayashi, Y. Zhang, P. Verheyen, W. Bogaerts, P. Edinger, C. Errando-Herranz, K. B. Gylfason *MEMS-Enabled Silicon Photonic Integrated Devices and Circuits* IEEE Journal of Quantum Electronics (2019)

Experience & Skills

- Cleanroom Fabrication Expertise
- Finite Element Modeling - **COMSOL**
- Layout Editors - **KLayout, L-Edit**
- PCB Layout - **Altium**
- Programming - **MATLAB** and **Python**
- MEMS Design
- Photonic Circuit Design - **IPKISS**
- Analog Circuit Design - **Cadence, HSPICE**
- Device Simulation - **Sentaurus Device**

Languages

- **English** Native Speaker
- **French** B1
- **German** C1/C2
- **Japanese** A2